Frustrated Quantum Magnets and Correlated Kondo Systems

Von der Fakultät für Elektrotechnik, Informationstechnik, Physik
der Technischen Universität Carolo-Wilhelmina
zu Braunschweig

zur Erlangung des Grades eines
Doktors der Naturwissenschaften
(Dr.rer.nat.)
genehmigte

DISSERTATION

von

Mohammad Siahatgar

geboren in Teheran

1. Referent: Prof. Dr. Gertrud Zwicknagl
2. Referent: Priv.-Doz. Dr. Peter Thalmeier
eingereicht am: 03.05.2012
mündliche Prüfung (Disputation) am: 22.06.2012
Druckjahr: 2012

Vorveröffentlichungen der Dissertation

Teilergebnisse aus dieser Arbeit wurden mit Genehmigung der Fakultät für Elektrotechnik, Informationstechnik, Physik, vertreten durch die Mentorin der Arbeit, in folgenden Beiträgen vorab veröffentlicht:

Publikationen

1. B. Schmidt, M. Siahatgar, und P. Thalmeier, “Frustrated local-moment models for iron pnictide magnetism”, *Phys. Rev. B*, vol. 81, p. 165101 (2010)

2. B. Schmidt, M. Siahatgar, P. Thalmeier, und A. A. Tsirlin, “The two-dimensional frustrated Heisenberg model on the orthorhombic lattice”, *Journal of Physics: Conference Series*, vol. 200, no. 2, p. 022055 (2010)

3. B. Schmidt, M. Siahatgar, und P. Thalmeier, “Ordered moment in the anisotropic and frustrated square lattice Heisenberg model”, *Phys. Rev. B*, vol. 83, p. 075123 (2011)

4. M. Siahatgar, B. Schmidt, und P. Thalmeier, “Staggered-moment dependence on field-tuned quantum fluctuations in two-dimensional frustrated antiferromagnets”, *Phys. Rev. B*, vol. 84, p. 064431 (2011)

5. M. Siahatgar, B. Schmidt, P. Thalmeier, und G. Zwicknagl, “Moment screening in the correlated Kondo lattice model”, Eingereicht bei *New Journal of Physics*

Tagungsbeiträge

1. M. Siahatgar, B. Schmidt, und P. Thalmeier, “The $S = 1/2$ Heisenberg model on the 2D orthorhombic lattice: A numerical study”, DPG-Frühjahrstagung (Poster), Regensburg, Deutschland (2010)

2. M. Siahatgar, B. Schmidt, und P. Thalmeier, “The 2D $S = 1/2$ Heisenberg model on the orthorhombic lattice”, Perspectives in Highly Frustrated Magnetism (Poster), Dresden, Deutschland (2011)

3. M. Siahatgar, B. Schmidt, und P. Thalmeier, “The 2D $S = 1/2$ Heisenberg model on an orthorhombic lattice”, Emergent Quantum States in Complex Correlated Matter (Poster), Dresden, Deutschland (2011)

4. M. Siahatgar, B. Schmidt, und P. Thalmeier, “Finite-size scaling analysis of the spatially anisotropic frustrated $S = 1/2$ Heisenberg model”, DPG-Frühjahrstagung (Poster), Dresden, Deutschland (2011)
5. M. Siahatgar, B. Schmidt, und P. Thalmeier, “Non-monotonic magnetic field dependence of the staggered-moment in two-dimensional frustrated antiferromagnets”, APS March Meeting (Vortrag), Boston, USA (2012)
6. B. Schmidt, M. Siahatgar, und P. Thalmeier, “Field-induced staggered moment stabilization in frustrated quantum magnets”, DPG-Frühjahrstagung (Vortrag), Berlin, Deutschland (2012)

Contents

List of Figures

List of Tables

I. Introduction

One of the primary subjects of study in the field of equilibrium statistical physics is the phenomena of order and disorder, or in other words, presence or absence of correlations and symmetries in a physical many-body system. In the context of quantum magnetism, the search for novel and exotic states has been the subject of much interest [1]. Above all, the effect of competing or "frustrated" interactions between magnetic moments on magnetic order have been studied since 1950. It started with investigation of the Ising model with antiferromagnetic interaction on a triangular lattice by G. H. Wannier [2], in which he showed that there is a very large degeneracy of ground-state present. The realizations of competing interactions were discovered later in helical magnetic structures by A. Yoshimori [3] and separately by J. Villain [4] and T. A. Kaplan [5] in 1959, and was studied more in subsequent work [6, 7]. Two decades later, with the introduction of the concept of "frustration" by G. Toulouse [8–10] and further contributions by J. Villain [11], the competing interactions in spin models in the context of spin glasses created more interest. The research on the subject gained momentum in 1980, when Villain and coauthors [12] proposed the idea of *order from disorder*, by considering a "domino model" of frustrated Ising spins on the square lattice with nearest neighbors interactions, including ferromagnetic exchanges in rows and alternating ferromagnetic and antiferromagnetic exchanges in columns. They concluded that the model exhibits ferromagnetic long range order at low temperatures but not at $T = 0$ [12]. This unusual property is one example which remarkably shows the effect of *fluctuations*, in lifting the degeneracies between different orderings without having required explicit perturbations. In quantum spin models at zero temperature, quantum fluctuations may also act similarly to provide a degeneracy-lifting mechanism [13–16].

The *exchange interaction* formulation in quantum mechanics stands for the change of the energy of two or more particles with overlapping wave functions. For electrons it manifests itself by taking into account the Coulomb force in addition to the Pauli exclusion principle. Direct exchange in orthogonal orbitals favors ferromagnetism [17]. However, antiferromagnetism is much more present in nature, and other mechanism such as direct exchange for non-orthogonal orbitals, or indirect exchange, e. g. via conduction electrons, seem to be the underlying mechanisms for it. Also, superexchange [18] in insulators is another strong and usually antiferromagnetic coupling, which, unlike direct exchange, requires at least one intermediate orbital.

A generalized Heisenberg Hamiltonian on a crystal is written as a sum of exchange terms, explicitly as a tensor product of spin operators, over all pairs in a many-electron system, including possible ferro- and antiferromagnetic couplings. This model, known as the quantum Heisenberg Model, is widely used to study the critical points and phase transitions of a magnetic system. For spin-$\frac{1}{2}$ systems, it is also equivalent to the low-energy limit of the half-filled, non-degenerate Hubbard Hamiltonian for large on-site Coulomb repulsion U. The ferromagnetic model with a negative coupling constant can successfully describe ferromagnetic Mott insulators such as EuO [19] or K_2CuF_4 [20], as far as their magnetic properties are concerned. The cuprate parent compound La_2CuO_4 on the other hand is an example of an antiferromagnetic Mott insulator with positive superexchange between $S = \frac{1}{2}$ Cu spins [21].

The central issue of this work is the effect of magnetic frustration which arises in magnets with several competing exchange interactions. It appears in situations where a certain type of local order, favored by physical interactions, cannot propagate throughout space [22]. For instance, frustration can occur in the Heisenberg model when spins do not find a unique orientation to minimize interaction energy with all their neighbors. In general, frustration happens either due to competing interactions (such as simultaneous ferro- and antiferromagnetic interactions or including interactions between more distanced neighbors), or by nearest neighbor antiferromagnetic interactions in certain lattice structures (such as in triangular, Kagomé, or two- or three-dimensional pyrochlore lattices), where the geometry of the lattice imposes constraints on minimization of the interaction energy. In the former case, such competitions can usually be released by changing a parameter in the system (e. g. temperature, pressure or magnetic field), to enhance a particular interaction and force the system into a different ordered state. In the latter case of “geometric frustration” a topic of great interest is the existence of a disordered “spin liquid” state characterized by only short range spin correlations in the ground-state. The hallmark effects of frustration are a degenerate ground-state or large number of low energy excited states. The former may lead to nonzero entropy at zero temperature [2] and the latter causes an anomalous low temperature thermodynamic behavior. Lifting the degeneracy by quantum fluctuations may be the source of new phases and dynamics.

Frustrated quantum magnetic systems in low dimensions have been the subject of extensive study over the last decades. In 1973, P. W. Anderson with the help of Hulthén's cluster approach [23] obtained a variational estimate for the ground-state energy of the triangular antiferromagnetic Heisenberg model [24], which was much lower than the result obtained from the best (three-sublattice) Néel state from a spin-wave theory. He postulated then, that this state may be a non-magnetic, probably disordered "resonating-valence-bond" (RVB) state. Further evidence was given together with P. Fazekas [25], where the RVB state has been suggested as the ground-state of a new "spin liquid" phase. Realizing such a phase experimentally, where the local magnetic moments are present in the system, but without showing any ordering down to low temperatures [26], is still an open problem. So far, no definite candidate has been found, and only a few possibilities are still under investigation [27–31] most having a two-dimensional Kagomé or a three-dimensional hyper-Kagomé structure [32, 33].

After the discovery of copper oxide superconductors, the Heisenberg model with spin-$\frac{1}{2}$ on the square lattice with nearest and next-nearest neighbor interaction, the so-called $J_1 - J_2$ model, gained renewed attention. A possible RVB state in this model has been proposed [34] as the fundamental starting point for the theory of high-T_c superconductivity [35]. However the cuprates have a Néel ordered ground-state [36] and their lattice symmetry and effective spin size were obtained from X-ray and neutron scattering experiments. The square lattice sites correspond to the copper atoms and spins in the two-dimensional copper–oxygen plane, which is the common structural feature of this family. In this context, the undoped cuprate superconductors are viewed as Mott insulators (in which electrons are localized in $d_{x^2-y^2}$ orbitals and have only their spin degree of freedom) with antiferromagnetic ordering [37]. The Heisenberg model has been largely successful in describing the magnetic state of cuprate parent compounds [38, 39], which is of the conventional Néel type instead of an RVB state. The magnetic order gradually disappears with increasing doping and subsequently superconductivity develops.

In this work the frustrated $J_1 - J_2$ Heisenberg model will be studied in detail with the help of both analytical spin-wave method and in particular numerical Exact Diagonalization (ED) and Finite-Temperature Lanczos Method (FTLM). The recent intense interest in this model stems from two facts: i) First, it is a generic model for studying the interplay of frustration and quantum fluctuations and its effect on the stability of magnetic order [35, 40, 41] and the possibility of nonmagnetic spin liquid phases and possible exotic nonmagnetic long range order, such as stacked dimer and spin nematic state. ii) Second, there are numerous quasi-2D transition metal compounds whose magnetism is described by this model, therefore it is of great practical importance, e.g. for explanation of thermodynamic properties (susceptibility, specific heat, ordered moment) as well as for the description of their dynamical response and spin-wave excitations.

We first give a brief qualitative description of the possible phases in this model which depend on the frustration ratio J_2/J_1. There are three different magnetically ordered regions, a ferromagnetic phase, a Néel antiferromagnetic phase with the ordering vector (π, π) as well as two degenerate columnar antiferromagnetic phases with ordering vectors $(\pi, 0)$ and $(0, \pi)$ along two different crystal directions. The degeneracy is lifted in the generalized $J_{1ab} - J_2$ model on the rectangular lattice which will also be investigated. Classically these are the only possible phases. However, quantum fluctuations diverge in the crossover regions between the antiferromagnetic phases because lines of zeros for the spin-wave energies appear. This destroys the ordering of spins in a narrow region around the phase boundary. There exists two proposals for the nature of these “disordered” regions, namely the valence bond crystal of spin dimers for $J_1 > 0$, and the spin-nematic phase for $J_1 < 0$. In the RVB state, which was originally proposed by Pauling [42] in metals, each pair (dimer) of spins form a singlet with $S = 0$, and the nonmagnetic ground-state is expressed as the superposition of all possible such dimers. This “resonating” property makes the state translationally invariant, but the spin dimers may also be arranged in a fixed stacking, then the translational symmetry is broken and a valence bond “crystal” is formed. This state has been suggested for the crossover region between the Néel and columnar antiferromagnetic phases [43]. For ferromagnetic $J_1 < 0$ the bond spin-nematic phase was proposed as a candidate for the transition region from the columnar antiferromagnetic to the ferromagnetic phase [44] In this hidden order phase the time reversal and translational symmetries are preserved while the spin-rotational SU(2) symmetry is broken which is equivalent to a quadrupolar type of long range bond correlations.

Considerable effort has been devoted to the investigation of these quantum phases [45, 46]. However, it should be stressed that to this date there is not a single quasi-2D compound known where they are realized. Therefore this work focuses rather on the magnetically ordered sectors of the phase diagram. There quantum fluctuations and frustration lead to characteristic effects in field dependence of the ordered and uniform moments and temperature dependence of the susceptibility which may be calculated by the above mentioned methods and compared to experiments in compound classes introduced below. Indeed our methods (ED with finite size scaling analysis and spin-wave theory) are restricted to the magnetically ordered regime and break down close to the classical phase boundaries. This will be used for an estimate of the width of the nonmagnetic sectors. A comparison of both analytical and numerical methods will show that the range of their validity is not identical, which prevents a precise determination of the extent of these sectors.

Our analysis of the magnetically ordered sectors is applicable to various classes of compounds which will be quantitatively studied in this work: 1) The isotropic J_1-J_2 model will be applied to a family of quasi-2D layered vanadium oxide compounds that are all within the sector of columnar antiferromagnetism. 2) The same model is also applicable to quasi-2D organic copper compounds (Cu-pyrazine) which are located in the Néel phase sector of the phase diagram. 3) The general anisotropic $J_{1a,b}-J_2$ model has also been much discussed for the columnar antiferromagnetism of Fe-pnictide compounds, although the latter are not Mott insulators (see Ref. [47] and references cited therein). Nevertheless in the analysis of spin-wave excitations determined by inelastic neutron scattering mainly this model has been used e.g. [48]. It leads to the surprising conclusion that the nearest neighbor interactions $J_{1a,b}$ along the orthorhombic a and b axes are strongly anisotropic, indeed may even have different signs. This provided the motivation to study this model in detail in the present work in the whole frustration-anisotropy parameter range. The physical origin of the pronounced anisotropy may be found in an underlying orbital order of Fe 3d orbitals [49]. It was also noticed that the experimental saturation moment from neutron diffraction may be smaller than the expected one (from LSDA calculations) by up to a factor two. Within the localized moment picture for Fe pnictides is has been proposed that this may be due to the frustration inherent in the $J_{1a,b}-J_2$ model. It will be demonstrated here that this cannot be upheld and that anisotropy has actually a stabilizing effects on the moment in the columnar antiferromagnetic region of the phase diagram.

In the localized spin models discussed so far the exchange frustration is already manifest at the level of the construction of the Hamiltonian. In itinerant electron systems, however, the appearance of frustration is a more subtle issue. In fact in a tight binding picture of noninteracting conduction electrons the scalar hopping amplitudes cannot be frustrated, irrespective of their range and the geometry of the underlying lattice. Frustration can only emerge through the effect of correlations which lead to local spin fluctuations and induced inter-site interactions with increasing interaction strength. This mechanism which is generally much less studied will be investigated in the context of the correlated Kondo lattice model. It is of great importance for the magnetism and quantum critical behavior of heavy fermion compounds. In particular, the competition or frustration between the on-site (Kondo-) singlet formation and correlation-induced inter-site magnetic correlations will be studied with numerical ED and analytical bond-operator method. This analysis will also be relevant for the physics of finite clusters of Kondo atoms on surfaces.

To conclude this introduction to the subject of this work a brief description of the content of the following sections will be given.

Chapter 2 introduces the spatially anisotropic model and describes the model Hamiltonian, as well as discussing a few realizations and motivations in some compound families.

In Chapter 3, the method of analytical spin-wave theory used in this work is described. Using a local coordination system defined by the moment orientation in a magnetic field and a linear approximation, the classical ground-state energy as well as the effects of quantum fluctuations are studied. The spin-wave spectra of the model and the magnetic field dependent properties such as the magnetization and the ordered moment are also discussed.

Chapter 4 explains the method of unbiased numerical exact diagonalization, used to diagonalize the spin Hamiltonian (described in Chapter 2) with the aim of the Lanczos algorithm. The calculation of the ground-state properties such as spin correlation functions and static structure factor and their evaluation in a finite system up to 30 spins are described. Furthermore, the finite-temperature Lanczos method has been widely incorporated to study the thermodynamic behavior of physical quantities over changing various system parameters. This method is based on a random sampling algorithm, and is used to obtain the temperature dependence of magnetic susceptibility, heat capacity, and 3^{rd} order susceptibility.

In Chapter 5, the numerical implementation of the ED method and the necessary finite-size scaling analysis is extensively described. A major problem for evaluating physical quantities within the exact diagonalization method for finite tiles is the proper choice among the numerous possible tiles. We present a novel and systematic way to select the best tiles for the finite-size scaling analysis. The general way to construct the reciprocal space, and incorporating point group symmetries are also described in this chapter.

Chapter 6 presents the numerical ED results obtained for the ground-state of the anisotropic $J_{1a,b}-J_2$ model model, and they are compared with those of the linear spin-wave theory. A complete survey of the model properties in the the whole parameter space is given and both methods show excellent agreement in the ordered regions. A detailed finite-size analysis on the ground-state quantities is carried out and the complete phase diagram of the model is presented. In the thermodynamic limit, results for the ground-state energy and the ordered moment are exhaustively investigated, and a discussion for the quality of the finite-size scaling fit and its relation to magnetically disordered phases is given. Our results show that anisotropy unexpectedly *stabilizes* the ordered moment. From this, we may conclude that frustration effects cannot be used to explain the observed low ordered moment in Fe-pnictides.

Chapter 7 gives the results for the thermodynamic quantities using the numerical FTLM technique. The magnetic susceptibility is calculated and applied to the experimental data of a quasi two-dimensional $S = \frac{1}{2}$ copper pyrazine compound in order to determine the exchange constants. A discussion of the effect of frustration and anisotropy on the susceptibility is given and used to determine the frustration ratio in Cu-pyrazine. This method is, however, not very accurate and may produce ambiguous results.

Chapter 8 therefore presents the results obtained by using a new method to determine the frustration ratio in two-dimensional quantum magnets. We conclusively demonstrate that the magnetization and in particular the staggered moment shows a variation with field that depends strongly on the frustration ratio J_2/J_1. The latter provides a new powerful criterion to determine this ratio and we apply this method to Cu-pyrazine.

Chapter 9 contains the conclusions of the in-depth investigation of the anisotropic $J_{1a,b}-J_2$ model in this work.

Chapter 10 addresses the itinerant correlated Kondo lattice model which describes in a generic way the frustration or competition between on-site singlet formation and emerging inter-site magnetic correlations due to correlation effects.. The model is introduced and its ground-state as well as finite-temperature properties are thoroughly investigated. In this model the dependence of the Kondo temperature scale on the Coulomb repulsion is examined. We report a new nonmonotonic dependence of the local moment on the correlation strength U. We also show that the Kondo temperature scale increases with U, resolving an existing controversy on this subject. We study the system both with exact diagonalization technique and the bond operator theory, and show that these two methods agree very well on the calculation of the local moment.

Finally, a brief summary of the main achievements of this work is given, concerning both development of numerical and analytical methods and their application to physical compounds and problems.

II. The Frustrated and Anisotropic $J_1 - J_2$ Heisenberg Model

Here we introduce and describe in detail the model Hamiltonian we study in the current work. Different system parameters and their role are briefly discussed and realizations of this model in several compounds are presented. The classical phase diagram of the system is introduced and some estimated and measured values for the exchange interactions constants are given in the following tables.

2.1. Model definition

The effective localized spin Hamiltonian we shall discuss in this work has the form

$$\mathcal{H} = \sum_{\langle ij \rangle} J_{ij}\, \mathbf{S}_i \cdot \mathbf{S}_j - g\mu_{\mathrm{B}} \mathbf{H} \sum_i \mathbf{S}_i \tag{2.1}$$

where the sum in the first term extends over bonds $\langle ij \rangle$ connecting sites i and j. $\mathbf{S}_i = (S_i^x, S_i^y, S_i^z)$ are the spin operators acting on a spin on site i. To preserve U(1) symmetry, the magnetic field points into the z direction defined by the anisotropy introduced above. The second term in Eq. 2.1 is the Zeeman energy where an isotropic g-factor has been assumed. We include this term to investigate uniform and staggered magnetizations as well as magnetocaloric properties.

2.1.1. Frustrated isotropic model

The Hamiltonian for the two-dimensional J_1 - J_2 with $S = \frac{1}{2}$ model on the *square lattice* is given by

$$\mathcal{H} = J_1 \sum_{\langle ij \rangle_1}^{N} \mathbf{S}_i \cdot \mathbf{S}_j + J_2 \sum_{\langle ij \rangle_2}^{N} \mathbf{S}_i \cdot \mathbf{S}_j. \tag{2.2}$$

The first sum is taken over bonds between nearest-neighbor sites along both a and b directions of the square lattice. $\langle ij \rangle_2$ denotes bonds connecting the next-nearest

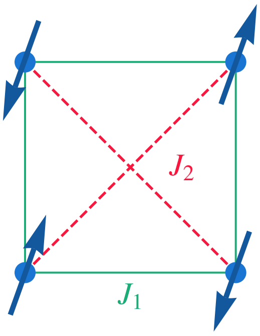

Figure 2.1.: Plaquettes of the lattice in the $J_1 - J_2$ model. The classical spin pattern of the Néel antiferromagnetic phase is shown as an example, to demonstrate that the nearest neighbor couplings, together with next-nearest neighbor antiferromagnetic interactions in general may lead to frustration (for the bonds shown in red dashed lines).

neighbors along the diagonals of a plaquette. An illustration of each plaquette of the lattice is shown in Fig. 2.1. As an example, the classical spin pattern of the Néel phase is also shown in the figure. Having antiferromagnetic nearest neighbor couplings, together with the next-nearest neighbor interactions generally may lead to frustration in this model, depending on the sign of J_1 and J_2.

We use a parametrization of the exchange constants which facilitates the discussion of the whole phase diagram. We define a frustration angle ϕ such that

$$\begin{aligned} J_1 &= J_{\mathrm{c}} \cos\phi, \\ J_2 &= J_{\mathrm{c}} \sin\phi, \\ J_{\mathrm{c}} &= \sqrt{J_1^2 + J_2^2}, \end{aligned}$$

where $\phi = \tan^{-1}\left(\frac{J_2}{J_1}\right)$ and J_{c} defines the overall energy scale of the model and is used as the energy unit. The possible classical phases for this system are ferromagnetic (FM) with $\boldsymbol{Q}_{\mathrm{FM}} = (0,0)$, Néel antiferromagnet (NAF) with $\boldsymbol{Q}_{\mathrm{NAF}} = (\pi,\pi)$, and columnar antiferromagnet (CAF) with $\boldsymbol{Q}_{\mathrm{CAF}} = (\pi,0)$ or degenerately equivalent $(0,\pi)$. The range of stability of these phases is shown in the right panel of Fig. 2.2, which illustrates the classical phase diagram. Here, the radius of the circle corresponds to J_{c}, and the frustration parameter ϕ denotes the angle counted from the horizontal axis $J_2 = 0$. It is obtained from a comparison of classical (i. e. mean field) ground-state energies $E^{\mathrm{cl}}(\phi, \mathbf{Q})$ for the three phases (Section 3.2). In their

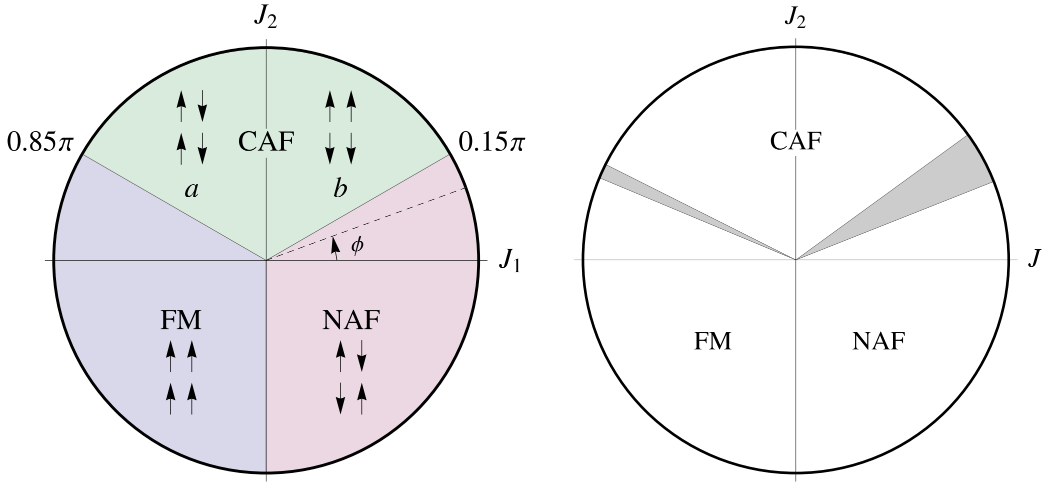

Figure 2.2.: Left: classical phase diagram of the Hamiltonian defined in Eq. 2.3 as a function of the frustration angle ϕ. ($-\pi \leqslant \phi \leqslant \pi$) The overall energy scale factor J_c is the radius of the circle and is the reference scale. The borders happen at $\phi = -\frac{3\pi}{2}, \cos^{-1}(-\frac{2}{\sqrt{5}})$, and $\cos^{-1}(\frac{2}{\sqrt{5}})$. Right: disordered regions with no magnetic order, obtained by including the quantum effects.

stability region we obtain

$$\begin{aligned} E_{\mathrm{NAF}}(\phi) &= 2(\sin\phi - \cos\phi) \\ E_{\mathrm{CAF}}(\phi) &= -2\sin\phi \\ E_{\mathrm{FM}}(\phi) &= 2(\sin\phi + \cos\phi). \end{aligned} \tag{2.3}$$

The left plot of Fig. 2.2 shows the disordered regions of the isotropic phase, where the magnetic order vanishes. These “nonmagnetic” phases are the regions in the phase diagram where the ordered moment (discussed in Section 3.5) is zero due to the effect of diverging quantum fluctuations. The true nature of theses phases and their possible hidden order (e. g. spin-nematic and columnar dimer) are not discussed in the present work, because to this date there are no compounds known where they are realized. The borders are determined by considering the breakdown of the finite-size scaling of the exact diagonalization result, as described in Section. 6.2.1.

2.1.2. Introducing spatial anisotropy

In addition to the isotropic model, we also investigate the effect of an additional spatial anisotropy in the ab plane. This is necessary because very often in 3d-oxide

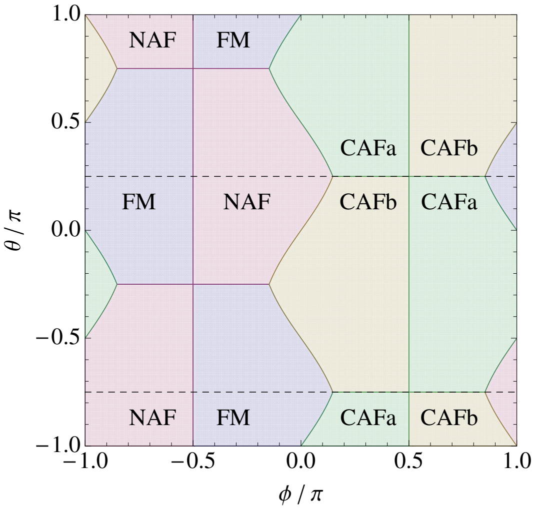

Figure 2.3.: Classical phase diagram of the Hamiltonian defined in Eq. 2.4 as a function of the frustration (ϕ) and anisotropy (θ) parameters. The dashed lines correspond to the isotropic case (Fig. 2.2).

compounds orthorhombic distortions of the square lattice are present. Therefore we consider a generalized model Hamiltonian on the *rectangular lattice*,

$$\mathcal{H} = J_{1a} \sum_{\langle ij \rangle_a}^{N} \mathbf{S}_i \cdot \mathbf{S}_j + J_{1b} \sum_{\langle ij \rangle_b}^{N} \mathbf{S}_i \cdot \mathbf{S}_j + J_2 \sum_{\langle ij \rangle_2}^{N} \mathbf{S}_i \cdot \mathbf{S}_j, \tag{2.4}$$

where now $\langle ij \rangle_a$ and $\langle ij \rangle_b$ are all nearest neighbor bonds along a and b directions, respectively. It is more convenient to define another angle θ, representing the degree of anisotropy between nearest neighbor interactions along a and b. This leads to the parametrization

$$\begin{aligned} J_{1a} &= \sqrt{2} J_{\mathrm{c}} \cos\phi \cos\theta, \\ J_{1b} &= \sqrt{2} J_{\mathrm{c}} \cos\phi \sin\theta, \\ J_2 &= J_{\mathrm{c}} \sin\phi, \\ J_{\mathrm{c}} &= \sqrt{\frac{1}{2}\left(J_{1a}^2 + J_{1b}^2\right) + J_2^2}. \end{aligned} \tag{2.5}$$

where $\tan\theta$ corresponds to the ratio of J_{1b} and J_{1a}, and ϕ stands for the frustration between the average interaction of first and second nearest neighbors.

For this general model the classical ground-state energy $E^{\mathrm{cl}}(\theta, \phi, \mathbf{Q})$ (Chapter 3) is given by

$$\begin{aligned} E_{\mathrm{NAF}}(\theta,\phi) &= 2\sin\phi - \sqrt{2}\cos\phi(\sin\theta + \cos\theta) \\ E_{\mathrm{CAFa}}(\theta,\phi) &= \sqrt{2}\cos\phi(\sin\theta - \cos\theta) - 2\sin\phi \\ E_{\mathrm{CAFb}}(\theta,\phi) &= \sqrt{2}\cos\phi(\cos\theta - \sin\theta) - 2\sin\phi \\ E_{\mathrm{FM}}(\theta,\phi) &= \sqrt{2}\cos\phi(\sin\theta + \cos\theta) + 2\sin\phi. \end{aligned} \tag{2.6}$$

Again only the three previous phases can have the lowest energy (now with two inequivalent columnar CAFa and CAFb phases). The lowest energy determines which phase is realized in a given (θ, ϕ) region. Fig. 2.3 displays a sketch of the classical phase diagram in the ϕ - θ plane. The horizontal (vertical) axis shows the frustration (anisotropy) parameter. Here, four classical phases FM, NAF, CAFa and CAFb exist. In the presence of anisotropy, the degeneracy between two columnar antiferromagnetic phases $\boldsymbol{Q}_{\mathrm{CAFa}} = (\pi, 0)$ and $\boldsymbol{Q}_{\mathrm{CAFb}} = (0, \pi)$ is lifted, except for $\theta = \frac{\pi}{4}$ and $-\frac{3\pi}{4}$ which both represent the isotropic model. Moreover, $\phi = 0$ corresponds to the unfrustrated case with $J_2 = 0$, where only first neighbor interactions exist. Furthermore, with $\phi = \pm\frac{\pi}{2}$ there are no first neighbor interactions ($J_{1a} = J_{1b} = 0, |J_2| = J_c$), and for $\phi = \frac{\pi}{2}$ the model is equivalent to the unfrustrated simple Néel case ($\theta = \frac{\pi}{4}, \phi = 0$) with two completely uncoupled sublattices. In the special case of $\theta = \frac{\pi}{2}$ and $\phi = 0$, one of the first neighbors interactions and also next-neighbors exchange are zero, hence we have only decoupled chains and the model is one dimensional.

2.2. Compounds

Both isotropic and anisotropic cases of the introduced model Hamiltonian have realization in a number of crystal structures [40]. In this work, we focus on three different classes of materials, in which this model is able to describe several aspects of their magnetic behavior.

2.2.1. Vanadium oxides

The J_1-J_2 model appears to describe well the thermodynamic and magnetic properties of two classes of insulating vanadium oxide compounds of the type $\mathrm{Li_2VO}X\mathrm{O_4}$ (X = Si, Ge) [57] and $AA'\mathrm{VO(PO_4)_2}$ (A, A' = Pb, Zn, Sr, Ba) [52,54]. They consist of vanadium oxide pyramid layers containing V^{4+} ions with $S = \frac{1}{2}$, as illustrated

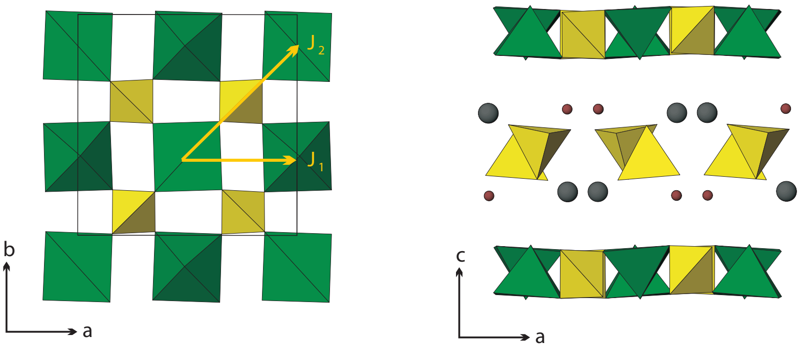

Figure 2.4.: Figure from Ref. [52]: crystal structure of BaCdVO$(PO_4)_2$: single [VOPO$_4$] layer (left) and stacking of the layers (right). Arrows indicate superexchange interactions J_1 (along the side of the square) and J_2 (along the diagonal of the square) between V atoms in the center of (green) VO$_5$ pyramids. Larger and smaller spheres denote Ba and Cd cations, respectively.

Label	Compound	ϕ/π	$J_c/(k_B K)$	Ref.
1	$Zn_2VO(PO_4)_2$	0.008	7.9	[53]
2	Li_2VOGeO_4	0.44	4.2	[54, 55]
3	Li_2VOSiO_4	0.47	6.3	[54, 55]
4	$BaZnVO(PO_4)_2$	0.66	10.5	[55]
5	$Pb_2VO(PO_4)_2$	0.66	10.8	[55]
	$Pb_2VO(PO_4)_2$	0.67	11.5	[54]
6	$SrZnVO(PO_4)_2$	0.74	12.2	[55]
7	$BaCdVO(PO_4)_2$	0.76	4.8	[52]
5'	$Pb_2VO(PO_4)_2$	0.60	6.8	[56]

Table 2.1.: Exchange interactions constants for various vanadium oxide compounds obtained from susceptibility $\chi(T)$ analysis. The frustration angle ϕ is calculated using Eq. 2.3 and the labels correspond to Fig. 2.5.

in Fig. 2.4 from Ref. [52] which shows the crystal structure of BaCdVO$(PO_4)_2$. Although the true crystal structure of these compounds corresponds to a two-dimensional lattice with lower symmetry than the square lattice, we may describe the physics using a $J_1 - J_2$ model on a square-lattice. The reason will be explained in Chapter 7 and it will be shown that for these compounds the anisotropy is playing only a minor role.

In Table 2.1 various vanadium compounds and their exchange interaction constants are listed and Fig. 2.5 shows their location in the phase diagram. Based on the analysis of thermodynamic and magnetic properties (Chapters 7 and 8) these

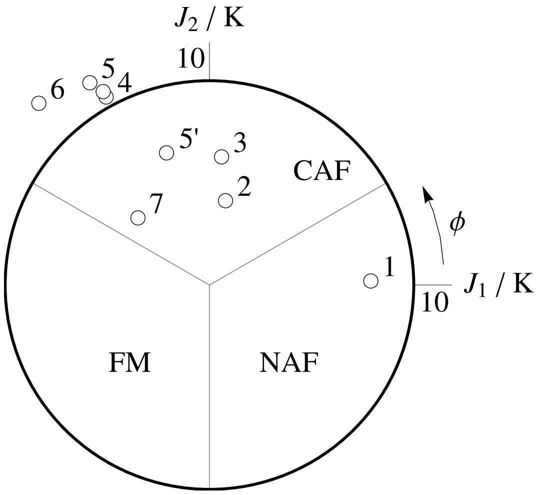

Figure 2.5.: Location of vanadium compounds in the phase diagram, based on the values from Table 2.1 with labels given in the first column.

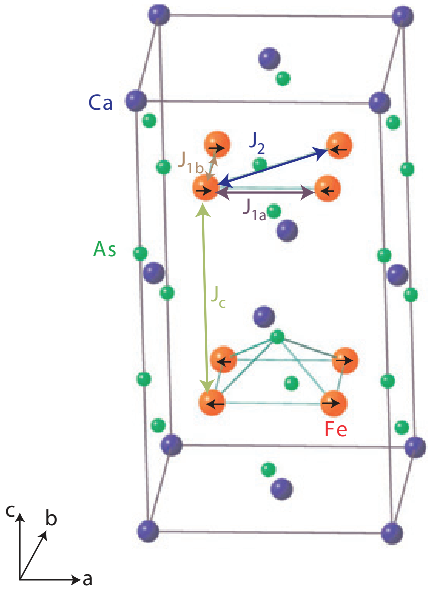

Figure 2.6.: Figure from Ref. [48]: Schematic view of the Fe spin ordering in $CaFe_2As_2$, consisting of two-dimensional CAFa structure stacked antiferromagnetically along c.

compounds are known to be mostly in the CAF phase.

Label	System	Ref.	S	SJ_{1a}	SJ_{1b}	SJ_2	SJ_c	ϕ/π	θ/π
1	$CaFe_2As_2$	[59]	–	41	10	21	36	0.19	0.08
C	$CaFe_2As_2$	[60]	0.4	24–37	7–20	28–34	33–45	0.29	0.13
D	$CaFe_2As_2$	[48]	0.22	49.9	-5.7	18.9	53.7	0.11	-0.04
B	$BaFe_2As_2$	[58]	0.28	17.5	17.5	35	39.1	0.35	0.25
5	$BaFe_2As_2$	[58]	0.54	36	-7	18	31.6	0.19	-0.06
6	$CaFe_2As_2$	[51]	0.75	27.4	-2.1	14.5	24.3	0.20	-0.02
7	$BaFe_2As_2$	[51]	0.84	36.1	-2.6	12.0	38.0	0.10	-0.02
8	$SrFe_2As_2$	[51]	0.84	35.3	2.2	13.4	28.4	0.16	0.02

Table 2.2.: Fe-pnictide exchange interactions (in meV) from experiment (top) and theory (bottom). J_c is the average exchange energy scale and θ and ϕ are anisotropy and frustration angles (Eq. 2.5). The effective spin S is obtained from the moment $\mu = 2S\mu_\mathrm{B}$.

2.2.2. Undoped parent compounds of Fe-pnictide superconductors

The generalized anisotropic $J_{1a,b}$ - J_2 Heisenberg model with large anisotropy has recently been invoked in the interpretation of spin-wave excitations for the undoped Fe-pnictide parent compounds [48, 58–60] even though the compounds are metallic. It has also been discussed whether the observation of small ordered moments can be understood within a frustrated local moment model. For a detailed discussion of these topics we refer to Chapter 6 as well as Ref. [47] and the numerous references cited therein.

Fig. 2.6 from Ref. [48] illustrates the spin ordering of Fe in crystal structure of $CaFe_2As_2$. Table 2.2 includes the values of the exchange interactions and frustration and anisotropy parameters for Fe-pnictides obtained from the fit to the measured data from Inelastic Neutron Scattering (INS) (top) and theoretical calculation from Local Spin Density Approximation (LSDA) (bottom). In the latter case they are obtained from mapping the LSDA energy to that of a classical Heisenberg model [51]. For some of the experimental values from INS, Fig. 2.7 shows the location of the compounds in the phase diagram. Different groups have given different values of (θ, ϕ) for the same compound.

2.2.3. Copper pyrazine perchlorate

In previous studies [61, 62] on $Cu(pz)_2(ClO_4)_2$, the spin-wave excitations, field dependent moment and ordering temperature $T_N(H)$ of this compound were determined. Based on these results and on earlier thermodynamic studies in [63, 64], it

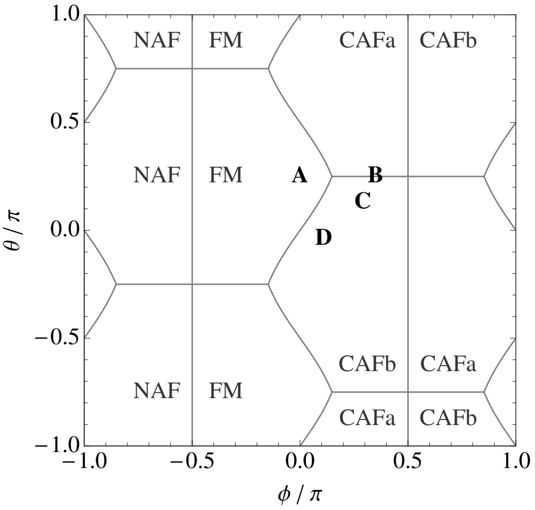

Figure 2.7.: Location of some parent compounds of the Fe-pnictides in the phase diagram, based on the experimental values from Table 2.2 with labels given in the first column. Here A represents the standard nearest-neighbor Heisenberg model ($J_{1a} = J_{1b} = J_1 = J_c$, $J_2 = 0$) and B, C, and D are given in Table 2.2.

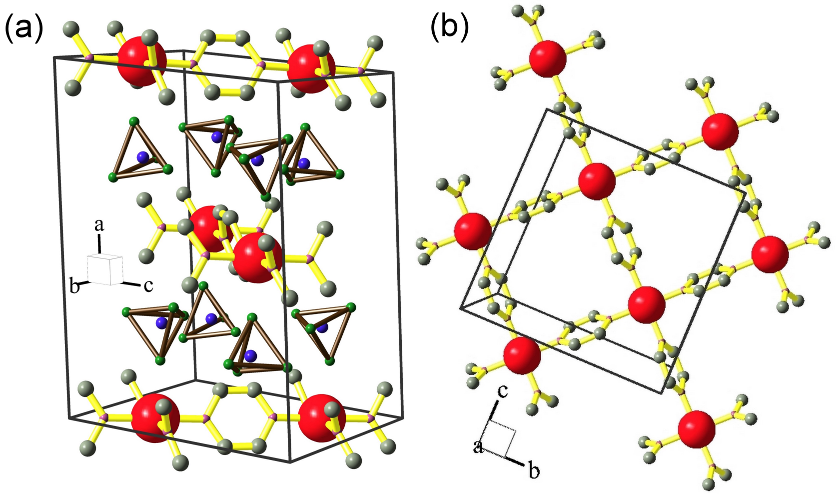

Figure 2.8.: Figure from Ref. [61]: (a) Three-dimensional view of the crystal structure of $Cu(pz)_2(ClO_4)_2$. The Cu^{2+} ions are shown as big spheres. The ClO_4 tetrahedra are located between the copper layers and pyrazine molecules link Cu^{2+} in *bc*-plane. (b) The projection of the crystal structure on the *bc*-plane shows the Cu^{2+} square-lattice structure. The square lattice are shifted by (0,0.5,0) from one layer to the next.

was suggested that Cu pyrazine is close to a pure two-dimensional square lattice Néel antiferromagnet with a frustration ratio $J_2/J_1 = 0.02$ or $\phi/\pi \approx 0.006$. The crystal structure of $\mathrm{Cu(pz)_2(ClO_4)_2}$ is shown from Ref. [61] in Fig. 2.8. In the present work, based on Ref. [65], we propose a new method for the determination of the frustration ratio in this and similar two-dimensional quantum antiferromagnets. We suggest to use the nonlinear field dependence of the staggered magnetization for the determination of the degree of frustration. In Chapters 7 and 8, we show that an analysis of the magnetic susceptibility by finite-temperature Lanczos method, and an analysis of the non-monotonic field dependence of the staggered moment, both give values for the frustration angle ϕ which are considerably larger than reported previously, although they are still deep within the NAF region.

III. Analytical Methods: The Linear Spin-Wave Analysis

We shall now describe the analytical linear spin-wave approximation which we apply to study the $J_{1a,b}-J_2$ Heisenberg model in an external field. To understand various aspects of frustration, in particular for uniform and staggered magnetization, the comparison of analytical results (even if approximate) to numerical exact diagonalization results is of great importance. We introduce a local coordinate system for all spins, aligned with the classical moment direction, and obtain the classical ground-state energy. Subsequently, we use a Holstein–Primakoff transformation followed by a Bogoliubov transformation in order to diagonalize the Hamiltonian and obtain total ground-state energy (including the contribution from quantum fluctuations), phase diagram, and spin-wave spectra. We also derive expressions for the ordered and induced moments, as well as the zero-temperature magnetic susceptibility at low magnetic field. The formal procedure is similar to the one discussed in Refs. [66–68] and [47].

3.1. Local coordinate system

The effective localized spin Hamiltonian we shall discuss here is of the form

$$\mathcal{H} = \sum_{\langle ij \rangle} J_{ij}\, \mathbf{S}_i \cdot \mathbf{S}_j - g\mu_{\mathrm{B}} \mathbf{H} \sum_i \mathbf{S}_i \tag{3.1}$$

where the sum in the first term extends over bonds $\langle ij \rangle$ connecting sites i and j. We assume an isotropic interaction in spin space, but the following formalism is valid as long as the interactions preserve U(1) symmetry. Without loss of generality, we define the global z axis by the magnetic field direction. Furthermore, we set

$$J_{ij} = \begin{cases} J_{1a} & \text{if} \quad \mathbf{R}_i - \mathbf{R}_j = \pm\,\hat{e}_x \\ J_{1b} & \text{if} \quad \mathbf{R}_i - \mathbf{R}_j = \pm\,\hat{e}_y \\ J_2 & \text{if} \quad \mathbf{R}_i - \mathbf{R}_j = \pm\,\hat{e}_x \pm \hat{e}_y \end{cases} , \tag{3.2}$$

i. e., we restrict the interactions to anisotropic nearest- and next-nearest neighbor exchange on a rectangular lattice. However, the general strategy is independent of the lattice geometry and exchange interactions. Thereafter, on each site i we introduce a local coordinate system, where the z' axis is oriented parallel to the local magnetic moment. The expansion of Eq. 3.1 in spin-wave coordinates has to be performed in this local system. We write

$$\begin{pmatrix} S_i^x \\ S_i^y \\ S_i^z \end{pmatrix} = \begin{pmatrix} \cos(\mathbf{Q}\cdot\mathbf{R}_i) & -\sin(\mathbf{Q}\cdot\mathbf{R}_i) & 0 \\ \sin(\mathbf{Q}\cdot\mathbf{R}_i) & \cos(\mathbf{Q}\cdot\mathbf{R}_i) & 0 \\ 0 & 0 & 1 \end{pmatrix} \begin{pmatrix} \cos\Theta & 0 & -\sin\Theta \\ 0 & 1 & 0 \\ \sin\Theta & 0 & \cos\Theta \end{pmatrix} \begin{pmatrix} S_i^{x'} \\ S_i^{y'} \\ S_i^{z'} \end{pmatrix} \tag{3.3}$$

with the ordering vector $\mathbf{Q}$ in the xy plane perpendicular to the magnetic field which points along the z axis. At finite magnetic field values, the spins are canted out of the xy plane and gradually aligned with the z axis (direction of the field). The respective canting angle Θ is measured relative to this axis, where $\Theta = 0$ corresponds to the fully polarized state (moments along z axis), and $\Theta = \frac{\pi}{2}$ to the state with vanishing magnetic field (moments in the xy plane).

3.2. Classical ground-state energy

In this local coordinate system, we rewrite the scalar products and the Zeeman term and obtain the classical Hamiltonian (i. e. the classical ground-state energy),

$$\mathcal{H}_{\text{cl}} = NS^2\left[J(\mathbf{Q}) + \cos^2\Theta\,(J(0) - J(\mathbf{Q}))\right] - NSh\cos\Theta, \tag{3.4}$$

with $h = g\mu_{\text{B}}H$, here we have introduced the Fourier transform

$$J(\mathbf{k}) = \frac{1}{N}\sum_{\langle ij\rangle} J_{ij}e^{-i\mathbf{k}(\mathbf{R}_i - \mathbf{R}_j)} = \frac{1}{2}\sum_n J_n e^{-i\mathbf{k}\cdot\mathbf{R}_n}. \tag{3.5}$$

Which satisfies $J(\mathbf{k}) = J(-\mathbf{k})$. The last sum runs over all bonds n connecting a fixed site i with its neighbors. Minimizing Eq. 3.4 with respect to Θ yields the classical canting angle Θ_c via

$$\cos\Theta_\mathrm{c} = \frac{h}{2S\left(J(0) - J(\mathbf{Q})\right)}, \tag{3.6}$$

and then Eq. 3.4 reads

$$\mathcal{H}_\mathrm{cl} = NS^2\left[J(\mathbf{Q}) - \cos^2\Theta_\mathrm{c}\left(J(0) - J(\mathbf{Q})\right)\right]. \tag{3.7}$$

Minimizing this Hamiltonian with respect to the components of $\mathbf{Q}$, leads to four well-known classical phases (Fig. 2.3) with ordering vectors

$$\mathbf{Q} = \begin{cases} 0 & \text{ferromagnet (FM)} \\ (\pi/a, \pi/b) & \text{Néel antiferromagnet (NAF)} \\ (\pi/a, 0) & \text{columnar antiferromagnet along } a \text{ (CAFa)} \\ (0, \pi/b) & \text{columnar antiferromagnet along } b \text{ (CAFb)} \end{cases}. \tag{3.8}$$

The minimization condition reduces to $\partial J(\mathbf{Q})/\partial\mathbf{Q} = 0$ and hence is field independent. Thus, the classical ground-state energies are

$$E_0^\mathrm{cl} = NS^2\begin{cases} J_{1a} + J_{1b} + 2J_2 & \text{FM} \\ 2J_2 - (J_{1a} + J_{1b}) - 2\left(J_{1a} + J_{1b}\right)\cos^2\Theta_\mathrm{c} & \text{NAF} \\ J_{1b} - (J_{1a} + 2J_2) - 2\left(J_{1a} + 2J_2\right)\cos^2\Theta_\mathrm{c} & \text{CAFa} \\ J_{1a} - (J_{1b} + 2J_2) - 2\left(J_{1b} + J_2\right)\cos^2\Theta_\mathrm{c} & \text{CAFb} \end{cases} \tag{3.9}$$

where $\cos\Theta_\mathrm{c} = h/h_\mathrm{s}$, and the critical or saturation fields for the antiferromagnetic phases where all moments are polarized along z axis are given by Eq. 3.6,

$$\begin{aligned} \frac{h_\mathrm{s}}{2S} &= J(0) - J(\mathbf{Q}) & (3.10) \\ &= -\begin{cases} 2\left(J_{1a} + J_{1b}\right) & \text{NAF} \\ 2\left(J_{1a} + 2J_2\right) & \text{CAFa} \\ 2\left(J_{1b} + 2J_2\right) & \text{CAFb} \end{cases}. & (3.11) \end{aligned}$$

In the above relation for these three classically ordered phases, the exchange interaction between those spins which are parallel to each other no longer enters, and only antiferromagnetic exchanges contribute to the saturation field, e. g. in the NAF phase the saturation field value is independent of the next-nearest neighbor interaction J_2, because they are already in a ferromagnetic alignment. Fig. 3.1 illustrates the saturation field dependence for $\theta = \frac{\pi}{4}$ and $\theta = 0$ with varying the frustration angle ϕ.

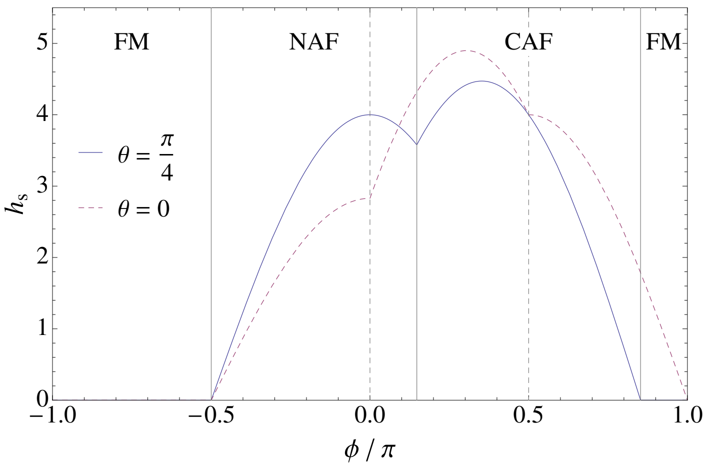

Figure 3.1.: Saturation field h_s as a function of the frustration ratio ϕ, for the isotropic case with $\theta = \frac{\pi}{4}$ (solid line) and maximally anisotropic $\theta = 0$ case (dashed lines). Horizontal solid (dashed) lines denote the classical phase boundaries for the isotropic (anisotropic) case. Names of phases are only mentioned for the isotropic model.

The extremal condition for $\mathcal{H}_\mathrm{cl}$ contains an additional solution having an incommensurate wave vector given by

$$\cos a\,\mathbf{Q}_x = -\frac{J_{1b}}{2J_2}, \quad \cos b\,\mathbf{Q}_y = -\frac{J_{1a}}{2J_2}, \tag{3.12}$$

with a ground-state energy

$$E_0^\mathrm{cl} = -\frac{J_{1a}J_{1b}}{8J_2}. \tag{3.13}$$

However, this energy for the incommensurate wave vector is always higher than or equal to the energy in Eq. 3.9 of the commensurate ground-state corresponding to the values chosen for the exchange constants.

From the classical ground-state energy in Eq. 3.9, one may already construct the phase diagram in the $\phi - \theta$ plane. The phase diagrams shown in Figs 2.2 and 2.3 in Chapter 2 are obtained in this way. However, for the following discussion it is important to include also the effect of quantum fluctuations.

3.3. The effect of quantum fluctuations

Starting from the classically ordered phases, one may construct a linear spin-wave analysis, and by calculating the effects of zero-point fluctuations in spin-wave approximation obtain an improved ground-state energy. This program has been successfully implemented before for the isotropic case [40, 69] to calculate an estimate for the reduction of the ordered moment and the extension of the instability region where magnetic order breaks down. Here, we describe the more general case and determine the importance of frustration and quantum fluctuations. In some regions of the $\phi-\theta$ phase diagram, the ground-state is degenerate of two or more classical phases, hence they show large quantum fluctuations which causes the reduction or even suppression of the ordered moment. These are strongly frustrated regions of the phase diagram and this approach however, cannot determine whether other more exotic hidden order is stabilized in this region. For the isotropic case, theses areas are shown in the left panel of Fig. 2.2, and their range is determined by the breakdown of the finite-size scaling analysis of exact diagonalization data (described in Chapter 5).

3.3.1. Holstein – Primakoff transformation

Returning to Eq. 3.1, now expressed in the local coordinate system, Eq. 3.3, we apply a Holstein-Primakoff transformation [70] first. In the following we suppress the primes referring to the local coordinate system. We introduce bosonic operators a_i and $a_i^\dagger$ that describe fluctuations of the ordered moment according to

$$\begin{aligned}
S_i^z &= S - a_i^\dagger a_i, && (3.14)\\
S_i^+ &= \sqrt{2S}\left(1-\frac{a_i^\dagger a_i}{2S}\right)^{\frac{1}{2}} a_i \to \sqrt{2S}a_i, && (3.15)\\
S_i^- &= \sqrt{2S}a_i^\dagger\left(1-\frac{a_i^\dagger a_i}{2S}\right)^{\frac{1}{2}} \to \sqrt{2S}a_i^\dagger, && (3.16)\\
S_i^x &= \frac{1}{2}\left(S_i^+ + S_i^-\right) \to \sqrt{\frac{S}{2}}\left(a_i + a_i^\dagger\right), && (3.17)\\
S_i^y &= \frac{1}{2}i\left(S_i^+ - S_i^-\right) \to -i\sqrt{\frac{S}{2}}\left(a_i - a_i^\dagger\right). && (3.18)
\end{aligned}$$

Subsequently we perform a $1/S$ expansion of scalar products, and keep only terms up to bilinear order in the boson operators. Details of the calculation can be found in Appendix A.3 and Ref. [47].

With introducing generalized inter- and intra-sublattice interactions $A(\mathbf{k})$ and $B(\mathbf{k})$, and an additional antisymmetric interaction $C(\mathbf{k})$ occurring only in finite magnetic fields,

$$\begin{aligned}
A(\mathbf{k}) &= J(\mathbf{k}) + \frac{1}{2}\left[J(\mathbf{k}+\mathbf{Q}) + J(\mathbf{k}-\mathbf{Q})\right] - 2J(\mathbf{Q}), \\
B(\mathbf{k}) &= J(\mathbf{k}) - \frac{1}{2}\left[J(\mathbf{k}+\mathbf{Q}) + J(\mathbf{k}-\mathbf{Q})\right], \\
C(\mathbf{k}) &= J(\mathbf{k}+\mathbf{Q}) - J(\mathbf{k}-\mathbf{Q}), \qquad (3.19)
\end{aligned}$$

and by introducing a Fourier representation of the spin-wave operators,

$$a_i^\dagger = \frac{1}{\sqrt{N}} \sum_{\mathbf{k}} a_{\mathbf{k}}^\dagger e^{-i\mathbf{k}\cdot\mathbf{R}_i}, \qquad (3.20)$$

the Hamiltonian will take the form

$$\begin{aligned}
\mathcal{H} &= NS(S+1)\left(J(\mathbf{Q}) + A(0)\cos^2\Theta\right) - \frac{1}{2}Nh(2S+1)\cos\Theta \\
&+ \frac{S}{2}\sum_{\mathbf{k}} \hat{\mathbf{a}}_{\mathbf{k}}^\dagger \boldsymbol{H}_{\mathbf{k}} \hat{\mathbf{a}}_{\mathbf{k}}, \qquad (3.21)
\end{aligned}$$

with,

$$\hat{\mathbf{a}}_{\mathbf{k}}^\dagger = \left(a_{\mathbf{k}}^\dagger,\, a_{-\mathbf{k}}\right) \qquad (3.22)$$

$$\boldsymbol{H}_{\mathbf{k}} = \begin{pmatrix} H_1 + H_{\mathrm{a}} & H_2 \\ H_2 & H_1 + H_{\mathrm{a}} \end{pmatrix}, \qquad (3.23)$$

$$H_1 = A(\mathbf{k}) - \cos^2\Theta\,(B(\mathbf{k}) + 2A(0)) + \frac{h}{S}\cos\Theta, \qquad (3.24)$$

$$H_2 = B(\mathbf{k})\left(1 - \cos^2\Theta_{\mathrm{c}}\right), \qquad (3.25)$$

$$H_{\mathrm{a}} = C(\mathbf{k})\cos\Theta. \qquad (3.26)$$

3.3.2. Bogoliubov transformations

The bilinear Hamiltonian of Eq. 3.21 may be diagonalized by introducing the Bogoliubov operators

$$\begin{aligned}
\alpha_{\mathbf{k}} &= u_{\mathbf{k}} a_{\mathbf{k}} + v_{\mathbf{k}} a_{-\mathbf{k}}^\dagger, \\
\alpha_{-\mathbf{k}}^\dagger &= v_{\mathbf{k}} a_{\mathbf{k}} + u_{\mathbf{k}} a_{-\mathbf{k}}^\dagger. \qquad (3.27)
\end{aligned}$$

They correspond to the magnon excitations described by the boson operators $\alpha_{\mathbf{k}}$. The Hamiltonian 3.21 will be diagonalized in the Fock space of Bogoliubov operators provided the coefficients $u_{\mathbf{k}}$ and $v_{\mathbf{k}}$ are given by

$$\begin{aligned} u_{\mathbf{k}}^2 &= \frac{1}{2}\left(\frac{H_1}{\sqrt{H_1^2 - H_2^2}} + 1\right) = \frac{1}{2}\left(\frac{A(\mathbf{k}) - \cos^2\Theta\Big(B(\mathbf{k}) + 2A(0)\Big) + \frac{h}{S}\cos\Theta}{E(h,\mathbf{k})} + 1\right) \\ v_{\mathbf{k}}^2 &= \frac{1}{2}\left(\frac{H_1}{\sqrt{H_1^2 - H_2^2}} - 1\right) = \frac{1}{2}\left(\frac{A(\mathbf{k}) - \cos^2\Theta\Big(B(\mathbf{k}) + 2A(0)\Big) + \frac{h}{S}\cos\Theta}{E(h,\mathbf{k})} - 1\right). \end{aligned} \tag{3.28}$$

These coefficients are needed below for calculating ground-state expectation values and magnon energies.

3.4. Ground-state properties

The diagonal form of the Hamiltonian can be finally written as

$$\begin{aligned} \mathcal{H} &= NS^2\left(J(\mathbf{Q}) - A(0)\cos\Theta_\mathrm{c}\right) \\ &+ NSJ(\mathbf{Q}) + \frac{S}{2}\sum_{\mathbf{k}} E(h,\mathbf{k}) \\ &+ S\sum_{\mathbf{k}} E(h,\mathbf{k})\,\alpha_{\mathbf{k}}^\dagger \alpha_{\mathbf{k}}. \end{aligned} \tag{3.29}$$

The sum over $\mathbf{k}$ in the equation above runs over the full crystallographic Brillouin zone. For the spin-wave energies $\omega(h,\mathbf{k}) = SE(h,\mathbf{k})$, we obtain the expression

$$E(h,\mathbf{k}) = \sqrt{\left[A(\mathbf{k}) - B(\mathbf{k})\cos^2\Theta\right]^2 - \left[B(\mathbf{k})\left(1-\cos^2\Theta\right)\right]^2} + C(\mathbf{k})\cos\Theta. \tag{3.30}$$

3.4.1. Total ground-state energy

We now calculate the total ground-state energy in spin-wave approximation to determine the zero-field phase diagram. We will also later in Section 6.1 give a comparison to the results for finite clusters obtained from exact diagonalization. Unless explicitly mentioned otherwise, we assume $\Theta = \Theta_\mathrm{c}$ from here on, i. e. we neglect corrections to the canting angle due to quantum fluctuations. The ground-state energy is given by the sum of the classical energy and the zero-point contribution of fluctuations of

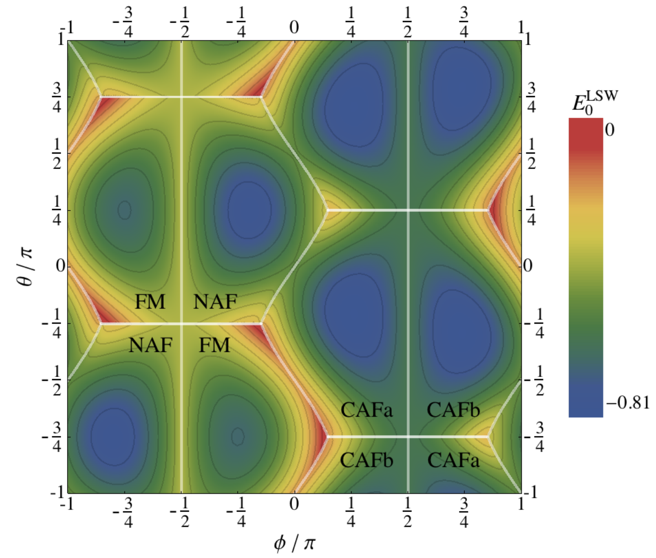

Figure 3.2.: Contour plot of the ground-state energy in linear spin-wave approximation of the frustrated Heisenberg Hamiltonian on the rectangular lattice as a function of the frustration angle ϕ and the anisotropy parameter θ. Energy unit is the overall energy scale J_c, and the magnetic field is zero. The white lines show the boundaries between the four classical phases, CAFa, CAFb, NAF and FM. cf. Fig. 6.1.

the magnons, with the dispersion from Eq. 3.30. We have

$$
\begin{aligned}
E &= E_{\mathrm{cl}} + E_{\mathrm{zp}} + S\sum_{\mathbf{k}} E(h,\mathbf{k})\,\alpha^{\dagger}_{\mathbf{k}}\alpha_{\mathbf{k}}, && (3.31)\\
E_{\mathrm{cl}} &= NS^2\left(J(\mathbf{Q}) - A(0)\cos^2\Theta_{\mathrm{c}}\right), &&\\
E_{\mathrm{zp}} &= NSJ(\mathbf{Q}) + \frac{S}{2}\sum_{\mathbf{k}} E(h,\mathbf{k}), && (3.32)
\end{aligned}
$$

where E_{zp} is the zero-point energy.

Figure 3.2 shows the total ground-state energy at zero field as a function of the frustration angle ϕ and the anisotropy parameter θ. The energy unit is J_c, and four magnetic phases appear (see caption) in a symmetric pattern in the ϕ - θ plane. We notice the following characteristics of the phase diagram:

i. The ground-state energy and phase diagram are invariant under the following symmetry transformations: reflections at the lines $\theta = \frac{\pi}{4}$ and $-\frac{3\pi}{4}$ and inversion at the points $(\phi,\theta) = (\pm\frac{\pi}{2}, \frac{3\pi}{4})$ and $(\pm\frac{\pi}{2}, -\frac{\pi}{4})$. Both operations lead to $(J_{1a}, J_{1b}) \rightarrow (J_{1b}, J_{1a})$ with J_2 unchanged. This corresponds to an interchange of the the columnar CAFa/b phases, while FM and NAF phases are left unchanged. The classical ground-state energy has even more symmetries. Thus, it is sufficient to consider only the parameter range $-\pi \leqslant \phi \leqslant \pi$ and $0 \leqslant \theta \leqslant \frac{\pi}{4}$, which can be mapped onto the whole phase diagram applying discrete symmetry operations under which the Hamiltonian 2.4 is invariant. This area is shown as shaded in the bottom panel of Fig. 3.2.

ii. In the isotropic case ($\theta = \frac{\pi}{4}$ and $-\frac{3\pi}{4}$), CAFa and CAFb are degenerate. By moving away from this symmetry line, one of the two phases is selected. Considering only this line gives the isotropic phase diagram, shown in Fig. 2.2.

iii. Apart from the ferromagnetic state, which is an eigenstate to the Hamiltonian, the spin-wave corrections stabilize the classical ground-state, i. e., the zero-point energy (Eq. 3.32) is negative for all values of ϕ and θ.

3.4.2. Spin-wave spectra

Here we focus on the excitation spectrum of the Hamiltonian 3.29 for some points in the (ϕ, θ) phase diagram, as illustrated in Fig. 3.3. This figure shows plots of the $\mathbf{k}$ dependence of the spin-wave excitations for different parameter sets (ϕ, θ). For simplicity, we scale $\mathbf{k}$ with the lattice constants and set $k_x a \to k_x$ and $k_y b \to k_y$. All plots refer to the crystallographic Brillouin zone. The selected frustration and anisotropy parameters correspond to Table 2.2 for some of the materials with suggestions from previous experiments on Fe-pnictides.

The top left spectrum (A) in Fig. 3.3 shows the well-known dispersion for the nearest-neighbor Heisenberg model for comparison. It has a Goldstone mode at the equivalent wave vectors $\mathbf{Q} = 0$ and $\mathbf{Q} = (\pm\pi, \pm\pi)$. The low-energy dispersion $\omega(\mathbf{k}) = SE(\mathbf{k})$ is linear around these points with

$$\omega(\mathbf{k}) = 2\sqrt{2}\, SJ_1 \sqrt{(k_x - Q_x)^2 + (k_y - Q_y)^2}. \tag{3.33}$$

The top-right plot (B) shows the dispersion for $(\phi, \theta)/\pi = (0.35, 0.25)$, corresponding to an isotropic exchange on the border between CAFa and CAFb phases. These parameters have been determined for $\mathrm{BaFe_2As_2}$ in Ref. [58]. The Goldstone modes are at $\mathbf{Q} = (0, \pm\pi)$ and $\mathbf{Q} = (\pm\pi, 0)$ and the equivalent points $\mathbf{Q} = 0$ and $\mathbf{Q} = (\pm\pi, \pm\pi)$, reflecting the two-fold degeneracy of the CAFa and CAFb phases. It should be noted however, that in the Fe-pnictides there are no true Goldstone modes due to additional single-ion anisotropies, which introduce a gap at these

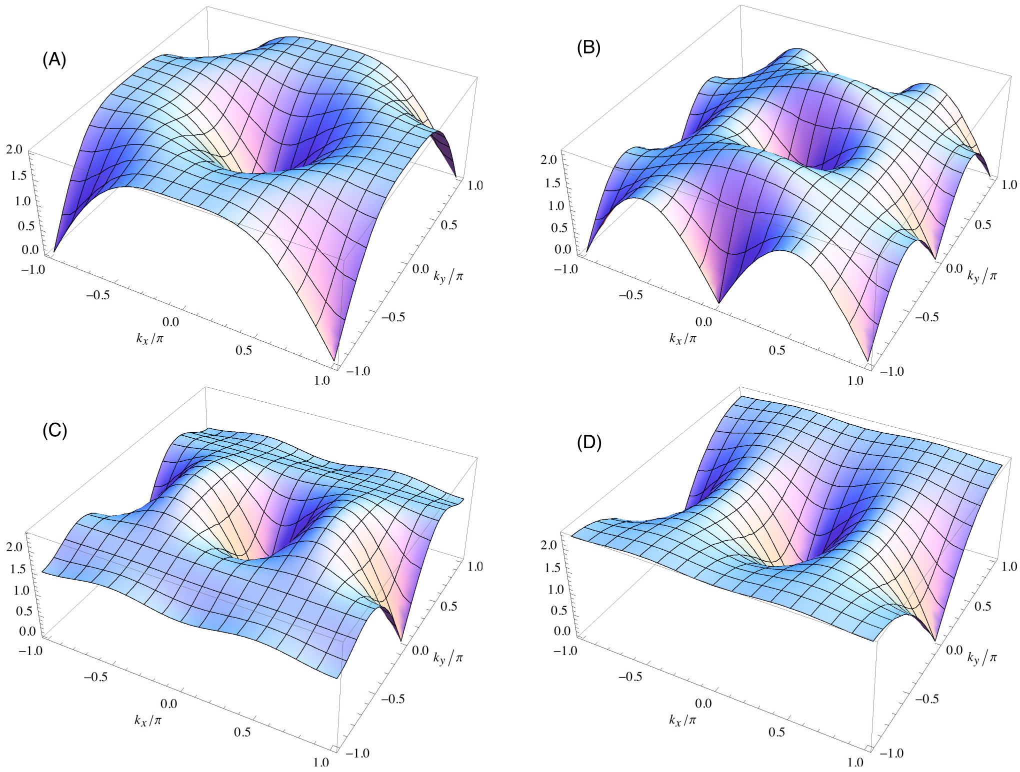

Figure 3.3.: Spin-wave spectra $E(h=0,\mathbf{k})/J_c$. Clockwise from top left:
(A) $(\phi,\theta)/\pi=(0,0.25)$ – NAF, isotropic exchange with $J_2=0$,
(B) $(\phi,\theta)/\pi=(0.35,0.25)$ – CAFa/b, isotropic exchange,
(C) $(\phi,\theta)/\pi=(0.29,0.13)$ – inside CAFa,
(D) $(\phi,\theta)/\pi=(0.11,-0.04)$ – even more inside CAFa.

points [48, 58]. The linear dispersion around the minima is

$$\begin{aligned}\omega_a(\mathbf{k}) &= 2S\sqrt{2J_2+J_{1a}}\times \\ &\sqrt{(2J_2+J_{1a})(k_x-Q_x)^2+(2J_2-J_{1b})(k_y-Q_y)^2}\end{aligned}\tag{3.34}$$

for the CAFa phase, and

$$\begin{aligned}\omega_b(\mathbf{k}) &= 2S\sqrt{2J_2+J_{1b}}\times \\ &\sqrt{(2J_2-J_{1a})(k_x-Q_x)^2+(2J_2+J_{1b})(k_y-Q_y)^2}\end{aligned}\tag{3.35}$$

for the CAFb phase.

For $(\phi,\theta)/\pi=(0.29,0.13)$, assigned to $CaFe_2As_2$ in Ref. [60], we show the spin-wave dispersion in the bottom left plot (C) of Fig. 3.3. With these parameters, the system is deep inside the CAFa phase. In contrast to the isotropic case, the dispersion around $\mathbf{Q}^* = (0, \pm\pi)$ and $(\pm\pi, \pm\pi)$ have a finite energy gap, while still being local minima (but with a quadratic $\mathbf{k}$ dependence). We have $E_a(\mathbf{k}) = 0$ remaining only at the wave vectors $\mathbf{k} = 0$ and $(\pm\pi, 0)$, characteristic for the CAFa phase.

Finally, the bottom right plot (D) in Fig. 3.3 displays the dispersion for $(\phi, \theta)/\pi = (0.11, -0.04)$. This alternative parameter set was proposed in Ref. [48] for $\mathrm{CaFe_2As_2}$. The local minima at $\mathbf{Q}^* = (0, \pm\pi)$ and $(\pm\pi, \pm\pi)$ discussed in the previous paragraph have almost disappeared, the dispersion at the zone boundary $k_y = \pm\pi$ is flat.

3.5. Field dependence of the ordered moment and magnetization

The most appropriate quantity for judging the degree of frustration in the local moment model is the size of the ordered ground-state moment, relative to its size in the unfrustrated ($J_2 = 0$) isotropic ($J_{1a} = J_{1b} = J_1$) Néel antiferromagnetic model. The latter is already reduced with respect to the classical value S to the well known value [71] of $m^0_{\mathbf{Q}} \sim 0.607S$. The stronger the frustration, the more reduction of the local moment, even below this value is expected.

3.5.1. Total magnetic moment

The total moment is the ground-state expectation value of the z component of the spin $\mathbf{S}'$ in the *local* coordinate system,

$$\begin{aligned} m_{\mathrm{tot}} &= \frac{1}{N}\sum_i \left\langle S_i^{z'} \right\rangle = S - \frac{1}{N}\sum_{\mathbf{k}} \left\langle a^\dagger_{\mathbf{k}} a_{\mathbf{k}} \right\rangle \\ &= S - \frac{1}{N}\sum_{\mathbf{k}} v^2_{\mathbf{k}}, \end{aligned} \tag{3.36}$$

In zero magnetic field ($\Theta = \frac{\pi}{2}$), this quantity is the same as the ordered moment $m_{\mathbf{Q}}$, defined by the projection of the canted spins onto the xy plane,

$$m_{\mathbf{Q}} = m_{\mathrm{tot}} \sin\Theta, \tag{3.37}$$

which we will discuss later. For the moment, inserting the expression for $v_{\mathbf{k}}$ required to bring the Hamiltonian into the diagonal form yields

$$m_{\mathrm{tot}} = S\left[1 - \frac{1}{2S}\left(\frac{1}{N}\sum_{\mathbf{k}} \frac{A(\mathbf{k}) - B(\mathbf{k})\cos^2\Theta_{\mathrm{c}}}{E(h,\mathbf{k})} - 1\right)\right]. \tag{3.38}$$

Due to quantum fluctuations, $m_{\mathrm{tot}} < S$ is smaller than in the classical case, except for the ferromagnetic phase. Near the boundaries of the CAFb and CAFa phases to the NAF phase, the ordered moment vanishes, indicating the failure of spin-wave theory due to strong frustrations. Also between the FM and CAF phases the latter lead to a vanishing $m_{\mathbf{Q}}$ in a small region. This shall be described in more details in Sections 6.2 and 6.3.

3.5.2. Uniform magnetization in magnetic field

The uniform magnetization of the system is the ground-state expectation value of the z component of the spin $\mathbf{S}$ in the *global* coordinate system,

$$m_0 = \frac{1}{N}\sum_i \langle S_i^z \rangle . \tag{3.39}$$

Since this is just the projection of the ordered magnetic moments onto the field direction, we can also write

$$m_0 = m_{\mathrm{tot}} \cos\Theta. \tag{3.40}$$

Here, Θ is *not* the classical canting angle Θ_{c}, since the latter does not include corrections due to quantum fluctuations. Thus, we have to regard Θ as independent variable again, return to the Hamiltonian before the replacement $\Theta \to \Theta_{\mathrm{c}}$, and minimize its corresponding ground-state energy with respect to Θ.

Because the $1/S$ corrections are already included in the ground-state energy obtained from Eqs. 3.29 and 3.30, we can equivalently use the definition of the uniform magnetization per site as the negative field derivative of $E_0(\Theta_{\mathrm{c}})$,

$$\begin{aligned} m_0 &= -\frac{1}{N}\frac{\partial}{\partial h} E_0(\Theta_{\mathrm{c}}) && (3.41)\\ &= -\frac{1}{N}\frac{\partial E_0(\Theta_{\mathrm{c}})}{\partial \cos\Theta_{\mathrm{c}}}\frac{\partial \cos\Theta_{\mathrm{c}}}{\partial h} && (3.42)\end{aligned}$$

with Θ_{c} given by Eq. 3.6 and the ground-state energy in linear spin-wave approximation

$$\begin{aligned} E_0(\Theta_\mathrm{c}) &= NS^2\left(J(\mathbf{Q}) - A(0)\cos^2\Theta_\mathrm{c}\right) + \\ & NSJ(\mathbf{Q}) + \frac{S}{2}\sum_{\mathbf{k}} E(h,\mathbf{k}). \end{aligned} \tag{3.43}$$

Then the result is given by

$$m_0 = S\frac{h}{h_\mathrm{s}}\left[1 + \frac{1}{2S}\frac{1}{N}\sum_{\mathbf{k}}\frac{B(\mathbf{k})\left(A(\mathbf{k}) - B(\mathbf{k})\right)}{A(0)E(h,\mathbf{k})}\right] \tag{3.44}$$

3.5.3. Ordered moment in magnetic field

The ordered or staggered moment $m_{\mathbf{Q}}$ in zero magnetic field has the same value as the total moment m_tot. For a finite field, it can be calculated as the projection of the total moment m_tot onto the plane perpendicular to the field direction, $m_{\mathbf{Q}} = m_\mathrm{tot}\sin\Theta_\mathrm{zp}$. Since $m_{\mathbf{Q}}$ is not a thermodynamic quantity, it cannot be expressed as a derivative of the ground-state energy, similar to the uniform moment where $m_0 \propto \partial E_0/\partial h$. Here, the canting angle Θ_zp is *not* the classical canting angle Θ_c, but we rather must include corrections due to zero point fluctuations. With increasing field the value of m_tot increases due to suppression of quantum fluctuations while the projection factor depending on Θ_zp decreases. This leads to a characteristic non-monotonic behavior of $m_{\mathbf{Q}}$ as function of field which we will use to determine the frustration angle ϕ (Chapter 8). The calculation of the ordered moment is described in Appendix A.4. The final expression is given by

$$\begin{aligned} m_{\mathbf{Q}} = \sin\Theta_\mathrm{c}\Bigg\{ S &- \frac{1}{2\sin^2\Theta_\mathrm{c}}\left[\frac{1}{N}\sum_{\mathbf{k}}\frac{A(\mathbf{k}) - B(\mathbf{k})\cos^2\Theta_\mathrm{c}}{E(h,\mathbf{k})} - 1\right] \\ &- \frac{\cos^2\Theta_\mathrm{c}}{2\sin^2\Theta_\mathrm{c}}\frac{1}{N}\sum_{\mathbf{k}}\frac{B(\mathbf{k})\left(A(\mathbf{k}) - B(\mathbf{k})\right)}{A(0)E(h,\mathbf{k})}\Bigg\}, \end{aligned} \tag{3.45}$$

which includes first-order corrections in $1/S$.

IV. Numerical Methods: Exact Diagonalization and FTLM

This chapter addresses the numerical method used in the present work and describes the exact diagonalization technique. This method provides the means for broad investigations into quantum model Hamiltonians applied to finite systems. We consider setting up the Hamiltonian matrix for the model defined in Chapter 2, and calculating the energy spectrum of the system. Lanczos tridiagonalization algorithm is used to determine the ground-state as well as a part of the spectrum of the matrix. The calculation of the ground-state properties such as magnetization and spin correlation functions are described. Moreover, the concept of random sampling and the finite-temperature Lanczos method for determining the temperature dependence of magnetic susceptibility and heat capacity are discussed.

4.1. The Hamiltonian matrix and its diagonalization

Given a Hamiltonian, e. g. the spin model of Eq. 2.4, one can construct its matrix representation by calculating the matrix elements with respect to a chosen basis set of vectors, such as configurations of spins. The selection of the basis is arbitrary and different sets can be used equivalently, while some might require more or less computational power. Additionally, symmetries in the Hamiltonian might be incorporated to reduce the size of the Hilbert space, therefore reducing the amount of calculations needed. For example, if the operator $S^z_{\mathrm{tot}} = \sum_i \langle S^z_i \rangle$ commutes with the Hamiltonian, i. e. the model has rotational symmetry around z, then the total spin component is conserved. Therefore the Hamiltonian matrix has a block diagonal form, where each block represents the system with a fixed S^z_{tot}. Furthermore, Bloch wave vectors should be considered for incorporating the translational invariance symmetry of the Hamiltonian, when periodic boundary conditions are applied. However, one should note that since the Hamiltonian 2.4 is composed only of spin operators, calculating the matrix elements requires transforming every wave vector

n	Hubbard	Heisenberg	Kondo
2	4	2	10
4	36	6	346
6	400	20	15 184
8	4 900	70	739 162
10	63 504	252	38 165 260
12	853 776	924	2 046 924 400
14	11 778 624	3432	112 738 423 360
16	165 636 900	12 870	6 332 299 624 282
18	2 363 904 400	48 630	361 077 477 684 436
20	34 134 779 536	184 756	20 836 827 035 351 596
22	497 634 306 624	705 432	1 214 171 997 616 258 240
24	7 312 459 672 336	2 704 156	71 321 835 387 812 803 696
26	108 172 480 360 000	10 400 600	
28	1 609 341 595 560 000	40 116 600	
30	24 061 445 010 950 400	155 117 520	
32	361 297 635 242 552 100	601 080 390	

Table 4.1.: Number of states for $S_z = 0$ for spin $\frac{1}{2}$ Hubbard-, Heisenberg- and Kondo-type models with N sites.

into its spin representation. This is usually the most time consuming part of the computations.

The size of the Hamiltonian matrix grows exponentially with the system size N. For instance, Hamiltonians containing only spin $\frac{1}{2}$ operators grow as 2^N in size. This rapid increase of Hilbert space size is even more pronounced for models including the charge degrees of freedom, as in Hubbard model where growth is given by 4^N and the Kondo lattice model with both local spin and itinerant charge and spin degrees of freedom (described in Chapter 10) where the growth is as 8^N. Even with reducing the Hilbert space size using symmetries of the Hamiltonian, this is the main limitation of the numerical calculations. Table 4.1 lists the actual numbers for these three classes of models. The numbers belong to the largest sector of the Hamiltonian with $S^z_{\text{tot}} = 0$ and the method to count them is described in Appendix A.2. We have done the calculations for the Heisenberg model up to 30 spins and the Kondo lattice model up to 16 (8 local and 8 itinerant) spins.

4.1.1. Diagonalization methods

Once the Hamiltonian matrix has been set up, many state-of-art algorithms can be employed for finding its eigenvalues and eigenvectors. We mention here two types of these algorithms which are widely used in standard applications in mathematics and computer science. A review of such algorithms can be found in Refs. [72] and [73].

Full diagonalization algorithms

A number of matrix diagonalization algorithms are capable of determining all the eigenvalues and eigenvectors of a matrix. With such algorithms, e. g. QR Algorithm [73, 74], Householder transformation [75] and Divide-and-conquer [76], one is able to use the full spectrum of the matrix to calculate the exact[1] zero-temperature and thermal averages of arbitrary operators. While these methods seem to be of great interest in studying physical systems, their limitation on the size of system is significant. In general, calculating eigenvalues on a matrix with rank m requires $\mathcal{O}(m^2)$ and eigenvectors of $\mathcal{O}(m^3)$ in time. Nevertheless, small test cases can be done with these algorithms in order to have an estimate of the error caused by approximate methods mentioned below.

Partial diagonalization algorithms

In most cases, a matrix obtained from representing a Hamiltonian in some convenient basis consists of mostly zero elements. These “sparse” matrices can be efficiently handled with eigendecomposition algorithms which calculate only a part of the eigenvalue spectrum. This category of iterative methods [77] work in the *Krylov subspace* generated from a starting vector a, and the matrix M, i. e. $\mathcal{K}_r(M, a) = \operatorname{span}\{a, Ma, M^2a, \ldots, M^{r-1}a\}$. These methods rapidly converge into one or few eigenvalues (of both ends of the spectrum with largest or smallest value). Krylov subspace methods are among the most successful methods available, and of their well known examples are the Arnoldi [78] and Lanczos [79] methods. The former is capable of dealing with general non-Hermitian matrices, while the latter is an adaptation of the power method [80] to find eigensystem of a Hermitian matrix [73].

---

[1] Here by the term “exact” in a numerical context we mean that the amount of error is controllable.

4.2. Lanczos algorithm

Cornelius Lanczos [ˈlaːntsoʃ] invented an iterative algorithm to transform a real or a complex symmetric matrix into a tridiagonal form. The eigenvalues of the resulting tridiagonal matrix are the same as the original matrix and its eigenvectors can be mapped back onto the eigenvectors of the original matrix. Two important properties of this algorithm should be mentioned here. First, there is no need to generate and store intermediate sub-matrices, and second, the extremal eigenvalues tend to converge long after a few iteration of the tridiagonalization procedure [73]. Hence, Lanczos diagonalization is a powerful method to study the ground-state and thermal properties of a moderately large Hamiltonian. The memory requirement of the algorithm is such that at each step of the iteration, only three vectors need to be stored in memory. Also, one can only store non-zero elements of the matrix, or equivalently just calculate them on the fly (as a tradeoff of memory and CPU time). These two features reduce the memory requirements of the implementation drastically.

The Lanczos algorithm in *infinite precision* constructs good approximations to the eigenvalues and eigenvectors of the original matrix. However, it suffers moderately from numerical roundoff errors due to the loss of orthogonality between Lanczos vectors, which are produced iteratively. Prior to the seminal work of Paige [81, 82] on the error analysis of the algorithm, the Lanczos method did not gain so much attention in practical use. One issue caused by the lack of orthogonality is the appearance of unrealistic “spurious” eigenvalues in the spectrum of the tridiagonal matrix. There are several ways to cope with that problem. The explicit way is to preserve the orthogonality at each step, by e. g. performing a Gram–Schmidt process [73] at each iteration, which is obviously a high-price trade-off of CPU time consumption. A simple method to detect the spurious eigenvalues is proposed by Cullum and Willoughby in Ref. [83], which is based on comparing the spectrum with eigenvalues of the matrix constructed from removing first row and column of the tridiagonal matrix. In our implementation, this problem does not show a high impact in the results, as it will become insignificant with the later described concept of random sampling.

Another drawback of the Lanczos algorithm is in resolving the correct degeneracy of eigenvalues. For that, the so-called Jacobi-Davidson algorithm [84] which is similar to Lanczos method provides the advantage of rapid convergence of the lowest eigenstates with true degeneracy count over having less speed and higher memory consumption [85]. Enhancements to the plain Lanczos algorithm, such as Block Lanczos or restart techniques are discussed in Ref. [73] and elsewhere.

4.3. Ground-state properties

One can obtain the ground-state energy and its state vector of the Hamiltonian 2.4 with high accuracy, with rather a few iterations in the Lanczos method. Given an operator $\mathcal{A}$ represented by counting operators, with the ground-state $|\psi_0\rangle$ we can calculate the operator expectation value $\langle\psi_0|\mathcal{A}|\psi_0\rangle$. If the operator itself commutes with the Hamiltonian, then matrix-vector operations are no longer needed, since the eigenvalues of the operators are the same as energies.

The Lanczos algorithm is also capable of calculating low-lying excited states of the system with Hilbert space size N_{st}. Being an iterative method, this method requires a starting vector of length N_{st}, which is generally set to a normalized random vector. Since we stop the iteration after $M \ll N_{\mathrm{st}}$ steps, only a small part of the spectrum is obtained. If the starting vector is perpendicular to a particular eigenstate of the system, the corresponding eigenvalue will not be generated during the iteration in Krylov subspace. This justifies choosing a random starting vector, and enables considering only a specific sector of the Hamiltonian by choosing the proper starting vector. Another trick introduced in [86] for obtaining arbitrary excited states is to shift the Hamiltonian by *a priori* constant value, i. e. $\mathcal{H} \to (\mathcal{H} - \lambda I)^2$. This is useful for example for the study of the energy gap in the system.

We now describe below how to calculate most important physical quantities, namely the static correlation functions, magnetic structure factor and ordered moment which are calculated in this context.

4.3.1. Spin correlation functions and static structure factors

In order to figure out the internal spin structure of the ground-state, looking at the correlation functions is a general starting point. They are defined as

$$\begin{aligned} C_{ij}^{\alpha\beta} &= \langle\psi_0\,|\,S_i^\alpha S_j^\beta\,|\,\psi_0\rangle, \\ C_{ij} &= \langle\psi_0\,|\,\mathbf{S}_i \cdot \mathbf{S}_j\,|\,\psi_0\rangle. \end{aligned} \tag{4.1}$$

But since we are dealing with rather small systems, only considering the value of the correlations might not be a suitable way to determine a possible underlying order. Instead, we evaluate the static structure factor, which is the Fourier transform of the equal-time spin correlation function. For a system with N spins and arbitrary vector $\boldsymbol{q}$, we have

$$\begin{aligned} S_N(\boldsymbol{q}) &= \frac{1}{\mathcal{N}} \sum_{i,j=1}^{N} \langle \mathbf{S}_i \cdot \mathbf{S}_j \rangle \, e^{i\boldsymbol{q}(\boldsymbol{r}_i - \boldsymbol{r}_j)} & (4.2) \\ &= \frac{N}{\mathcal{N}} \left[\langle \mathbf{S}_1 \cdot \mathbf{S}_1 \rangle + \sum_{j=2}^{N} \langle \mathbf{S}_1 \mathbf{S}_j \rangle \, e^{i\boldsymbol{q}(\boldsymbol{r}_1 - \boldsymbol{r}_j)} \right]. & (4.3) \end{aligned}$$

Eq. 4.3 is only valid when translational symmetry is preserved in the Hamiltonian. The normalization constant $\mathcal{N}$ here should be taken with care. At high temperatures, the individual spins of the finite system become uncorrelated, i. e.

$$\lim_{T\to\infty} \langle \mathbf{S}_i \cdot \mathbf{S}_j \rangle = \langle \mathbf{S}_i \rangle \langle \mathbf{S}_j \rangle = 0, \quad i \neq j. \tag{4.4}$$

Therefore,

$$\lim_{T\to\infty} S_N(\boldsymbol{q}) = \frac{N}{\mathcal{N}} \langle \mathbf{S}_1 \cdot \mathbf{S}_1 \rangle = \frac{N}{\mathcal{N}} S(S+1). \tag{4.5}$$

Thus, one might set $\mathcal{N} = N$ in order to get a size-independent limiting value for the structure factor at high temperatures. But, this would be inappropriate for the identification of the structure factor with an ordered moment, discussed in the next Section.

4.3.2. Magnetization and uniform and staggered moments

The total magnetization of the system is the ground-state expectation value of the z component of the spin $\mathbf{S}$, and at zero-temperature is defined as

$$M_N = \frac{1}{N} \sum_{i=1}^{N} \langle S_i^z \rangle = \frac{1}{N} \langle S_{\text{tot}}^z \rangle. \tag{4.6}$$

Due to the spontaneous symmetry breaking of the infinite lattice, at zero magnetic field the system does not exhibit magnetic ordering. However, in any *finite* system the ground-state has $S_{\text{tot}}^z = 0$ because of its degeneracies. Instead, we directly look at the correlation functions to study the ordering of spins, and consider the following two methods for calculating the magnetization in the system.

Ordered moment: 1st method of calculation

In the thermodynamic limit, we can identify the static structure factor with the square of the moment at the ordering vector $\boldsymbol{q}$,

$$M_N^2(\boldsymbol{q}) = S_N(\boldsymbol{q}), \tag{4.7}$$

where the ground-state expectation value is evaluated in the $S^z_{\text{tot}} = 0$ and $\mathbf{k} = 0$ subspace of the Hilbert space. In the thermodynamic limit, if $\mathbf{Q}$ is the ordering vector of the corresponding classical phase, we can then identify

$$M^2(\mathbf{Q}) = \lim_{N\to\infty} M_N^2(\mathbf{Q}) = \zeta(\mathbf{Q}) \lim_{N\to\infty} S_N(\mathbf{Q}). \tag{4.8}$$

with the appropriate normalization $\mathcal{N}$ of $S_N(\mathbf{Q})$. Here we have introduced a factor

$$\zeta(\mathbf{Q}) = \begin{cases} 1, & \mathbf{Q} = 0 \text{ or } (\pi,\pi) \\ 2, & \mathbf{Q} = (\pi,0) \text{ or } (0,\pi) \end{cases} \tag{4.9}$$

to account for the additional lattice rotation symmetry breaking in the CAFa and CAFb phases [87].

For a perfectly ordered classical state with wave vector $\mathbf{Q}$, the ordered moment assumes its maximum value, $M(\mathbf{Q}) = S$, and we have

$$\langle \mathbf{S}_i \cdot \mathbf{S}_j \rangle = \langle S_i^z S_j^z \rangle = S^2 e^{-i\mathbf{Q}(\mathbf{R}_i - \mathbf{R}_j)}, \quad i \neq j. \tag{4.10}$$

Assuming perfect order for the finite tile under consideration too, we have

$$\begin{aligned} S_N(\mathbf{Q}) &= \frac{N}{\mathcal{N}} \left[S(S+1) + (N-1)S^2 \right] \\ &= \frac{1}{\mathcal{N}}\, NS\,(NS+1)\,. \end{aligned} \tag{4.11}$$

If we require $M_N(\mathbf{Q}) = S$ also in this case, we have to set

$$\mathcal{N} = N\left(N + \frac{1}{S}\right), \tag{4.12}$$

which is the normalization we use for any tile included into our finite-size scaling analysis for $M_N(\mathbf{Q})$. This is in accordance with Refs. [87, 88], and slightly deviates from the $\mathcal{N} = N^2$ normalization commonly used by many authors.

In the ferromagnetic regime, although the fully polarized (all-up) state is an eigenstate of the Hamiltonian, the structure factor at the antiferromagnetic ordering vectors for finite systems remains small, but finite. Assuming perfect order again, we get for the individual terms in the sum in Eq. 4.3

$$\langle \mathbf{S}_1 \cdot \mathbf{S}_1 \rangle = S(S+1), \quad \langle \mathbf{S}_1 \cdot \mathbf{S}_j \rangle = S^2, \quad j \neq 1, \tag{4.13}$$

leading to

$$S_N(\mathbf{Q}) = \frac{N}{\mathcal{N}} \left[S(S+1) + S^2 \sum_{j=2}^{N} e^{-i\mathbf{Q}\mathbf{R}_j} \right]. \tag{4.14}$$

Let us restrict to tiles with an even area N, which is a necessary condition for being compatible with at least one of the non-ferromagnetic phases of the $J_{1a,b}-J_2$ model (see Section 5.3.1). The sum in the above equation contains only exponentials which can acquire the values $+1$ or -1 for $\mathbf{Q} = (\pi,\pi)$, $(\pi,0)$, or $(0,\pi)$. For each of these three wave vectors, there are $N/2$ sites with distance $\mathbf{R}_j$ to site 1 which have phase $+1$, and $N/2$ sites with phase -1. Site 1 obviously belongs to the former, such that we have $N/2-1$ terms left in the sum over the exponentials above having phase $+1$, and we get

$$\sum_{j=2}^{N} e^{-i\mathbf{Q}\mathbf{R}_j} = \left(\frac{N}{2} - 1\right) \times (+1) + \frac{N}{2} \times (-1) = -1. \tag{4.15}$$

With $\mathcal{N}$ given by Eq. (4.12), we therefore have

$$S_N(\mathbf{Q}) = \frac{S}{N + 1/S} \tag{4.16}$$

for all three antiferromagnetic wave vectors in the ferromagnetic phase. As required, this value vanishes in the thermodynamic limit $N \to \infty$.

Ordered moment: 2^{nd} method of calculation

An alternative way of calculating the ordered moment in the thermodynamic limit is mentioned for example in Refs. [88,89]. For the infinite system, in an ordered phase with a staggered moment, the spin correlation function factorizes for large distances $|\mathbf{R}_i - \mathbf{R}_j|$, and Eq. 4.10 simplifies as

$$\lim_{|\mathbf{R}_i - \mathbf{R}_j| \to \infty} |\langle \mathbf{S}_i \cdot \mathbf{S}_j \rangle| = |\langle \mathbf{S}_i \rangle \langle \mathbf{S}_j \rangle| = M^2(\mathbf{Q}). \tag{4.17}$$

Working with a finite compact tile, we can extrapolate the spin correlation function for a single pair of spins, defining lattice points i and j such that their distance on the tile is maximized taking into account the periodic boundary conditions. Without loss of generality, we can restrict ourselves to finding the pair $(1, j)$ or just site j being maximally apart from the origin, and define

$$\tilde{M}_N^2(\mathbf{Q}) = |\langle \mathbf{S}_1 \cdot \mathbf{S}_j \rangle|_{j=\max} . \tag{4.18}$$

For a square with size $N = L^2$, L even, the point $\mathbf{R}_{\max} = (\frac{L}{2}, \frac{L}{2})$, i.e., the center of the square, has maximum distance from the origin. However, in most cases, due to the lack of a lattice point located in the geometrical center of the tile, there will be, for even N, *two* sites j having the same maximum distance from the origin. For our calculations, we just select one of them. We then can give an estimate for the ordered moment as

$$M^2(\mathbf{Q}) = \lim_{N \to \infty} \tilde{M}_N^2(\mathbf{Q}). \tag{4.19}$$

4.4. Finite-temperature properties

Jaklič and Prelovšek [90] introduced the finite-temperature Lanczos method (FTLM). In this method combining Lanczos diagonalization and random sampling, one is able to evaluate finite-temperature static and dynamic quantities in small many-body quantum systems. In their method, the thermal averaging over all states is reduced to a random sampling over Lanczos starting vectors.

In general, the statistical average of a general operator $\mathcal{A}$ at general temperature T is

$$\langle \mathcal{A} \rangle = \mathcal{Z}^{-1} \sum_n^{N_{\mathrm{st}}} \langle n | e^{-\beta \mathcal{H}} \mathcal{A} | n \rangle, \quad \mathcal{Z} = \sum_n^{N_{\mathrm{st}}} \langle n | e^{-\beta \mathcal{H}} | n \rangle, \tag{4.20}$$

where $\beta = 1/(k_B T)$ and the sum is over the complete basis set of wave functions $|n\rangle, n = 1 \ldots N_{\mathrm{st}}$ spanning the Hilbert space of the Hamiltonian $\mathcal{H}$. By iterating the Lanczos algorithm with a starting vector $|\phi_n^0\rangle$, a set of $m = 1 \ldots M$ orthonormal vectors, $|\phi_n^m\rangle$, are generated and energies ϵ_n^m and their corresponding eigenvectors

$|\psi_n^m\rangle$ are found. Eq. 4.20 in these basis is then written as

$$\begin{aligned}\langle\mathcal{A}\rangle &= \mathcal{Z}^{-1}\sum_n^{N_0}\sum_m^{M}\langle n|\psi_n^m\rangle e^{-\beta\epsilon_n^m}\langle\psi_n^m|\mathcal{A}|n\rangle, \\ \mathcal{Z} &= \sum_n^{N_0}\sum_m^{M}|\langle n|\psi_n^m\rangle|^2 e^{-\beta\epsilon_n^m}. \end{aligned} \tag{4.21}$$

This sum is exactly equivalent to Eq. 4.20 for $N_0 = N_{\mathrm{st}}$ and $M = N_{\mathrm{st}} - 1$, i. e. for full sampling. However, an approximation, first for reduced number of Lanczos basis set $M \ll N_{\mathrm{st}}$, and second for partial sampling $N_0 \ll N_{\mathrm{st}}$, leads to very good and accurate results [90]. The latter is done by choosing a different random starting vector each time for restarting the Lanczos iteration. Usually with $N_0 \sim 100$ Lanczos iterations and $M = M_0 \sim 50 \ll N_{\mathrm{st}}$, a good description of the temperature dependence of $\langle\mathcal{A}\rangle$ is obtained. However, for rather low temperatures one needs $N_0 \sim 1000$ random samplings. A detailed analysis of the approximation error can be found in Ref. [91]. Another similar method is introduced by Aichhorn et al. [92] which by using a modified approximation of operator expectation values produces less numerical errors at $T \to 0$, with the price of requiring a significant CPU time compared to the finite-temperature Lanczos method.

We focus now on evaluating four different quantities using the finite-temperature Lanczos method, and discuss the calculation of heat capacity, magnetic susceptibility, third order magnetic susceptibility, and the magnetocaloric effect. The latter is described here for completeness only and no results will be presented in this work.

4.4.1. Heat capacity

The heat capacity is given by the fluctuations of internal energy according to

$$C_V(T) = \frac{1}{Nk_{\mathrm{B}}}\frac{1}{T^2}\left(\langle\mathcal{H}^2\rangle - \langle\mathcal{H}\rangle^2\right), \tag{4.22}$$

The thermal averages above can be easily calculated with Eq. 4.21, since they only require the energies calculated from Lanczos iterations of different random samples.

4.4.2. Magnetic susceptibility

Magnetic susceptibility can be similarly calculated from the 2^{nd} order cumulant of spin operators. By definition [93],

$$\chi = \frac{\partial M}{\partial H} = -\left(\frac{\partial^2 F}{\partial H^2}\right), \tag{4.23}$$

where F is the magnetic Helmholtz free energy and H is the uniform magnetic field strength. In terms of the partition function we have

$$F = -\frac{1}{\beta}\ln\mathcal{Z}, \quad \mathcal{Z} = \mathrm{Tr}\, e^{-\beta\mathcal{H}}. \tag{4.24}$$

Hence,

$$\begin{aligned} \chi &= -\frac{\partial^2}{\partial H^2}\left(\frac{1}{\beta}\ln\mathcal{Z}\right) \\ &= -\frac{1}{\beta}\left[\frac{1}{\mathcal{Z}}\frac{\partial^2\mathcal{Z}}{\partial H^2} - \left(\frac{1}{\mathcal{Z}}\frac{\partial\mathcal{Z}}{\partial H}\right)^2\right] \end{aligned} \tag{4.25}$$

Assuming the field dependence of the Hamiltonian of the form $\mathcal{H} = \mathcal{H}_0 - H S^z_{\mathrm{tot}}$ with $S^z_{\mathrm{tot}} = \sum_i S^z_i$,

$$\langle S^z_{\mathrm{tot}}\rangle = \frac{1}{\mathcal{Z}}\,\mathrm{Tr}\, S^z_{\mathrm{tot}} e^{-\beta\mathcal{H}}. \tag{4.26}$$

Then we have

$$\frac{1}{\mathcal{Z}}\frac{\partial\mathcal{Z}}{\partial H} = \beta\langle S^z_{\mathrm{tot}}\rangle, \quad \frac{1}{\mathcal{Z}}\frac{\partial^2\mathcal{Z}}{\partial H^2} = \beta^2\langle (S^z_{\mathrm{tot}})^2\rangle. \tag{4.27}$$

Therefore, one can express the magnetic susceptibility in terms of the fluctuation of the total spin component according to

$$\chi = \beta\left[\left\langle (S^z_{\mathrm{tot}})^2\right\rangle - \langle S^z_{\mathrm{tot}}\rangle^2\right]. \tag{4.28}$$

We calculate the thermodynamic dependence of the magnetic susceptibility using this relation, in which the operator averages are evaluated using the finite-temperature Lanczos method.

4.4.3. 3rd order susceptibility

The third-order or nonlinear susceptibility is defined as the third-order coefficient of an expansion of the magnetization for small magnetic field densities, i. e.,

$$\begin{aligned} M &= H\chi + \frac{1}{3!}\chi''' H^3 + \cdots , \\ \chi''' &= \beta^3 \left[\left\langle (S^z_{\mathrm{tot}})^4 \right\rangle - 3 \left\langle (S^z_{\mathrm{tot}})^2 \right\rangle^2 \right] . \end{aligned} \tag{4.29}$$

We present results for the third-order susceptibility only for the Kondo lattice model (Chapter 10). For the J_1-J_2 model, we refer to Ref. [94].

4.4.4. The magnetocaloric effect

The magnetocaloric effect (MCE) is defined as the change in the temperature of a sample, by adiabatically changing the magnetic field [69],

$$\Gamma_{\mathrm{mc}} := \left(\frac{\partial T}{\partial H} \right)_S = - \frac{\left(\dfrac{\partial S}{\partial H} \right)_T}{\left(\dfrac{\partial S}{\partial T} \right)_H} = - \frac{T}{C_V} \left(\frac{\partial M}{\partial T} \right)_H , \tag{4.30}$$

where T is the temperature of the system, and H the magnetic field density. From Eq. 4.24 for the expression of the free energy in terms of the partition function, we obtain

$$\left(\frac{\partial T}{\partial H} \right)_S = T \frac{\langle \mathcal{H} \rangle \left\langle S_z^{\mathrm{tot}} \right\rangle - \left\langle \mathcal{H} S_z^{\mathrm{tot}} \right\rangle}{\langle \mathcal{H}^2 \rangle - \langle \mathcal{H} \rangle^2} . \tag{4.31}$$

In Ref. [69], the magnetocaloric properties of the two-dimensional frustrated J_1-J_2 model on a square lattice is investigated.

V. Numerical Implementation: Tile Selection and Finite-Size Effects

As previously described in Chapter IV, the exact diagonalization technique is limited to dealing with rather small clusters cut from the infinite lattice. In this chapter, we describe a finite-size scaling analysis and use it to evaluate the physical quantities in the thermodynamic limit ($N \to \infty$). This analysis enables the comparison between the numerical calculations and analytical methods such as the linear spin-wave approximation (Chapter III). The first ingredient is the computation of the ground-state energy (Section 4.3) and the structure factor (Section 4.3.1) for different system sizes. In the following, we explain how to generate possible finite clusters and select the most suitable one for each system size, in order to use them for the extrapolation to the thermodynamic limit.

5.1. Definitions

5.1.1. Lattice

Here we define the underlying lattice for the spin model for arbitrary dimension m. A basic requirement is a unique description of the lattice structure [95–98]. Let $A = \{\boldsymbol{a}_i \in \mathbb{R}^n : 1 \leqslant i \leqslant n\}$ be a set of n linearly independent vectors. The group $\mathcal{L}(A) := \{\sum_i^n x_i \boldsymbol{a}_i : x_i \in \mathbb{Z}\}$ is called a *lattice* generated by A as its *basis* vectors. These basis vectors also define an n-dimensional parallelotope, which is known as the *fundamental region* of the lattice, and contains a number of points in $\mathbb{Z}^n$, namely the *lattice points.* The lattice can be represented also by a matrix composed of the basis vectors as its columns, $\mathbf{A} = (\boldsymbol{a}_1\ \boldsymbol{a}_2\ \cdots\ \boldsymbol{a}_n) \in \mathbb{R}^{n\times n}$. Hence, $\mathcal{L}(\mathbf{A}) = \{\mathbf{A}\boldsymbol{x} : \boldsymbol{x} \in \mathbb{Z}^n\}$. Note that the selection of the basis vectors for a given lattice is not unique, e.g. swapping two basis vectors or multiplying each by -1 as well as adding them to each other generates the same group.

Recalling the definition of the *unimodular* matrix $\mathbf{U}$ as a square matrix with determinant ±1, generally,

$$\mathcal{L}(\mathbf{A}) = \mathcal{L}(\mathbf{B}) \Leftrightarrow \mathbf{A} = \mathbf{U}\mathbf{B}. \tag{5.1}$$

This means that there is a unimodular matrix which links two matrices generating the same lattice. Consequently, the determinant of the generating matrix is a property of the lattice, and is usually denoted by $\mathrm{d}(\mathcal{L}\,(\mathbf{A})) := \det(\mathbf{A})$. For simplicity and without losing generality, we limit ourselves only to the lattices with basis vectors in $\mathbb{Z}^n$. Hereafter, the number of lattice points inside the parallelotope is $N := \det(\mathbf{A})$.

The point $\boldsymbol{p}$ is inside the parallelotope if and only if,

$$0 \leqslant \det(\mathbf{A}_i) < \det(\mathbf{A}) = N, \qquad i = 1 \dots n, \tag{5.2}$$

where $\mathbf{A}_i$ is the matrix formed by replacing the ith column of $\mathbf{A}$ by $\boldsymbol{p}$. This follows from demanding the modulus of projections of $\boldsymbol{p}$ onto $\boldsymbol{a}_i$ be smaller than one, and subsequently using Cramer's rule for solving the resulting system of equations. We use the criterion 5.2 to find the coordinates of the inner lattice points. Moreover, these points can be written in the form of $\sum_i \frac{n_i}{N}\boldsymbol{a}_i$, with $n_i \in \mathbb{Z}$ and $0 \leqslant n_i < N$, where the edge vectors $\boldsymbol{a}_i$ define the *local coordinate system.*

Each of the lattice points can be labeled to represent a site with a spin $\frac{1}{2}$. For the periodic boundary conditions case, the near-boundary sites are linked to a site on the neighboring cell, which is equivalent to a point inside. The labeling for outer points is resolved by mapping them back with corresponding required translation(s) by the lattice basis vectors.

5.1.2. The Hermite normal form

We are looking for a way to uniquely define and construct the lattice. The aim is to characterize each inequivalent lattice tiling uniquely by a square, non-singular matrix $\mathbf{H} = (h_{ij})$, that is defined to be in Hermite normal form if and only if

- it has only integer entries, $h_{ij} \in \mathbb{Z}$,
- is in upper triangular form, i.e. $i > j \Rightarrow h_{ij} = 0$,
- its diagonal elements are positive, $h_{ii} \geqslant 0$, and,
- in each row, the entries to the right of the diagonal are at least zero and less than the diagonal element, i.e. for $i < j$, we have $0 \leqslant h_{ij} < h_{ii}$.

It can be shown [95, p. 45] that every rational, non-singular square matrix **A** can be brought into the Hermite normal form by a series of elementary column operations, i.e., there exists a unimodular matrix **U** such that,

$$\mathbf{AU} = \mathbf{H}. \tag{5.3}$$

H is then called the Hermite normal form of **A**. Furthermore, the Hermite normal form of a lattice is unique[1], i.e. for two Hermite normal form matrices **H** and **H**′,

$$\mathcal{L}(\mathbf{H}) = \mathcal{L}(\mathbf{H}') \Leftrightarrow \mathbf{H} = \mathbf{H}'. \tag{5.4}$$

Therefore, Hermite normal form matrices can be used to uniquely generate and identify individual lattices.

5.1.3. Two dimensional lattices

The general concept introduced above will now be applied to lattices in two dimensions ($n = 2$). In this case, the fundamental region of the lattice is a parallelogram, which we name a "tile". As an example, Fig. 5.1 illustrates the lattice generated by $A = \left(\begin{smallmatrix} 4 & 1 \\ -2 & 3 \end{smallmatrix}\right)$. The tile spanned by the two defining vectors of the lattice contains 14 distinct lattice points. The corresponding Hermite normal form matrix is given by $H = \left(\begin{smallmatrix} 14 & 5 \\ 0 & 1 \end{smallmatrix}\right)$, which is obtained by multiplying the basis vectors matrix by the unimodular matrix $U = \left(\begin{smallmatrix} 3 & 1 \\ 2 & 1 \end{smallmatrix}\right)$.

For a given total number of lattice points N, there exists a finite number of matrices in the Hermite normal form. In other words, there are a certain number of Hermite normal form matrices with a given determinant. Hence, a given N fixes the number of different lattice tilings which are represented by different Hermite normal form matrices. These matrices can be enumerated as

$$H(N) = \left\{ \left(\begin{smallmatrix} h_{11} & h_{12} \\ 0 & h_{22} \end{smallmatrix}\right) \in \mathbb{Z}^2 : 0 \leqslant h_{12} < h_{11} \text{ and } h_{11}h_{22} = N \right\}. \tag{5.5}$$

Because of the constraint h_{22} and h_{12} are sufficient for the enumeration. As an example, for $N = 4$ we have

$$H(4) = \left\{ \begin{pmatrix} 1 & 0 \\ 0 & 4 \end{pmatrix}, \begin{pmatrix} 2 & 0 \\ 0 & 2 \end{pmatrix}, \begin{pmatrix} 2 & 1 \\ 0 & 2 \end{pmatrix}, \begin{pmatrix} 4 & 0 \\ 0 & 1 \end{pmatrix}, \begin{pmatrix} 4 & 1 \\ 0 & 1 \end{pmatrix}, \begin{pmatrix} 4 & 2 \\ 0 & 1 \end{pmatrix}, \begin{pmatrix} 4 & 3 \\ 0 & 1 \end{pmatrix} \right\}. \tag{5.6}$$

---

[1] For the proof see [96].

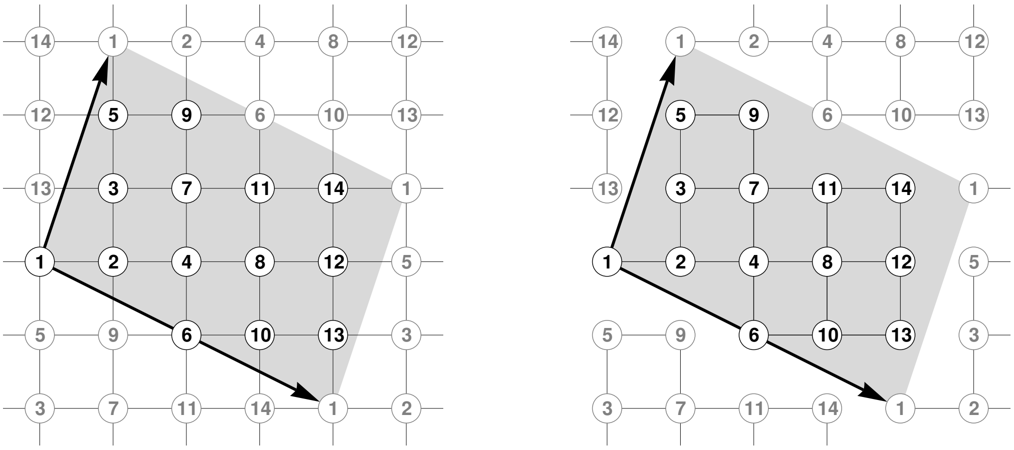
(a) Periodic

(b) Open

Figure 5.1.: Example of a lattice in two dimensions with its fundamental parallelogram containing 14 sites. The edge vectors are $\mathbf{a}_1 = (4, -2)$ and $\mathbf{a}_2 = (1, 3)$, and the numbers are the labels for shown lattice points. The fundamental region is shaded and nearest-neighbors interactions for different boundary conditions are shown as connecting lines.

The total number of these matrices, hence the number of possible inequivalent lattice tilings, is listed for tiles having lattice points between 4 and 36 in Table 5.1. Once we have constructed a matrix in the Hermite normal form, its columns can be used to represent the basis vectors of the lattice. Note that multiplying by any unimodular matrix leads to generating different basis vectors, but the same lattice. Hence, for the naming of a tile we refer to the matrix elements of the Hermite normal matrix form, and use the naming scheme N:h_{22}-h_{12} for a unique labeling. Appendix A.1 contains a list of tiles used in the calculations as well as their shape and other properties.

A number of lattices are associated to each other by symmetry operations such as rotation or reflection. It would be dependent on the other aspects of the model Hamiltonian whether they are actually equivalent for the calculations or not. This will become more clear in Section 5.3, where we introduce a criterion to select between different tiles for our calculations.

In the following, we describe the reciprocal lattice and how to generate it. This is useful to reduce the size of the matrices representing the Hamiltonian, by working in a basis reflecting the periodicity of the infinite lattice.

N	$\sigma_1(N)$	N	$\sigma_1(N)$	N	$\sigma_1(N)$
4	7	15	24	26	42
5	6	16	31	27	40
6	12	17	18	28	56
7	8	18	39	29	30
8	15	19	20	30	72
9	13	20	42	31	32
10	18	21	32	32	63
11	12	22	36	33	48
12	28	23	24	34	54
13	14	24	60	35	48
14	24	25	31	36	91

$\sum_{N=4}^{36} \sigma_1(N) = 1090$

Table 5.1.: Total number of different Hermite normal form matrices $\sigma_1(N)$, containing N distinct lattice points. For $4 \leqslant N \leqslant 36$ there are totally 1090 distinct matrices.

5.2. Reciprocal space and Brillouin zone construction

The reciprocal lattice is a convenient concept for discussion of Fourier transforms in the direct lattice. Mathematically speaking, the reciprocal lattice is the set of all $\boldsymbol{k}$ vectors which satisfy the equation $e^{i\boldsymbol{k}\cdot\boldsymbol{r}} = 1$ for all lattice points $\boldsymbol{r}$. Alternatively, using the matrix representation of the lattice basis vectors, this condition can be written as

$$(\boldsymbol{b}_1\ \boldsymbol{b}_2\ \cdots\ \boldsymbol{b}_n)^T \ := \ 2\pi\ (\boldsymbol{a}_1\ \boldsymbol{a}_2\ \cdots\ \boldsymbol{a}_n)^{-1}, \tag{5.7}$$

where the $\boldsymbol{a}_i$ ($\boldsymbol{b}_i$) are the direct (reciprocal) lattice basis vectors.

In two dimensions ($n = 2$), with $\boldsymbol{a}_1 = (a_{11}, a_{12})$ and $\boldsymbol{a}_2 = (a_{21}, a_{22})$, Eq. 5.7 reads as

$$\begin{aligned} \boldsymbol{b}_1 &= \frac{2\pi}{N}\begin{pmatrix} a_{22} \\ -a_{21} \end{pmatrix}, \\ \boldsymbol{b}_2 &= \frac{2\pi}{N}\begin{pmatrix} -a_{12} \\ a_{11} \end{pmatrix}. \end{aligned} \tag{5.8}$$

Hence, for a translation vector $\boldsymbol{r} = r_1\boldsymbol{a}_1 + r_2\boldsymbol{a}_2$, and a vector in k-space (wave vector)

$\boldsymbol{k} = k_1\boldsymbol{b}_1 + k_2\boldsymbol{b}_2$, by construction we can write

$$\boldsymbol{k} \cdot \boldsymbol{r} = 2\pi(k_1 r_1 + k_2 r_2). \tag{5.9}$$

The coefficients $r_1 = \frac{n_1}{N}$ and $r_2 = \frac{n_2}{N}$ with integer n_1 and n_2 are the projections of the lattice points of a tile onto the edge vectors, and k_1 and k_2 are integers. Note that these two vectors are both expressed in the local coordinate system, which should be always used when dealing with the products between direct and reciprocal spaces, such as $\boldsymbol{k} \cdot \boldsymbol{r}$.

The Brillouin zone is the primitive cell in the reciprocal space. For its determination, we consider the edge vectors $\boldsymbol{g}_i = 2\pi\hat{\boldsymbol{e}}_i$, where $\hat{\boldsymbol{e}}_i$ are the unit vectors in the Cartesian coordinate system. Using Eq. 5.7, the local coordinate system expression of $\boldsymbol{g}_i$ for general n is

$$\begin{aligned}(\boldsymbol{g}_1\ \boldsymbol{g}_2\ \cdots\ \boldsymbol{g}_n) &:= 2\pi\mathbf{I}_n \\ &= (\boldsymbol{a}_1\ \boldsymbol{a}_2\ \cdots\ \boldsymbol{a}_n)^T\ (\boldsymbol{b}_1\ \boldsymbol{b}_2\ \cdots\ \boldsymbol{b}_n),\end{aligned} \tag{5.10}$$

which in two dimensions reduces to

$$\begin{aligned}\boldsymbol{g}_1 &= a_{11}\boldsymbol{b}_1 + a_{21}\boldsymbol{b}_2, \\ \boldsymbol{g}_2 &= a_{12}\boldsymbol{b}_1 + a_{22}\boldsymbol{b}_2.\end{aligned} \tag{5.11}$$

The vectors $\boldsymbol{g}_i$ define the Brillouin zone in the reciprocal space, which contains exactly N wave vectors $\boldsymbol{k} = k_1\boldsymbol{b}_1 + k_2\boldsymbol{b}_2 =: (k_1, k_2)$. A similar approach leading to Eq. 5.2 can be used to enumerate these points, i.e. the condition for all $\boldsymbol{k}$ vectors to be inside the Brillouin zone is

$$0 \leqslant \det(\mathbf{G}_i) < N, \qquad i = 1 \dots n, \tag{5.12}$$

with $\mathbf{G}_i$ defined by replacing the ith column of $(\boldsymbol{g}_1\ \boldsymbol{g}_2\ \cdots\ \boldsymbol{g}_n)$ by $\boldsymbol{k}$.

As an example, Fig. 5.2 illustrates the real and reciprocal lattices for tile number 14:1-9. The wave vectors available to this tile are shown by full circles in Fig. 5.2b. The basis vectors $\boldsymbol{b}_1$ of the reciprocal lattice is orthogonal to $\boldsymbol{a}_2$, and $\boldsymbol{b}_2$ is orthogonal to $\boldsymbol{a}_1$. Also shown is the first Brillouin zone of the lattice with edge vectors (reciprocal lattice vectors) $\boldsymbol{g}_1$ and $\boldsymbol{g}_2$.

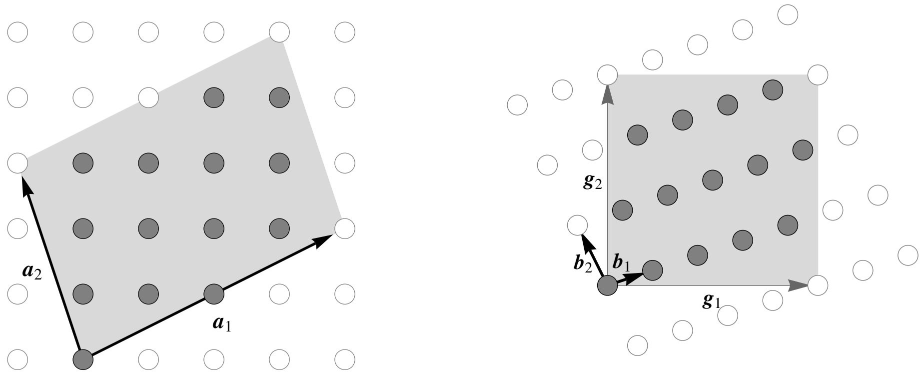

(a) (b)

Figure 5.2.: Tile 14:1-9 in (a) the direct space, and (b) the corresponding reciprocal lattice.

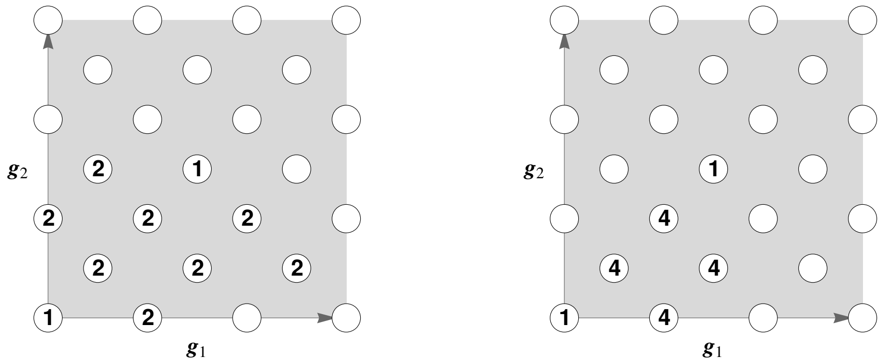

(a) $\mathcal{C}_2$ (b) $\mathcal{C}_4, \mathcal{C}_{4\mathcal{V}}$

Figure 5.3.: Invariant wave vectors with their weight for tile 18:3-3, using two set of point group symmetry operations. The numbers represent the weight for each invariant wave vector.

5.2.1. Point group symmetries

A number of point group symmetries can be used to identify equivalent wave vectors in the reciprocal lattice. Unnecessary calculations can be avoided by computing the eigenvalues and eigenvectors only at inequivalent wave vectors. The recipe is to apply the point group operations to the wave vectors of a tile, followed by a translation mapping the tile back to the origin. This leads to the determination of several classes of $\boldsymbol{k}$ vectors, which map onto each other, and thus are interchangeable for the sake of eigensystem calculations. Each wave vector belongs to exactly one class, and out of these classes, one vector can be selected as an invariant $\boldsymbol{k}$ vector to represent the whole class. Besides, the number of equivalent wave vectors in the class should also be considered as the "weight" for that $\boldsymbol{k}$ vector when performing $\boldsymbol{k}$-space summations. Fig. 5.3 shows the tile 18:3-3 in reciprocal space, with the invariant $\boldsymbol{k}$ vectors and their weights are specified, when two different point group symmetry operations (e.g. $\mathcal{C}_{2\mathcal{V}}$ and $\mathcal{C}_{4\mathcal{V}}$) are applied.

However, one should note that these wave vectors are equivalent because of the lattice symmetry. It might be the case that the model Hamiltonian contains some spatially anisotropic interaction between the spins on different lattice sites. Therefore, this lower symmetry of the Hamiltonian breaks the spatial symmetry of the tile, and should be used instead in the calculations.

For the two dimensional case, we have incorporated $\mathcal{C}_2$ and $\mathcal{C}_4$ rotational symmetries, as well as the mirror plane reflections. For the $\mathcal{C}_{2\mathcal{V}}$ group, two sets of mirror planes exists, because the point group $\mathcal{C}_{4\mathcal{V}}$ contains two isomorphic subgroups $\mathcal{C}_{2\mathcal{V}}^{\text{rect}}$ and $\mathcal{C}_{2\mathcal{V}}^{\text{dia}}$, corresponding to a tile with either a rectangular shape (mirrors parallel to the edges) or a diamond-like shape (mirrors along the diagonals).

5.3. Selection criterion

For a specified system size, calculations on different tiles can produce different results for physical quantities. For instance, the value of the ground-state energy for the $S = \frac{1}{2}$ Néel antiferromagnet is shown in Fig. 5.4 for different tiles, where this effect is quite pronounced. Thus, selecting the "right" class of tile which may be used to extract the properties of the infinite lattice is of the utmost importance for numerical calculations of ground-state energy, correlation functions and moments. For this selection, we will now introduce two sufficiently powerful criteria.

5.3.1. Classical phase compatibility

The system parameters of the model Hamiltonian govern the location in the classical phase diagram. In each classical phase, the corresponding arrangement of spins with that ordering has a large weight in the linear superposition of the basis states. The tiling should not suppress this classical ordering of spins. In other words, in order to have a true representation, the arrangement of the spins on the finite tile should obey the pattern of the classical phase on the infinite lattice. This cannot always be the case when using the periodic boundary conditions for the finite tiles. As an example

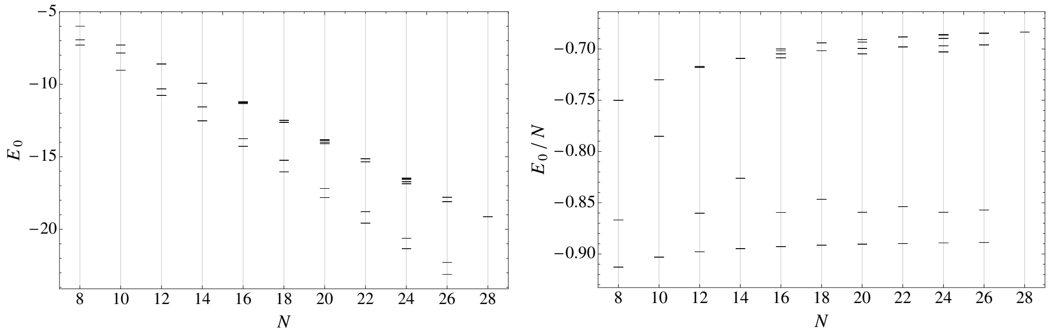

(a) Ground-state energy.

(b) Ground-state energy per site.

Figure 5.4.: The ground-state energy of the Néel antiferromagnetic model for different tiles and system sizes. Each dash corresponds to the energy of one possible lattice.

illustrated in Fig. 5.5, consider the tile 10:1-7 in the Néel antiferromagnetic phase with the ordering vector (π, π) (Fig. 5.5a). The antiferromagnetic pattern of the spins, shown as arrows inside the lattice points, is preserved when tiling the lattice. However, for the same tile in the columnar antiferromagnetic phase along b direction with the ordering vector $(0, \pi)$, incompatibilities occur by repetition of equivalent lattice points (Fig. 5.5b). These incompatibilities impose an additional constraint on the interactions of the spins, which act similar to geometrical frustration (Chapter 1). The result of the calculation on this tile and on this phase therefore leads to a higher ground-state energy and a lower degree of magnetic ordering of the spins. Thus, this tile has to be rejected and we have to choose another tile compatible to this phase, e.g. 10:2-3 (Fig. 5.5c). For our computations, we use only those tiles which are compatible to the corresponding classical phase, i.e., do not introduce frustration when periodic boundary conditions are applied. This will reduce the number of acceptable tiles to a fraction of all possible tiles for each size.

A tile is compatible to a classical phase if and only if its reciprocal lattice contains the according ordering vector $\boldsymbol{q}$. Therefore, the equation

$$n_1 \boldsymbol{b}_1 + n_2 \boldsymbol{b}_2 = \boldsymbol{q}, \tag{5.13}$$

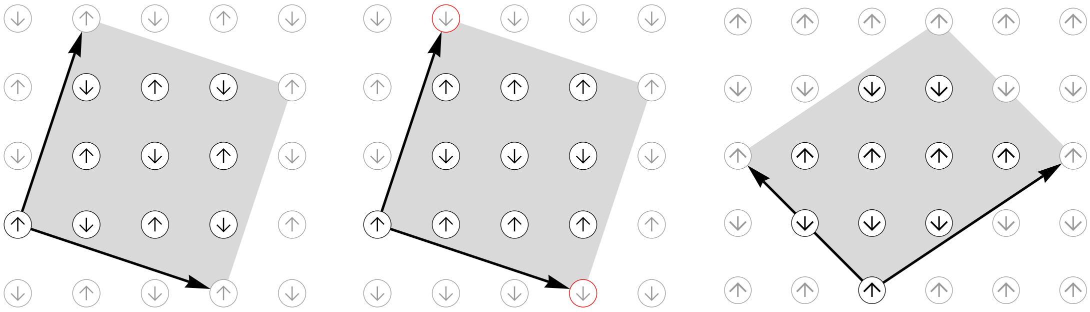
(a) 10:1-7, NAF (b) 10:1-7, CAFb (c) 10:2-3, CAFb

Figure 5.5.: Comparing the classical phase compatibilities of tiles 10:1-7 and 10:2-3, in two classical phases NAF and CAFb.

should have an integer solution for n_i. Using Eq. 5.8 the above equations reads

$$\begin{aligned}\frac{2\pi}{N}(n_1a_{22}+n_2a_{12}) &= q_1,\\ \frac{2\pi}{N}(-n_1a_{21}+n_2a_{11}) &= q_2.\end{aligned} \tag{5.14}$$

We are interested in the four classical phases of the $J_1 - J_2$ Heisenberg model discussed below. The solutions for Eq. 5.14 are:

- **FM** with $\boldsymbol{q} = (0,0)$,
  $n_1 = n_2 = 0$. All tiles are trivially compatible with the ferromagnetic phase.

- **CAFa** with $\boldsymbol{q} = (\pi,0)$,
  $n_1 = \frac{a_{11}}{2}$ and $n_2 = \frac{a_{21}}{2}$. Thus the coefficients a_{11} and a_{21} must be even numbers. All tiles with the edge vectors $\boldsymbol{a}_1$ and $\boldsymbol{a}_2$ having even x components contain the classical columnar Néel state with the ordering vector along this direction.

- **CAFb** with $\boldsymbol{q} = (0,\pi)$,
  $n_1 = \frac{a_{12}}{2}$ and $n_2 = \frac{a_{22}}{2}$. Here the coefficients a_{12} and a_{22} must be even numbers. All tiles with the edge vectors $\boldsymbol{a}_1$ and $\boldsymbol{a}_2$ having even y components contain the classical columnar Néel state with the ordering vector along this direction.

- **NAF** with $\boldsymbol{q} = (\pi,\pi)$,
  $n_1 = \frac{a_{11}+a_{22}}{2}$ and $n_2 = \frac{a_{12}+a_{21}}{2}$. Here the coefficients a_{11} and a_{22} and

separately a_{12} and a_{21} must both be even or both odd simultaneously. As we discuss tiles with even size N only, a_{11} and a_{22} must be even.

- **All** four phases,
  all components of the edge vectors $\boldsymbol{a}_1$ and $\boldsymbol{a}_2$ must even individually be compatible with all phases in the classical phase diagram of the $J_1 - J_2$ model.

5.3.2. Compactness parameter

For the analysis, finally only one out of all possible compatible tiles of a given size N should be selected. We use the concept of “squareness” or “compactness” of a tile for selecting the proper tiles for the finite-size scaling. The idea is to determine the ratio of the hyper-volume to the hyper-surface of the parallelotope generated by the lattice basis vectors. For the n-dimensional parallelotope we define the parameter

$$\begin{aligned} \rho(\mathbf{A}) &:= \frac{|\det \mathbf{A}|}{||\mathbf{A}||}, \\ ||\mathbf{A}|| &= \left(\frac{1}{n} \sum_{i=1}^{n} \sqrt{\det\left(\mathbf{A}_i^T \mathbf{A}_i\right)} \right)^{n/(n-1)}, \end{aligned} \tag{5.15}$$

for a non-singular integer $n \times n$ matrix $\mathbf{A}$, where $\mathbf{A}_i$ is the non-square matrix formed by dropping the ith column of $\mathbf{A}$. $\rho(\mathbf{A})$ is the “compactness” (or “squareness in two dimensions) parameter of the n-dimensional parallelotope spanned by the lattice basis vectors. We have $0 < \rho(\mathbf{A}) \leqslant 1$, and $\rho(\mathbf{A}) = 1$ exactly where $\mathbf{A}$ describes a hyper-cube, which is the most compact lattice tiling in n dimensions. In two dimensions and for the edge vectors $\boldsymbol{a}_1$ and $\boldsymbol{a}_2$, Eq. 5.15 is proportional to the ratio of the area to the square of the perimeter of a tile, i.e.

$$\rho\left(\begin{smallmatrix} a_{11} & a_{12} \\ a_{21} & a_{22} \end{smallmatrix}\right) = 4 \frac{a_{11}a_{22} - a_{12}a_{21}}{\left(\sqrt{a_{11}^2 + a_{12}^2} + \sqrt{a_{21}^2 + a_{22}^2}\right)^2}. \tag{5.16}$$

However, calculating $\rho(\mathbf{H})$ for the Hermite normal form representation of a lattice tiling is not useful. According to Eq. 5.3, a single Hermite normal form matrix $\mathbf{H}$, represents a whole class $\mathcal{L}(\mathbf{H})$ of tiles, which all describe the same lattice. But in general, two matrices $\mathbf{A} \neq \mathbf{A}'$ with $\mathcal{L}(\mathbf{A}) = \mathcal{L}(\mathbf{A}')$ have $\rho(\mathbf{A}) \neq \rho(\mathbf{A}')$. So, for each $\mathbf{H}$ we choose the particular tile which has the maximum compactness parameter among all matrices of its class,

$$\mathbf{A}_{\max} : \rho(\mathbf{A}_{\max}) = \max_{\mathbf{A}\in\mathcal{L}(\mathbf{H})} \rho(\mathbf{A}), \tag{5.17}$$

and assign $\rho(\mathbf{A}_{\max})$ to each lattice as its compactness parameter, described by the Hermite normal form matrix $\mathbf{H}$.

To find the maximum in Eq. 5.17 one has to generate all the possible matrices corresponding to a given $\mathbf{H}$. From Eq. 5.3, the matrix $\mathbf{A}$ being a member of $\mathcal{L}(\mathbf{H})$ has the form

$$\mathbf{A} = \mathbf{H}\mathbf{U}^{-1}. \tag{5.18}$$

In order to find all the matrices $\mathbf{A}$, we have to list all the possible unimodular matrices, via its generating group $GL_n(\mathbb{Z})$. The generator matrices are

- $\mathbf{I}_n$, the identity matrix,
- $\mathbf{S}^{(i)}$, the matrix obtained from $\mathbf{I}_n$ by replacing s_{ii} with -1, and
- $\mathbf{U}^{(jk)}$, the matrix obtained from $\mathbf{I}_n$ by setting u_{jk} to 1.

Therefore, we can enumerate all powers of the above matrices to generate the unimodular group, and use Eq. 5.18 to construct different matrices belonging to the same lattice. Another way is to use the lattice reduction algorithms, such as the LLL algorithm [99]. By giving an integer lattice basis as input, the goal of such algorithms is to provide a new set of basis with short and nearly orthogonal vectors. This near orthogonality condition in these algorithms have to be defined as the compactness parameter in order to obtain the most compact vectors. In two dimensions, there is a simple and efficient way of reduction, similar to the Euclidean algorithm for the greatest common divisor of two integers. The method is iterative, and it is based on subtracting the larger vector from the smaller one, until the maximum squareness parameter is reached.

Finally, the selection criterion of the tiles, to be used in the finite-size scaling analysis, is to choose the tile having the largest compactness parameter, out of all classically compatible tiles. The resulting list of the tiles is displayed in Table 5.2, in which label, classical phase compatibility, squareness, and point groups for selected lattice tilings between 8 and 36 sites are presented. For each even area N and for each classical phase, the list contains the compatible tile with maximum squareness as defined in Eq. 5.15. For $N = 12$ and 24, the tiles compatible with all classical phases are included too, although they have a comparatively small squareness. The

Tile	NAF	CAFa	CAFb	□	$\mathcal{C}_2$	$\mathcal{C}_{2\mathrm{V}}^{\mathrm{rect}}$	$\mathcal{C}_{2\mathrm{V}}^{\mathrm{rect}}$	$\mathcal{C}_4$	$\mathcal{C}_{4\mathrm{V}}$
8:2-2	●	●	●	1.000	●	●	●	●	●
10:1-3	●	–	–	1.000	●	–	–	●	–
10:1-4	–	–	●	0.966	●	–	–	–	–
10:2-2	–	●	–	0.966	●	–	–	–	–
12:3-0	–	–	●	0.980	●	●	–	–	–
12:4-0	–	●	–	0.980	●	●	–	–	–
12:1-5	●	–	–	0.960	●	–	●	–	–
12:2-2	●	●	●	0.901	●	–	–	–	–
14:1-3	●	–	–	0.961	●	–	–	–	–
14:1-4	–	–	●	0.938	●	–	–	–	–
14:2-3	–	●	–	0.938	●	–	–	–	–
16:4-0	●	●	●	1.000	●	●	●	●	●
18:3-3	●	–	–	1.000	●	●	●	●	●
18:1-4	–	–	●	0.975	●	–	–	–	–
18:2-4	–	●	–	0.975	●	–	–	–	–
20:2-4	●	●	●	1.000	●	–	–	●	–
22:1-6	–	–	●	0.981	●	–	–	–	–
22:2-4	–	●	–	0.981	●	–	–	–	–
22:1-5	●	–	–	0.961	●	–	–	–	–
24:1-10	–	–	●	0.988	●	–	–	–	–
24:2-5	–	●	–	0.988	●	–	–	–	–
24:1-7	●	–	–	0.980	●	–	●	–	–
24:4-0	●	●	●	0.960	●	●	–	–	–
26:1-5	●	–	–	1.000	●	–	–	●	–
26:1-10	–	–	●	0.964	●	–	–	–	–
26:2-5	–	●	–	0.964	●	–	–	–	–
28:1-8	–	–	●	0.986	●	–	–	–	–
28:4-3	–	●	–	0.986	●	–	–	–	–
28:2-4	●	●	●	0.961	●	–	–	–	–
30:5-0	–	–	●	0.992	●	●	–	–	–
30:6-0	–	●	–	0.992	●	●	–	–	–
30:1-5	●	–	–	0.974	●	–	–	–	–
32:4-4	●	●	●	1.000	●	●	●	●	●
34:1-13	●	–	–	1.000	●	–	–	●	–
34:1-14	–	–	●	0.992	●	–	–	–	–
34:2-5	–	●	–	0.992	●	–	–	–	–
36:6-0	●	●	●	1.000	●	●	●	●	●

Table 5.2.: Label, classical phase compatibility, squareness, and point group symmetries for selected lattice tilings between 8 and 36 sites. For each even area N and for each classical phase, the list contains the compatible tile with maximum squareness as defined in Eq. 5.16. Those tiles compatible with all four classical phases are typeset in bold.

tile labels have the form $N{:}h_{22}\text{-}h_{12}$, with the elements of the Hermite normal form of the lattice. Those tiles compatible with all four classical phases, required for the discussion of the spatially isotropic model with columnar order, are typeset in bold.

5.3.3. Survey of other strategies for lattice tilings selection

For having a successful finite-size scaling analysis, it is common practice to select tiles according to certain geometrical or topological properties. We also briefly describe three different schemes applied in the past to the spin $\frac{1}{2}$ models and compare them to the more general selection scheme used in this work.

Haan et al. [100] discuss the spin $S = \frac{1}{2}$ nearest-neighbor Heisenberg antiferromagnet with helical boundary conditions and define an asymmetry parameter $A = |\ell_1 - \ell_2|/(\ell_1 + \ell_2)$, where ℓ_i are the lengths of the edge vectors of the tiles under consideration. A square-shaped tile (considered as "good") has $A = 0$, but this is true for general diamond-shaped tiles, too. Those tiles having "small A" are selected for scaling.

Restricting to strictly square-shaped tiles having at least $\mathcal{C}_4$ point-group symmetry is the recipe used by Schulz et al. [87] for discussing ground-state energy and ordered moment of the $S = \frac{1}{2}$ antiferromagnetic $J_1 - J_2$ model. However, with this criterion only very few (two to four) tiles are eventually used for a linear least-squares fit.

Another approach can be found in Ref. [101], discussing the $S = \frac{1}{2}$ nearest-neighbor XY and Heisenberg antiferromagnets with periodic boundary conditions. The authors introduce a parameter called the *topological imperfection* of a tile, where a topologically perfect tile is defined as follows: A given lattice point on a tile contains n_1 nearest neighbors, n_2 next-nearest neighbors, and so on, up to the $i_{\max}$th-nearest neighbors where the sum over the n_i reaches the tile area N (distance is measured as the minimal number of hops needed to get from one point to another.) If for all $i < i_{\max}$ we have $n_i = 4i$, which is the number of ith nearest neighbors on the infinite lattice, a tile is considered as topologically perfect. This concept is then extended to the notion of topologically perfect bipartite Néel lattices, i.e., the same conditions as described above are applied individually to each of the two sublattices for antiferromagnetic Néel order. However, tiles are eventually chosen by hand in order to achieve a smooth finite-size scaling behavior of the ground-state energy per site and the square of the magnetization or staggered moment, respectively.

The examples given above are in no way exhaustive, but illustrate one problem common to any finite-size scaling analysis, which becomes particularly apparent when applied to the full phase diagram of the $J_{1a,b}$-J_2 model. Firstly, only very few tilings might survive the final selection, making a linear two-parameter χ^2 fit to the ground-state energy or squared ordered moment of the $J_{1a,b}$-J_2 model questionable, not to speak about higher-order correction terms included in the fitting procedure [102]. Secondly, the selection contains some arbitrariness which in our case would lead to selecting different tiles for scaling for different sets of exchange parameters, even within the same classical phase.

Thirdly and as discussed before, given the edge vectors $\boldsymbol{a}_i$ of a particular parallelogram, there is not a unique way to tile the square lattice. For example, upon replacing $\boldsymbol{a}_1$ by, say $2\boldsymbol{a}_2 - \boldsymbol{a}_1$, we get a new tile with identical area which leads to an identical structure of the resulting torus when introducing periodic boundary conditions.

It should be remarked here that having more tiles "in-between", leads to a more stable scaling analysis. Thus, selecting the maximum squareness tiles for comparatively small N is very important for an accurate finite-size scaling. The general framework presented in this work is capable of producing and selecting these systematically. In fact, the effect of an increased scaling stability is more important than going to larger system sizes and bigger lattice tilings.

5.4. Finite-size analysis

The final ingredient for setting up a finite-size scaling analysis is the corresponding scaling laws. In Refs. [102], the area dependence of the ground-state properties of the two-dimensional antiferromagnetic Heisenberg model has been derived using the chiral perturbation theory. In particular, for the ground-state energy density and the ordered moment, the following scaling behavior has been found:

$$E_{0N} = E_0 + \beta c \frac{1}{N^{3/2}} + \frac{c^2}{4\rho}\frac{1}{N^2} + \mathcal{O}\left(\frac{1}{N^{5/2}}\right), \tag{5.19}$$

$$M_N^2(\boldsymbol{q}) = M^2(\boldsymbol{q}) + \alpha \frac{M^2(\boldsymbol{q})}{c\chi_\perp}\frac{1}{N^{1/2}} + \mathcal{O}\left(\frac{1}{N}\right), \tag{5.20}$$

where $c = \sqrt{\rho/\chi_\perp}$ is the spin-wave velocity, ρ the spin stiffness constant, and $\chi_\perp$ the transverse susceptibility. $\alpha = 0.620704$ and $\beta = -1.437745$ are numerical constants. The leading term in the scaling can also be obtained from renormalization-group calculations for the nonlinear σ model [103, 104].

These results were proposed for the isotropic unfrustrated case. Since our extension in range and anisotropy of the interactions is limited, we argue that the frustrated anisotropic model is in the same universality class as this model, and the form of the scaling functions does not change. However, the individual coefficients in Eqs. (5.20) and (5.20) might change, and no longer represent the spin-wave velocity and the spin stiffness constant. Therefore, from Ref. [89] we apply the following size dependences for the ground-state energy and the ordered moment with general coefficients,

$$E_{0N} = E_0 + \frac{e_1}{N^{3/2}} + \frac{e_2}{N^2}, \tag{5.21}$$

$$M_N^2(\boldsymbol{q}) = M^2(\boldsymbol{q}) + \frac{m_1^2}{N^{1/2}} + \frac{m_2^2}{N}, \tag{5.22}$$

where the latter scaling function is applied to both $M_N(\boldsymbol{q})$ and $\tilde{M}_N(\boldsymbol{q})$ (Eq. 4.18). Due to the limited and comparatively small number of system sizes available for our scaling analysis, we keep only the first two terms for our analysis, except for the usual Néel isotropic antiferromagnet model with only first neighbor interaction.

We have calculated the ground-state energies E_{0N}, structure factors $M_N^2(\boldsymbol{q})$, and long-distance correlation functions $\tilde{M}_N^2(\boldsymbol{q})$ at the respective ordering vectors for tilings of 12 different sizes N, between 8 and 30, producing roughly 20 000 datasets altogether.

VI. Results for Ground-State Properties

In this chapter, we present the ground-state properties of the spatially anisotropic Heisenberg model introduced in Chapter II, employing a finite-size scaling analysis, as described in Chapter V. Ground-state energy, correlation functions and structure factors, as well as the ordered moment are determined by exact diagonalization (Chapter IV), on different lattice geometries and for various system parameters. The extrapolated results to the thermodynamic limit are compared to the linear spin-wave analysis (Chapter III). Finally, a detailed description of the quality of the fit for the finite-size scaling analysis and its relation to the ordered phases and the intermediate regions is discussed.

6.1. Ground-state energy

The energy eigenvalues of the Hamiltonian (Eq. 2.4) are calculated in the subspace with total spin $S_z = 0$ for all wave vectors $\boldsymbol{k}$. The ground-state energy is the lowest energy among different $\boldsymbol{k}$ vectors, which for the tiles with $N \equiv 2 \pmod 4$, happens for the classical ordering vector $\boldsymbol{k} = \boldsymbol{Q}$, and for the other tiles at $\boldsymbol{k} = 0$.

6.1.1. Phase diagram

The result of the computation of the ground-state energy on a single tile (20:2-6) for the whole phase diagram is shown in Fig. 6.1. The horizontal axis corresponds to the frustration angle ϕ, and the vertical axis to the anisotropy parameter θ (both varying between $-\pi$ to π). The white lines in the left plot are the borders of the classical phases. The results are in good agreement with the linear spin-wave approximation, shown in Fig. 3.2. In this plot, for $\phi = \pm\frac{\pi}{2}$ the nearest neighbor interactions vanish ($J_{1a} = J_{1b} = 0$), hence the tile is actually composed of two decoupled lattices, and we have a constant ground-state energy along the lines. Moreover, on the borders of the ferromagnetic and the columnar phases, the ground-state energy has pronounced maxima. This indicates an instability of the magnetic phases, which will be confirmed by calculation of the ordered moment. The highest peak belongs

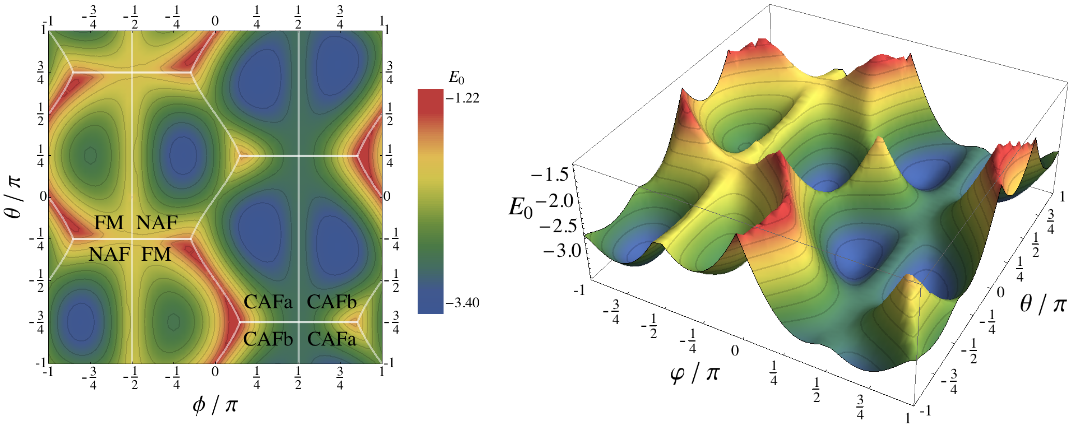

Figure 6.1.: Contour and 3D plots of the ground-state energy as a function of anisotropy (θ) and frustration (ϕ) parameters for the tile 20:2-6. The white lines show the boundaries between the four classical phases, CAFa, CAFb, NAF and FM. cf. Fig. 3.2.

to the isotropic case $\theta = \frac{\pi}{4}$ and $\theta = \frac{3\pi}{4}$, at the corner where all antiferromangetic phases meet, and a sharp peak is present for $\phi = \cos^{-1}(\frac{2}{\sqrt{5}})$ and $\phi = \cos^{-1}(-\frac{2}{\sqrt{5}})$, respectively. This suggests that it might be difficult to find an actual material in those regions of the phase diagram. On the other hand, deep inside the ordered phases, the ground-state energy forms a nearly flat valley.

6.1.2. Finite-size scaling analysis

Figs. 6.2–6.6 exhibit the dependence of the ground-state energy per site (E_{0N}) on the inverse tile size for selected model parameters. We plot $-E_{0N}$ in order to be consistent with previous studies [87, 101]. In each plot, the inset displays schematically the position in the classical phase diagram (Section 2.1.2). In the following, energies are all measured in units of J_c, unless otherwise stated. The short horizontal dashes show the calculated energies for those tiles compatible with the corresponding classical phases for a given parameter set mentioned above the abscissa as labels for the plots. The open circles indicate the ground-state energy of those tiles having the maximum squareness parameter (Eq. 5.16). We have also determined E_{0N} for those tiles incompatible with the classical phase. In these cases, we get consistently much higher values for E_{0N} (the reason is discussed in Section 5.3.1). We omit these energies in the plots. Furthermore, there are tiles which are compatible to the classical phase, but have a small squareness parameter ($\rho < \frac{1}{2}$), corresponding to very

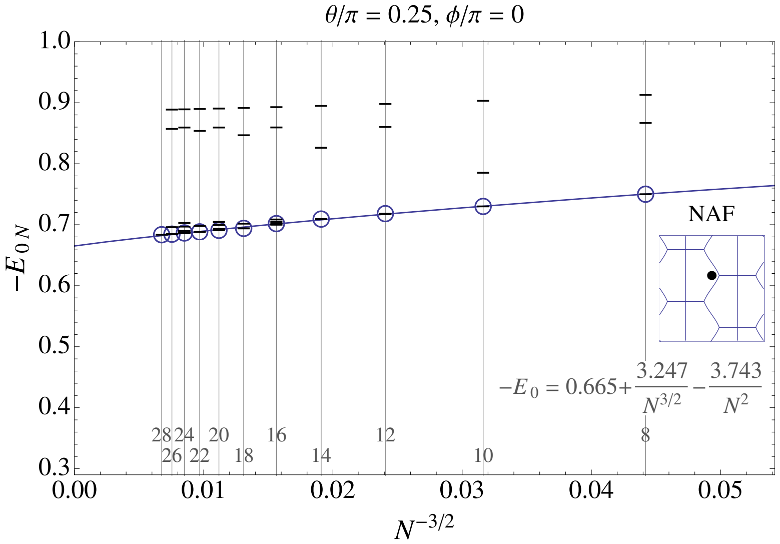

Figure 6.2.: The ground-state energy of the Néel antiferromagnetic Heisenberg model as a function of $N^{-3/2}$. Dashes correspond the energy of the compatible tiles for each area, and circles are those with the maximum squareness parameter. The numbers near the abscissa denote the tile size N. The inset plot shows the position in the phase diagram, cf. Fig. 2.3.

skewed parallelogram, which are even in some cases equivalent to ladders or chains. These tiles have a much higher ground-state energy and lie considerably above the scaling fit line in the plots. Hence, tiles with small squareness cannot be used for the scaling procedure. The formula of the finite-size scaling function is also given in the inset of the plots. Note that, not always the tile with the highest squareness parameter has the highest ground-state energy (lowest in the plot) as compared to the other compatible tiles with the same area N. However, these differences are small and not visible on the scale of figures.

Fig. 6.2 shows the ground-state energy of the conventional isotropic unfrustrated antiferromagnetic Heisenberg model ($J_{1a} = J_{1b} = J_c$ and $J_2 = 0$) as a function of $N^{-3/2}$. The fit extrapolates to the thermodynamic value of 0.66(5), which is in good agreement with previously reported values from other methods and studies, e.g. Refs. [87, 101] and references cited therein.

In the FM phase, the classical ferromagnetic arrangement of the spins is the true ground-state. Thus, the ground-state energy per site is just the sum of all bond values, i.e. $\frac{1}{4}(J_{1a} + J_{1b} + 2J_2)$. Moving to the NAF phase, Fig. 6.3 shows the ground-state energy of two points in the phase diagram, with (a) for the isotropic ($\theta = \frac{\pi}{4}$)

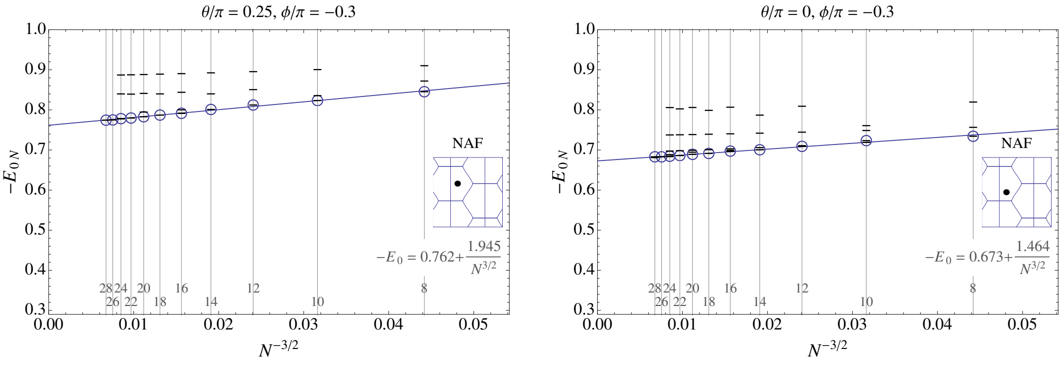

(a) Isotropic ($\theta = \frac{\pi}{4}$) (b) Maximally anisotropic ($\theta = 0$)

Figure 6.3.: The ground-state energy for two points in the NAF phase. Plot symbols and legends are the same as Fig. 6.2.

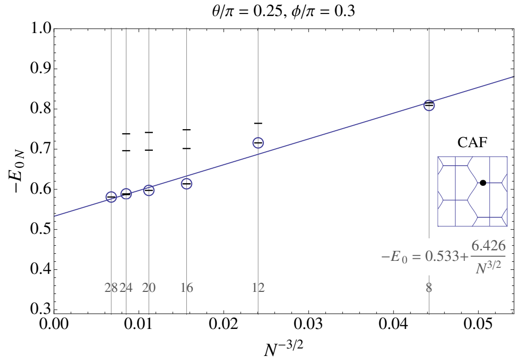

Figure 6.4.: The ground-state energy of the isotropic model in the CAF phase. Plot symbols and legends are the same as Fig. 6.2.

and (b) for the maximally anisotropic ($\theta = 0$) cases. Deep inside ordered phases, the fitting is quite stable and the extrapolation leads the value of $E_0 = -0.76(2)$ and $E_0 = -0.67(3)$, respectively. The (π, π) order is stabilized by introducing a ferromagnetic J_2, thus we obtain a lower ground-state energy as compared to the Néel case.

Fig. 6.4 also illustrates the scaling behavior of the isotropic model in the CAF phase with $\phi = 0.3\pi$. Here, exchange constants are both antiferromagnetic, and the competition between them leads to a columnar order. Since $J_{1a} = J_{1b}$, there exists two degenerate ordering vectors $(\pi, 0)$ and $(0, \pi)$, labeled by CAFa and CAFb, respectively. In this case, only those tiles containing both CAFa and CAFb classical phases have truly the symmetries required by the Hamiltonian. Hence, only

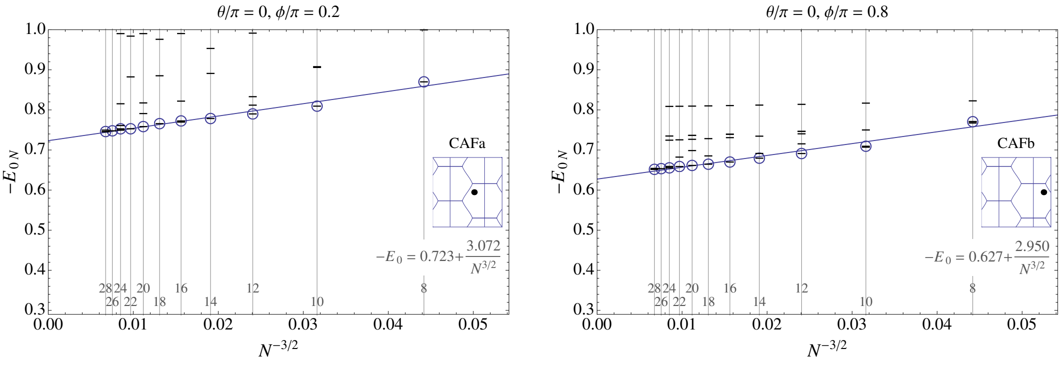

(a)

(b)

Figure 6.5.: The ground-state energy in (a) CAFa and (b) CAFb phases. Plot symbols and legends are the same as Fig. 6.2.

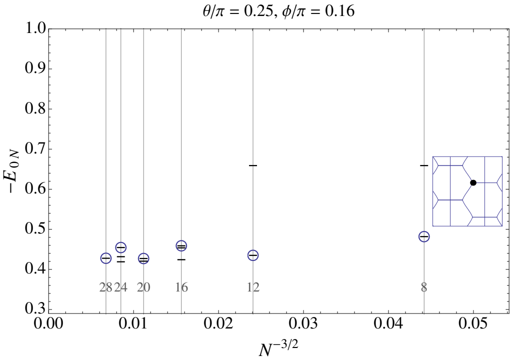

Figure 6.6.: The size dependence of the ground-state energy in the disordered regime at the CAF/FM border. In this case, a reliable linear scaling result cannot be obtained from the results of the most squared tiles, denoted here by circles.

the tiles with size $N \equiv 0 \pmod 4$ are acceptable for scaling (see page 54), leaving most of the tiles unavailable for the scaling analysis as compared to the Néel phase (Fig. 6.2). In the anisotropic case, CAFa and CAFb phases are no longer equivalent, and an example of the finite-size scaling in these phases is shown in Fig. 6.5, both in the maximally anisotropic case. Compared to the isotropic model, the extrapolated value for the ground-state energy is lower. This indicates that an in-plane $\mathcal{C}_2$ (rectangular) anisotropy stabilizes the columnar order.

All of the previous figures have one property in common, which is their location deeply inside the corresponding classically ordered phases, and they show a "good"

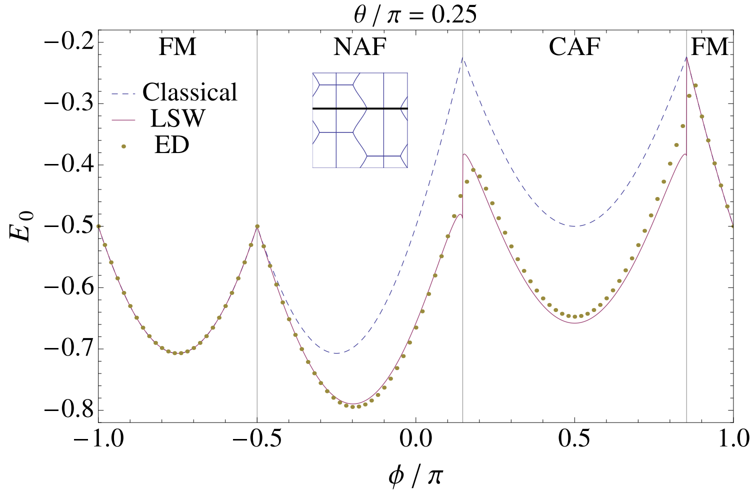

Figure 6.7.: The ground-state energy as function of the frustration angle ϕ, for the isotropic model with fixed $\theta = \frac{\pi}{4}$. The dashed line is the classical energy, and the spin-wave results including zero-point fluctuations, are shown as the solid line. Dots indicate the values for the energy E_0, obtained from extrapolating the exact diagonalization data.

scaling behavior for the ground-state energy. We discuss the quality of the fit and the precise meaning of “good scaling” in Section 6.3. In contrast, the situation is considerably different when approaching the disordered regimes at the borders of the columnar phases (the origin of disorder is explained later in Section 6.2.1). Even with our confining conditions for selecting tiles, no successful scaling can be built in the region where the transition from the Néel to the CAF phase occurs. In fact, an area dependence as given by Eq. 5.21 no longer seems to apply, and the concept of choosing the most square-like tiles for the scaling apparently becomes inappropriate. An example of this behavior is displayed in Fig. 6.6, corresponding to the well-known disordered case of the isotropic model with $J_2/J_1 \approx 1/2$. In other words, in and near the disordered regions at the edges of the columnar phases in the phase diagram, the finite-size scaling is not a useful method by itself anymore. The reason is that the scaling relations are only appropriate for the antiferromagnetic order. This will be described in more detail, by focusing on the behavior of the correlation functions and the ordered moment in Section 6.3.

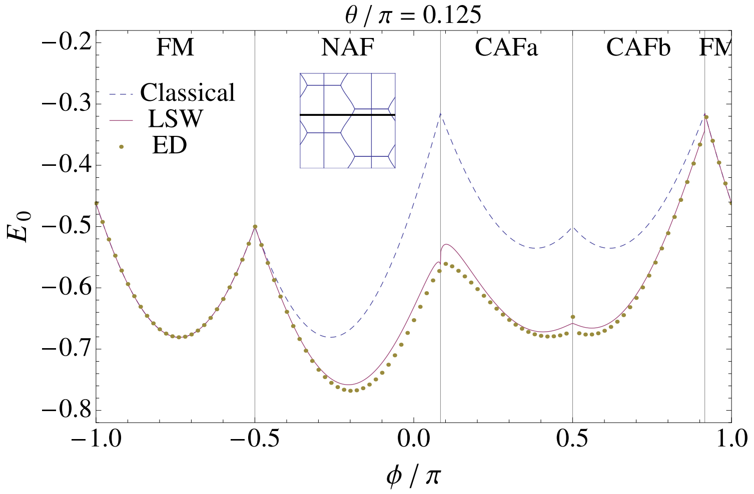

Figure 6.8.: The ground-state energy as function of the frustration angle ϕ, for the model with intermediate anisotropy with $\theta = \pi/8$. Plot elements are as in Fig. 6.7.

6.1.3. Extrapolation to the thermodynamic limit: ground-state energy

Here we describe the systematic behavior of the ground-state energy E_0 in the thermodynamic limit ($N \to \infty$). The results are obtained from our finite-size scaling analysis discussed in the previous section. Figs. 6.7 – 6.9 depict the energy dependence on the frustration angle ϕ for different anisotropy values. The dashed line on the plots shows the classical energy, and the solid line displays the result from the linear spin-wave theory, which includes the corrections due to zero-point fluctuations of magnons (Section 3.4). The dots denote our scaled exact diagonalization results, according to Eq. 5.21. For some of the dots, the details of the finite-size scaling analysis is given in Figs. 6.2 – 6.6.

Figs. 6.7, 6.8, and 6.9 correspond to the isotropic model ($\theta = \pi/4$), an intermediate anisotropy ($\theta = \pi/8$), and the maximally anisotropic ($\theta = 0$) cases, respectively. Clearly in the plots, inside the magnetic phases we have overall a very good agreement between the numerical data and the results obtained from linear spin-wave calculations (solid line). This supports the the validity of both methods. However, in the disordered regions at the borders of the columnar phase, the numerical data lead to a fit with comparatively poor quality, and the reliability of the numerical result is reduced. Linear spin-wave theory breaks down here too, albeit in a slightly different parameter range. The nature of these breakdowns is discussed in more details with studying the correlation functions and the ordered moment, in Section 6.3.

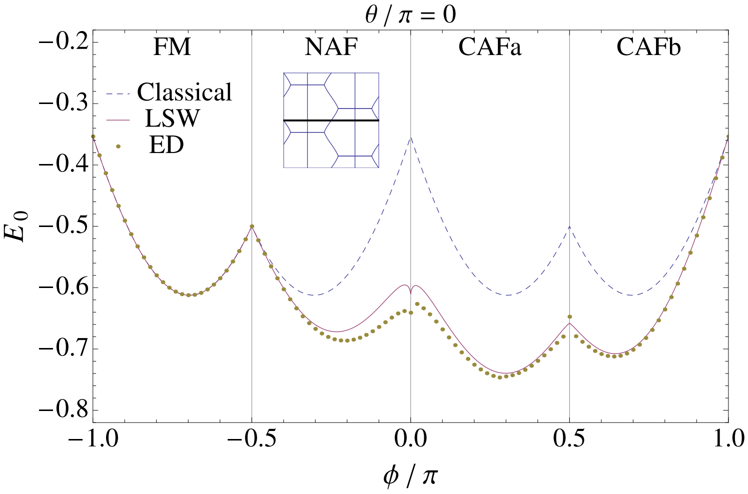

Figure 6.9.: The ground-state energy as function of the frustration angle ϕ, for the maximally anisotropic model with $\theta = 0$. Plot elements are as in Fig. 6.7.

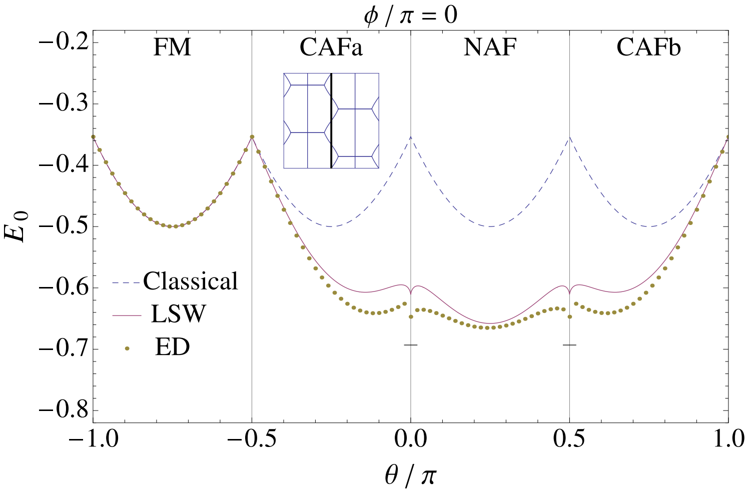

Figure 6.10.: The ground-state energy as function of the anisotropy parameter θ, for the unfrustrated model with $\phi = 0$ ($J_2 = 0$). Plot elements are the same as Fig. 6.7. Dashes denote the result $E_0 = J_c \ln 2$ from Bethe ansatz calculations for the one-dimensional $S = \frac{1}{2}$ spin chain.

Next, we consider the unfrustrated ($J_2 = 0$) but anisotropic ($J_{1a} \neq J_{1b}$) model with only nearest-neighbor interactions. Fig. 6.10 shows the dependence of the ground-state energy per site E_0, on the anisotropy parameter θ for the fixed frustration angle $\phi = 0$. As before, the agreement with linear spin-wave theory (solid

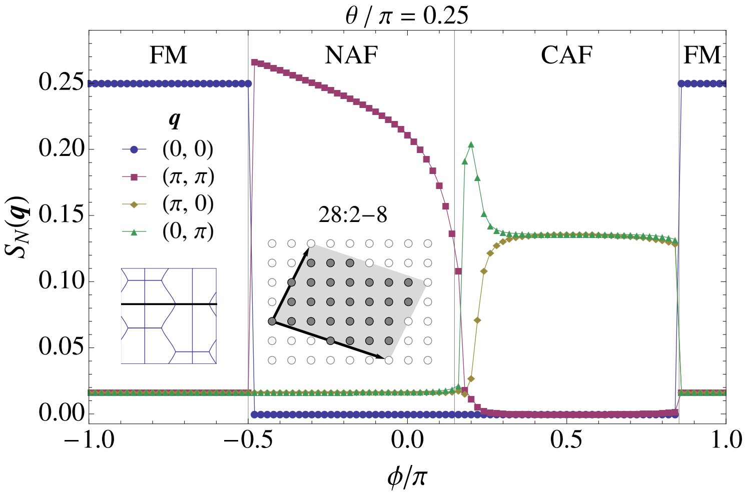

Figure 6.11.: The structure factor $S_N(\boldsymbol{q})$ for the tile 28:2-8 at the wave vectors corresponding to the four classically ordered phases, as a function of the frustration angle ϕ for the isotropic model. Inset contains an illustration of the tile in direct space and the position in the phase diagram.

line) inside the magnetic phases is good, but not at the borders of the Néel phase. For $\theta = 0$ and $\theta = \frac{\pi}{2}$, we have $J_{1b} = 0$ and $J_{1a} = 0$, respectively. Therefore, the lack of interactions between the lattice sites in one direction turns the tile into an array of short decoupled chains. Two dashes in Fig. 6.10 at $\theta = 0$ and $\theta = \frac{\pi}{2}$, denote the exact result of $E_0 = J_c \ln 2$, derived from Bethe ansatz calculations for the one-dimensional $S = \frac{1}{2}$ spin chain [23]. Here, the finite-size scaling of these usually short chains, as well as the linear spin-wave analysis in one dimension, are not successful, although the former results are more close to the exact value. However, this is an extreme case and we discuss it here primarily to show the limits of the finite-size scaling method when applied to the strongly anisotropic models.

6.2. Structure factor and ordered moment

In Chapter IV, we discussed about the spin structure factor and its calculation for testing the magnetic ordering. From the structure factor we obtained the ordered moment which is related to to the Neutron diffraction (ND) experimental data. Here, using the ground-state wave-function obtained by diagonalizing the Hamiltonian matrix, the structure factor calculated for all four ordering wave vectors is obtained using Eq. 4.3 for the largest system that we are considering (tile 28:2-8 with 28 spins), and the results are shown in Fig. 6.11. Starting from the left-side, the ferromagnetic phase has the fully polarized ground-state. Thus, we have $S_N(0) = S^2 = \frac{1}{4}$, and in accordance with Eq. 4.16, for the antiferromagnetic wave vectors $\boldsymbol{q} \neq 0$ we get $S_{28}(\boldsymbol{q}) = \frac{1}{60}$ (see Section 4.3.1). Entering the Nèel antiferromagnetic region, the mismatch between the value of the structure factors at the $(0,0)$ ordering in the FM phase and the $\boldsymbol{Q}_{\mathrm{NAF}} = (\pi,\pi)$ ordering in the NAF phase ($\phi \approx -\pi/2$) is only a finite-size effect and will be suppressed by increasing the cluster size. Now we continue to the columnar phase, because the tile 28:2-8 is not a square it has only the $\mathcal{C}_2$ point-group symmetry, hence the equivalence between two wave vectors $\boldsymbol{Q}_{\mathrm{CAFa}} = (\pi,0)$ and $\boldsymbol{Q}_{\mathrm{CAFb}} = (0,\pi)$ existing for the infinite system (and any tile having at least $\mathcal{C}_4$ symmetry) is no longer present. This manifests itself in a different ϕ dependence of the two structure factors $S(\pi,0) \neq S(0,\pi)$, which is also evident from Fig. 6.11, in particular close to the CAF/NAF border. For the calculations of the ordered moment, we take the average of these two values of the structure factor, $S(\boldsymbol{Q}_{\mathrm{CAF}}) = \frac{1}{2}\left[S(\boldsymbol{Q}_{\mathrm{CAFa}}) + S(\boldsymbol{Q}_{\mathrm{CAFb}})\right]$.

6.2.1. Finite-size scaling analysis

By determining the expectation values of the spin correlation functions $\langle \mathbf{S}_i \cdot \mathbf{S}_j \rangle$, we can now calculate the finite-size equivalent $M_N^2(\boldsymbol{q})$ of the ordered moment applying the two methods described in Section 4.3.2. In the same way as for the ground-state energy in the previous sections, we choose the most square shaped tile, for each tile area N and fit Eq. 5.22 to the resulting data points. Again, aside from the conventional Néel antiferromagnet, we ignore the last term in Eq. 5.22 and use a linear scaling only.

Isotropic nearest-neighbor exchange

Fig. 6.12 illustrates the extrapolation of the ordered moment, calculated for the unfrustrated ($J_2 = 0$) isotropic antiferromagnetic Heisenberg model ($\phi = 0$, $\theta = \pi/4$). The top plot shows the derived results from the structure factor, and the bottom plot shows $\tilde{M}^2(\boldsymbol{q})$ obtained from the longest distance correlation function. As before, the horizontal dashes denote the values for different tiles, and those with the maximum squareness parameter are specified by circles. From the top figure it is evident that the most square-like tiles have also the largest structure factor at the ordering vector $\boldsymbol{Q}_{\mathrm{NAF}} = (\pi,\pi)$ for the NAF phase. The solid lines in both plots denote the fit of $M_N^2(\boldsymbol{q})$, which yields the value of $M(\boldsymbol{Q}_{\mathrm{NAF}}) = 0.30(3)$ in the

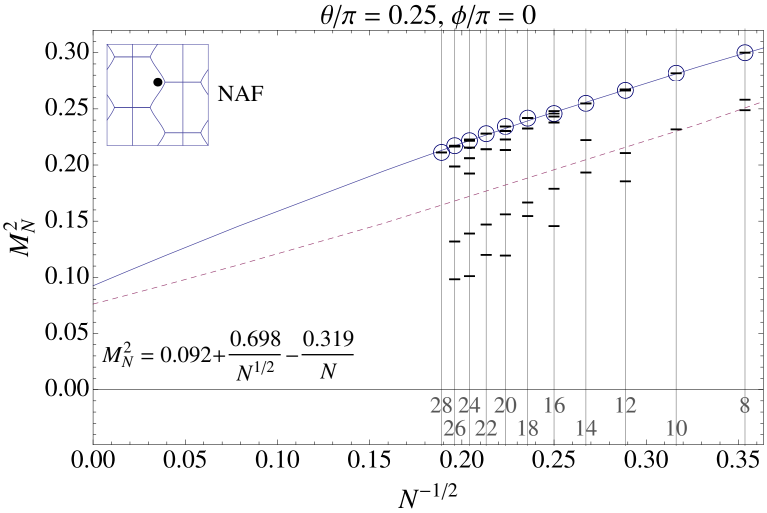

(a) 1st method: structure factor, Eq. 4.3

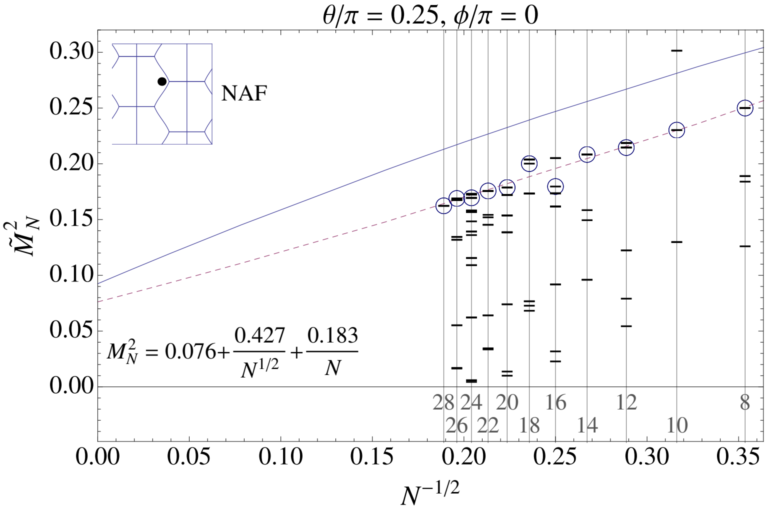

(b) 2nd method: longest distance correlation, Eq. 4.18

Figure 6.12.: Finite-size scaling of the ordered moment for the isotropic nearest-neighbor antiferromagnetic Heisenberg model. The horizontal dashes denote (a) the structure factor and (b) the longest distance correlations of different tiles. The circles correspond to those tiles with maximum squareness, which are used for the scaling analysis and the extrapolation.

thermodynamic limit. This is in excellent agreement with previous studies [87, 89, 101]. The same fit applied to $\tilde{M}_N^2(\boldsymbol{q})$, indicated by the dashed lines in the figures,

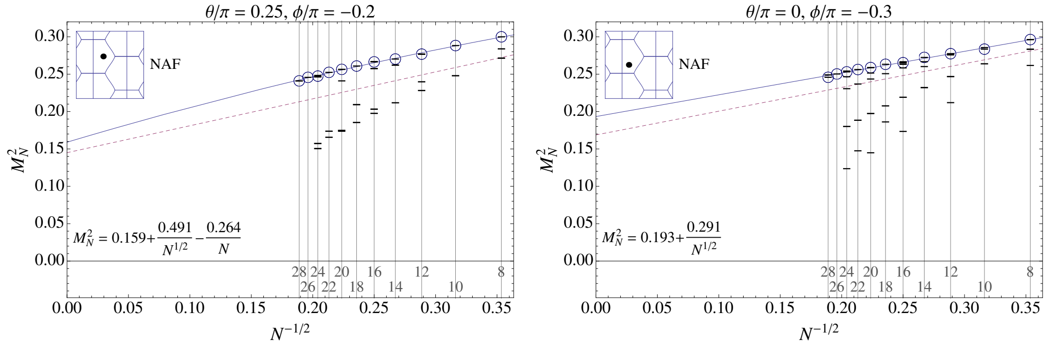

(a) Isotropic ($\theta = \frac{\pi}{4}$)

(b) Maximally anisotropic ($\theta = 0$)

Figure 6.13.: The ordered moment, calculated using the 1st method, corresponding to a point in the NAF phase. Plot symbols and legends are the same as Fig. 6.12.

gives a slightly lower value of $\tilde{M}(\boldsymbol{Q}_{\mathrm{NAF}}) = 0.27(6)$ for the thermodynamic limit. This may be taken as a good indicator for the accuracy within which we can determine asymptotic ($N \to \infty$) values of the ordered moment.

An error analysis of the fit of Eq. (5.22) using all three terms has been applied to both $M_N^2(\boldsymbol{q})$ and $\tilde{M}_N^2(\boldsymbol{q})$ separately, which will be explained in more details in Section 6.3. The relative error is larger for the latter method, which is a consequence of the fact that only a single correlation function is evaluated, whereas in the first method, in the Fourier sum all possible $\langle \mathbf{S}_i \cdot \mathbf{S}_j \rangle$ are used.

Next-nearest neighbors and spatial anisotropy

The scaling of the ordered moment for ferromagnetic next-nearest neighbor exchange $J_2 < 0$ ($\phi = -0.2\pi$), both in the isotropic ($J_{1a} = J_{1b}$) and maximally anisotropic ($J_{1b} = 0$) cases are shown in left and right of Fig. 6.13 respectively. The horizontal dashes denote $M_N^2(\boldsymbol{Q}_{\mathrm{NAF}})$ for individual tiles, and the solid line represents a fit with Eq. 5.22 to the values for the tiles with maximum squareness parameter (circles in the plot). The dashed lines corresponds to the fit of $\tilde{M}_N^2(\boldsymbol{q})$ for the same set of tiles. (individual values are not shown). Again, a comparison of the extrapolated values for $M^2(\boldsymbol{q})$ from the two different scaling procedures can serve as an indicator of the quality of the finite-size scaling analysis.

Fig. 6.14 displays the scaling of the ordered moment in the columnar phase with an antiferromagnetic J_2. Like before, only those tiles which are compatible with

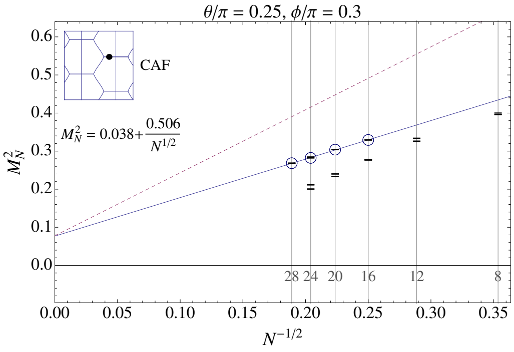

Figure 6.14.: The ordered moment, calculated using the 1st method, of the isotropic model in the CAF phase. Plot elements are the same as Fig. 6.12.

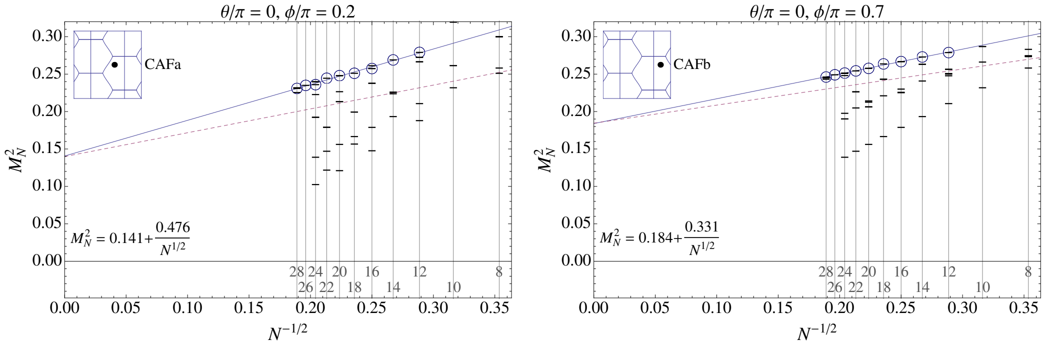

(a)

(b)

Figure 6.15.: The ordered moment, calculated using the 1st method, in (a) CAFa and (b) CAFb phases. Plot elements are the same as Fig. 6.12.

both columnar phases can be used for the calculations. This is equivalent to the compatibility with all four classical phases, and keeps only half of the tiles (with $N = 4\ell$, $\ell \in \mathbb{N}$) suitable for the fitting. Moreover, in the infinite system which has $\mathcal{C}_{4\mathrm{V}}$ point-group symmetry, the wave vectors $(\pi, 0)$ and $(0, \pi)$ are equivalent. However, most finite tiles have a spatial symmetry lower than $\mathcal{C}_4$ (see Table 5.2), meaning that the equivalence between $(\pi, 0)$ and $(0, \pi)$ is lost. For this reason, we take the average of the structure factor at these two wave vectors and use the resulting data points for the scaling. However, this is not needed in the anisotropic case ($\theta \neq \pi/4$ and $\theta \neq -3\pi/4$), as shown in Fig. 6.15, since CAFa and CAFb are now different phases, and a larger number of lattices are available for the scaling. Note that, in Fig. 6.14 we plot the area dependence of the structure factor and the

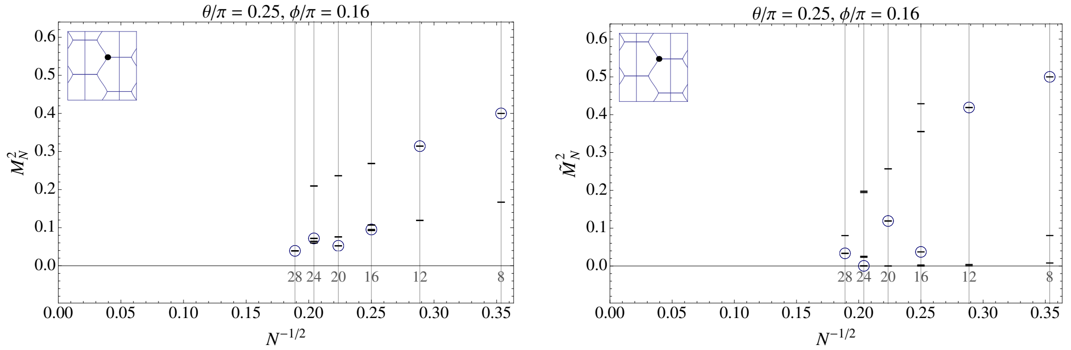

(a) 1^{st} method: structure factor, Eq. 4.3 (b) 2^{nd} method: long-distance correlation, Eq. 4.18

Figure 6.16.: The size dependence of the structure factor in the disordered regime at the CAF-FM border. Plot elements are the same as Fig. 6.12. In this case, a reliable linear scaling result cannot be obtained from the results of the most squared tiles, denoted here by circles.

longest distance correlation function including the factor of $\zeta(\boldsymbol{q}) = 2$ introduced in Eq. 4.9. This factor is due to the breaking of the spatial symmetry, induced by the columnar order.

Magnetically disordered regimes

In the disordered region between the Néel and the columnar phase of the isotropic model ($J_{1a} = J_{1b} = J_1$, $J_2/J_1 \approx 1/2$), the behavior of both the structure factor and the correlation functions do not show a systematic dependence on the tile size, similar to the case of the ground-state energy (which itself equals to a correlation function between nearest neighbors). It is also clear from Fig. 6.16, which illustrates the calculated values for both $M_N^2(\boldsymbol{q})$ (left) and $\tilde{M}_N^2(\boldsymbol{q})$ (right). This erratic behavior of both quantities is due to the fact that the nature of the ground-state in this region is non-magnetic. Thus, determining only the magnetic structure factor and ordered moment cannot lead to a true quantitative analysis in the sense of Eq. 5.22.

There exists a very similar behavior also for $J_2/J_1 \approx -1/2$ (with ferromagnetic J_1) in the cross-over spin-nematic region of the phase diagram. To see more details, Fig. 6.17 displays the longest distance correlation function $\langle \mathbf{S}_1 \cdot \mathbf{S}_{\max} \rangle$, used in Eq. 4.18, in the narrow region between CAF and FM phase and as a function of the frustration angle ϕ or tiles of different size. The solid vertical line represents the classical phase boundary. Apart from the eight-site tile, which is too small because

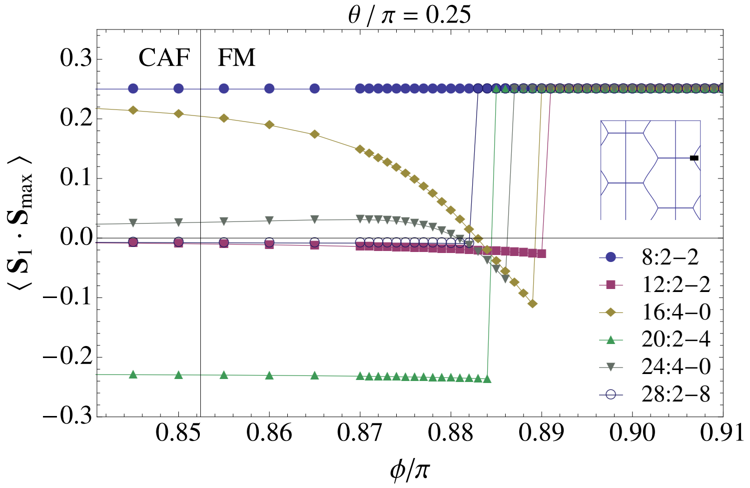

Figure 6.17.: Dependence of the longest distance correlation function on the frustration angle ϕ in the spin-nematic region between the CAF and FM phases of the isotropic model. Only the tiles with maximum squareness which are compatible to all four classical phases are used. The legend in the plot lists the individual tiles and their symbols.

the longest distance sites have only one site between, $\langle \mathbf{S}_1 \cdot \mathbf{S}_{\max} \rangle$ decreases for each tile where a sudden jump to the ferromagnetic value of $\langle \mathbf{S}_1 \cdot \mathbf{S}_{\max} \rangle = S^2 = \frac{1}{4}$. Those correlation functions which are ferromagnetic in the columnar phase even change their sign before the jump (they are positive because longest distance sites are on the same sublattice). This sign change can even serve as a clue to the breakdown of columnar order. However, the transition to the ferromagnetic correlations in the region of $0.881\pi < \phi < 0.891\pi$ seen here does not have a systematic dependence of tile size. Hence, an extrapolation to the thermodynamic limit would not be possible for any finite size. This will be discussed more quantitatively in Section 6.3.

To conclude for the scaling of the ordered moment, we note that as for the previously discussed ground-state energy, one can carry out a very well defined scaling procedure to the thermodynamic limit for the stable Néel and columnar phases. The recipe is the careful selection of the classically compatible tiles with the maximum squareness parameter. However, in the disordered regions at the corner of the NAF, CAFa and CAFb honeycomb (see Fig. 3.2) scaling is impossible. This is an indication of the imminent breakdown of magnetic order due to quantum fluctuations. Similar conclusions have been obtained already from the linear spin-wave theory [47].

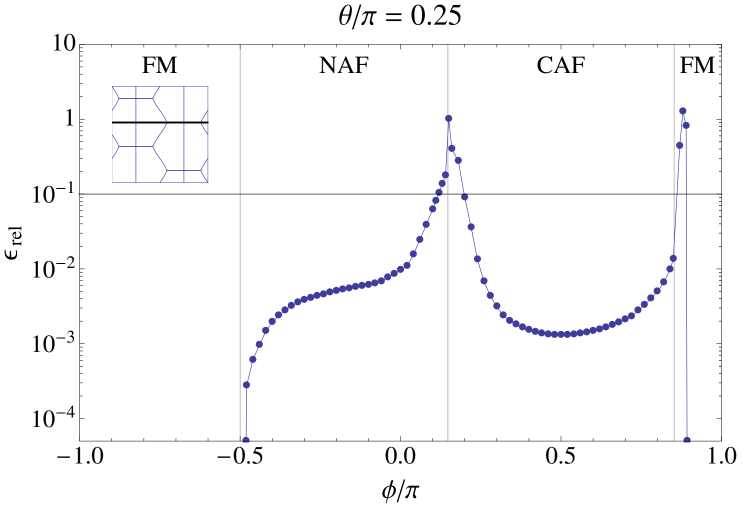

Figure 6.18.: Relative error ϵ_{rel} as defined in Eq. 6.1 of the fits to $M_N^2(\boldsymbol{q})$ for the isotropic model. Note the logarithmic scale of the ordinate. The error in the magnetically disordered regions is at least one order of magnitude larger than in the ordered sectors of the phase diagram. The solid horizontal line denotes the value $\epsilon_{\text{rel}} = 0.1$, indicating the maximum error acceptable for having at least one significant digit in $M^2(\boldsymbol{q})$.

6.3. Quality of the fit

For the linear scaling (dropping the last term in Eqs. 5.21 and 5.22) applied for extrapolating the results to the infinite lattice, studying the quality of the scaling is crucial. There exist several measures which can be used to characterize its quality. An appropriate one here is the relative error in the ∞-norm, defined as

$$\begin{aligned} \epsilon_{\text{rel}} &= \frac{|f-d|_\infty}{|f|_\infty} \sim 10^{-p}, \qquad (6.1)\\ |\{x_1, x_2, \dots\}|_\infty &= \max\left(|x_1|, |x_2|, \dots\right). \end{aligned}$$

Here, f is the set of values to be fitted at the points $1/N$, and d the set of data calculated for the maximum-squareness tiles with area N. The exponent p in the above equation can be interpreted as the number of significant digits [73] for the extrapolated value f_0 in the limit $N \to \infty$. Therefore, a value of $\epsilon_{\text{rel}} \geqslant 0.1$ means that there are no significant digits in the extrapolated value, and 0.1 is the maximum error tolerated.

Figure 6.18 displays this error for scaling of the ordered moment for the isotropic model as a function of the frustration angle ϕ. The behavior of the fitting error of

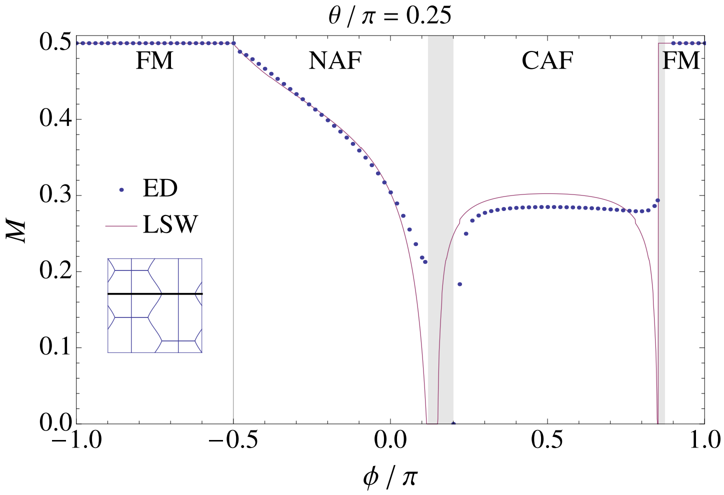

Figure 6.19.: The ordered moment as function of the frustration angle ϕ, for the isotropic model with fixed $\theta = \pi/4$. The solid line corresponds to the linear spin-wave results, and dots are the extrapolation using the structure factor of the tiles with the maximum squareness parameter. The gray-shaded areas in the top plot represent the range of frustration angles ϕ where the relative error of $M^2(\boldsymbol{q})$ is above 0.1, i.e. no significant digits present for the extrapolated value (cf. Fig. 6.24).

the ground-state energy values is also reminiscent of this plot. In the ferromagnetic phase, the fully polarized state is the ground-state, and the error reflects the numerical round-off errors, i.e., the accuracy of the floating point operations with an order of 10^{-15}. These values have been excluded from the figure (We have determined $M_N^2(\boldsymbol{q})$ in the ferromagnetic region in order to verify the correctness of the numerical implementation). In the well-ordered region of NAF and CAF we have $\epsilon_{\mathrm{rel}} = \mathcal{O}(10^{-3}) \ldots \mathcal{O}(10^{-2})$, and we can regard the scaling procedure in these intervals as stable. In contrast, in the magnetically disordered regions at the borders of the columnar phases, the strong increase in ϵ_{rel} clearly indicates that the scatter of the points is much too high for making the extrapolated value reliable. The solid horizontal line in Fig. 6.18 denotes $\epsilon_{\mathrm{rel}} = 0.1$, below that the extrapolated values for $M^2(\boldsymbol{q})$ have at least one significant digit. In other words, a magnetic order parameter $M^2(\boldsymbol{q})$ to be used to characterize the nature of the ground state can be obtained exclusively in those regions having $\epsilon_{\mathrm{rel}} < 0.1$.

6.3.1. Extrapolation to the thermodynamic limit: ordered moment

In Fig. 6.19 the extrapolated values for the ordered moment $M^2(\boldsymbol{q})$ are plotted (dots) as a function of the frustration angle ϕ for the isotropic case. Inside the ordered regimes of the phase diagram, the results are in excellent agreement with the linear spin-wave theory (solid line). There are differences near the borders of the columnar phase, shown by the gray-shaded areas, which denotes the range of frustration angles ϕ with the error $\epsilon_{\text{rel}} > 0.1$ (see Eq. 6.1). This area is slightly shifted from the interval where the moment $M^2(\mathbf{Q})$ calculated in spin-wave approximation vanishes. At these magnetically disordered regions, the numerical results tend to become unreliable, and no significant digit can be attained with the extrapolation of the finite-size scaling data. In particular, in the spin-nematic region of the isotropic model, a qualitative difference exists between linear spin-wave theory and exact diagonalization. For the former, increasing ϕ leads to tiny region around the classical CAF/FM phase boundary where the ordered moment vanishes before jumping to saturation in the FM phase. But, the extrapolated values for $M(\boldsymbol{q})$ remain non-zero at any frustration angle ϕ. This behavior is displayed in greater details in Fig. 6.20, where a zoom of Fig. 6.19 is shown for the CAF/FM border. We see that the extrapolated moments have a nearly constant ϕ dependence $M(\boldsymbol{Q}_{\text{CAFa}}) \approx M^{\phi=0}(\boldsymbol{Q}_{\text{NAF}})$ in the columnar phase for $\phi/\pi \leqslant 0.855$, as it does in the FM phase with $M(\boldsymbol{Q}_{\text{FM}}) = S$ for $\phi/\pi \geqslant 0.874$. However, for $0.855 < \phi/\pi < 0.874$, $M_N(\boldsymbol{q})$ suddenly shows erratic behavior for different tile sizes (as Fig. 6.17 confirms for the longest distance correlation function too), correspondingly we have $\epsilon_{\text{rel}} > 0.1$ with no significant digits for $M^2(\boldsymbol{q})$ in that range of the frustration angle.

We can extrapolate $M_N(\boldsymbol{q})$ again to a stable full polarization again at the point $\phi = 0.874\pi$. This can be considered as an upper bound of the border between the spin nematic and FM phase. According to Fig. 6.17, the minimum value for ϕ where we get a stable $M(\boldsymbol{q}) = S$ decreases as a function of tile size, disregarding the smallest eight-site tile. However, the true order parameter for the spin nematic phase is not of magnetic type, and therefore the behavior of $M(\boldsymbol{q})$ cannot be used to understand the properties of this phase, in particular the parameter range within which it exists. Instead, one would have to calculate the spin nematic order parameter [44] in a similar way.

Similarly, the extrapolation results for an intermediate anisotropy $\theta = \pi/8$ and the maximally anisotropic case $\theta = 0$ are shown in Fig. 6.21 and Fig. 6.22, respectively. Again, a good agreement exists between the linear spin-wave analysis and

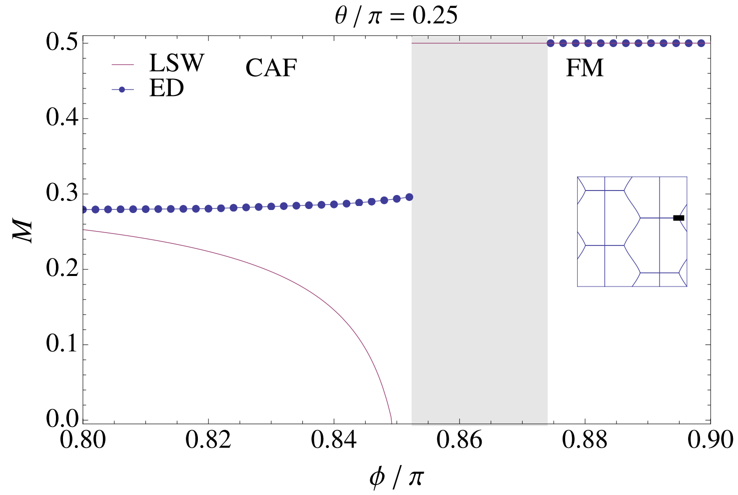

Figure 6.20.: The ordered moment $M(\boldsymbol{q})$ as a function of the frustration angle ϕ, for the isotropic $\theta = \pi/4$ case around the nematic region between columnar and FM phases. The solid line indicates the result from linear spin-wave theory, and the dots display the scaled exact diagonalization values. The gray area shows the region where the relative error of the extrapolated value for $M^2(\boldsymbol{q})$ is above 0.1 (cf. Fig. 6.24).

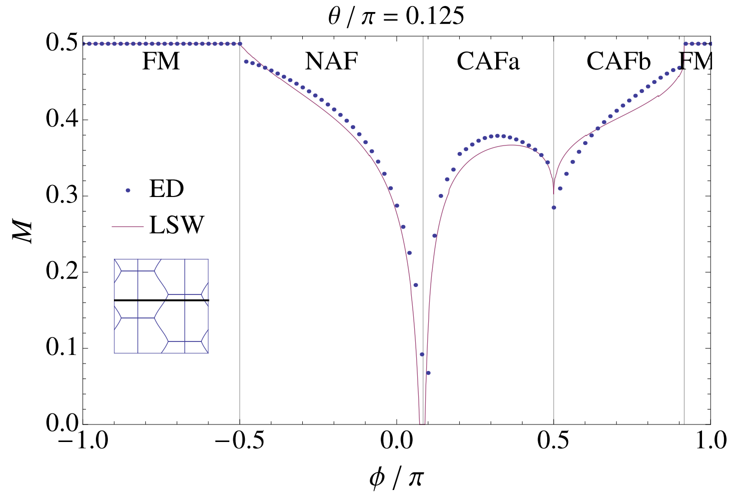

Figure 6.21.: The ordered moment as a function of the frustration angle ϕ, for the model with intermediate anisotropy with $\theta = \pi/8$. Plot elements are as in Fig. 6.19.

the finite-size scaling results. In plots, $\phi = \pi/2$ corresponds to the decoupled two sublattices with $J_{1a} = J_{1b} = 0$, $J_2 = J_c$ in which we have the universal value of 0.3034 for the Néel case. Due to the scaling of only small tiles (half of the original

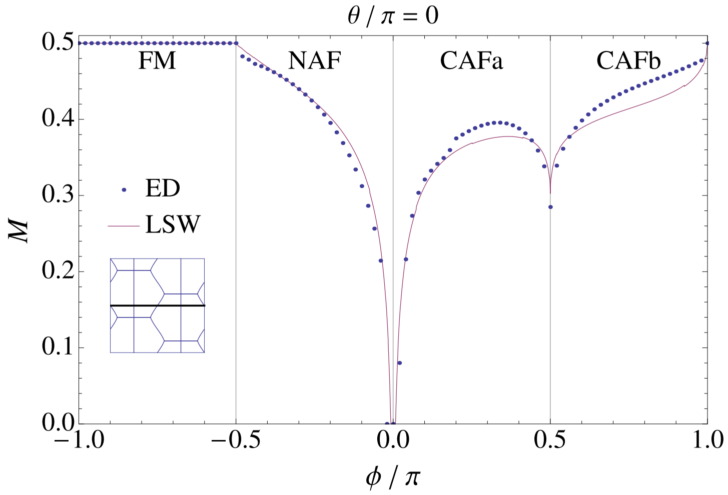

Figure 6.22.: The ordered moment as function of the frustration angle ϕ, for the maximally anisotropic model with $\theta = 0$. Plot elements are as in Fig. 6.19.

lattice) the value of the extrapolation is slightly less than expected. Compared to the isotropic case, there are two quantitative differences. First, the region where the ordered moment vanishes is smaller. Second and most important, inside the columnar antiferromagnetic phases, the ordered moment is restored to even larger values than for isotropic exchange, i.e. anisotropy stabilizes the ordered moment, in particular for the CAFb phase. Also, the symmetry around the point $\phi = \pi/2$ is lost, and M is restored in the CAFb phase towards the saturation value upon entering the FM phase. There is no region around the CAFb/FM border where M is suppressed as in the isotropic case.

A zero ordered moment implies that, at least within our approximations, the order parameter for the corresponding classical phase is destroyed by quantum fluctuations. Historically, this was one of the first indications of the appearance of an intermediate phase without magnetic order. Our findings suggest that the well-known disordered phase for the isotropic $J_1 - J_2$ model for the antiferromagnetic exchange couplings extends to the whole range of anisotropic interactions with arbitrary ratios of θ (J_{1b}/J_{1a}).

This is *not* the case for the CAFa/b-FM crossover, where numerically already at a deviation $\Delta\theta/\theta < 0.01$ from the isotropic value $\theta = \pi/4$, the ordered moment remains finite and well-defined around the classical CAFa/b-FM transition point. Fig. 6.23 illustrates this behavior and shows the ordered moment as a function of

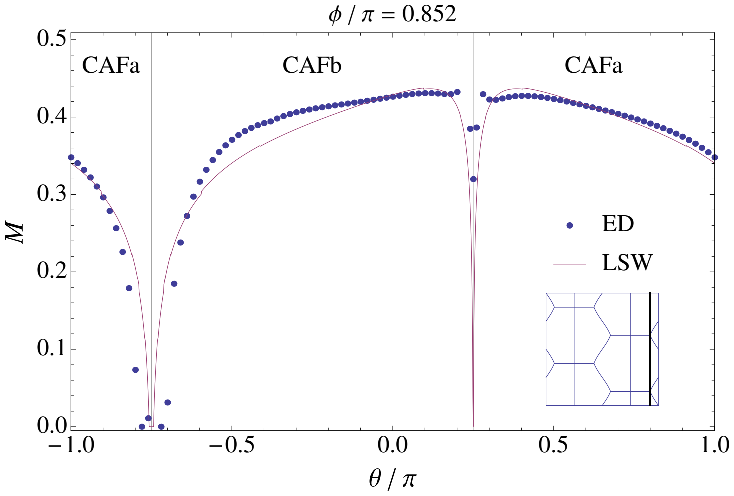

Figure 6.23.: Ordered moment for $\phi/\pi = 0.852$ as a function of the anisotropy parameter θ. The frustration angle is chosen such that in the isotropic case $\theta = \phi/4$, the system is in the disordered regime at the CAFa/b-FM corner.

the anisotropy parameter for the fixed frustration angle $\phi/\pi = 0.8520$. This is the same value as in the intermediate region for the isotropic case and the two sharp drops at $\theta = -3\pi/4$ and $\pi/4$ correspond to the disordered regimes at the CAFa/b-NAF corner and the CAFa/b-FM corner in the phase diagram, respectively. At the CAFa/b-FM corner around $\theta = \pi/4$, we have zero ordered moment only for a tiny range $0.2493 < \theta/\pi < 0.2507$.

Finally, the ordered moment dependence on the anisotropy angle θ, for the unfrustrated case with only nearest neighbor interaction ($\phi = 0$, $J_2 = 0$) is presented in Fig. 6.24. At the values $\theta = \pi/4$ and $-\pi \leqslant \theta \leq -3/4\pi$, the isotropic model is recovered with the well-known values $M(\boldsymbol{Q}_{\mathrm{NAF}}) \approx 0.30$ and $M(\boldsymbol{Q}_{\mathrm{FM}}) = S = \frac{1}{2}$, respectively. We emphasize again that the points $\theta = 0$ and $\theta = \pi/2$ at the borders of the Néel phase correspond to arrays of independent chains. Therefore, the moment suppression at these points is not a frustration effect (which is in fact absent for $\phi = 0$), but a result of the effective one-dimensional character of the model, where no magnetic moment exists at any wave vector.

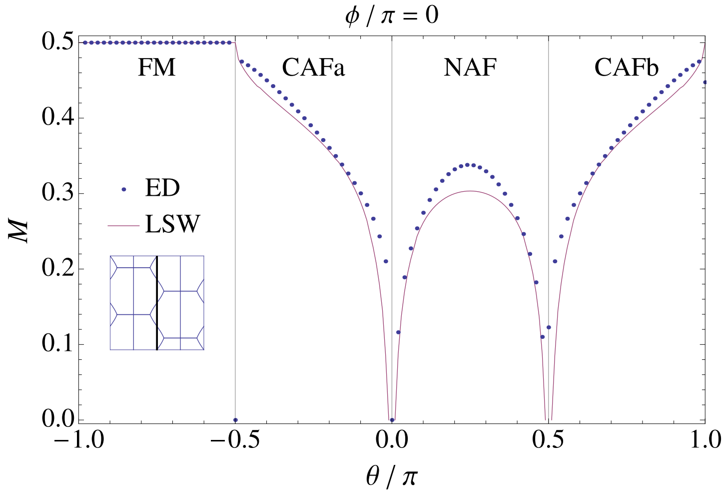

Figure 6.24.: The ordered moment as function of the anisotropy parameter θ, for the unfrustrated model with $\phi = 0$ ($J_2 = 0$).

VII. Results for Finite-Temperature Properties

As introduced in Chapter IV, the finite-temperature Lanczos method (FTLM) provides a powerful tool to study the thermodynamic averages of arbitrary operators built from spin operators. Here, we focus on the temperature dependence of the magnetic susceptibility (Section. 4.4.2), in particular we look at the behavior of its peak value and position as function of different system parameters and tile sizes. We describe aspects of the susceptibility behavior for parent compounds of the Fe-pnictides superconductors and layered V^{2+} ($S = \frac{1}{2}$) compounds, as well as fitting to the experimental data available for a quasi-two-dimensional Cu-pyrazine compound. The latter analysis can be used for the determination of the exchange interaction constants and therefore degree of frustration, which is of central importance to characterize frustrated two-dimensional quantum magnets.

7.1. Magnetic Susceptibility

7.1.1. Application to quasi-2D $\mathrm{Cu(pz)_2(ClO_4)_2}$

To demonstrate the strength of finite-temperature Lanczos method, we apply it to the quasi-two-dimensional antiferromagnet $\mathrm{Cu(pz)_2(ClO_4)_2}$. In previous works [61,62] the spin-wave excitations, field dependent moment and ordering temperature $T_N(H)$ of this compound were determined. Based on these results and on earlier thermodynamic studies [63, 64] it was proposed that Cu-pyrazine is close to a pure Néel antiferromagnet with a frustration ratio of $J_2/J_1 = 0.02$ or $\phi/\pi \approx 0.006$. However, the field dependence of staggered moment was not analyzed in this respect. We will present a detailed analysis of magnetic field dependence of the staggered moment in Section 8.2. The results of this analysis for the frustration ratio $\frac{J_2}{J_1}$ will be compared to the following analysis of $\chi(T)$ using the finite-temperature Lanczos method.

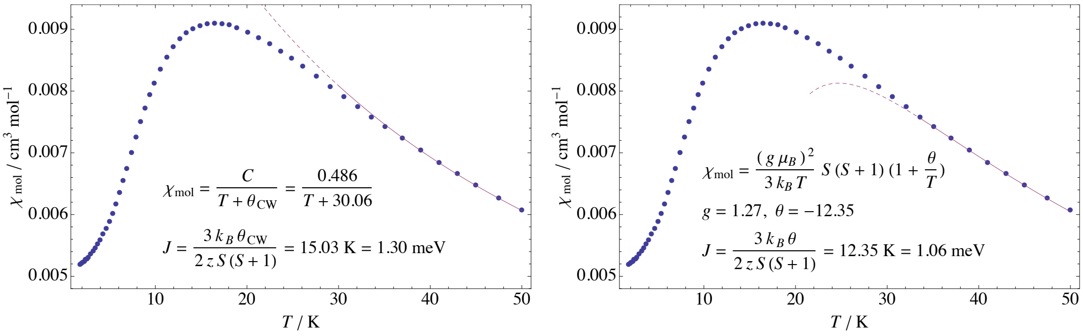

(a) Curie – Weiss law

(b) High-temperature expansion

Figure 7.1.: Curie – Weiss and high-temperature fit of the tail of the magnetic susceptibility of the measured powder sample in Ref. [64]. The solid line is the actual fit and the dashed line is its continuation to lower temperatures where deviations start. The best fit parameters are given in the inset.

First we discuss two common approximations for $\chi(T)$. In the mean-field approximation, the leading term in the magnetic susceptibility $\chi(T)$ is given by the Curie–Weiss law,

$$\chi(T) = \frac{C}{T + \theta_{\mathrm{CW}}}, \tag{7.1}$$

Alternatively, a high-temperature expansion starting from fully uncorrelated spins at $T \gg T_N$ leads to the form [93],

$$\begin{aligned} \chi_{\mathrm{mol}}(T) &= \frac{(g\mu_B)^2}{3k_B T} S(S+1)\left[1 + \frac{\theta}{T} + \mathcal{O}\left(\frac{\theta}{T}\right)^2\right], \\ \theta &= \frac{S(S+1)}{3}\frac{J}{k_B}, \qquad J = \sum_j J_{1j}. \end{aligned} \tag{7.2}$$

Fig. 7.1 shows the best fit of both formulas to the high-temperature tail of the susceptibility of the measured data in Ref. [64]. However, using Eqs. 7.2 and 7.1 to fit the measured data does not yield a unique solution for J_1 and J_2, since it is only dependent on the sum of exchange interactions. Similar studies [63, 64] based on series expansion for fitting $\mathrm{Cu(pz)_2(ClO_4)_2}$ artificially set $J_2 = 0$ ($\phi = 0$) from the outset. J_2 is later determined from details of the spin-wave dispersion [61, 62]. In the current context, we perform an unbiased analysis with a possible non-zero J_2 by fitting the finite-temperature Lanczos method data with variable ϕ and J_c to the experimental data. The result for the best fit from various cluster sizes is

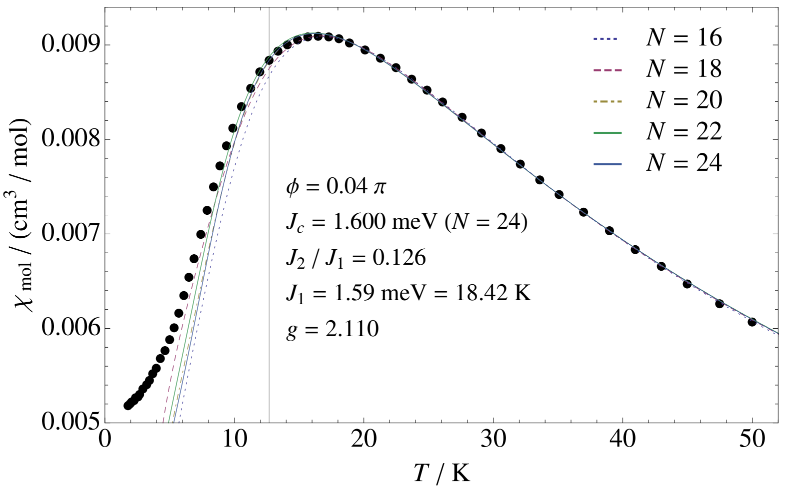

Figure 7.2.: Uniform magnetic susceptibility from the finite-temperature Lanczos method for various tile sizes N. Fitting to experimental values (dots) for Cu(pz)$_2$(ClO$_4$)$_2$ starts above the vertical line (below the maximum). Optimal fit parameters J_1 and J_2 are indicated in the inset. The g value is obtained from $g\mu_B H_s = 4J_1$.

shown in Fig. 7.2. The dots correspond to the powder susceptibility measured in Refs. [64, 105, 106]. The finite-temperature Lanczos results are calculated with a magnetic field of 1 kOe to be compatible with Ref. [64]. In order to reduce the influence of finite-size effects only data points slightly below the maximum in $\chi(T)$ up to the highest temperature are included for the fit. Best fitting leads to a $J_2/J_1 = 0.12$ or $\phi/\pi = 0.04$. From the value of J_1 and the measured saturation field $H_s = 52\,\mathrm{T}$, we get a gyromagnetic ratio $g = \frac{4J_1}{\mu_B H_s} = 2.11$, which is in good agreement with the observed result from Electron Spin Resonance (ESR) technique [64] (see Section 8.1). For $\phi/\pi > 0.04$, the agreement around the maximum of $\chi(T)$ becomes worse. This result indicates already that Cu(pz)$_2$(ClO$_4$)$_2$ has a finite but moderate frustration.

7.1.2. Localized model for parent compounds of Fe-pnictides

As described in Section 2.2, Inelastic Neutron Scattering (INS) results have shown that low energy spin excitations of the parent compounds of the 122 family of Fe-pnictides can be well described by a $J_{1a,b} - J_2$ local moment model with exchange interactions according to Table 2.2. Since they are all located in the CAFa region of the phase diagram, one expects that the low (zero) frequency susceptibility

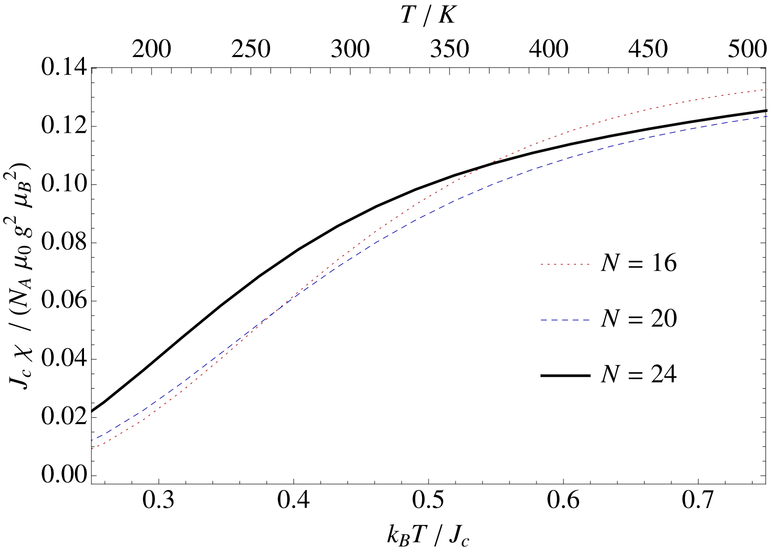

Figure 7.3.: Temperature dependence of the uniform magnetic susceptibility for $\phi/\pi = 0.35$, and $\theta/\pi = 0.25$ as for $BaFe_2As_2$ with $J_c = 58.5$ meV [58], corresponding to a temperature variation between 170 and 510 K.

follows the outcome of the same model, at least qualitatively. To verify this conjecture we performed finite-temperature Lanczos calculations as e.g. described in Ref. [47, 107] for various finite clusters. The result is shown in Fig. 7.3 for a parameter set corresponding to $BaFe_2As_2$ as from Ref. [58]. For temperatures $T \lesssim 0.25 J_c$ the calculation becomes unreliable due to finite size effects. The temperature range corresponds to 170 K at the lower and 510 K at the upper boundary. The linear increase in T observed for $BaFe_2As_2$ from 150 K to 300 K is qualitatively reproduced, although the absolute increase is too large. This increase with temperature cannot be easily explained within the itinerant model for Fe 3d electrons, which would predict a constant Pauli susceptibility. One has to involve higher order many body corrections [108] to obtain the qualitatively correct increase. We also mention that in the combined itinerant-localized model of Ref. [109] the linear temperature dependence was also attributed to the local moment contribution. At the very least our calculation shows clearly that in the present range of measurement one should *not* yet expect the high temperature Curie law $\chi(T) \sim 1/T$ in the local moment picture of Fe-pnictides. This should be expected only quite above the maximum temperature for $\chi(T)$, which is at about $1.1\,J_c$ or 750 K in the case of Fig. 7.3.

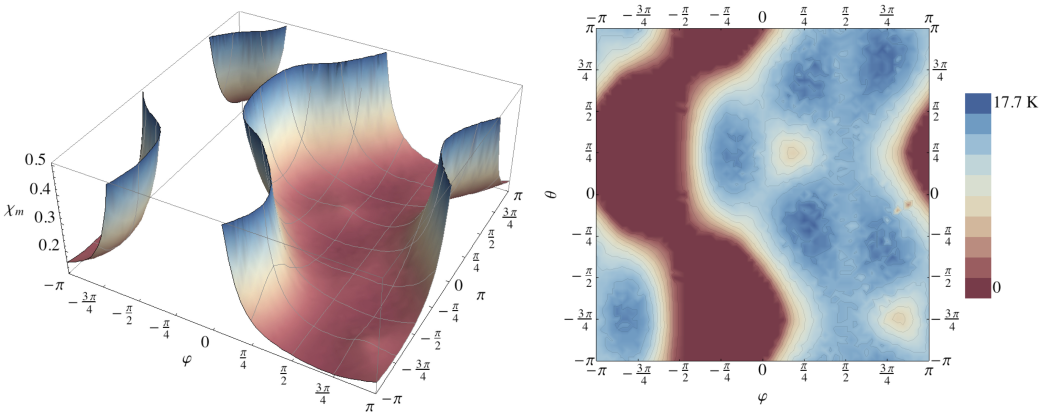

Figure 7.4.: Left: maximum value χ_M of the magnetic susceptibility $\chi(T)$. Right: contour plot of the temperature T_M at which the maximum susceptibility occurs.

7.2. Frustration and anisotropy dependence of the susceptibility peak

The position and height of the susceptibility peak are experimentally directly accessible quantities and in particular allow conclusion on the frustration ratio. The frustrated $S = \frac{1}{2}$ Heisenberg model on the square lattice, the $J_1 - J_2$ model, appears to describe well the thermodynamic and magnetic properties of two classes of vanadium compounds of type $\mathrm{Li_2VO}X\mathrm{O_4}$ (X = Si, Ge) [57] and $AA'\mathrm{VO(PO_4)_2}$ (A, A' = Pb, Zn, Sr, Ba) [52, 54] (Section 2.2). However, their crystal structure corresponds to a lattice with lower symmetry [110]. We therefore consider the impact of an additional anisotropy of the nearest-neighbor interactions in the *ab* plane, as characterized by the anisotropy parameter θ. We have calculated the thermal behavior of the magnetic susceptibility and its dependence on the frustration and anisotropy parameters for the whole phase diagram for a cluster of 20 sites with the finite-temperature Lanczos method. Fig. 7.4 presents the result of this calculation for the position T_M (right panel) and the maximum χ_M (left panel) of the peak of the susceptibility. The peak shows little change for different size and tile geometries, but we present it as a global picture of the susceptibility behavior. In the ferromagnetic region of the phase diagram the susceptibility is divergent. Deep inside the antiferromagnetic (Néel and collinear) regions, the parameter dependence is weak. In the right panel of Fig. 7.4, apart from the “dip” which occurs in the nonmagnetic columnar-dimer phase for $(\theta, \phi) \simeq (0.15\pi, 0.25\pi)$, also the maximum

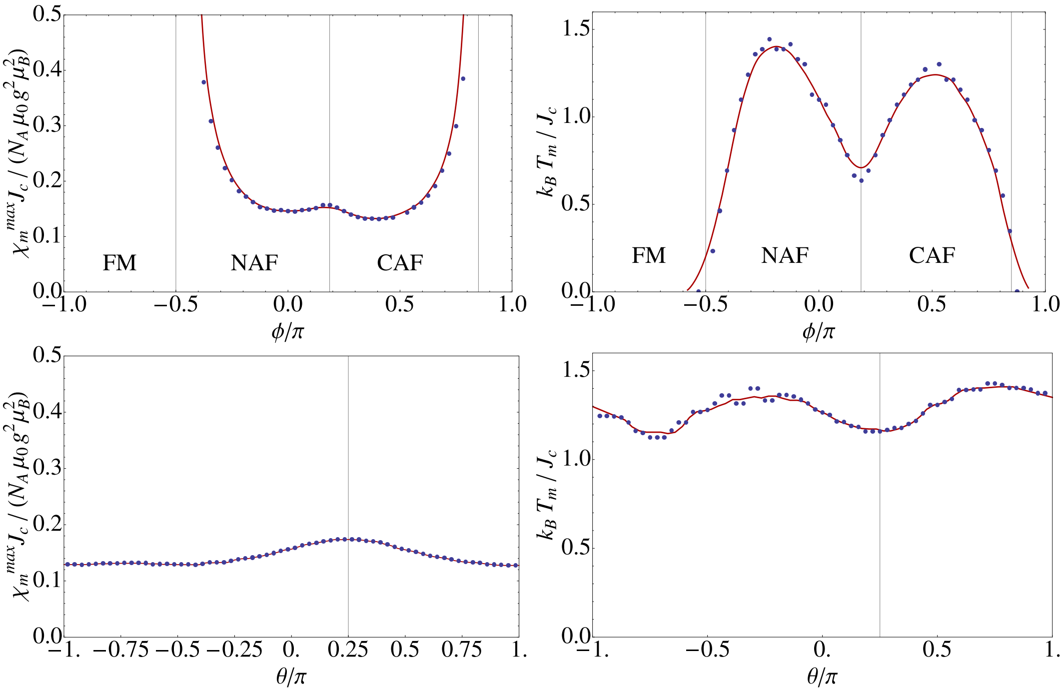

Figure 7.5.: Finite-temperature Lanczos method results for the magnetic susceptibility $\chi(T)$. Figures on the left show the value and those on the right show the temperature where $\chi(T)$ reaches its maximum. Top: dependency on the frustration angle ϕ for the isotropic model $\theta = \pi/4$. The vertical lines distinguish three different classical phases, FM, NAF and CAF. In particular the maximum position is suppressed in the strongly frustrated region $\phi \simeq 0.15\pi$. Bottom: dependency on the anisotropy parameter θ at fixed frustration angle $\phi = 0.625\,\pi$. The vertical line shows the isotropic case, $\theta = \pi/4$.

position depends only weakly on the anisotropy.

In Fig. 7.5, the finite-temperature Lanczos method results for a tile of size 20 are shown in greater details. These plots can be seen as horizontal (upper panels) and vertical (lower panels) cuts through Fig. 7.4. The position (right) and the value (left) of the broad maximum of the magnetic susceptibility $\chi(T)$ are plotted as a function of the frustration (ϕ) and the anisotropy (θ) parameters. The top curves correspond to the isotropic case ($J_{1a} = J_{1b}$, $\theta = \frac{\pi}{4}$), while the bottom curves show the effect of the anisotropy parameter θ for constant $\phi = 0.625\,\pi$ (in CAF regime, corresponding to the values of frustration angles for vanadates). Compared to the upper panels, the changes both in value and temperature in the lower plot are quite small. Therefore, introducing an anisotropy within the columnar phase has comparatively little effect on the temperature dependence of $\chi(T)$. This is also confirmed by the behavior of the ground-state energy (shown in Fig. 6.1) which shows the same relative weak dependence on system parameters inside the antiferromagnetically ordered phases. This explains the validity of the square-lattice Heisenberg model in describing the experimental results on the thermodynamics of the compounds which might have a symmetry lower than the tetragonal one.

VIII. Results for Field Dependence of Magnetic Moments

The goal of this chapter is to provide insight about the behavior of the quantum Heisenberg J_1-J_2 model in the presence of an external magnetic field. By adding a Zeeman term to our model Hamiltonian, we study the dependence of the uniform and ordered magnetic moments, including the effect of quantum fluctuations on the moment. Similar to the previous chapters, the results from the linear spin-wave analysis and the exact diagonalization are presented, and a finite-size scaling analysis of the latter will be compared to the former approximation. In addition, a best fit analysis for the measured Neutron diffraction data of the Cu-pyrazine compound is presented, in order to introduce a novel method for determining the degree of the frustration in quasi-two-dimensional systems. We also present results for the uniform magnetic moment up to the saturation field and compare it to the experiments in two-dimensional vanadates.

8.1. Magnetic moment

The model Hamiltonian including the magnetic field term reads as,

$$\mathcal{H} = J_1 \sum_{\langle ij \rangle_1} \boldsymbol{S}_i \cdot \boldsymbol{S}_j + J_2 \sum_{\langle ij \rangle_2} \boldsymbol{S}_i \cdot \boldsymbol{S}_j - g\mu_B \boldsymbol{H} \sum_i \boldsymbol{S}_i. \tag{8.1}$$

Here $J_1 = J_c \cos\phi$ and $J_2 = J_c \sin\phi$ are the nearest and next-nearest neighbors exchange constants with $J_c = (J_1^2 + J_2^2)^{\frac{1}{2}}$ giving the overall energy scale. The additional Zeeman term defines the z-axis as the direction of the magnetic field, i.e. $g\mu_B \boldsymbol{H} =: H\hat{z}$. The field dependent total moment is then given by

$$m_{\text{tot}}^2(H) = m_0^2(H) + m_{\mathbf{Q}}^2(H), \tag{8.2}$$

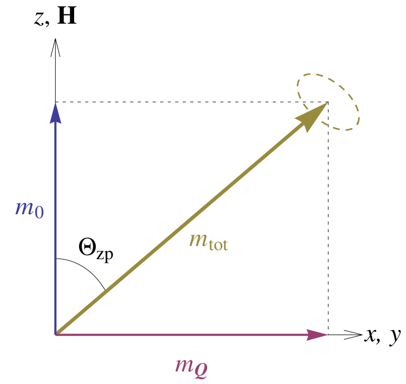

Figure 8.1.: The field dependent total moment (m_{tot}) consisting of uniform (m_0) and staggered moment ($m_{\mathbf{Q}}$) perpendicular and parallel to the xy plane, respectively. Ellipse indicates spin-wave excitations.

consisting of uniform ($m_0 = m_{\mathrm{tot}} \sin \Theta_{\mathrm{zp}}$, see Eq. 3.44) and staggered moment ($m_{\mathbf{Q}} = m_{\mathrm{tot}} \cos \Theta_{\mathrm{zp}}$, see Eq. 3.45) perpendicular and parallel to the xy-plane, respectively. This is explained in Fig. 8.1, where in the classical picture, the magnetic moments align themselves with the magnetic field direction. At finite values of H, the spins are canted out of the xy plane. The respective canting angle Θ_{zp} (not to be confused with the anisotropy parameter θ) is measured relative to the field direction (global z axis); $\Theta_{\mathrm{zp}} = 0$ corresponds to the fully polarized state, and $\Theta_{\mathrm{zp}} = \frac{\pi}{2}$ to the state with vanishing magnetic field. The former happens at fields above the saturation field H_{sat}, where all the moments align themselves parallel with each other. In the classical picture ($\Theta_{\mathrm{zp}} \to \Theta_c$) the moments of length S simply rotate in the field leading to a linear $m_0^{\mathrm{cl}} = S(H/H_{\mathrm{sat}})$ (see Eqs. 3.6 and 3.10). Including quantum (zero point) fluctuations by considering the spin-wave approximation results in a smaller uniform moment m_0 (see Section 3.5) and a nonlinear magnetization curve $m_0(H)$.

8.1.1. Uniform magnetization

The total magnetization of the system is the ground-state expectation value of the z component of the spin $\boldsymbol{S}$ in the global coordinate system,

$$m_0 = \frac{1}{N} \sum_i \langle S_i^z \rangle \,. \tag{8.3}$$

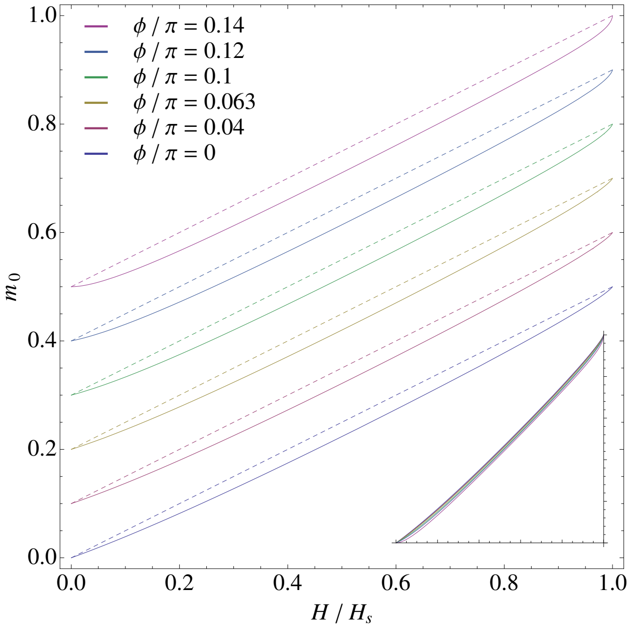

Figure 8.2.: The linear spin-wave results for the field dependent uniform moment per site as a function of the applied magnetic field H/H_{sat}, with different frustration parameters ϕ in the NAF phase. Between each pair of adjacent curves an offset $\Delta m = 0.1$ is inserted. The solid lines denote the field dependence in the isotropic case, and the dashed lines present the classical value. The inset shows all the curves without offset.

The Hamiltonian 8.1 may be diagonalized in the local coordinate system of the canted spins, leading to the spin-wave energies $E(H, \mathbf{k})$ (Section 3.4) . The uniform moment is then given by the ground-state expectation value of the total moment projected onto the field direction (Section 3.5). Fig. 8.2 displays a set of curves of $m_0(H)$ for different frustration angles, obtained by the linear spin-wave approximation in the NAF phase. The magnetic field is normalized to the respective saturation field. The solid curves show the field dependence of the induced moment m_0 in the isotropic case $\theta = \pi/4$, $J_{1a} = J_{1b}$, and the dashed curves show the same quantity in the classical approximation with $\cos\Theta_c = H/H_{\text{sat}}$. By increasing the frustration parameter, the bending of the curves is increasing only by a small amount (see inset for comparison). Thus the dependence of the uniform moment on the frustration parameter ϕ in the NAF phase with both antiferromagnetic J_1 and J_2 is weak. However, close to the strongly frustrated region ($\phi \simeq 0.15\pi$, $J_2/J_1 = 0.5$) the total moment vanishes and spin-wave approximation breaks down. In this case the magnetization curve develops a plateau at $m_0 = \frac{1}{2}S$ in a very narrow interval of ϕ [40, 111, 112].

Later in Section 8.2 we primarily use the more pronounced staggered moment field dependence to identify the degree of frustration, e. g. in the Cu-pyrazine compound, which is known to be in the NAF phase from previous studies [62].

Alternatively, the uniform magnetization can be calculated directly from the exact diagonalization of finite clusters. Since the Zeeman term commutes with the rest of the Hamiltonian, usually there is no need to perform further diagonalizations to calculate the change in the ground-state or thermodynamic properties. For example, for calculating the ground-state energy dependence on the magnetic field, it is sufficient to look at all different spin sectors (i. e. Hamiltonian matrix blocks) distinguished by different S_z^{tot} and calculate the lowest energy in each of them. The energy of different spin sectors in the magnetic field changes as $E(H; S^z_{\mathrm{tot}}) = E(H = 0; S^z_{\mathrm{tot}}) + g\mu_B H S^z_{\mathrm{tot}}$. Therefore, one just has to find at which spin sector (S^z_{tot}), $E(H)$ leads to the lowest value (among all possible S^z_{tot}) for a given field H. Since we have only a finite number of possible configuration of spins, $S^z_{\mathrm{tot}} = 0, 1 \ldots SN$, each sector will be the ground-state for an interval of values of the magnetic field H, determined by the adjacent level crossings. This level crossings lead to a steplike field dependence for all ground-state properties, such as the magnetization. The exact diagonalization results of the uniform magnetization per site for some finite clusters is shown in Fig. 8.3. The value of the moment is shown with the dashed line, and the horizontal gridlines specify different spin sectors. Each vertical gridline is the field value at which the ground-state changes to a different spin sector. Clearly, with increasing the tile size, these steps become smaller and a more continuous magnetization curve emerges. But, with the help of a procedure known as Bonner – Fisher construction [113], one can obtain an improved picture of the behavior of the magnetization. The idea is that instead of having constant values at each level, one can consider the position of the midpoints at each step. These midpoints, obtained firstly from the magnetization values, and secondly from those fields where a level crossing happens (both from horizontal and vertical segments), lead to a smoother magnetization curve. Hence, they can be used in addition to the actual levels to present the magnetization. This is depicted in Fig. 8.3, where the solid line and the black dots are the exact diagonalization results of finite clusters, and the corresponding Bonner – Fisher construction, respectively. However, one should keep in mind that there is actually no “new” information generated via this method, and the midpoints are only representatives within their corresponding spin

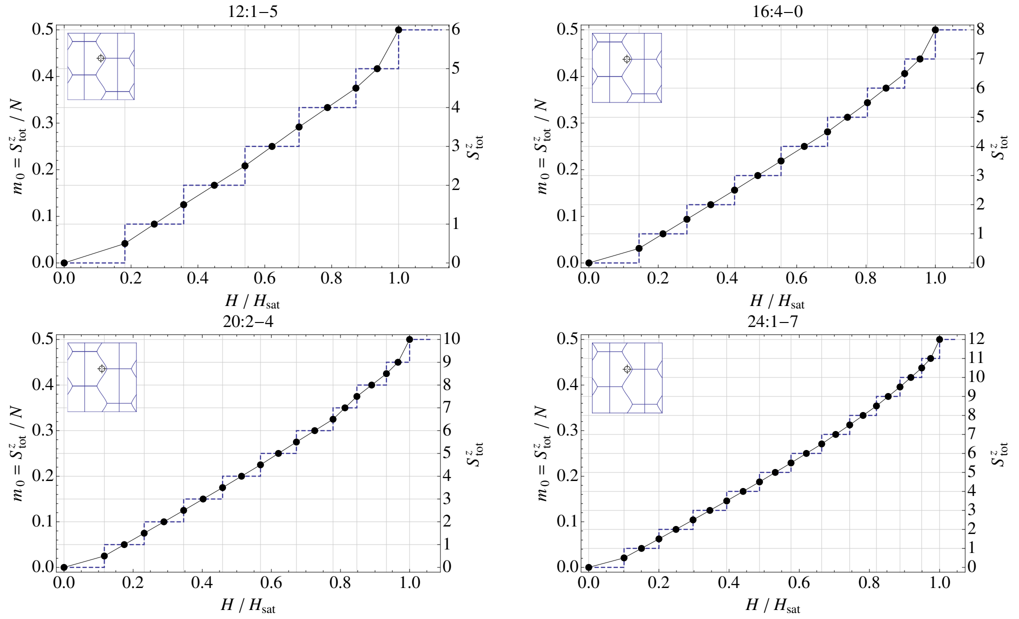

Figure 8.3.: Bonner-Fisher construction of the uniform magnetization as a function of the magnetic field for the Néel antiferromagnet for tile sizes $N = 12, 16, 20$ and 24.

sectors. In particular, those points coming from the averaging over two neighboring spin sectors (dots on the vertical gridlines in Fig. 8.3) correspond to no real physical value and are just an estimated mean value. Another aspect worth mentioning is that the level crossings happen with $\Delta S = 1$ in the NAF phase and $\Delta S = 2$ in some regions of the CAF phase. Details are discussed in Ref. [69].

Fig. 8.4 compares the results from the two theoretical methods and the experimental data on the Cu-pyrazine high-field magnetization data from Ref. [64]. The top panel shows the overlay of all Bonner – Fisher constructions from different cluster sizes (different symbols), and the result from the linear spin-wave analysis (the same as Fig. 8.2) as black lines. All different tiles with sizes $8 \leqslant N \leqslant 30$ contribute to the uniform magnetization in a similar trend (although only $N \geqslant 16$ are shown here) and a small size dependence is observed. It happens only at low fields where the finite-size effects are most prominent. The bottom panel shows also the good agreement to the measured magnetization of Cu-pyrazine. The saturation field $H_{\text{sat}} = 490$ kOe has been used for normalizing the high-field data [64], and given the small size of the clusters involved, the Bonner – Fisher constructions represent closely its experimental behavior.

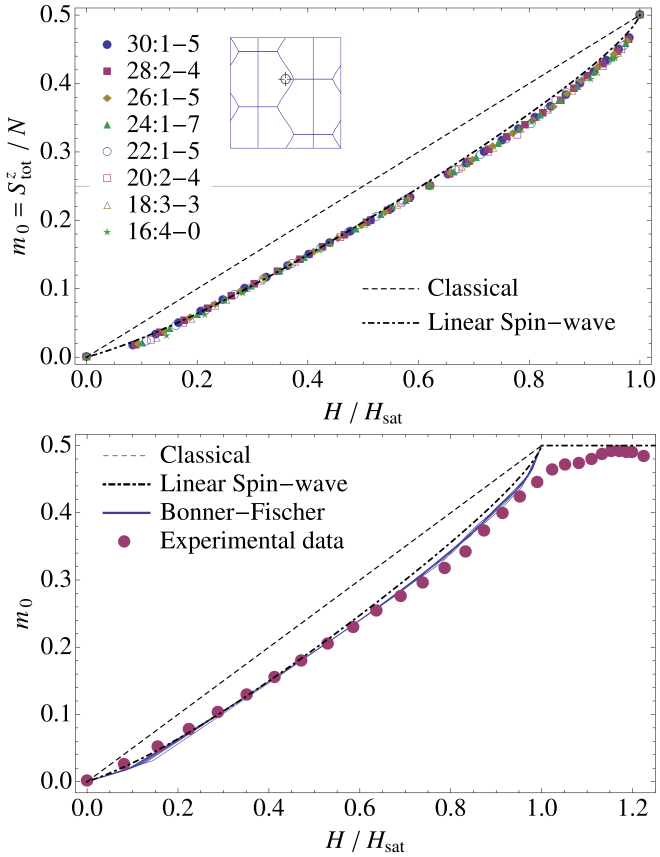

Figure 8.4.: Uniform magnetization (Section 4.3.2) calculated from the Bonner – Fisher construction of the exact diagonalization data and the linear spin-wave analysis for the simple Néel antiferromagnetic model, compared in the bottom panel to the experimental high-field magnetization data of Cu-pyrazine. The saturation field for the latter is 490 kOe [64]. The dependency of the uniform moment on the frustration angle deep inside NAF phase is small.

The same analysis can be applied also the the uniform moment behavior of vanadium compounds. For two classes of vanadium compounds of type $\mathrm{Li_2VO}X\mathrm{O_4}$ ($X =$ Si, Ge) [57] and $AA'\mathrm{VO(PO_4)_2}$ (A, $A' =$ Pb, Zn, Sr, Ba) [52, 54], V-oxide pyramid layers contain V^{4+} ions with $S = \frac{1}{2}$. From the analysis of the temperature dependence of the heat capacity and the magnetic susceptibility in zero (or small) fields, the frustration ratio J_2/J_1 can be obtained [107]. However, an ambiguity remains with respect to the relative sign of the two exchange constants, which can be resolved by analyzing the behavior of the saturation fields in these materials [69].

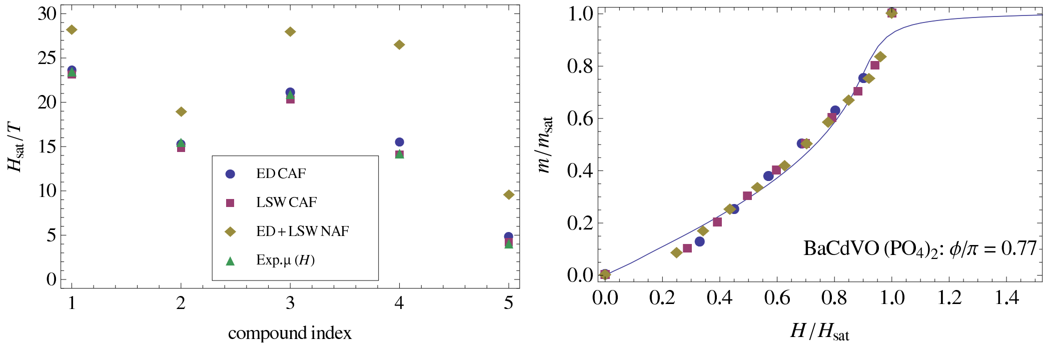

Figure 8.5.: Left: Comparison of saturation fields from exact diagonalization and spin-wave theory with $\theta = \frac{\pi}{4}$, and from high-field experiments [114]. The compounds are (1) $PbZnVO(PO_4)_2$, (2) $Na_{1.5}VOPO_4F_{0.5}$, (3) $Pb_2VO(PO_4)_2$, (4) $SrZnVO(PO_4)_2$, and (5) $BaCdVO(PO_4)_2$. The agreement with the saturation fields for the columnar phase gives a direct proof that all compounds have CAF order. Right: Magnetization for $BaCdVO(PO_4)_2$ [52]. Solid line denotes experimental data and filled symbols the data from $T = 0$ Lanczos calculations for different cluster sizes.

The left-hand side of Fig. 8.5 shows a comparison of the saturation fields determined by linear spin-wave theory and exact diagonalization for the columnar (CAF) and Néel (NAF) antiferromagnetic phases with the experimental values determined from high-field measurements [114]. The predicted theoretical values are based on fits of our finite-temperature Lanczos method data and of a high-temperature series expansion [52, 54, 114, 115] to the temperature dependences of the low-field susceptibilities. The experiments agree surprisingly well with the predicted CAF values, demonstrating that all compounds order in a columnar magnetic structure at low temperatures.

On the right-hand side of Fig. 8.5, the field dependence of the magnetization for $BaCdVO(PO_4)_2$ is displayed, together with zero-temperature data from our Lanczos calculations for different cluster sizes using a Bonner – Fisher construction [69, 113]. Given the small size of the clusters involved, the agreement is good, apart from low fields, where finite-size effects are most prominent.

8.1.2. Staggered magnetization (ordered moment)

Similar to the uniform moment m_0 in Section 8.1.1, staggered moment $m_{\mathbf{Q}}$ can also be calculated by the ground-state expectation value of the total moment m_{tot}

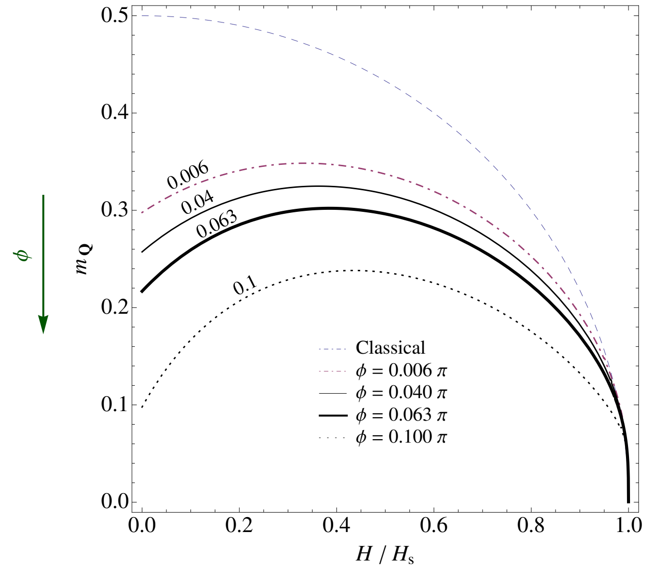

Figure 8.6.: The field dependence of the ordered moment in the NAF phase for several frustration parameters ϕ. The dashed line is the classical result. $\Delta m(\phi) = \frac{1}{2} - m_{\mathbf{Q}}(H = 0, \phi)$ is the zero-field moment reduction due to quantum fluctuations.

projected onto the plane perpendicular to the field. In Section 3.5 we obtained

$$\begin{aligned} m_{\mathbf{Q}} \quad = \quad & \sin\Theta_c \left\{ S - \frac{1}{2\sin^2\Theta_c} \left[\frac{1}{N} \sum_{\mathbf{k}} \frac{A_{\mathbf{k}} - B_{\mathbf{k}} \cos^2\Theta_c}{E_{\mathbf{k}}(H)} - 1 \right] \right. \\ & \left. - \frac{\cos^2\Theta_c}{2\sin^2\Theta_c} \frac{1}{N} \sum_{\mathbf{k}} \frac{B_{\mathbf{k}} \left(A_{\mathbf{k}} - B_{\mathbf{k}}\right)}{A_0 E_{\mathbf{k}}(H)} \right\} \end{aligned} \tag{8.4}$$

The calculated staggered moment $m_{\mathbf{Q}}$ from the linear spin-wave approximation is shown in Fig. 8.6. The result for various frustration parameters ϕ in the NAF phase are shown with different line types, and the dashed blue line corresponds to the classical rotation of the total moment out of the plane (Fig. 8.1). The field dependence of the staggered moment is strongly influenced by the frustration angle. In contrast to the classical case, it exhibits nonmonotonic behavior. This appears because of two behaviors. First, the size of the total moment *increases* with field, due to suppression of quantum fluctuation, up to the classical value S at the saturation field. Second, the moments are canted out of the plane, which reduces the staggered projection. From $m_{\mathbf{Q}}(H = 0)$ we clearly see that quantum fluctuations progressively reduce the ordered moment from the classical value $m_{\mathbf{Q}}^{\mathrm{cl}} = 0.5$ with increasing frustration angle ϕ. For larger frustration parameters one approaches the region of the nonmagnetic phase ($\phi/\pi \simeq 0.15$) where the spin-wave theory eventually breaks down ($m_{\mathbf{Q}}(H=0) \to 0$). The suppression of quantum fluctuations by the applied field become effective for large frustrations. Therefore the initial slope of $m_{\mathbf{Q}}(H)$ increases strongly with ϕ. This turns out to be an excellent method to determine ϕ.

8.1.3. The structure factor

To investigate magnetic long-range order in the context of the exact diagonalization on finite clusters, one has to look at the magnetic structure factor and its finite-size scaling behavior. A similar path as in Sections 4.3.2 and 6.2 will be followed, but with a difference in the normalization of the structure factor for the case of non-zero magnetic fields. Following the definition of the structure factor from Eq. 4.3,

$$\begin{aligned} S_{\alpha\beta}(\boldsymbol{q};H) &:= \frac{1}{\mathcal{N}_{\alpha\beta}(H)} \sum_{i,j=1}^{N} \left\langle S_i^\alpha S_j^\beta \right\rangle e^{i\boldsymbol{q}(\boldsymbol{r}_i-\boldsymbol{r}_j)} \\ &= \frac{N}{\mathcal{N}_{\alpha\beta}(H)} \left(\left\langle S_1^\alpha S_1^\beta \right\rangle + \sum_{j=2}^{N} \left\langle S_1^\alpha S_j^\beta \right\rangle e^{i\boldsymbol{q}(\boldsymbol{r}_1-\boldsymbol{r}_j)} \right), \end{aligned} \tag{8.5}$$

where S_i^α is the α-component of the spin operator at site i and the last equality holds for translationally invariant systems only. Special cases are:

- **Zero magnetic field**; with $H=0$, there is no distinction between different axes and in a perfectly ordered state with the ordering vector $\boldsymbol{Q}$ for all $i \neq j$ we have $\langle \boldsymbol{S}_i \cdot \boldsymbol{S}_j \rangle = \langle S_i^z S_j^z \rangle = S^2 e^{-i\boldsymbol{Q}(\boldsymbol{r}_i-\boldsymbol{r}_j)}$, leading to the previously discussed normalization of $\mathcal{N}_{\alpha\beta}(H=0) = N(N+\frac{1}{S})$,

- **On-site term**; regardless of the magnetic field value, $\langle \boldsymbol{S}_i \cdot \boldsymbol{S}_i \rangle = \langle \boldsymbol{S}_i^2 \rangle = S(S+1)$.

- **Fully polarized state** with $H \geqslant H_{\text{sat}}$; where for all $i \neq j$, $\langle S_i^x S_j^x \rangle = \langle S_i^y S_j^y \rangle = 0$ and $\langle S_i^z S_j^z \rangle = S^2$.

The latter case leads to a non-vanishing value for $S_{xx}(\boldsymbol{q}, H_{\text{sat}}) + S_{yy}(\boldsymbol{q}, H_{\text{sat}})$ at any finite N, due to the on-site contribution. For this reason, we drop the on-site terms in the sum for the transverse coefficients of the structure factor. In this case, the correct normalization would have the form $\mathcal{N}_{xx}(H \neq 0) = N(N-1)$, and we get the correct limiting value when extrapolating to infinitely large systems, $N \to \infty$. To summarize, the normalizations of the structure factor we use in the magnetic field for $S = \frac{1}{2}$ are

$$\begin{aligned} S_{\alpha\alpha}(\boldsymbol{q};0) &= \frac{1}{N+2}\left(\frac{1}{4} + \sum_{j=2}^{N} \left\langle S_1^\alpha S_j^\alpha \right\rangle e^{i\boldsymbol{q}(\boldsymbol{r}_1 - \boldsymbol{r}_j)}\right), \\ S_{zz}(0;H) &= \frac{1}{N}\left(\frac{1}{4} + \sum_{j=2}^{N} \left\langle S_1^z S_j^z \right\rangle\right), \\ S_{xx}(\boldsymbol{q};H) = S_{yy}(\boldsymbol{q};H) &= \frac{1}{N-1}\sum_{j=2}^{N} \left\langle S_1^x S_j^x \right\rangle e^{i\boldsymbol{q}(\boldsymbol{r}_1 - \boldsymbol{r}_j)}. \end{aligned} \tag{8.6}$$

Using these normalizations, Fig. 8.7 shows the outcome of the calculation of the structure factor using the Bonner – Fisher construction of the exact diagonalization results of finite tiles. From top to bottom panels, the parallel and transverse components of the structure factor, as well as their sum are presented. In the top plot, the values are indeed exactly the same as the square of the total S^z per site (Fig. 8.4 top).

For the transverse components, the value at $H = 0$ is the same as before which was used for the finite-size scaling and leads to the known value of 0.30(3) for the magnetic moment in the unfrustrated anisotropic Néel case. A similar trend for the size dependence of the structure factor at a non-zero magnetic field is also observed here. This gives us a motivation to employ again a similar finite-size scaling analysis, which will be described in more details in the next section. The bottom plot also depicts the sum of parallel and transverse components which corresponds to the square of the total magnetic moment m_{tot}^2. For them a similar but separate finite-size scaling can be done.

8.1.4. Finite-size scaling of the ordered moment

Motivated by the successful finite-size scaling of the zero-field structure factor in the ordered phases, one can perform a similar analysis in the presence of the magnetic field. However, one cannot simply use all tile sizes together in the finite-size scaling procedure. For a given field strength H, different tiles can have different magnetizations. Therefore, we have to work with constant magnetization, instead of constant magnetic field strength. Because of the level crossings, the values of the structure factor for all tiles do not correspond to the same value of fields for all tiles,

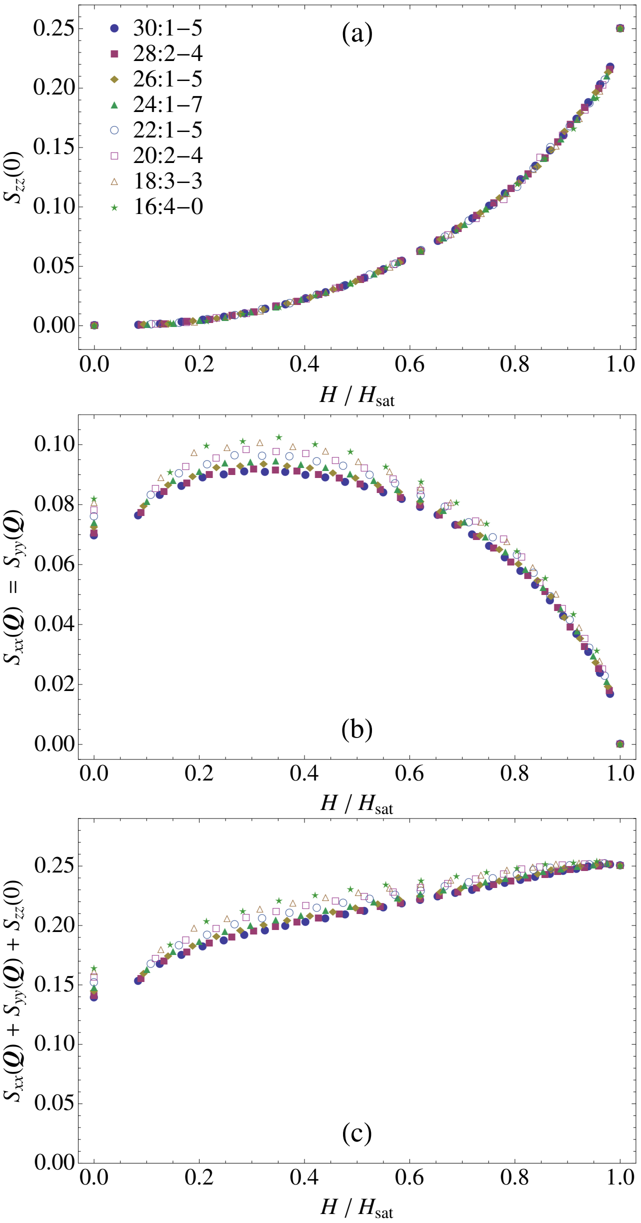

Figure 8.7.: The field dependence of the structure factor in the unfrustrated ($\phi = 0$) Néel state of the antiferromagnetic Heisenberg model using Bonner – Fisher construction (Section 4.3.2). (a) The uniform structure factor $S(0)$. (b) The staggered structure factor $S_{xx}(\boldsymbol{Q})$, excluding the on-site terms. (c) Sum of structure factors, which equals to the total moment m_{tot}^2, including on-site terms for $S(0)$ and excluding them for $S(\boldsymbol{Q})$.

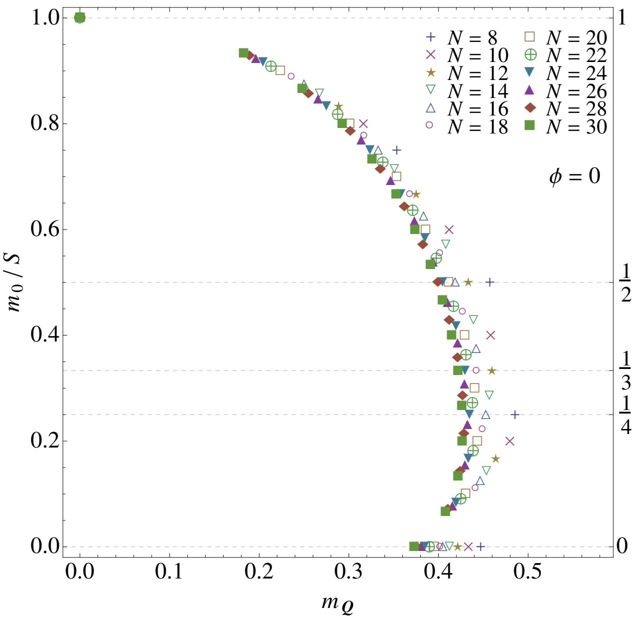

Figure 8.8.: Parametric plot of the uniform and the staggered moments calculated from the exact diagonalization of finite clusters, for the unfrustrated Néel antiferromagnet. Symbols denote values for different tiles with sizes $8 \leqslant N \leqslant 30$. Field increases from $H = 0$ to H_{sat} by going from lower right to upper left corner.

but rather on some intervals which might not even overlap. We have to choose here between those levels which belong to the same class (same S^z_{tot}) and this restricts us to use all possible system sizes for the scaling at a particular total spin number. In order to illustrate this, Fig. 8.8 shows the parametric dependence of both uniform and staggered moments (m_0 vs. $m_{\mathbf{Q}}$) for system sizes $8 \leqslant N \leqslant 30$. The field is the variable parameter in the plot. Zero magnetic field $H = 0$ corresponds to $m_0 = 0$, in the lower right corner (zero field staggered moment), and $H = H_{\text{sat}}$ corresponds to $m_0 = S$ in the upper left corner (saturated uniform moment). The vertical (horizontal) axis corresponds to the uniform (staggered) moment, and each unique symbol locates total moment for a particular tile at a specific magnetization. Level crossings of the structure factor for each size leads to a set of points for each cluster. In this sense, the values on the horizontal axis are in $H = 0$ and the vertical axis for $H = H_{\text{sat}}$ (top-left corner of the diagram). Here, instead of determining the intervals by the magnetic field (as in Fig. 8.3), we can compare the levels by their total S_z number per site (uniform moment). Only those clusters which can realize a particular value for the total moment, create a meaningful set of finite-size data.

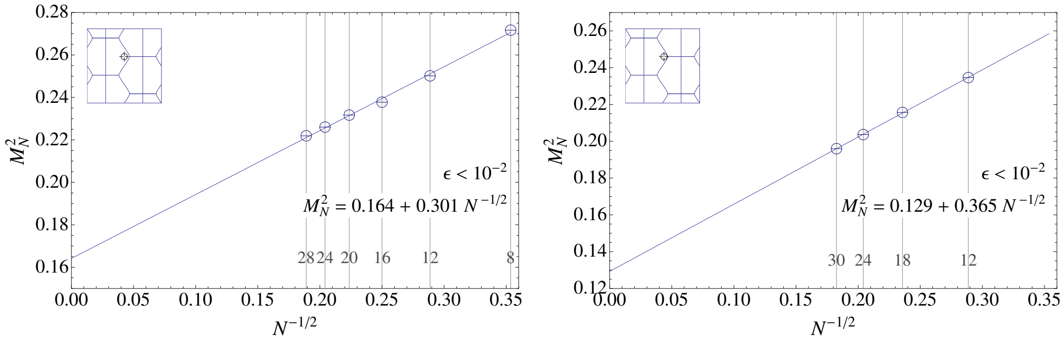

(a) $\phi = 0, S^z_{\text{tot}} = \frac{1}{2}$

(b) $\phi = 0.04\pi, S^z_{\text{tot}} = \frac{1}{3}$

Figure 8.9.: Finite-size scaling of the square of structure factor M_N^2 (see Section 6.2.1) for a sector with non-zero total spin for (a) unfrustrated ($\phi = 0$) and (b) frustrated cases ($\phi \neq 0$). The scaling function and the relative error (Section 6.3) is given in the plot.

As an example, consider the spin sector which has a total moment $m_0/S = \frac{1}{3}$ (the center dashed line in Fig. 8.8). Since we have $m_0 = \frac{n}{N}S$ with $n = 0, 1, \ldots N$ for a tile with size N, only those tiles with $N \equiv 0$ (mod 3/S) can allow for this value of $\frac{1}{3}$, which will be N =12, 18, 24, 30 and so on. Only these system sizes can be used to extrapolate the value of the staggered moment on this spin sector. This limits the number of points available for the scaling analysis to just a fraction of allowed tiles. Yet, within our available cluster sizes, a finite-size scaling for the spin sectors $\frac{1}{2}$, $\frac{1}{3}$, and $\frac{1}{4}$ can be done using at least three data points. Two examples of such scaling plots are shown in Fig. 8.9 for (a) the unfrustrated $\phi = 0$ case with $S^z_{\text{tot}} = \frac{1}{2}$ and (b) $\phi = 0.04\pi$ with $S^z_{\text{tot}} = \frac{1}{3}$. The same scaling formula as Eq. 5.20 is used here and the error defined in Eq. 6.1 indicates two digits accuracy for the extrapolated value. The extrapolated results from this scaling analysis and their comparison with the linear spin-wave approximation are presented in Fig. 8.10. The dashed line shows the classical value and the dot-dashed line in all panels corresponds to the unfrustrated ($\phi = 0$) case. For three different values of frustration angle $\phi = 0, 0.04\pi$ and 0.063π, the agreement between the extrapolated result and the spin-wave approximation is very good. This demonstrates the power of the finite-size scaling analysis and also the validity of the linear spin-wave approximation.

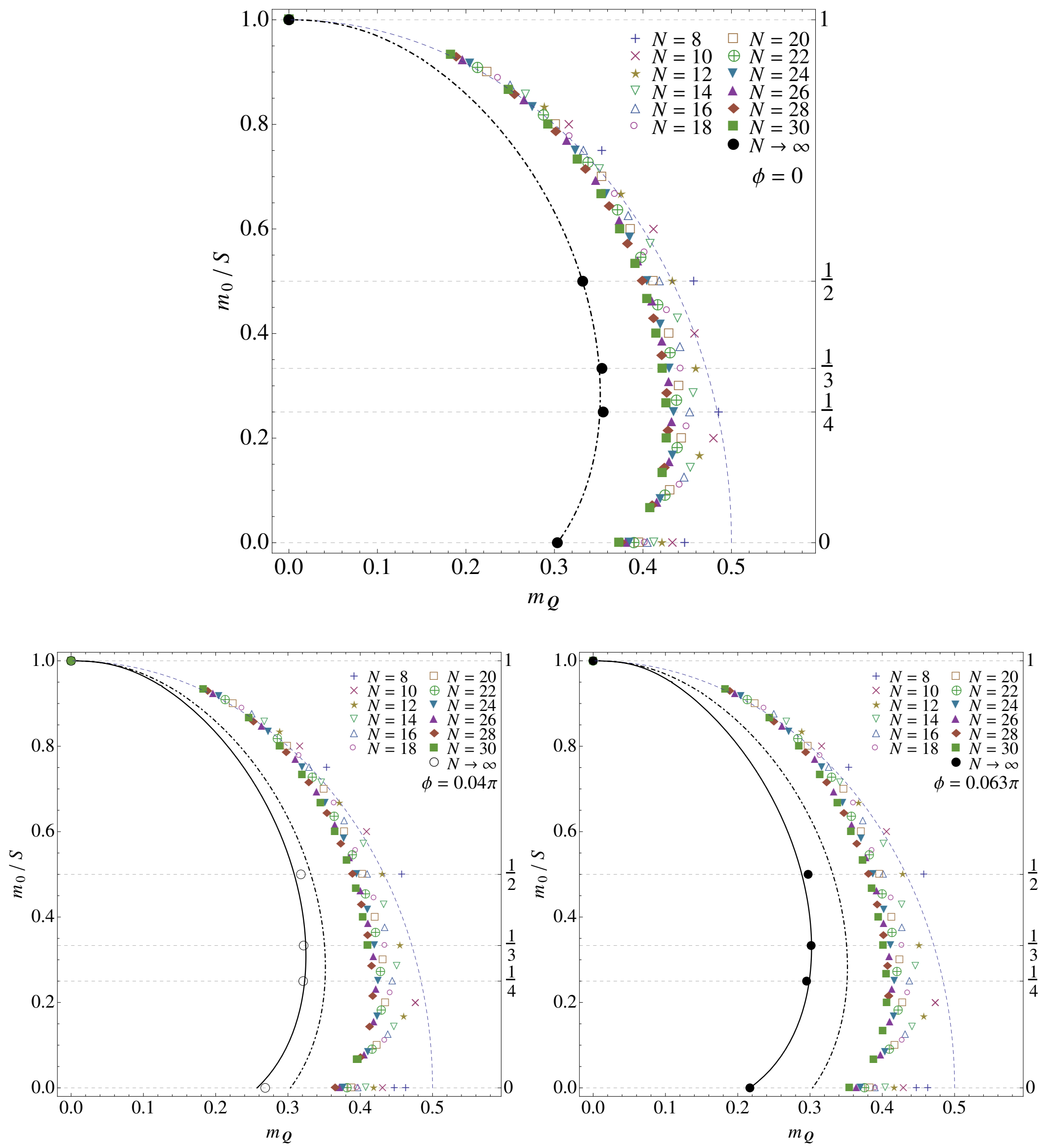

Figure 8.10.: Parametric representation of uniform and staggered moment as function of field. Here $H = 0$ at the lower right and $H = H_s$ at the upper left corner. Frustration parameters shown are (a) $\phi = 0$ (unfrustrated) (b) $\phi = 0.04\pi$ and (c) $\phi = 0.063\pi$. The dashed line is the classical value. Symbols denote the value of the moment for different tiles with sizes $8 \leqslant N \leqslant 30$. Black lines correspond to the linear spin-wave results and the black symbols are from the finite-size scaling of the exact diagonalization. Dot-dashed line denotes the value for the unfrustrated model ($\phi = 0$).

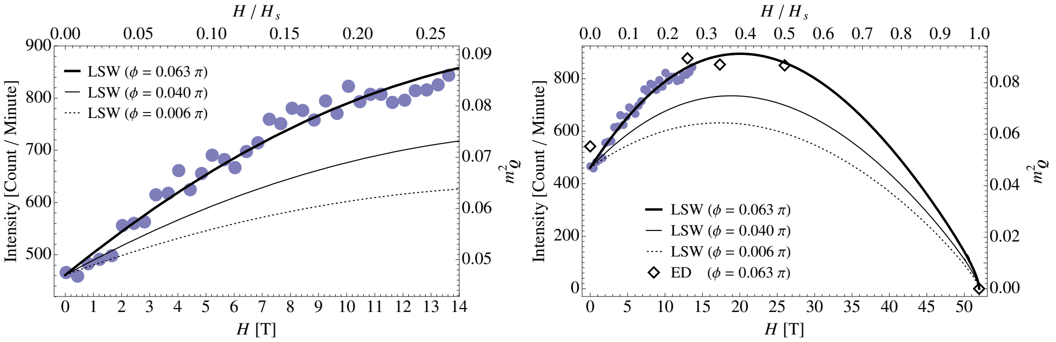

Figure 8.11.: Fitting the ordered moment to the inelastic neutron scattering data in order to determine the frustration parameter ϕ. The solid thick line corresponds to the best fit parameter $\phi = 0.063\pi$. The dotted line is the unfrustrated case and the thin line is the relative increase of the moment for a lower value of $\phi = 0.04\pi$ which was obtained from the fitting of the powder susceptibility measurements (Section 7.1.1).

8.2. Comparison with experimental results for Cu-pyrazine

We concluded in Section 8.1.2 that the field dependence of the ordered moment provides a method to determine the frustration angle ϕ. To demonstrate the strength of this method we apply it to the quasi-two-dimensional Néel antiferromagnet $\mathrm{Cu(pz)_2(ClO_4)_2}$, using both exact diagonalization and spin-wave calculations. In Section 7.1.1 we used the finite-temperature Lanczos method results to fit the measured susceptibility data of Cu-pyrazine and obtained the value of $\phi = 0.04\pi$ or $J_2/J_1 \simeq 0.126$ for the degree of frustration. However, the fit to $\chi(T)$ does not necessarily yield an accurate and unique solution, since it depends primarily on $\Theta_{\mathrm{CW}} = J_1 + J_2$, but only weakly on the individual exchange constants [107, 116], and the complementary values ϕ and $\phi' = \frac{\pi}{2} - \phi$ having identical Θ_{CW} corresponding to Néel and columnar antiferromagnetic order cannot be distinguished from an analysis of $\chi(T)$ alone [116]. It is therefore important to check this value of ϕ independently. One possibility is to analyze the field dependence of the ordered moment, which can be obtained from neutron diffraction data. The square of the ordered moment $|m_{\mathbf{Q}}|^2$ is proportional to the scattering intensity. This has been measured for Cu-pyrazine in Ref. [61] for up to about $\frac{1}{4}$ of the saturation field ($H \lesssim 14\,\mathrm{T}$), and we fit these data to the staggered moment calculated by the linear spin-wave approximation and exact diagonalization method. Here, we consider two fit parameters, namely the frustration angle ϕ and the normalization of the neutron scattering intensity, which we treat as a free fit variable. Since the change in the ordered moment with field is considerably large $m^2(H = 14\,\mathrm{T}) \approx 2m^2(H = 0)$, a rather substantial frustration ratio seems necessary to reproduce it. The results are shown in Fig. 8.11 which yield the value of $\phi = 0.063\pi$, which is somewhat larger than the value $\phi = 0.04\,\pi$ from the finite-temperature Lanczos method comparison to $\chi(T)$. The experimental data in Fig. 8.11 are determined with $7 - 8\%$ relative accuracy [61].

For comparison we also show the moment for $\phi/\pi = 0.04$ (thin line) and the nearly unfrustrated Néel antiferromagnet with $J_2/J_1 = 0.02$ or $\phi/\pi = 0.006$ (dotted line). For the latter the frustration ratio has been determined by a series expansion analysis of zone boundary spin-wave spectra in Ref. [62], but the predicted field induced staggered moment increase is much too small. To get a more pronounced moment increase with field, one has to increase the frustration ϕ, as is evident from Fig. 8.6, and for $\phi/\pi = 0.063$ the experimentally observed increase is obtained in Fig. 8.11. The discrepancy to the finite-temperature Lanczos method value of $\phi = 0.04\pi$ may possibly be caused by the background subtraction process [61] which introduces an additional uncertainty with respect to the absolute size of moment increase. In this sense Cu-pyrazine is not an ideal example due to the relatively large non-magnetic background observed. We point out that the analysis of $m_{\mathbf{Q}}(H)$ also can resolve an ambiguity of possible values for ϕ and this observation may be used as a tool in other cases where the ordered structure is not known.

Finally, for comparison (as in Fig. 8.11) the finite-size scaling of the exact diagonalization results for the moment are shown as open diamonds. Because the finite size scaling is only possible for discrete values of the uniform moment, only few values with $H/H_{\mathrm{sat}} \leq 0.3$ in right panel of Fig. 8.11 are available, nevertheless the agreement is satisfactory.

IX. Conclusions on the $J_{1a,b} - J_2$ Model

We have discussed thoroughly the properties of the spatially anisotropic Heisenberg model on the square lattice, with first and second neighbors interactions. The $J_1 - J_2$ model is one exemplary system in studying the effects of quantum fluctuations and quantum phase transitions driven by frustration. In this work, we have investigated in detail the localized moment $J_{1a,b} - J_2$ model, in particular the effect of the in-plane anisotropy and the frustration. In Chapter 2, the model Hamiltonian has been introduced and the classical phase diagram of the system was presented. Chapters 3 and 4 describe two methods, linear spin-wave approximation and exact diagonalization, which we use for studying the properties of the system. The finite-size scaling analysis based on the results of finite systems is presented in Chapter 5 and the results of the ground-state properties are discussed in Chapter 6. Furthermore, Chapters 7 and 8 contains the description of the calculations in finite temperatures and presence of an external magnetic field, respectively.

9.1. Finite-size scaling of the exact diagonalization data

In order to obtain reliable values of ground-state energy and ordered moment size in the thermodynamic limit, we have investigated the finite size scaling procedure applied to the exact diagonalization results of finite clusters. We have also compared these numerical results with linear spin-wave theory [47].

The implementation of a stable finite-size scaling procedure requires precise criteria for the usefulness of the many possible tiles of varying sizes and shapes used to tile the infinite lattice. We have introduced and described in great detail, how all possible tilings with a given area N of the square or rectangular lattice can be generated (Sections 5.1.3). Then, we have classified systematically the clusters according to their spatial symmetry, compatibility with classical magnetic phases and their geometrical compactness or squareness (Section 5.3). We have found that a restriction to tiles which have compatibility with classical phases and maximal squareness lead to a very stable scaling behavior of ground state energy and ordered moment in the region of NAF and CAF phases. This is a major procedural progress as compared to earlier scaling strategies [87, 100, 101].

The agreement of exact diagonalization results with spin-wave calculations was found to be generally good. Both methods predict the breakdown of magnetic order in the transition regions at the borders of the columnar magnetic phases as function of frustration but also in the regions where the model attains effective quasi-one-dimensional character as function of the anisotropy for $J_2 = 0$. As in earlier investigations for the isotropic model, it remains difficult to quantify the exact size of the interval on the ϕ or θ axes where the ordered moment vanishes.

9.2. Application to the parent compounds of Fe-pnictides

This local moment model has been surprisingly useful to explain phenomenologically the low energy magnetic excitations for Fe-pnictides, which were obtained by Inelastic Neutron Scattering experiments, albeit with the assumption of possibly very anisotropic exchange interactions. It should be noted that the compounds are metallic, thus the application of a local moment picture is not a priori justified. The exchange anisotropy may have its microscopic origin in underlying orbital order as proposed in [49, 117] but this is still not completely understood. The very usefulness of the local moment picture may be a consequence of Hund's rule correlations in the multi-orbital state of Fe-pnictides [117].

It has been a recurrent topic to explain the comparatively small ordered moments in Fe-pnictides as the effect of enhanced quantum fluctuations in the ground state due to large degeneracy caused by frustrated $J_{1a,b}$ and J_2 exchange bonds. We have investigated this scenario in detail using spin-wave approximation and the exact diagonalization Lanczos method to calculate the ground-state energy, phase diagram and moment reduction by quantum fluctuations as function of anisotropy and frustration parameters (Chapter 6).

We found that generally the anisotropy lifts the degeneracy between CAFa/b phases and extends their stability range as a function of frustration. Furthermore, the anisotropy reduces or closes the instability gap on the phase boundary to the NAF or FM phase, respectively (Section 3.4.2). Most importantly we have shown that in the CAFa sector of the anisotropic model relevant for the Fe-pnictides the moment reduction by quantum fluctuations is generally *less* than for the simple unfrustrated nearest neighbor Néel antiferromagnet. This is evident from Fig. 9.1 where the ordered moment values according to Table 9.1 (dots) are compiled and

	System	Ref.	ϕ/π	θ/π
1	$CaFe_2As_2$	[59]	0.19	0.08
C	$CaFe_2As_2$	[60]	0.29	0.13
D	$CaFe_2As_2$	[48]	0.11	-0.04
B	$BaFe_2As_2$	[58]	0.35	0.25
5	$BaFe_2As_2$	[58]	0.19	-0.06
6	$CaFe_2As_2$	[51]	0.20	-0.02
7	$BaFe_2As_2$	[51]	0.10	-0.02
8	$SrFe_2As_2$	[51]	0.16	0.02

Table 9.1.: Compilation of the frustration and anisotropy parameters based on experimental (top) and theoretical (bottom) values of the exchange interactions from Table 2.2. The first column holds the labels used in Fig. 9.1 (letters and numbers).

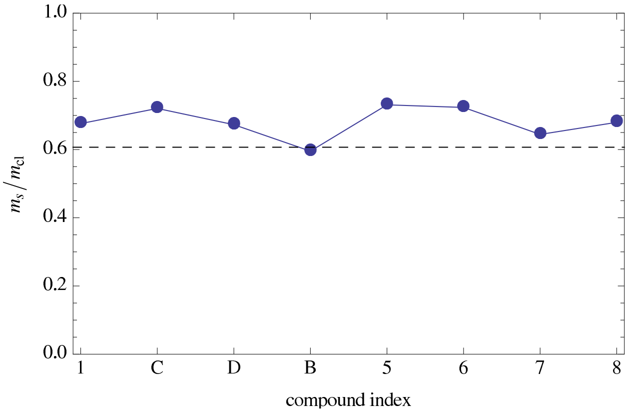

Figure 9.1.: Ordered moments normalized to the classical constant $m_{cl} = S$ for the compounds listed in Table 2.2 calculated with Eq. 3.38. The dashed horizontal line indicates $m_s(\phi = 0, \theta = \pi/4)$ for the simple $J_2 = 0$, $J_{1a} = J_{1b}$ nearest-neighbor Heisenberg model.

compared with the value corresponding to the simple nearest-neighbor unfrustrated isotropic Néel antiferromagnet (dashed line).

This result is in part due to the stabilization of the moment due to the effect of the anisotropy. In fact, the frustration angle for $BaFe_2As_2$ (denoted by D in Fig. 9.1) is rather close to the strongly frustrated value $\phi = 0.15\pi$ of the *isotropic* ($\theta = \pi/4$) model. Nevertheless, it is at a considerable distance from the anisotropic CAFa/NAF instability line and hence shows only moderate moment reduction. Therefore, from Fig. 9.1 we conclude that frustration and quantum fluctuation effects within a local moment picture cannot be used to explain the surprisingly small ordered moment of the Fe-pnictides. However, we note that this conclusion does not invalidate the usefulness of the $J_{1a,b}$-J_2 local moment model for the interpretation of spin-wave excitation results of Inelastic Neutron Scattering. In classical (linear) spin-wave theory only the products SJ_i enter the spin-wave velocity and dispersion and therefore the shape of the dispersion does not depend on the size of the spin S within this approximation. Finally, one needs a more microscopic viewpoint including the itinerant multi-orbital nature of the magnetic state. Such proposals have been made within recent ab initio calculations using the full orbital basis [118–120].

9.3. Nonmagnetic regions of the phase diagram with exotic orders

In a corollary to the calculation of the ordered moment, we address a result of our analysis not immediately relevant for Fe-pnictides because it is related to the magnetic instability at the CAF/FM boundary ($\phi/\pi = 0.852$). Close to the classical NAF/CAF and CAF/FM boundaries the relative error of energy and moment increases and the scaling procedure becomes unstable, because a systematic dependence of E_{0N} and $M_N(\mathbf{Q})$ on the tile area N ceases to exist. In these regions, a quantitative prediction of the size of the ordered moment becomes very difficult, if not impossible. The frustration effects of competing exchange interactions lead to large quantum fluctuations which in turn cause the breakdown of magnetic order.

There are two-dimensional local moment compounds [40] e. g. BaCdVO$(PO_4)_2$ (Table 2.1) where the frustration angle is quite close to classical CAF/FM boundary ($\phi = 0.85\pi$), contrary to the Fe-pnictides. It has been shown for the isotropic model that the true ground-state in this region is of the spin-nematic hidden order state [44, 46]. Although spin-wave theory is not adequate to fully address this question we have shown (Fig. 6.23) that the columnar order at the boundary recovers immediately when turning on even a tiny anisotropy of nearest neighbors exchange constants $J_{1a,b}$. Since small anisotropies usually exist in such compounds we predict that the spin nematic state of the isotropic $J_1 - J_2$ model will be very hard to find in a real compound.

9.4. Finite-temperatures and magnetic field dependence properties: Application to $\mathrm{Cu(pz)_2(ClO_4)_2}$

In Chapters 7 and 8, we have presented the analysis of field dependence of ordered moment using exact diagonalization for finite clusters and compared with spin-wave theory. The staggered moment exhibits pronounced non-monotonic behavior as function of magnetic field, which depends on the degree of frustration given by $\phi = \tan^{-1}(J_2/J_1)$. This provides a powerful means to extract the frustration ratio which is more accurate and less ambiguous than using temperature dependence thermodynamic quantities alone. We have applied this method to $\mathrm{Cu(pz)_2(ClO_4)_2}$ and conclude primarily from the ordered moment field dependence, that it is a quasi-two-dimensional antiferromagnet with intermediate frustration. This method may be used more generally for frustrated antiferromagnets. In particular it should also be applicable when the field dependent ordered moment is extracted from analysis of NMR splittings rather than from neutron diffraction data. Since it requires the existence of an ordered moment it will, however, not be useful for compounds corresponding to the disordered regimes of the $J_1 - J_2$ phase diagrams, if they should indeed exist.

9.5. Future extensions and open questions

Since its early discussion in 1987 by Anderson [34], the $J_1 - J_2$ model gained a lot of attention after the discovery of layered copper-oxide high-temperature superconductors. The model has been derived from the Hubbard model by going to the strong coupling limit, which essentially catches the physics of highly correlated electronic system. In two-dimensions, quantum fluctuations are considerable enough to reduce the size of the ordered moment by nearly 40% of its classical value. However, adding orbital degrees of freedom to similar models might lead to a better picture of the magnetism of Fe-pnictides even in the localized picture. Further issues are the origin of orbital and magnetic order in the already metallic parent compounds of Fe-pnictides based on an itinerant picture [49, 117, 121] and their relation to the superconducting pairing mechanism [122].

Finally, the question on the true nature of the non-magnetic regions and their exotic orderings in the $J_1 - J_2$ model is another subject of further discussions and studies. Considering interactions between more neighbors or different lattice geometries (e. g. checkerboard, trigonal, kagomé, honeycomb) will generally lead to rich phase diagrams which is a theoretical subject of intensive current interest.

X. Frustration in Itinerant Systems: The Correlated Kondo Lattice Model

In this chapter we investigate the correlated Kondo lattice model, which is also known as Kondo-Hubbard model. We calculate its ground-state properties such as correlation functions and the ordered moment, as well as the temperature behavior of magnetic susceptibility and heat capacity, using the numerical exact diagonalization method and analytical bond operator theory. The dependence of the Kondo temperature scale over the Coulomb repulsion is investigated, and in the limit of the Kondo necklace model, analytical mean field results are compared with those of numerical exact diagonalization for a finite tile. Although there is no explicit spin frustration built into this model, the latter arises through many body correlations which lead to a competition between on-site singlet formations and antiferromagnetic inter-site correlations.

10.1. Introduction

The understanding of strong correlations in mixed valent and heavy f-electron compounds is mostly based on two generic models described by the Anderson lattice Hamiltonian or, in the special case of almost integer valence, by the Kondo lattice Hamiltonian [123,124]. The latter model which will be the subject of this work represents an extreme limit where correlations in the f-orbitals are taken as infinitely large due to the Coulomb integral $U_f \gg t$ with t denoting the hopping energy of conduction (c) electrons. On the other hand, the Coulomb interaction U of conduction electrons (and also the one between c- and f-electrons) is completely neglected in this model. The $U = 0$ Kondo and Anderson models have the advantage of a simple and meaningful mean field solution [124,125] with the constraint of only singly occupied f orbital implemented by an auxiliary boson in mean field approximation. In the lattice this leads to hybridized quasiparticle bands with an exponentially reduced hybridization gap. Close to the half filled case with one c- and f- electron per site they have an effective mass $m^* \gg m_b$ much larger than the conduction electron band mass m_b [123]. The mean field Kondo lattice model may be merged with local density band structure calculations in the renormalized band theory [126] leading to a powerful method to calculate realistic Fermi surfaces for Ce and Yb heavy fermion compounds, including crystalline electric field effects.

It has been known that a strong Coulomb repulsion among the conduction electrons significantly alters the electronic properties of a metal. First and foremost, the kinetic energy as measured by the (effective) bandwidth will be reduced and eventually vanish at a metal-to-insulator transition. Second, the trend towards localization is accompanied by the appearance of magnetic correlations.

The central focus in this section is the influence of the above-mentioned correlation effects on the screening of local moments. Of particular interest, is the question how the Kondo energy scale is affected by conduction electron correlations. We adopt a two-dimensional Hubbard model at half-filling for the conduction electrons where correlation effects have been found to affect strongly the electronic properties. As the interacting conduction electron Hamiltonian, i. e. the two-dimensional Hubbard model, cannot be solved exactly for an infinitely extended system, we extract the relevant information from suitably chosen finite clusters. This approach seems justified considering the local character of the quantities to be investigated. The relevance of the cluster approach is assessed by comparing its results to the predictions of a constrained mean-field theory for an infinite system in the limit of extremely strong Coulomb repulsion.

Attempts to include the effect of correlations between conduction electrons which may become important when the latter originate from d-orbitals have so far been mostly limited to the Kondo impurity models using various analytical techniques like perturbation theory [127, 128] and $1/N_f$ expansion for small U, a Schrieffer-Wolff approach [129] and RVB ansatz [127] for large U, a scaling approach [130] and also numerical techniques like Numerical Renormalization Group (NRG) [131]. In the impurity problem it was concluded that the Kondo energy scale T^* increases with U [127, 128].

Concerning concentrated systems with magnetic moments at every lattice site the situation is rather controversial. In the case of non-interacting conduction electrons ($U = 0$) the electronic properties will be determined by the competition between the energy gain due to (local) Kondo singlet formation and to developing (long-range) magnetic correlations. It is to be expected that the subtle balance between these two tendencies will be affected by conduction electron repulsion.

The correlated Anderson lattice problem was treated with a Gutzwiller variational method [132] and the one-dimensional correlated Kondo lattice with Density Matrix Renormalization Group (DMRG) approach [133]. It was further investigated with Quantum Monte Carlo (QMC) simulations and a fermionic bond operator method [134] used before in the uncorrelated case [135]. The strongly correlated ($U \gg t$) “Kondo necklace” limit of the Kondo lattice was treated using Exact Diagonalization (ED) [136]. It was suggested [132] that the Kondo scale actually decreases for increasing U, in contrast to the impurity results. The competition of singlet formation and induced inter-site RKKY coupling and its signature in thermodynamics was studied in Ref. [137] using ED and finite temperature Lanczos Method (FTLM) methods for finite clusters of the two-dimensional uncorrelated Kondo lattice and in Ref. [138] for one-dimensional chains in the strongly correlated limit.

The present work which uses the unbiased numerical ED and FTLM methods as well as the analytical bond operator technique has two clear objectives: i) First, to investigate the characteristic $T = 0$ on-site and inter-site correlations and local paramagnetic moment $\langle \mu_{\mathrm{loc}}^2 \rangle$ systematically in the whole (J_K, U) parameter range of the correlated Kondo lattice model, where J_K is the local antiferromagnetic exchange coupling. In particular the total local paramagnetic moment is an excellent measure for the formation or breakup of the Kondo singlet state as function of control parameters [137]. We will show that it exhibits an unexpected non-monotonic behavior that has not been reported before. ii) Second, we calculate the finite temperature behavior of susceptibility and specific heat with FTLM on a small tile of the square lattice. From the maximum position we may extract the characteristic “Kondo” temperature scale T^*, and in particular, we investigate its systematic dependence on the correlation strength U. We will resolve the ambiguity mentioned before and show that T^* increases monotonically with U. The ED and FTLM calculations will be performed on small Kondo clusters with open boundary conditions which have a more realistic one-particle density of states than the one with periodic boundary conditions [137].

It should be stressed from the outset that in the context of the FTLM calculations on a finite cluster the meaning of T^* is that of an average energy of low energy singlet-triplet excitations obtained from the maximum in the temperature dependent susceptibility and specific heat. This is indeed the way how an estimate of T^* in a real concentrated Kondo compound may be obtained. It is not the same as the genuine single ion Kondo temperature T_K in the continuum limit which is exponentially small compared to the hopping energy. This difference between lattice and single ion Kondo scales appears already within approximate analytical theories [124].

Nevertheless, a comparison of ED numerical results for finite clusters with analytical results obtained by the bond operator method for the extended lattice and in the large U limit is useful and legitimate. Since the former are exact, it allows one to judge how far the large U model approximation is justified and give an estimate of the reliability and accuracy of the bond operator approximation. This theory has previously been used for quantum critical properties of the localized model in the large U limit, e. g. in Refs. [139–141] and references cited therein. A generalized fermionic version has also been applied to the finite U case [135]. In this comparison we focus on the paramagnetic local moment size and on-site correlations as function of U and on the finite temperature susceptibility.

We note that the investigation of finite Kondo atom clusters on nonmagnetic surfaces is also of potential experimental interest. So far single magnetic Co adatoms embedded in metallic Cu_n clusters [142] and two site Co-Co Kondo clusters connected by Cu_n chains [143] have been investigated. However, in these cases of a metallic substrate it is the simple conduction electron density of the substrate surface that plays the dominant role for the Kondo properties. The present investigation would be relevant for correlated Kondo clusters weakly adsorbed on an inert insulating substrate without chemical bonding of substrate and Kondo atoms. This has, to our knowledge, not been experimentally realized until now. Nevertheless, the above examples indicate that the investigation of finite-size Kondo clusters is of great interest in itself and not only in view of the bulk Kondo lattice materials.

10.2. Model definition and single particle spectrum

The correlated Kondo lattice model (KLM), sometimes called Kondo-Hubbard (KLU) model, contains three terms. As in the non-interacting model there is the hopping term for conduction electrons $c_{i\sigma}$ ($\sim t$) and the Kondo exchange term ($\sim J_K$) to localized spins $\boldsymbol{S}_i$ at every site. Their localization may be considered as result of their large repulsion U_f. As mentioned before, the Coulomb repulsion U for conduction electrons is usually neglected in the lattice model, although well studied for the Kondo impurity case. It is, however, very interesting to include its effect, both because it is physically present, in particular in intermetallic 3d-4f compounds and also because it allows to study theoretically the continuous crossover from the

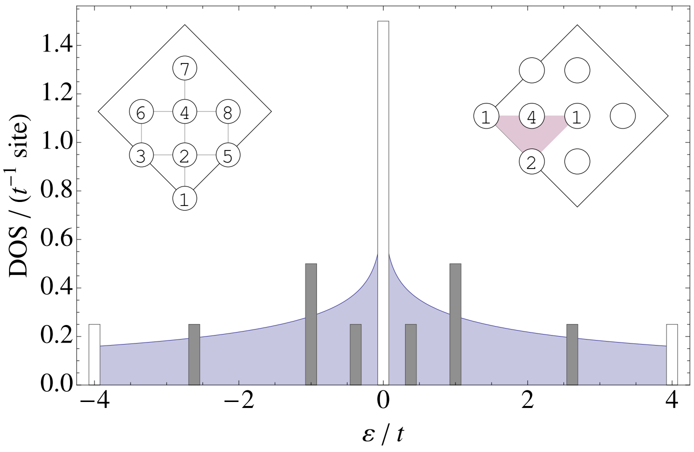

Figure 10.1.: Single particle DOS for the two-dimensional next neighbors tight binding model in the continuum limit (full line) with logarithmic singularity at Fermi level for half filling ($\epsilon = 0$). Number of states for 8 site cluster is shown for OBC (full bars) and PBC (open bars). Left inset: Eight site cluster. Right inset: **k**-points for PBC.

metallic Kondo screening case to the insulating case of interacting local spin dimers. The model is given by

$$H_{\mathrm{KLU}} = -t \sum_{i,j;\sigma} c^{\dagger}_{i\sigma} c_{j\sigma} + U \sum_{i} n_{i\uparrow} n_{i\downarrow} + J_{\mathrm{K}} \sum_{i} \boldsymbol{\tau}_i \cdot \boldsymbol{S}_i, \tag{10.1}$$

where $n_{i\sigma} = c^{\dagger}_{i\sigma} c_{i\sigma}$. In two dimensions, the first nearest neighbor hopping term leads to the single particle spectrum given by the dispersion $\epsilon_{\mathbf{k}} = -t(\cos k_x + \cos k_y)$. In the continuum limit ($N \to \infty$), it leads to a well known density of states (DOS) function shown in Fig. 10.1 by the full line, which has a logarithmic singularity a $\epsilon = 0$ corresponding to the half filling. As was done in Ref. [137] for the uncorrelated KL model ($U = 0$), we will use the exact diagonalization with Lanczos method for finite square lattice tiles. For the systematic classification of finite size tiles on the square lattice we refer to [144]. Due to the large number of eight states per site $\{S_z = \pm\frac{1}{2}\} \otimes \{n = 0; n = 1(\tau_z = \pm\frac{1}{2}); n = 2\}$ in the KLU model only tiles with eight sites can be used (see inset of Fig. 10.1). This precludes also finite-size scaling such as may be performed in the one dimensional case [133, 145]. Furthermore as in Ref. [137], we restrict to the half filled case with the number of conduction electrons given by $n_c/N = 1$ ($N = 8$). Due to small cluster size (N) n_c can have only discrete values and therefore the next possible value $n_c/N = 3/4$ in the singlet spin sector is already far from the interesting half filled case.

As discussed before [137], one may choose both open and periodic boundary conditions for the tiles (OBC and PBC respectively). Their single particle spectrum differs greatly. While for PBC most of the states are put directly at the Fermi energy, giving little resemblance to the continuum DOS the spectrum is more realistic for OBC with more even distribution of energies (Fig. 10.1). It was shown in the case $U = 0$ [137] that this leads to a qualitatively different moment screening or singlet formation for small J_K. In this work we use exclusively OBC. Naturally, since there is a finite gap between occupied and unoccupied conduction electron states for half filling (Fig. 10.1), the true continuum behavior of the infinite Kondo lattice cannot be literally described, the numerical ED results presented in the following rather describe finite “Kondo molecules”. As mentioned in the introduction, they may in fact be artificially generated by adsorption of 3d clusters on nonmetallic surfaces. On the other hand, we will focus mostly on the local moment and on-site or nearest neighbor correlations. At least in the strong correlation limit ($U/t \gg 1$), it turns out that the local quantities obtained numerically for the eight-site cluster agree rather well with the infinite lattice results (Section 10.5).

10.3. Numerical determination of the local moment and thermodynamic properties

To determine the ground-state and thermodynamic properties of our system, we diagonalize the Hamiltonian iteratively on a small tile, applying the Lanczos algorithm. We also use the low-lying states and their energies to construct thermodynamic expectation values, in particular to calculate the partition function and its derivatives [91]. We stress that this unbiased method is exact and reliable for finite clusters and can therefore be used as a reference to compare with other numerical or analytical methods. We note that the large number of (eight) states per site prevents the use of larger clusters and the application of a finite-size scaling procedure such as described in detail in previous chapters for a two-dimensional $S = \frac{1}{2}$ model with just two states per site. Therefore, using the Lanczos method for the present model, one is limited to tiles with eight sites. Even then the largest subspace with total spin $S^z_{\text{tot}} = 0$ has dimension 739 162 (38 165 260 for $N = 10$ sites). Nevertheless, as the comparison with analytical results will show, the local moment and on-site correlations for the small tile give a realistic approximation to the extended Kondo

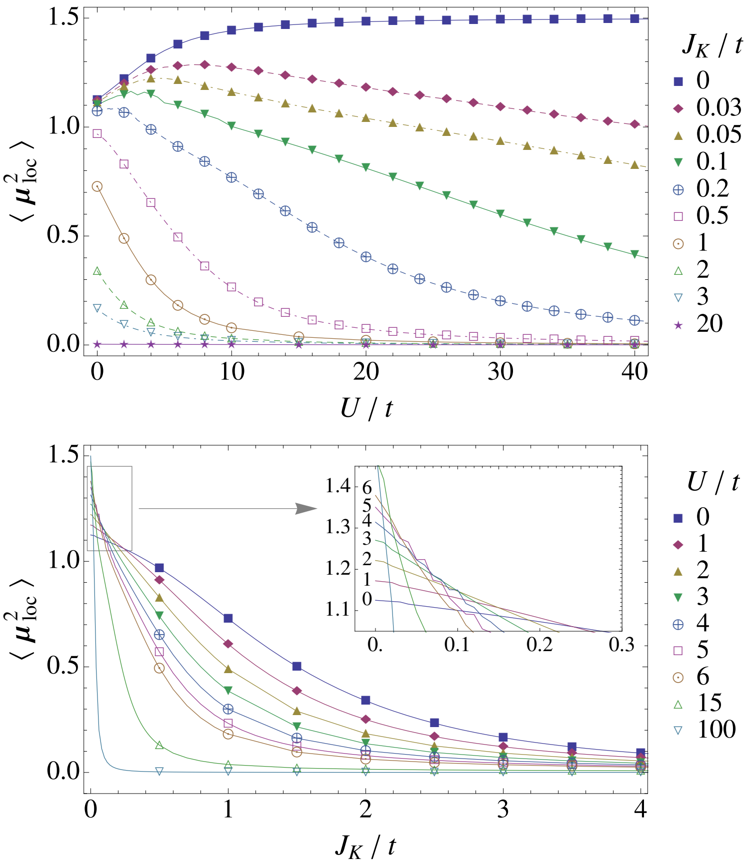

Figure 10.2.: (a) Effective paramagnetic total moment squared as function of U/t for various J_K/t. A flat maximum of the moment appears for weak Kondo coupling. (b) Corresponding variation of $\langle \mu^2_{\rm loc} \rangle$ as function of J_K/t for different U.

lattice behavior.

The total paramagnetic local moment is given by

$$\langle \mu^2_{\rm loc} \rangle = \left\langle \boldsymbol{S}_i^2 \right\rangle + \left\langle \boldsymbol{\tau}_i^2 \right\rangle + 2 \left\langle \boldsymbol{S}_i \cdot \boldsymbol{\tau}_i \right\rangle . \tag{10.2}$$

It contains the spin fluctuations of both the itinerant and localized spins and their antiferromagnetic on-site correlations due to the Kondo coupling. This is a central quantity for investigating the influence of correlations on the Kondo effect because the Coulomb repulsion U tends to localize the $\boldsymbol{\tau}$ spins and thus influences strongly their singlet formation with $\boldsymbol{S}$ spins. For the uncorrelated case ($U = 0$) it was shown previously that the on-site Kondo coupling also induces effective RKKY inter-site coupling between the localized spins. This mechanism is still present for non-zero U but it has to compete with the effective superexchange. Therefore, in addition to the total moment we will also investigate the on-site singlet correlation $S_{\mathrm{KS}} = \langle \boldsymbol{\tau}_i \cdot \boldsymbol{S}_i \rangle$ and nearest neighbor (i,j) correlation function $S_{ij} = \langle \boldsymbol{S}_i \cdot \boldsymbol{S}_j \rangle$. Due to the smallness of the cluster it is only reasonable to calculate it up to next nearest neighbors. The same would be true for the correlation function $\langle \boldsymbol{S}_i \cdot \boldsymbol{\tau}_j \rangle$ characterizing the "screening cloud" of a given localized spin $\boldsymbol{S}_i$ which is not evaluated here because its characteristic length scale is much larger than the cluster size. In the case of a single Kondo impurity in the continuum limit, it extends over a range of $\xi = v_F/T_K$ where v_F is the Fermi velocity and T_K the single ion Kondo temperature. Note however, that even in this simple case the screening cloud and its length scale ξ have not yet been observed in reality [146].

With the FTLM approach [91] it is possible to calculate the temperature dependence of various important thermodynamic quantities like specific heat $C(T) = N_A k_B \hat{C}(T)$ and uniform susceptibility $\chi(T) = N_A \mu_0 (g\mu_B)^2 \hat{\chi}(T)$ per mole as cumulants of simple operators, e. g.,

$$\begin{aligned} \hat{\chi}(T) &= \frac{1}{N}\frac{1}{k_{\mathrm{B}}T}\left[\left\langle (S^z_{\mathrm{tot}})^2 \right\rangle_T - \langle S^z_{\mathrm{tot}} \rangle^2_T \right] \\ S^z_{\mathrm{tot}} &= \sum_{i=1}^{N} (S^z_i + \tau^z_i) \\ \hat{C}(T) &= \frac{1}{N}\frac{1}{(k_{\mathrm{B}}T)^2}\left[\left\langle (H_{\mathrm{KLU}})^2 \right\rangle_T - \langle H_{\mathrm{KLU}} \rangle^2_T \right], \end{aligned} \tag{10.3}$$

where N_{A} is the Avogadro number, μ_0 is the magnetic permeability, μ_{B} and k_{B} are the Bohr magneton and the Boltzmann constant, g is the gyromagnetic ratio, and N is the size of our tiles (or number of sites). For simplicity, we assume the same gyromagnetic ratio for both the $\boldsymbol{\tau}$ and the $\boldsymbol{S}$ spins. The thermal expectation values are to be calculated with the statistical operator $\rho(T) = \exp(-\beta H_{\mathrm{KLU}})$, $\beta = 1/(k_{\mathrm{B}}T)$. In this work we restrict to zero magnetic field, and as we are working with a finite system size N, we can safely set $\langle S^z_{\mathrm{tot}} \rangle_T = 0$ in the first equation. Numerically, for each set of Hamiltonian parameters $\{t, U, J_{\mathrm{K}}\}$, the calculation of thermal averages involves two averaging procedures: First, a random starting wave function is chosen, and the Lanczos algorithm yields up to $\mathcal{O}(100)$ extremal eigenvectors and eigenvalues. Second, between 100 and 500 of these Lanczos runs with different starting wave functions are performed. All eigenvalues and eigenfunctions obtained in this way are subsequently used to calculate the traces over the statistical operator as indicated

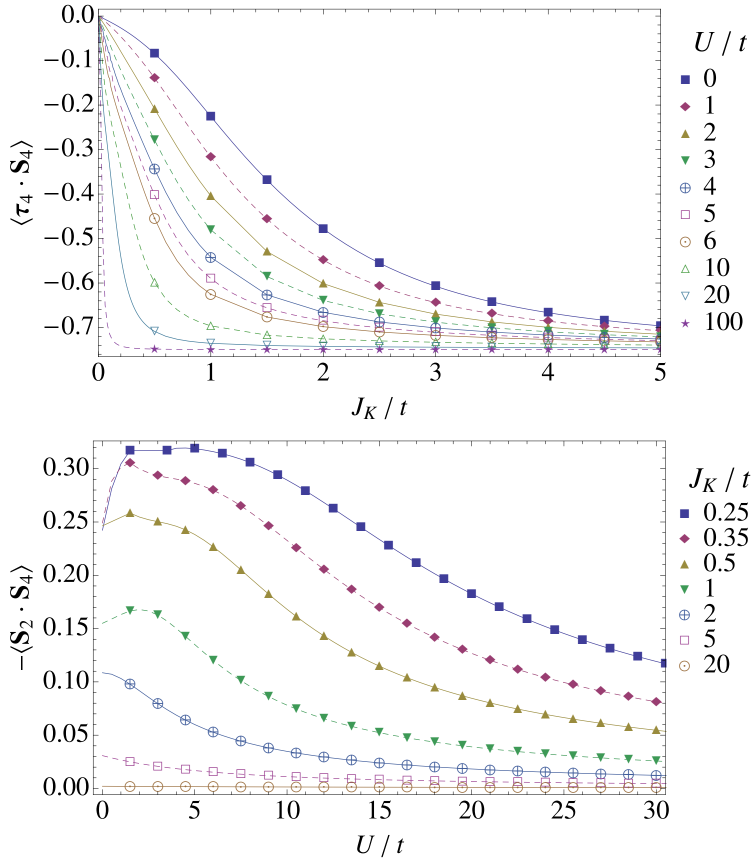

Figure 10.3.: (a) On-site Kondo-singlet formation between localized $\boldsymbol{S}$ and itinerant $\boldsymbol{\tau}$ spins as function of Kondo coupling, for various strengths of Coulomb repulsion. (b) Nearest neighbor antiferromagnetic correlations between localized spins as function of U/t for various Kondo coupling strengths. For $U = 0$ the nearest neighbor coupling is of induced RKKY type while for larger U it is dominated by the superexchange term.

in Eqs. 10.3, leading to the desired thermal expectation values. For details we refer to Ref. [91] and Chapter 4.

Although we do not consider the magnetization M (per site) of the correlated Kondo model explicitly, we may get some information about finite field properties by calculating the third-order susceptibility defined through the expansion

$$M = \chi \cdot B + \frac{1}{3!}\chi^{(3)} \cdot B^3 + \dots \tag{10.4}$$

for an applied magnetic field B. Here, $\chi^{(3)}(T) = (N_A\mu_0)(g\mu_B)^4\hat{\chi}^{(3)}(T)$ is given by a higher order cumulant according to

$$\hat{\chi}^{(3)}(T) = \frac{1}{N}\frac{1}{(k_{\mathrm{B}}T)^3}\left[\left\langle (S_z^{\mathrm{tot}})^4 \right\rangle_T - 3\left\langle (S_z^{\mathrm{tot}})^2 \right\rangle_T^2 \right]. \tag{10.5}$$

This quantity is a measure of the nonlinearity of magnetization at low field strength B. It has been discussed previously for a localized spin model [94] and plays a significant role in the discussion of some heavy fermion compounds [147].

10.4. Discussion of numerical results

First, we discuss results for the total local paramagnetic moment presented in Fig. 10.2a. Two counteracting trends determine its size: On one hand the increase in U localizes the $\boldsymbol{\tau}$-spins and leads to an increase of $\langle \boldsymbol{\tau}_i^2 \rangle$ from 3/8 for $U = 0$ to 3/4 for $U/t \gg 1$. On the other hand for finite J_K, the Kondo term establishes the antiferromagnetic on-site singlet correlation $\langle \boldsymbol{\tau}_i \cdot \boldsymbol{S}_i \rangle < 0$. Therefore, in the case J_K=0 the moment increases monotonically from $9/8 = 1.125$ to $2 \cdot (3/4) = 1.5$, while for any finite J_K in the large U limit when $\boldsymbol{\tau}_i$ becomes localized the moment will decrease due to singlet formation. For moderate J$_K$, there is an initial increase of $\langle \mu_{\mathrm{loc}}^2 \rangle$ with U due to the first correlation effect and eventually a decrease due to the effect of J_K when $\boldsymbol{\tau}$ spins become localized at larger U. In between a maximum in $\langle \mu_{\mathrm{loc}}^2 \rangle$ develops as function of U. For larger J$_K$, the singlet formation effect is so strong that it overwhelms the increase in $\langle \boldsymbol{\tau}_i^2 \rangle$ and therefore no maximum appears beyond J_K/t=0.1. This effect is completely dominated by local correlations and should not be strongly influenced by the tile size. The corresponding local moment dependence on J_K for various U is shown in Fig. 10.2b. For the uncorrelated $U = 0$ case the singlet formation leads to a continuous decrease of $\langle \mu_{\mathrm{loc}}^2 \rangle$ with J_K. Increasing U facilitates this formation due to the localization of $\boldsymbol{\tau}$ spins and the decrease becomes progressively steeper as function of J_K. In the limit $U \to \infty$ an arbitrary small J_K will lead to the singlet ground-state.

The singlet formation may also be monitored directly by the on-site correlation $\langle \boldsymbol{\tau}_i \cdot \boldsymbol{S}_i \rangle$ which is shown in Fig. 10.3a. Starting from zero at $J_K = 0$, it becomes increasingly antiferromagnetic for growing J_K until the singlet value $-3/4$ is reached. Again the latter is approached more rapidly with increasing correlation strength U. The nearest neighbor induced antiferromagnetic spin correlations are presented in Fig. 10.3b. For $U = 0$ these correlations are of the induced RKKY type [137]. They decrease with increasing J_K, because their evolution is impeded by the increasing singlet formation. For a fixed but small J_K the antiferromagnetic inter-site correlation first increases for small U due to the reduction of single and double occupancies and for larger U it falls off again due to the reduction of the superexchange $4t^2/U$ with increasing U. For larger J_K this effect is more pronounced as function of U.

A recurrent topic in previous analytical theories of the correlated Kondo impurity model is the U-dependence of the Kondo energy scale. From a practical viewpoint, it is frequently taken as the maximum position T^* of magnetic specific heat or susceptibility which corresponds to an average singlet-triplet excitation energy. In the present context of finite size tiles the U or J_K dependence of the characteristic temperature scale T^* can be conveniently obtained from the FTLM results according to Eq. 10.3 for both quantities. Although it is not identical to the single ion Kondo temperature T_K of the impurity model one may expect a comparable qualitative dependence on U or J_K.

The contour plot of $C_V(T)$ in the T - U plane is shown in Fig. 10.4 for $J_K/t = 0, 2$ respectively. The former corresponds to the case of the pure Hubbard model. It illustrates that the high temperature peak at $U = 0$ due to uncorrelated charge fluctuations splits into a lower temperature spin fluctuation peak associated with $J = 4t^2/U$ and a broad continuum at very high temperatures. The charge fluctuation peak at $U = 0$ correspond to the excitation energy of $\approx 0.75\,t$ between the highest occupied and lowest unoccupied states around $\epsilon = 0$ in Fig. 10.1. The behavior as function of U may be viewed as a precursor of the thermodynamic Mott-Hubbard transition for a finite tile size. When J_K is turned on the specific heat peak is dominated by the lowest singlet triplet excitation energies. It increases linearly for small U (bottom panel of Fig. 10.4) and reaches a plateau around $U \approx 6\,t$ corresponding to the highest excitation energies in Fig. 10.1.

To get rid of the influence of charge fluctuations we also calculated the spin susceptibility with FTLM. The results are presented in Figs. 10.5 and 10.6 as function of J_K, U respectively. In the former, the top panel shows a contour plot of the evolution of susceptibility maximum or Kondo temperature scale T^* (black dots) as function of J_K for constant $U/t = 4$. For comparison the T^* maxima for the uncorrelated $U = 0$ Kondo lattice tile are also given in the lower panel of Fig. 10.5 by crosses. In both cases T^* increases linearly with J_K in the strong coupling limit $J_K/t \gg 1$. For small J_K the values for $U = 0$ are considerably below the results for finite U which indicates the increase of the Kondo temperature scale T^* with U. This is also seen

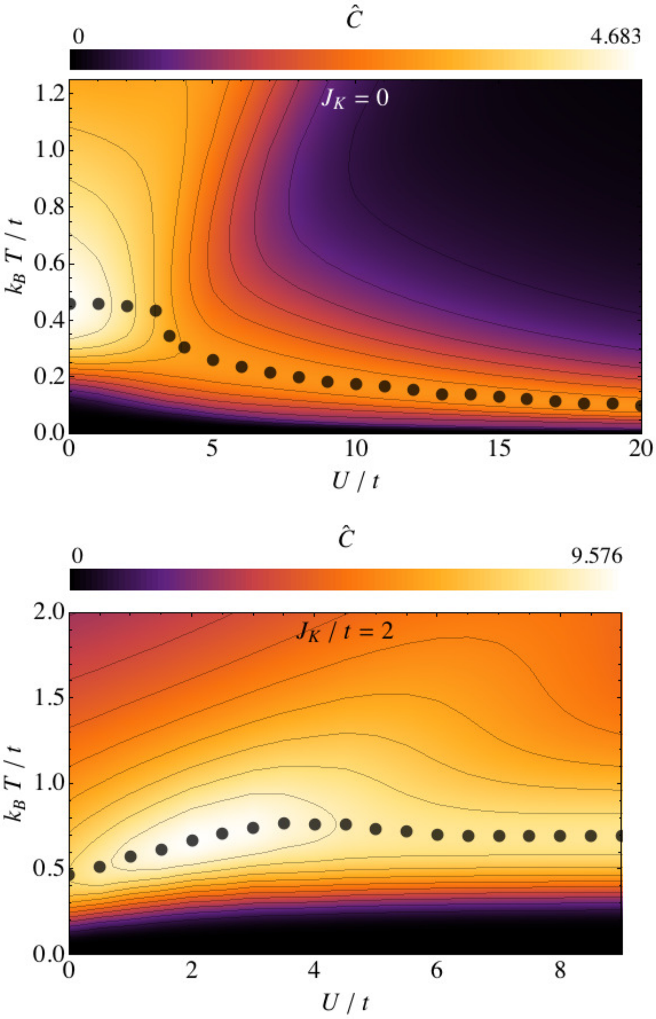

Figure 10.4.: Specific heat from FTLM as function of temperature and interaction strength U. Top: for the eight site Hubbard tile ($J_K = 0$) the $C(T) = N_A k_B \hat{C}(T)$ evolution as function of U shows the splitting of charge and spin fluctuation peaks (upper and lower peaks respectively) for $U > 4t \approx W/2$ ($W = 8\,t$ is the total bandwidth). Bottom: for finite J_K the $U = 0$ peak defines the Kondo temperature scale due to singlet formation. It increases with U until it reaches a plateau for $U > 4t$.

directly in Fig. 10.6 where T^* (black dots) can be seen to increase linearly with U for small U and reach a plateau for $U > 6\,t$ similar as for the specific heat peak before. In that figure, we also included the peak position of the third order susceptibility $\hat{\chi}^{(3)}(T)$ (white dots) which also increases with U. This quantity is experimentally

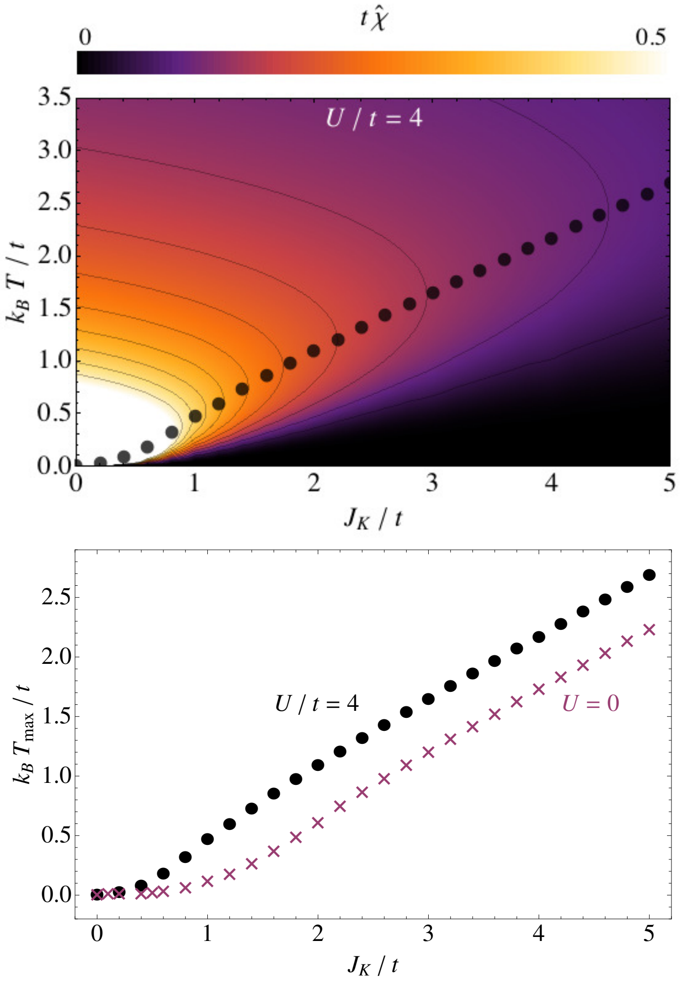

Figure 10.5.: Susceptibility from FTLM as function of temperature and Kondo coupling J_K. Top: contour plot of dimensionless $t\hat{\chi}(T, J_K)$. The maximum (black dots) defines the Kondo temperature scale T^* of singlet formation for $U/t = 4$. It increases monotonically with J_K. Bottom: for comparison T^* for the non-interacting ($U = 0$) case is shown by white crosses demonstrating the increase of T^* with U.

accessible [147]. It peaks at a systematically lower temperature than the first order susceptibility. The reason is that it characterizes the strongest nonlinear increase of the local moment with field which happens precisely in the temperature region where the screened local moment and susceptibility at zero field drops to zero (see Fig. 10.6). For comparison the size of the spin gap from analytical calculation in the large U limit (Eq. 10.13) shown by white crosses is seen to be sandwiched between

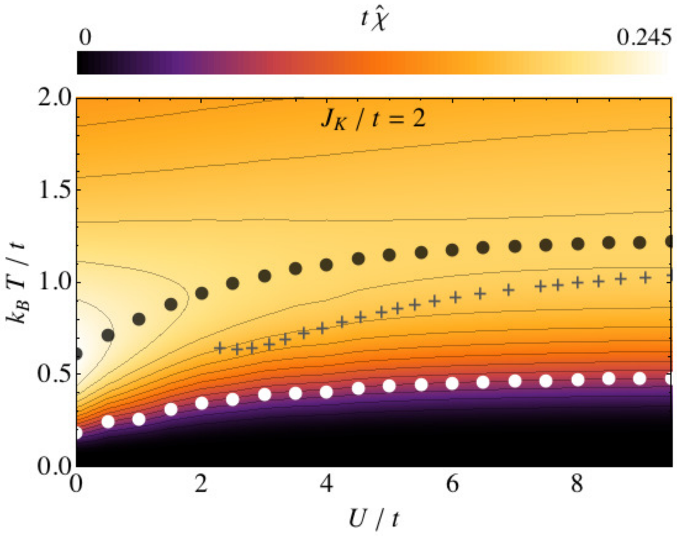

Figure 10.6.: Susceptibility in (T, U) plane for fixed J_K. The Kondo temperature scale (black dots) increases first linearly with U and then reaches a plateau qualitatively similar to the specific heat result in Fig. 10.4. For comparison we also show the temperature of the $\chi^{(3)}(T)$ maximum (white dots) and the triplon gap Δ_t (Eq. 10.13) of the large-U Kondo necklace model (black crosses).

the above FTLM values for the first order (black dots) and third order (white dots) susceptibility peak positions.

10.5. Bond operator treatment of the strongly correlated "Kondo necklace" limit

A deeper insight into the phases and excitations of low-dimensional quantum magnets requires the application of both numerical and analytical techniques. As demonstrated e. g. by the spin-wave analysis of the frustrated two-dimensional spin systems (Chapters 1-9, and Ref. [144] and references cited therein) analytical results for the extended system, even if approximate or only available in limiting cases, are very helpful to understand the systematics of numerical ED results for finite clusters. It is therefore perfectly legitimate to proceed in a similar way for Kondo lattice models. Because we focus on the paramagnetic phase, we will however use the bond operator approach as the appropriate analytical technique for comparison in the large U limit.

In the following we will derive such analytical results in the limit of large conduction electron correlations ($U \gg 2zt$, $z = 4$ is the coordination number) at half filling ($n_c = 1$). In this case, the charge fluctuations may be eliminated from the hopping and Hubbard terms leading to a pure exchange term of the now also localized conduction electron spins $\boldsymbol{\tau}_i$. Thus, the appropriate large U limit of the model in Eq. 10.1 is a localized two-dimensional spin Hamiltonian [148] given by

$$H_{KN} = J \sum_{\langle ij \rangle} \boldsymbol{\tau}_i \cdot \boldsymbol{\tau}_j + J_K \sum_i \boldsymbol{\tau}_i \cdot \boldsymbol{S}_i. \tag{10.6}$$

Here, the kinetic hopping term in Eq. 10.1 is replaced by an effective inter-site spin exchange $J = 4t^2/U$ in the strong correlation limit of conduction electrons. The above Hamiltonian is of the generalized “Kondo-necklace” type (in two-dimensions) originally studied for one-dimensional chains with only the xy inter-site terms included [149]. It has, however, later been extended to higher dimension and including all components in the intra- and inter-site exchange with possible uniaxial anisotropies for both [139–141]. The model may also be viewed as an asymmetric bilayer Heisenberg model [150] with $\boldsymbol{\tau}_i$ and $\boldsymbol{S}_i$ spins residing on different layers and only the former coupled by inter-site exchange J. These are generic models to describe quantum phase transitions between a singlet (“Kondo”) phase favored by the second term and an antiferromagnetically ordered phase favored by the first term. The transition occurs when the control parameter J/J_K is larger than the value $(J/J_K)_c$ defining the Quantum Critical Point (QCP). In two-dimensions, we have in the present isotropic model $(J/J_K)_c = 0.88$ [140, 141]. Such transitions are frequently found in f-electron compounds where the control parameter may be varied by pressure or doping (i. e. chemical pressure). The above model allows to study the characteristic quantum critical behavior around the QCP disregarding the charge fluctuations. It has been investigated using numerical methods like Monte Carlo (MC) simulations [151, 152], exact diagonalization methods [136] and dynamical mean field theory (DMFT) and also analytical methods like bond operator approach in mean field [139–141] or hard-core boson treatment [153]. In this approach the Kondo necklace Hamiltonian in Eq. 10.6 is mapped to a model of interacting singlet (s) and triplet ($t_\alpha, \alpha = x, y, z$) bosons by the bond-operator transformation [154]. These bosons describe the singlet and triplet states $|s\rangle = s^\dagger|0\rangle$ and $|t_\alpha\rangle = t_\alpha^\dagger|0\rangle$ ($\alpha = x, y, z$) of the pair of spins ($\boldsymbol{\tau}_i, \boldsymbol{S}_i$) coupled by J_K at every site

i. In terms of bosonic operators the spins are given by

$$\begin{aligned} S_{i,\alpha} &= \frac{1}{2}(s_i^\dagger t_{i,\alpha} + t_{i,\alpha}^\dagger s_i - i\epsilon_{\alpha\beta\gamma} t_{i,\beta}^\dagger t_{i,\gamma}) \\ \tau_{i,\alpha} &= \frac{1}{2}(-s_i^\dagger t_{i,\alpha} - t_{i,\alpha}^\dagger s_i - i\epsilon_{\alpha\beta\gamma} t_{i,\beta}^\dagger t_{i,\gamma}), \end{aligned} \tag{10.7}$$

where $\alpha, \beta, \gamma = x, y, z$ and $\epsilon_{\alpha\beta\gamma}$ is the totally antisymmetric tensor. The conventional spin and boson commutation rules are fulfilled. The restriction to physical states (only one boson per site) is expressed by the constraint $s_i^\dagger s_i + \sum_\alpha t_{i,\alpha}^\dagger t_{i,\alpha} = 1$ which may be implemented either on the mean field level or by hard core boson technique. The former is chosen here.

10.5.1. Ground-state energy and triplon excitations

In mean field approximation the bond operator transformation leads to a bilinear bosonic Hamiltonian

$$\begin{aligned} H_{\mathrm{KN}}^{\mathrm{MF}} &= \sum_{\mathbf{k},\alpha} \left(\frac{1}{2} J\bar{s}^2 \gamma_{\mathbf{k}} + \frac{1}{4} + \mu \right) t_{\mathbf{k},\alpha}^\dagger t_{\mathbf{k},\alpha} + \\ &\quad \sum_{\mathbf{k}} \frac{1}{4} J\bar{s}^2 \gamma_{\mathbf{k}} \left(t_{\mathbf{k},\alpha}^\dagger t_{-\mathbf{k},\alpha}^\dagger + t_{\mathbf{k},\alpha} t_{-\mathbf{k},\alpha} \right), \end{aligned} \tag{10.8}$$

where μ is the chemical potential introduced to ensure the constraint and $\bar{s} = \langle s \rangle$ is the mean field singlet amplitude. Furthermore, we define $t_{\mathbf{k}\alpha} = \frac{1}{\sqrt{N}} \sum_i \exp(i\mathbf{k} \cdot \mathbf{R}_n) t_{i\alpha}$ and $\gamma_{\mathbf{k}} = (\cos k_x + \cos k_y)$. Here, we restrict to the nonmagnetic phase where the triplet amplitude $\bar{t} \equiv 0$. In this case $\bar{s}$ is always close to one. This Hamiltonian may be diagonalized by the Bogoliubov transformation

$$\begin{aligned} a_{\mathbf{k},\alpha} &= \cosh(\phi_{\mathbf{k}}) t_{\mathbf{k},\alpha} + \sinh(\phi_{\mathbf{k}}) t_{-\mathbf{k},\alpha}^\dagger \\ a_{-\mathbf{k},\alpha}^\dagger &= \sinh(\phi_{\mathbf{k}}) t_{\mathbf{k},\alpha} + \cosh(\phi_{\mathbf{k}}) t_{-\mathbf{k},\alpha}^\dagger, \end{aligned} \tag{10.9}$$

with

$$\begin{aligned} \tanh(2\phi_{\mathbf{k}}) &= \frac{2f_{\mathbf{k}}}{d_{\mathbf{k}}} \\ f_{\mathbf{k}} &= \frac{1}{4} J\bar{s}^2 \gamma_{\mathbf{k}} \\ d_{\mathbf{k}} &= \mu + \frac{1}{4} J_K + \frac{1}{2} J\bar{s}^2 \gamma_{\mathbf{k}}. \end{aligned} \tag{10.10}$$

Diagonalization leads to the bosonic triplon Hamiltonian

$$
\begin{aligned}
H_{\mathrm{KN}}^{\mathrm{MF}} &= E_0 + \sum_{\mathbf{k}} \sum_{\alpha=x,y,z} \omega_{\mathbf{k}} a_{\mathbf{k},\alpha}^{\dagger} a_{\mathbf{k},\alpha} \\
\frac{E_0}{N} &= \left(\mu(\bar{s}^2-1) - \frac{3}{4} J_K \bar{s}^2\right) + \frac{3}{2N} \sum_{k} (\omega_{\mathbf{k}} - d_{\mathbf{k}}) \\
\omega_{\mathbf{k}} &= \sqrt{d_{\mathbf{k}}^2 - 4 f_{\mathbf{k}}^2},
\end{aligned} \tag{10.11}
$$

where $\omega_{\mathbf{k}}$ is the threefold degenerate ($\alpha = x, y, z$) triplon dispersion and $E_0(\mu, \bar{s})$ the ground-state energy. Minimization of the latter leads to self-consistency equations for the chemical potential μ and singlet amplitude $\bar{s}$ given by

$$
\begin{aligned}
\frac{3}{2N} \sum_{\mathbf{k}} \frac{d_{\mathbf{k}}}{\omega_{\mathbf{k}}} &= \frac{5}{2} - \bar{s}^2 \\
\frac{3J}{2N} \sum_{\mathbf{k}} \frac{d_{\mathbf{k}} - 2 f_{\mathbf{k}}}{\omega_{\mathbf{k}}} \gamma_{\mathbf{k}} &= \frac{3}{2} J_K - 2\mu.
\end{aligned} \tag{10.12}
$$

The smooth dependence of μ and $\bar{s}$ on the control parameter J_K/J is shown in the inset of Fig. 10.7. It also extends continuously across the QCP into the antiferromagnetic region [141].

The bond operator method also gives an explicit expression for the singlet-triplet gap which is defined as $\Delta_t = \omega_{\mathbf{Q}}$ with $\mathbf{Q} = (\pi, \pi)$ [140]. Using Eqs. 10.10 and 10.11 and setting $J = 4t^2/U$ we obtain

$$
\Delta_t = \left(\mu + \frac{1}{4} J_K\right) \left[1 - 2 \frac{8 t^2 \bar{s}^2}{U(\mu + \frac{1}{4}) J_K}\right]^{\frac{1}{2}}. \tag{10.13}
$$

This expression for the gap may be compared to the Kondo temperature scale T^* from the susceptibility maximum obtained in FTLM finite cluster calculations.

10.5.2. The paramagnetic effective local moment

In the numerical calculation the central quantity in the correlated Kondo model is the local paramagnetic moment $\langle \mu_{\mathrm{loc}}^2 \rangle$, which is a direct measure of the singlet formation as function of J_K/t and U/t. This also extends to the large U limit where the local moment may be calculated analytically within bond operator approach. To gain a better understanding of the numerical results, a comparison with the an-

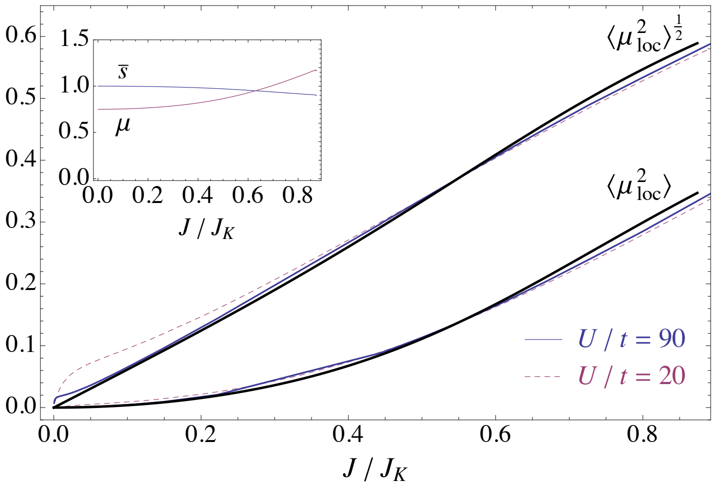

Figure 10.7.: Paramagnetic local moment and its square in the large U-limit as function of J/J_K where $J = 4t^2/U$. Thick line gives the result of bond operator theory. Thin and broken line are ED results for the eight site cluster in the large U limit. The good agreement suggests that finite-size effects for the local moments are small. The inset shows the dependence of singlet amplitude $\bar{s}$ and chemical potential μ in mean field bond operator theory (Section 10.5).

alytical method for large U is helpful. In spirit this is similar to the comparison of ED results for the $J_1 - J_2$ Heisenberg model with analytical spin-wave calculations (Chapter 3). The elementary excitations here are, however, gapped triplon modes in the paramagnetic ("Kondo singlet") regime rather than spin-waves in the antiferromagnetic broken symmetry state.

First, we transform the expression for $\langle \mu_{\rm loc}^2 \rangle$ given in Eq. 10.2 to bond operator basis. Using the defining relations in Eq. 10.7 with $\theta_\alpha = \frac{1}{2}\left(\mathbf{t}^\dagger \times \mathbf{t}\right)_\alpha$ we derive the operator identity

$$\begin{aligned} \mu_{loc}^2 &= 4\sum_\alpha \theta_\alpha^\dagger \theta_\alpha \\ \langle \mu_{loc}^2 \rangle &= 12 \langle \theta_x^\dagger \theta_x \rangle, \end{aligned} \tag{10.14}$$

where we used the spin-space isotropy or degeneracy of triplon modes for the expectation value. Using the explicit expressions for θ_α, defining $u_{\mathbf{k}} = \cosh(\phi_{\mathbf{k}})$, $v_{\mathbf{k}} = \sinh(\phi_{\mathbf{k}})$ and performing a Fourier transformation, we obtain a concise form of the moment:

$$\frac{1}{6}\langle\mu_{loc}^2\rangle = \big(\frac{1}{N}\sum_{\mathbf{k}} v_{\mathbf{k}}^2\big)\big(\frac{1}{N}\sum_{\mathbf{k}} u_{\mathbf{k}}^2\big) - \big(\frac{1}{N}\sum_{\mathbf{k}} u_{\mathbf{k}}v_{\mathbf{k}}\big)^2. \tag{10.15}$$

The positiveness of the moment squared is ensured by Cauchy–Schwarz inequality. Using Eq. 10.10 we can write

$$\begin{aligned} u_{\mathbf{k}}^2 &= \frac{1}{2}\left(\frac{d_{\mathbf{k}}}{\omega_{\mathbf{k}}}+1\right) \\ v_{\mathbf{k}}^2 &= \frac{1}{2}\left(\frac{d_{\mathbf{k}}}{\omega_{\mathbf{k}}}-1\right) \\ u_{\mathbf{k}}v_{\mathbf{k}} &= \frac{f_{\mathbf{k}}}{\omega_{\mathbf{k}}} \\ u_{\mathbf{k}}^2+v_{\mathbf{k}}^2 &= \frac{d_{\mathbf{k}}}{\omega_{\mathbf{k}}}. \end{aligned} \tag{10.16}$$

Inserting these explicit expressions into Eq. 10.15 we obtain the final result for the paramagnetic moment as

$$\langle\mu_{loc}^2\rangle = \frac{3}{2}\left[\frac{1}{N}\sum_{\mathbf{k}}\left(\frac{d_{\mathbf{k}}+2f_{\mathbf{k}}}{d_{\mathbf{k}}-2f_{\mathbf{k}}}\right)^{\frac{1}{2}}\frac{1}{N}\sum_{\mathbf{k}}\left(\frac{d_{\mathbf{k}}-2f_{\mathbf{k}}}{d_{\mathbf{k}}+2f_{\mathbf{k}}}\right)^{\frac{1}{2}}-1\right], \tag{10.17}$$

where $d_{\mathbf{k}}$ and $f_{\mathbf{k}}$ are defined in Eq. 10.10. From this closed expression the moment may be obtained by the two-dimensional momentum integration.

It is worthwhile to consider the expression of $\langle\boldsymbol{\mu}_{loc}^2\rangle$ in the strong Kondo coupling limit $J/J_K \ll 1$ (or $4t^2/UJ_K \ll 1$). We define $\epsilon_{\mathbf{k}} = 2f_{\mathbf{k}}/d_{\mathbf{k}}$ and use $\omega_{\mathbf{k}} = d_{\mathbf{k}}\sqrt{1-\epsilon_{\mathbf{k}}^2}$. Expanding Eq. 10.2 in terms of $\epsilon_{\mathbf{k}}$ we get

$$\langle\mu_{loc}^2\rangle = \frac{3}{2}\left[\frac{1}{N}\sum_{\mathbf{k}}\epsilon_{\mathbf{k}}^2 - \left(\frac{1}{N}\sum_{\mathbf{k}}\epsilon_{\mathbf{k}}\right)^2\right], \tag{10.18}$$

which may be further evaluated to give

$$\langle\mu_{loc}^2\rangle = \frac{3}{8}\left(\frac{\bar{s}^2 J}{\mu+\frac{1}{4}J_K}\right)^2 = \frac{3}{8}\left(\frac{4t^2\bar{s}^2}{U(\mu+\frac{1}{4}J_K)}\right)^2. \tag{10.19}$$

Where in the last expression we replaced $J = 4t^2/U$. This equation demonstrates that the local moment is decreasing with increasing J_K (note that μ and $\bar{s}$ also depend on J_K/J) and with increasing correlation U. This is what the full numerical calculation of Eq. 10.17 discussed below indeed confirms.

10.5.3. Spin correlations and high temperature susceptibility

To obtain a more detailed insight into the Kondo singlet formation and the influence of Coulomb correlations on it we have previously also calculated the evolution of on-site spin correlations in the ED approach. It is desirable to calculate them with bond operator approximation in large U limit for comparison with numerical results. We consider the on-site spin correlation function $S_{\mathrm{KS}}(i) = \langle \boldsymbol{\tau}_i \cdot \boldsymbol{S}_i \rangle$ between localized and itinerant spins and also the complementary partial local moments $\langle \boldsymbol{\tau}_i^2 \rangle$ and $\langle \boldsymbol{S}_i^2 \rangle$. Transforming to bond operator representation and using the isotropy we obtain

$$\begin{aligned} S_{\mathrm{KS}}(i) &= \frac{1}{4}\left[\langle \mu_{loc}^2 \rangle - 3\bar{s}^2 \langle (t_{ix} + t_{ix}^\dagger)^2 \rangle\right] \\ \langle \boldsymbol{\tau}_i^2 \rangle = \langle \boldsymbol{S}_i^2 \rangle &= \frac{1}{4}\left[\langle \mu_{loc}^2 \rangle + 3\bar{s}^2 \langle (t_{ix} + t_{ix}^\dagger)^2 \rangle\right]. \end{aligned} \tag{10.20}$$

The equality $\langle \boldsymbol{\tau}_i^2 \rangle = \langle \boldsymbol{S}_i^2 \rangle$ is only valid in the localized limit but does not hold in the original KLU model defined in Eq. 10.1 for small U. The site index i is suppressed i. f. because these local quantities are uniform. Expressing the triplet operators t_x and $t_x^\dagger$ in terms of triplon eigenmodes by using Eq. 10.9 this leads to

$$\langle (t_x + t_x^\dagger)^2 \rangle = \frac{1}{N} \sum_{\mathbf{k}} (u_{\mathbf{k}} + v_{\mathbf{k}})^2. \tag{10.21}$$

From Eq. 10.16 we finally obtain

$$\begin{aligned} S_{\mathrm{KS}} &= \frac{1}{4}\left[\langle \mu_{loc}^2 \rangle - 3\bar{s}^2 \frac{1}{N} \sum_{\mathbf{k}} \left(\frac{d_{\mathbf{k}} + 2f_{\mathbf{k}}}{d_{\mathbf{k}} - 2f_{\mathbf{k}}}\right)^{\frac{1}{2}}\right] \\ \langle \boldsymbol{\tau}_i^2 \rangle = \langle \boldsymbol{S}_i^2 \rangle &= \frac{1}{4}\left[\langle \mu_{loc}^2 \rangle + 3\bar{s}^2 \frac{1}{N} \sum_{\mathbf{k}} \left(\frac{d_{\mathbf{k}} + 2f_{\mathbf{k}}}{d_{\mathbf{k}} - 2f_{\mathbf{k}}}\right)^{\frac{1}{2}}\right]. \end{aligned} \tag{10.22}$$

If we take the sum of these expression according to Eq. 10.2, one obtains again the total local moment.

The total moment in the large-U (localized spin) limit calculated in Section 10.5.2 is a zero-temperature quantity determined by quantum fluctuations in the ground-state. On the other hand, the effective moment of a localized spin system is obtained from the high-temperature behavior of the susceptibility. The latter may be calculated from a high-temperature expansion. In this section, we want to investigate how these effective moments are related and how well the high temperature expansion agrees with the FTLM results in the large-U limit.

First, we give the high-temperature expansion for the total local moment at finite temperature T:

$$\langle\mu_{\mathrm{loc}}^2\rangle(T) = \left\langle \boldsymbol{S}_i^2 \right\rangle_T + \left\langle \boldsymbol{\tau}_i^2 \right\rangle_T + 2\left\langle \boldsymbol{S}_i \cdot \boldsymbol{\tau}_i \right\rangle_T \,, \tag{10.23}$$

where

$$\langle\mathcal{A}\rangle_T = \frac{1}{\mathcal{Z}}\,\mathrm{Tr}\left(A\mathrm{e}^{-\beta H_{\mathrm{KN}}}\right), \quad \mathcal{Z} = \mathrm{Tr}\left(\mathrm{e}^{-\beta H_{\mathrm{KN}}}\right)$$

is the thermal expectation value of $\mathcal{A}$ formed with the Kondo necklace Hamiltonian. Expanding the statistical operator for large k_BT we obtain

$$\begin{aligned}\langle\mu_{\mathrm{loc}}^2\rangle(T) &= 2S(S+1)\left[1 - \frac{S(S+1)}{3}\frac{J_{\mathrm{K}}}{k_{\mathrm{B}}T} + \mathcal{O}\left(\frac{J_{\mathrm{K}}}{k_{\mathrm{B}}T}\right)^2\right] \\ &\equiv \hat{\mu}_{\mathrm{loc}}^2(T) + \mathcal{O}\left(\frac{J_{\mathrm{K}}}{k_{\mathrm{B}}T}\right)^2 . \end{aligned} \tag{10.24}$$

The prefactor is the paramagnetic moment of uncorrelated spins, where the factor 2 is due to the presence of two spins $\boldsymbol{\tau}$ and $\boldsymbol{S}$ per site with $\tau = S = \frac{1}{2}$. The parenthesis gives the first order high-temperature correction of the local moment which depends only on the local Kondo exchange J_{K}. Likewise we can calculate the high temperature uniform susceptibility, which was defined previously as

$$\hat{\chi}(T) = \frac{1}{N}\frac{1}{k_{\mathrm{B}}T}\left\langle \left(S_z^{\mathrm{tot}}\right)^2 \right\rangle_T , \tag{10.25}$$

where the same g-factor has been assumed for both $\boldsymbol{\tau}$- and $\boldsymbol{S}$-spins. Evaluating the thermal average in high-temperature approximation as before and using $\tau = S$ one obtains for the high temperature susceptibility

$$\begin{aligned}\hat{\chi}(T) &= \frac{1}{3}\frac{1}{k_{\mathrm{B}}T}2S(S+1)\left[1 - \frac{S(S+1)}{3}\frac{J_{\mathrm{K}}}{k_{\mathrm{B}}T} - \frac{S(S+1)}{3}\frac{zJ}{k_{\mathrm{B}}T}\right] \\ &\approx \frac{1}{3}\frac{1}{k_{\mathrm{B}}T} \times \langle\mu_{\mathrm{loc}}^2\rangle(T)\left[1 - \frac{S(S+1)}{3}\frac{zJ}{k_{\mathrm{B}}T}\right] . \end{aligned} \tag{10.26}$$

Formally, we can regard the last expression as the first two terms of a high-temperature expansion of a Curie–Weiss type susceptibility

$$\hat{\chi}(T) = \frac{\hat{\chi}_0(T)}{1 + \Theta/T} \tag{10.27}$$

with an effective noninteracting Curie susceptibility $\hat{\chi}_0(T)$ and a Weiss temperature Θ given, respectively by

$$\begin{aligned} \hat{\chi}_0(T) &= \frac{1}{3}\frac{1}{k_\mathrm{B}T}\,\hat{\mu}^2_\mathrm{loc}(T) \\ k_\mathrm{B}\Theta &= \frac{S(S+1)}{3}zJ, \end{aligned} \tag{10.28}$$

i. e. $k_\mathrm{B}\Theta = J$ for $S = \frac{1}{2}$ and $z = 4$. We write the high-temperature behavior of the susceptibility $\hat{\chi}(T)$ in this suggestive form to stress that the temperature dependent effective moment screening is due to the Kondo coupling J_K, and the Weiss temperature Θ due to the effective magnetic inter-site exchange J. One may conjecture that this expression may be valid beyond its formal expansion regime. This may be checked by comparing Eq. 10.26 with the unbiased FTLM results for $\hat{\chi}(T)$ and $\hat{\mu}^2_\mathrm{loc}(T)$.

10.6. Comparison with numerical results

It is an interesting question whether the previous analytical mean field results for the large U limit can be qualitatively compared to the numerical ED results for finite tiles in Section 10.4. The most obvious quantity to check this is $\langle\mu^2_\mathrm{loc}\rangle$. The comparison is shown in Fig. 10.7. The inset of this figure gives the dependence of μ and $\bar{s}$ on J/J_K as obtained from the self-consistent solution of Eq. 10.12 almost up to the quantum critical value $(J/J_K)_c = 0.88$ where the singlet-triplet spin gap vanishes and antiferromagnetic order would set in. We stay in the paramagnetic parameter range throughout this work. The antiferromagnetic region of the two-dimensional Kondo necklace region has been explored in Refs. [140, 141].

The main Fig. 10.7 shows the dependence of the local moment $\langle\mu^2_{loc}\rangle^{\frac{1}{2}}$ and its square on J/J_K from bond-operator mean field theory (full black line) and from numerical results for the eight site cluster model in the large U limit with $J = 4t^2/U$. Here, large U means large as compared to the tight binding bandwidth $W = 2zt = 8t$. The numerical results for various U/t in this limit are given as dashed lines. The agreement of analytical and numerical results is surprisingly good. This proves two points: First, the mean-field bond operator technique gives reliable on-site properties in the ground-state. This is in agreement with the observation [141] that values for $(J/J_K)_c$ that determine the quantum critical point between Kondo singlet and

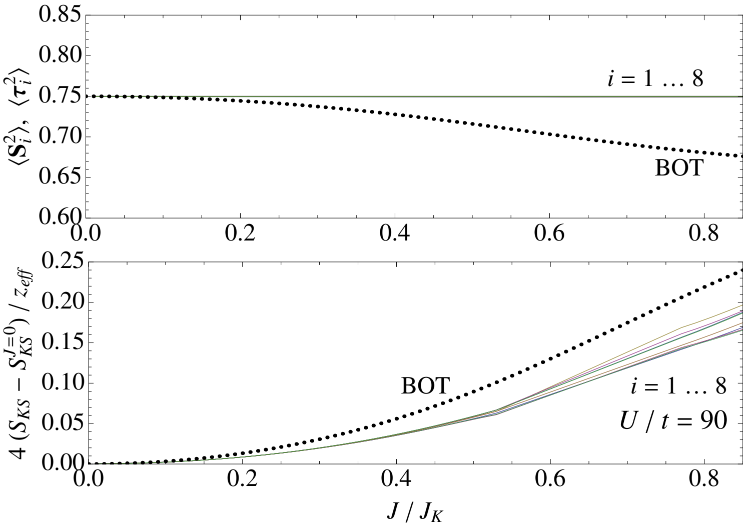

Figure 10.8.: Comparison of partial moments (top) and on-site antiferromagnetic correlations $S_{\mathrm{KS}}(i) = \langle \boldsymbol{\tau}_i \cdot \boldsymbol{S}_i \rangle$ (bottom) from ED (full lines) and bond operator theory (BOT) (dotted line). The results for S_{KS} have been scaled by the effective coordination number of a given cluster site ($z_{\mathrm{eff}} = 1..4$; for BOT $z_{\mathrm{eff}} = 4$). The deviations in both quantities have different signs and almost cancel in the total local moment $\langle \mu^2_{\mathrm{loc}} \rangle$(Fig. 10.7).

AF phase are well reproduced by that theory. Second, the agreement points to the fact that the numerical finite size effects on a local quantity like $\langle \mu^2_{\mathrm{loc}} \rangle$ are apparently quite moderate. Noticeable deviations in the numerical and analytical results appear at larger J/J_K when the quantum critical point to antiferromagnetic order is approached or when U/t becomes too small.

The comparison may also be made for the on-site spin correlation functions $S_{\mathrm{KS}}(i)$ and the partial moments $\langle \boldsymbol{\tau}^2 \rangle$ and $\langle \boldsymbol{S}^2 \rangle$ which are equal in the large U limit. The latter is shown in top panel of Fig. 10.8 with numerical results from ED giving the proper local moment value 3/4 and the results from bond operator theory lying below. Their difference increases with increasing J, i.e. decreasing U. On the other hand the on-site AF Kondo correlation presented in bottom panel of Fig. 10.8 shows the analytical result lying above the numerical ED value by a similar amount. The latter depends on the effective coordination number of the considered site in the finite cluster. The total moment $\langle \mu^2_{\mathrm{loc}} \rangle$ is the sum of these individual contributions and because of the opposite sign of the differences the add up to zero approximately.

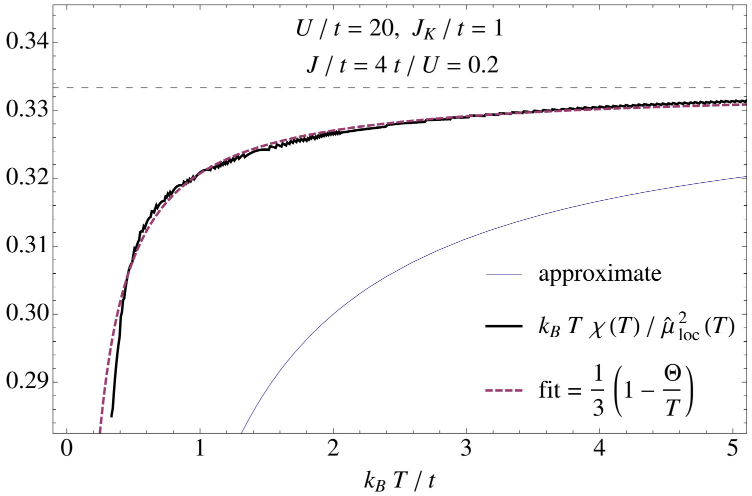

Figure 10.9.: Susceptibility and effective moment from FTLM (upper full line). Dashed line is obtained from high-temperature expansion formula using $k_B\Theta = 0.0379t$ as a fit parameter. It is considerably smaller than in Eq. 10.26 due to reduced coordination number in finite clusters. Lower full lines from high temperature expansion with Θ given by Eq. 10.28 using the approximate expression for $\chi(T)$ in Eq. 10.26.

This explains why numerical ED and analytical bond operator results for $\langle\mu^2_{\mathrm{loc}}\rangle$ in Fig. 10.7 agree so well despite the small cluster size.

Including the previous results [140, 141] on quantum critical properties of the Kondo necklace model we can conclude that the energetics and local correlations are well described by the mean field bond operator method but that the description of inter-site correlations and their U dependence is well beyond this approximation.

Finally, we come to the high-temperature expansion for local moment and susceptibility in the large U limit and its comparison to the FTLM results. According to Eq. 10.26 the ratio $T\chi(T)/\hat{\mu}^2_{\mathrm{loc}}(T)$ should be proportional to the Curie–Weiss factor in this equation. This comparison is shown in Fig. 10.9. It is seen that the result of the high-temperature expansion lies considerably below the curve obtained from FTLM. Part of this discrepancy may be due to the fact that in FTLM the effective (average) coordination number in the eight site tile is smaller than $z = 4$. Therefore, in order to compare with high-temperature expansion we may consider an effective Curie–Weiss temperature Θ_{eff} as fit parameter in Eq. 10.26. Then the temperature dependence of $\chi(T)$ from FTLM is well reproduced by the form of the high-temperature expansion results in Fig. 10.9.

10.7. Discussion and conclusion

In this work we investigated the local moment screening and spin correlations and in particular thermodynamic properties of the correlated Kondo lattice or Kondo-Hubbard model. We have focused primarily on the systematic dependence of local moment, spin correlations and susceptibility on the control parameters J_K and U, and then on the U-dependence of the characteristic temperature scale T^*. We used unbiased and exact numerical techniques like ED and FTLM for small tiles for the whole range of U/t and J_K/t as well as approximate analytical bond-operator method for the large U-limit of the extended Kondo necklace model which contains only localized spins. In this limit both methods give excellent agreement on the dependence of the Kondo-screened total paramagnetic local moment (Fig. 10.7) on U or $J = 4t^2/U$. Our ED and FTLM investigation may also be of particular relevance for finite nano-clusters of Kondo atoms adsorbed on surfaces.

A first central result obtained for smaller U and J_K is a clear non-monotonic behavior of $\langle \mu_{\text{loc}}^2 \rangle$ on correlation strength is observed in the ED results. This non-monotonic U-dependence is also observed in the on-site and inter-site spin correlations where the latter are of mixed RKKY and superexchange character. It is the result of competing effects of conduction electron localization by U and local singlet formation due to J_K.

The second central conclusion concerns the dependence of the Kondo temperature scale T^* on correlation strength U for which controversial results have been reported previously. Our FTLM susceptibility and the analytical results presented in Fig. 10.6 show that it increases monotonically with U and reaches a plateau in the large U limit. In this limit the Kondo scale corresponds to the spin-gap for triplon excitations at the antiferromagnetic wave vector $\mathbf{Q} = (\pi, \pi)$.

Furthermore, a high-temperature expansion for the susceptibility of the Kondo necklace model leads to an effective Curie–Weiss type expression, where the local susceptibility is modified only by the Kondo term and the Curie–Weiss temperature is only due to the superexchange term. The resulting temperature dependence is similar to that of FTLM results in the large U limit and if the effective Curie–Weiss temperature is used as a fit parameter a quantitative agreement over large temperature region is obtained.

XI. Summary

This work investigates in detail the physical properties of the frustrated quantum Heisenberg model on the square lattice with spatial anisotropy, together with the correlated Kondo lattice model. We have used the analytical linear spin-wave theory, to determine the classical ground-state as well as the effects of quantum fluctuations. The phase diagram of the system has been obtained, and the spin-wave spectra as well as the behavior of the magnetization and the ordered moment in the presence of magnetic field is studied. In addition, numerical exact diagonalization technique has been used to obtain the ground-state as well as the finite-temperature properties. Ground-state energy, as well as spin correlation functions and static structure factors are calculated using the Lanczos algorithm. A detailed finite-size scaling analysis of the ground-state properties is carried out, and a new method for selecting most compatible tilings of the infinite lattice, and the way to construct those is described thoroughly. We have shown that with choosing the most square tiles, we can successfully construct a stable finite-size scaling analysis in the ordered regions of the phase diagram. A detailed description of the quality of the scaling is given and is related to the magnetically disordered regions of the phase diagram. Furthermore, with the help of the random sampling algorithm, the temperature dependence of the magnetic susceptibility is obtained and used to characterize the exchange coupling constants of the copper pyrazine compound. Besides, we have demonstrated the rather strong effect of frustration over field dependence of the ordered moment, and used this behavior to propose a new method to determine the frustration ratio in this and similar compounds. We also studied the effects of anisotropy over the ordered moment, and show that it counter-intuitively stabilizes the ordered moment, hence it cannot be used to explain the observed low ordered moment in Fe-pnictides. Moreover, we investigated the correlated Kondo lattice model, which is a paradigm for the competition of singlet formation and magnetic order. The model is introduced and its ground-state as well as finite-temperature properties are obtained. The dependence of the Kondo temperature scale over the Coulomb repulsion U is examined. We report a new nonmonotonic dependence of the local moment on the correlation strength U. We also show that the Kondo temperature scale increases with U, resolving an existing controversy on this subject. We study the system both with exact diagonalization technique and the bond operator theory, and show that these two methods agree very well on the calculation of the local moment in the large U limit.

A. Appendix

A.1. Listing of tiles

Here we present the actual geometry of most square tiles having area size N between 8 and 36, corresponding to Table 5.2. Each sites is (arbitrary) labeled by a number, and periodic boundary condition has been used to map the sites outside the tile back again into the actual tiling.

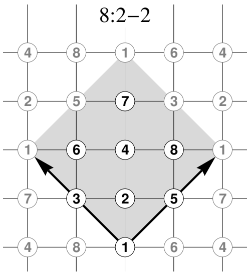

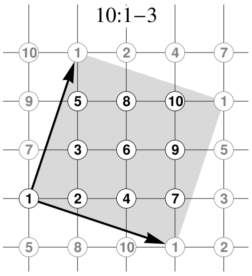

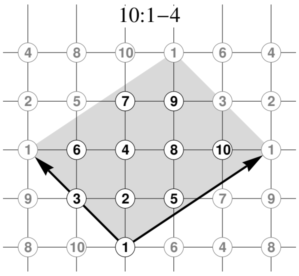

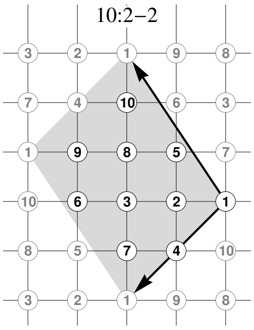

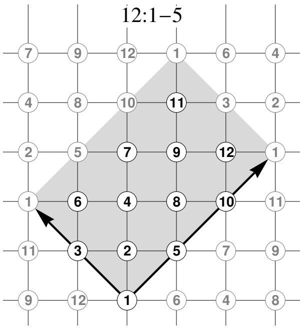

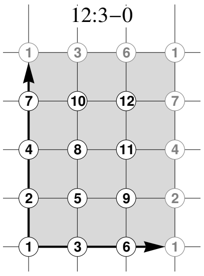

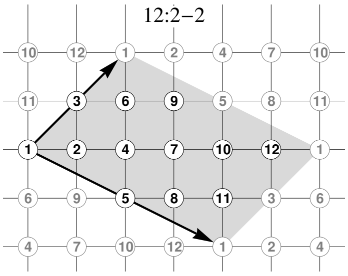
12:2−2

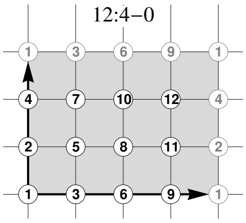
12:4−0

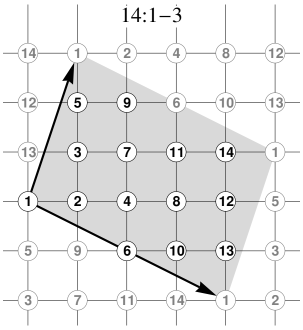
14:1−3

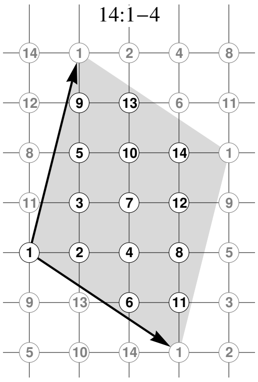
14:1−4

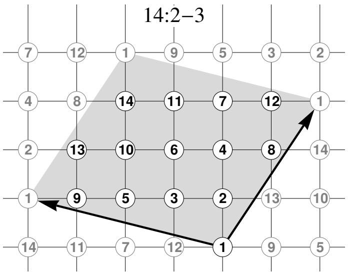
14:2−3

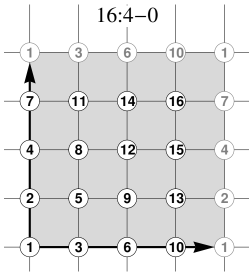
16:4−0

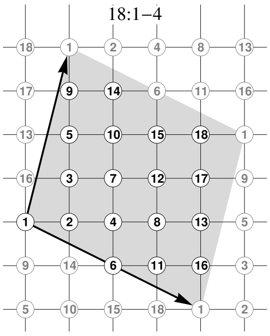
18:1−4

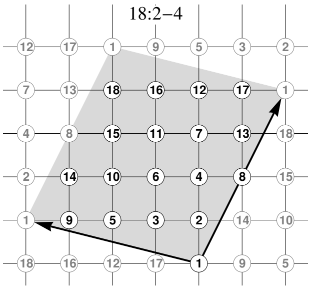
18:2−4

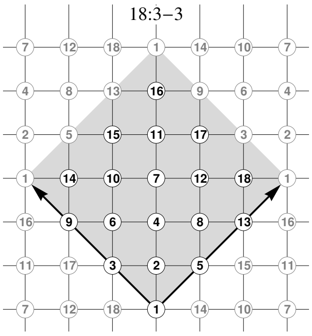
18:3−3

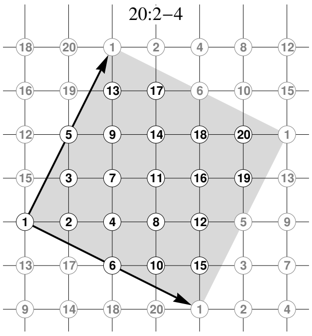
20:2−4

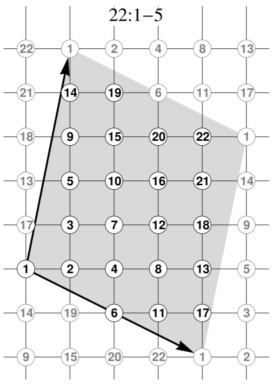
22:1−5

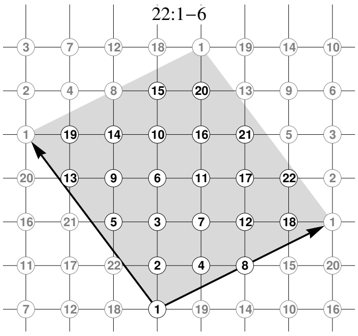
22:1−6

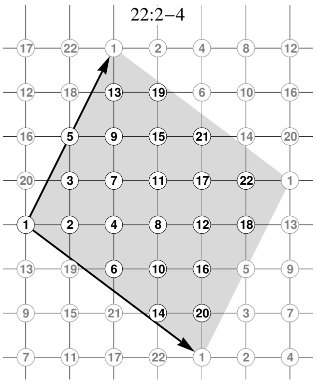
22:2−4

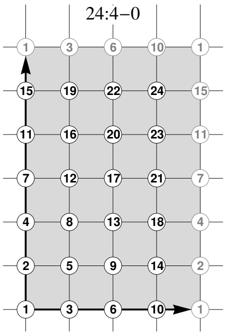
24:4−0

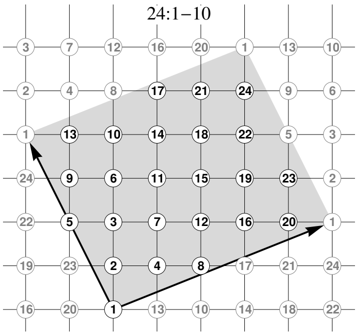
24:1−10

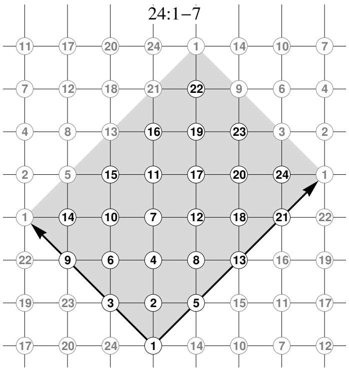
24:1−7

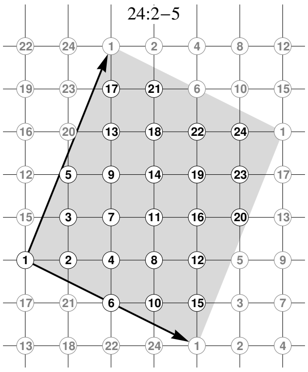
24:2−5

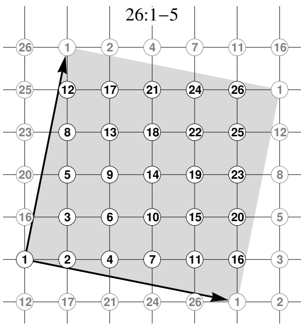
26:1−5

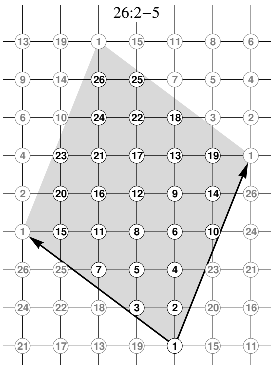
26:2−5

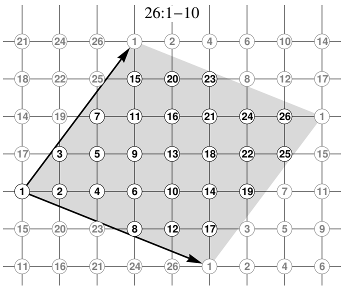
26:1−10

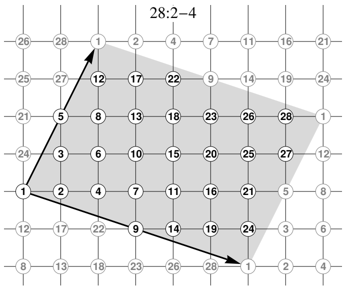
28:2−4

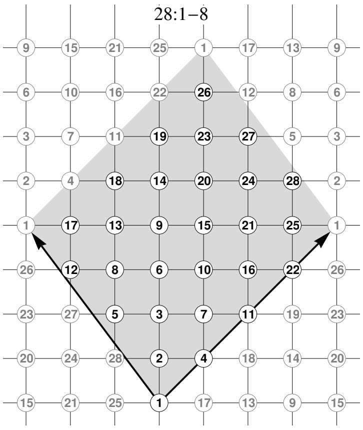
28:1−8

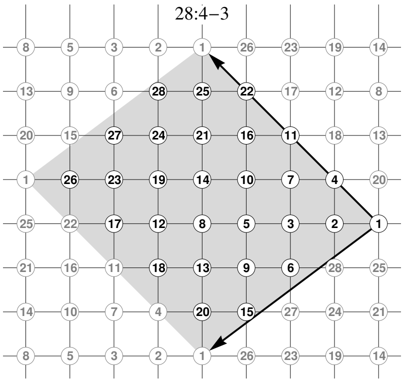
28:4−3

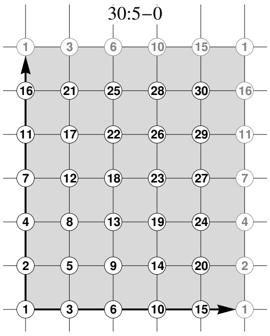
30:5−0

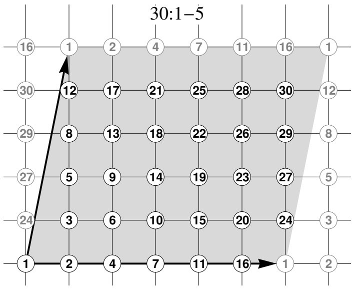
30:1−5

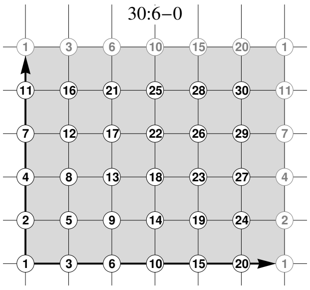
30:6−0

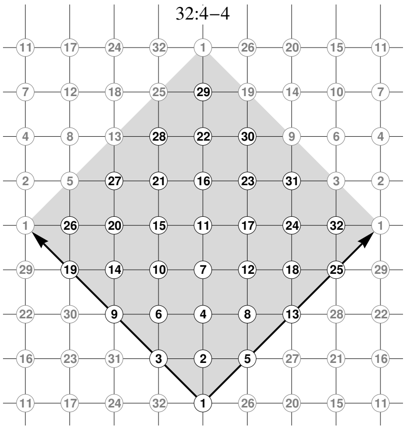
32:4−4

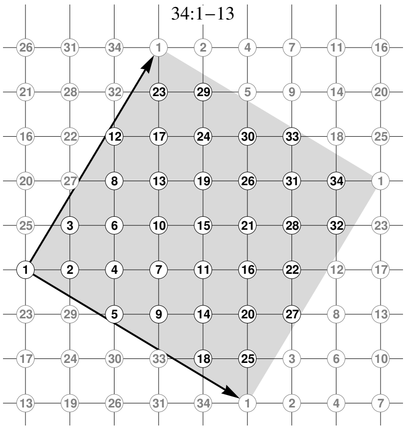
34:1−13

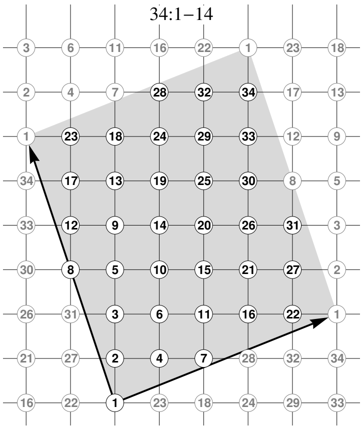

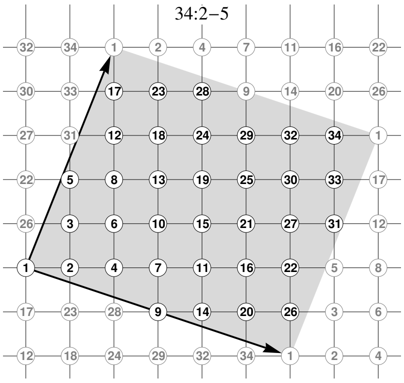

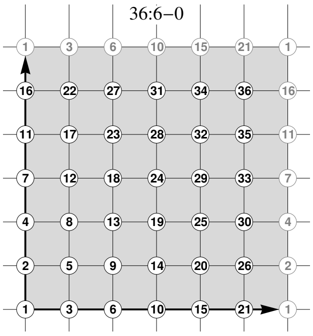

In the following table, we list the top 9 tiles having the largest squareness parameter (Eq. 5.16) for each area size N. For each tile, the edge vectors in cartesian coordinates and the squareness parameter ($\square$) are given here.

				N				
(a_{11}, a_{12})	(a_{21}, a_{22})	$\square$	(a_{11}, a_{12})	(a_{21}, a_{22})	$\square$	(a_{11}, a_{12})	(a_{21}, a_{22})	$\square$
				8				
(2, 2)	(-2, 2)	1	(3, -2)	(1, 2)	0.938	(3, 2)	(-1, 2)	0.938
(2, 1)	(-2, 3)	0.938	(2, 3)	(-2, 1)	0.938	(3, 1)	(-2, 2)	0.892
(3, -1)	(2, 2)	0.892	(2, 0)	(0, 4)	0.889	(4, 0)	(0, 2)	0.889
				10				
(3, -1)	(1, 3)	1	(3, 1)	(-1, 3)	1	(3, 2)	(-2, 2)	0.966
(3, -2)	(2, 2)	0.966	(-2, 3)	(-2, -2)	0.966	(2, -2)	(2, 3)	0.966
(4, -2)	(1, 2)	0.889	(4, 2)	(-1, 2)	0.889	(2, 1)	(-2, 4)	0.889

				N				
(a_{11}, a_{12})	(a_{21}, a_{22})	□	(a_{11}, a_{12})	(a_{21}, a_{22})	□	(a_{11}, a_{12})	(a_{21}, a_{22})	□
				12				
(3, 0)	(0, 4)	0.98	(4, 0)	(0, 3)	0.98	(3, 3)	(-2, 2)	0.96
(3, -3)	(2, 2)	0.96	(3, 0)	(1, 4)	0.946	(3, 0)	(-1, 4)	0.946
(4, 1)	(0, 3)	0.946	(0, 3)	(-4, 1)	0.946	(4, 0)	(1, 3)	0.936
				14				
(4, 2)	(-1, 3)	0.961	(4, -2)	(1, 3)	0.961	(3, 1)	(-2, 4)	0.961
(2, 4)	(-3, 1)	0.961	(3, 2)	(-1, 4)	0.938	(3, -2)	(1, 4)	0.938
(2, 3)	(-4, 1)	0.938	(4, 1)	(-2, 3)	0.938	(3, 4)	(-2, 2)	0.914
				16				
(4, 0)	(0, 4)	1	(3, -2)	(2, 4)	0.981	(3, 2)	(-2, 4)	0.981
(4, -2)	(2, 3)	0.981	(-2, 3)	(-4, -2)	0.981	(4, 0)	(-1, 4)	0.97
(4, 0)	(1, 4)	0.97	(4, 1)	(0, 4)	0.97	(0, 4)	(-4, 1)	0.97
				18				
(3, 3)	(-3, 3)	1	(4, 2)	(-1, 4)	0.975	(4, -2)	(1, 4)	0.975
(2, 4)	(-4, 1)	0.975	(4, 1)	(-2, 4)	0.975	(4, -3)	(2, 3)	0.972
(4, 3)	(-2, 3)	0.972	(3, 2)	(-3, 4)	0.972	(3, 4)	(-3, 2)	0.972
				20				
(4, -2)	(2, 4)	1	(4, 2)	(-2, 4)	1	(4, 0)	(0, 5)	0.988
(5, 0)	(0, 4)	0.988	(4, 0)	(-1, 5)	0.966	(4, 0)	(1, 5)	0.966
(5, 1)	(0, 4)	0.966	(0, 4)	(-5, 1)	0.966	(5, 0)	(-1, 4)	0.961
				22				
(4, -2)	(3, 4)	0.981	(4, 2)	(-3, 4)	0.981	(4, -3)	(2, 4)	0.981
(-2, 4)	(-4, -3)	0.981	(5, 2)	(-1, 4)	0.973	(5, -2)	(1, 4)	0.973
(2, 5)	(-4, 1)	0.973	(4, 1)	(-2, 5)	0.973	(2, 4)	(-5, 1)	0.961
				24				
(5, 2)	(-2, 4)	0.988	(5, -2)	(2, 4)	0.988	(4, -2)	(2, 5)	0.988
(-2, 5)	(-4, -2)	0.988	(4, -4)	(3, 3)	0.98	(4, 4)	(-3, 3)	0.98
(3, 4)	(-3, 4)	0.96	(4, 0)	(0, 6)	0.96	(4, -3)	(4, 3)	0.96

				N				
(a_{11}, a_{12})	(a_{21}, a_{22})	$\Box$	(a_{11}, a_{12})	(a_{21}, a_{22})	$\Box$	(a_{11}, a_{12})	(a_{21}, a_{22})	$\Box$
				26				
(5, 1)	(-1, 5)	1	(5, -1)	(1, 5)	1	(-2, 4)	(-5, -3)	0.98
(5, -3)	(2, 4)	0.98	(4, -2)	(3, 5)	0.98	(4, 2)	(-3, 5)	0.98
(5, -2)	(3, 4)	0.964	(5, 2)	(-3, 4)	0.964	(2, 5)	(-4, 3)	0.964
				28				
(4, -4)	(3, 4)	0.986	(4, 4)	(-3, 4)	0.986	(-4, 4)	(-4, -3)	0.986
(4, -3)	(4, 4)	0.986	(6, 2)	(-2, 4)	0.961	(6, -2)	(2, 4)	0.961
(2, 6)	(-4, 2)	0.961	(4, 2)	(-2, 6)	0.961	(5, 4)	(-2, 4)	0.947
				30				
(5, 0)	(0, 6)	0.992	(6, 0)	(0, 5)	0.992	(5, 0)	(-1, 6)	0.977
(5, 0)	(1, 6)	0.977	(6, 1)	(0, 5)	0.977	(0, 5)	(-6, 1)	0.977
(6, 0)	(-1, 5)	0.974	(6, 0)	(1, 5)	0.974	(5, 1)	(0, 6)	0.974
				32				
(4, 4)	(-4, 4)	1	(5, -4)	(3, 4)	0.984	(5, 4)	(-3, 4)	0.984
(4, 3)	(-4, 5)	0.984	(4, 5)	(-4, 3)	0.984	(5, 1)	(-2, 6)	0.981
(2, 6)	(-5, 1)	0.981	(6, 2)	(-1, 5)	0.981	(6, -2)	(1, 5)	0.981
				34				
(5, -3)	(3, 5)	1	(5, 3)	(-3, 5)	1	(5, 2)	(-2, 6)	0.992
(5, -2)	(2, 6)	0.992	(-2, 5)	(-6, -2)	0.992	(6, -2)	(2, 5)	0.992
(-2, 4)	(-7, -3)	0.931	(7, -3)	(2, 4)	0.931	(4, -2)	(3, 7)	0.931
				36				
(6, 0)	(0, 6)	1	(5, -4)	(4, 4)	0.99	(5, 4)	(-4, 4)	0.99
(-4, 5)	(-4, -4)	0.99	(4, -4)	(4, 5)	0.99	(6, 0)	(-1, 6)	0.986
(6, 0)	(1, 6)	0.986	(6, 1)	(0, 6)	0.986	(0, 6)	(-6, 1)	0.986

A.2. Calculation of the size of the Hilbert space

Here we briefly describe the calculation of the size of the Hilbert space, in the Heisenberg model and the Hubbard model given in Table 4.1. In the former case, there are 2 states per site. For an even number of sites n, the sector of the Hilbert space with the largest size corresponds to $S^z = \sum_i S_i^z = 0$. For the $S = \frac{1}{2}$ model, this is achieved by having $\frac{n}{2}$ "up" spins distributed over n sites. Hence, the total number of possible configuration is

$$N_{S_z=0} = \binom{n}{\frac{n}{2}}. \tag{A.1}$$

For $S_z = k/2$, we have correspondingly

$$N_{\text{Heisenberg}}(n, k = 2S_z) = \binom{n}{\frac{n+k}{2}}. \tag{A.2}$$

In the Hubbard model there are 4 states per site. For a given total $S_z = 0$ at half filling, we can distribute

1. m up-spins on n sites,
2. $\frac{n}{2} - m$ double-occupancies on $(n - m)$ sites, and
3. $\frac{n}{2} - m$ empty states on $(n - m) - \left(\frac{n}{2} - m\right) = \frac{n}{2}$ sites,

with $m \leq \frac{n}{2}$ and n an even number. The total number of states for given m therefore amounts to

$$N_{S_z=0}^m = \binom{n}{m}\binom{n-m}{\frac{n}{2}-m}\binom{\frac{n}{2}}{m} = \frac{n!}{(m!)^2\left(\left(\frac{n}{2}-m\right)!\right)^2}. \tag{A.3}$$

Summing over m yields the final expression for the total number of states for $S_z = 0$

$$\begin{aligned} N_{S_z=0} &= \sum_{m=0}^{n/2} \frac{n!}{(m!)^2\left(\left(\frac{n}{2}-m\right)!\right)^2} \\ &= 2^n \left(\frac{(n-1)!!}{(n/2)!}\right)^2. \end{aligned} \tag{A.4}$$

A.3. Linear spin-wave theory: Holstein – Primakoff transformation

After performing the Holstein – Primakoff transformation for the spin operators Eqs. 3.15 – 3.18, we keep only terms up to bilinear order in the boson operators. The individual terms in the Hamiltonian then acquire the form

$$\begin{aligned}
S_i^x S_j^x &\rightarrow \frac{S}{2}\left(a_i^\dagger a_j + a_i a_j^\dagger + a_i a_j + a_i^\dagger a_j^\dagger\right), && \text{(A.5)}\\
S_i^y S_j^y &\rightarrow \frac{S}{2}\left(a_i^\dagger a_j + a_i a_j^\dagger - a_i a_j - a_i^\dagger a_j^\dagger\right), && \text{(A.6)}\\
S_i^z S_j^z &\rightarrow S^2 - S\left(a_i^\dagger a_i + a_j^\dagger a_j\right), && \text{(A.7)}\\
S_i^x S_j^y - S_i^y S_j^x &\rightarrow -\mathrm{i}S\left(a_i^\dagger a_j - a_i a_j^\dagger\right), && \text{(A.8)}\\
S_i^y S_j^z - S_i^z S_j^y &\rightarrow -\mathrm{i}\sqrt{\frac{S^3}{2}}\left(a_i - a_i^\dagger - a_j + a_j^\dagger\right), && \text{(A.9)}\\
S_i^x S_j^z + S_i^z S_j^x &\rightarrow \sqrt{\frac{S^3}{2}}\left(a_i + a_i^\dagger + a_j + a_j^\dagger\right). && \text{(A.10)}
\end{aligned}$$

The Hamiltonian up to the bilinear order then reads

$$\begin{aligned}
\mathcal{H} \rightarrow E_{\mathrm{cl}} \\
+ \frac{S}{2}\sum_{\langle ij\rangle}\Bigg[&\left(a_i^\dagger a_j + a_i a_j^\dagger\right)\left(J_{ij}\cos(\mathbf{Q}\cdot\mathbf{R}_{ij})\left(\cos^2\Theta + 1\right) + J_{ij}\sin^2\Theta\right)\\
&+ \left(a_i a_j + a_i^\dagger a_j^\dagger\right)\left(J_{ij}\cos(\mathbf{Q}\cdot\mathbf{R}_{ij})\left(\cos^2\Theta - 1\right) + J_{ij}\sin^2\Theta\right)\\
&- 2\left(a_i^\dagger a_i + a_j^\dagger a_j\right)\left(J_{ij}\cos(\mathbf{Q}\cdot\mathbf{R}_{ij})\sin^2\Theta + J_{ij}\cos^2\Theta\right)\\
&- 2\mathrm{i}\left(a_i^\dagger a_j - a_i a_j^\dagger\right) J_{ij}\sin(\mathbf{Q}\cdot\mathbf{R}_{ij})\cos\Theta\\
&- \mathrm{i}\sqrt{2S}\left(a_i - a_i^\dagger - a_j + a_j^\dagger\right) J_{ij}\sin(\mathbf{Q}\cdot\mathbf{R}_{ij})\sin\Theta\\
&+ \sqrt{2S}\left(a_i + a_i^\dagger + a_j + a_j^\dagger\right)\left(J_{ij} - J_{ij}\cos(\mathbf{Q}\cdot\mathbf{R}_{ij})\right)\cos\Theta\sin\Theta\Bigg]\\
+ h\sum_i \Bigg[&a_i^\dagger a_i\cos\Theta - \sqrt{\frac{S}{2}}\left(a_i + a_i^\dagger\right)\sin\Theta\Bigg]. \qquad \text{(A.11)}
\end{aligned}$$

The Fourier transformations Eq. 3.20 then leads to the final form in Eq. 3.21.

A.4. Linear spin-wave theory: staggered magnetization

We define the ordered or the staggered moment as the projection of the canted spins onto the xy plane,

$$m_{\mathbf{Q}} = m_{\mathrm{tot}} \sin \Theta_{\mathrm{zp}}. \tag{A.12}$$

Only for vanishing magnetic field h this definition agrees with the total ordered moment. Instead of Θ_{c} we have to use Θ_{zp} to include also the corrections to the canting angle. Θ_{zp} can be calculated by minimizing of the ground-state energy, including the zero-point fluctuation. The final form is then given by

$$\begin{aligned}
&\cos \Theta_{\mathrm{zp}} \\
&= \cos \Theta_{\mathrm{c}} \left[1 + \frac{1}{2S} \left(\underbrace{\frac{1}{N} \sum_{\mathbf{k}} \frac{A(\mathbf{k}) - B(\mathbf{k}) \cos^2 \Theta_{\mathrm{c}}}{E(h,\mathbf{k})} - 1}_{\text{corrections to } m_{\mathrm{tot}}} + \underbrace{\frac{1}{N} \sum_{\mathbf{k}} \frac{B(\mathbf{k}) \left(A(\mathbf{k}) - B(\mathbf{k}) \right)}{A(0) E(h,\mathbf{k})}}_{\text{corrections to } m_0} \right) \right] \\
&= \cos \Theta_{\mathrm{c}} \left[1 + \frac{1}{2SA(0)} \frac{1}{N} \sum_{\mathbf{k}} \frac{A(0) \left(A(\mathbf{k}) - B(\mathbf{k}) \cos^2 \Theta_{\mathrm{c}} \right) + B(\mathbf{k}) \left(A(\mathbf{k}) - B(\mathbf{k}) \right)}{\left(A(\mathbf{k}) - B(\mathbf{k}) \right)^{1/2} \left(A(\mathbf{k}) - B(\mathbf{k})(2 \cos^2 \Theta_{\mathrm{c}} - 1) \right)^{1/2}} - \frac{1}{2S} \right].
\end{aligned} \tag{A.13}$$

Here $m_0 = m_{\mathrm{tot}} \sin \Theta_{\mathrm{zp}}$ is the uniform moment, Eq. 3.44. Using Θ_{zp} in Eq. A.12, we obtain

$$\begin{aligned}
m_{\mathbf{Q}} &= m_{\mathrm{tot}} \sqrt{1 - \cos^2 \Theta_{\mathrm{zp}}} \\
&= m_{\mathrm{tot}} \left\{ 1 - \cos^2 \Theta_{\mathrm{c}} \left[1 + \frac{1}{2S} \left(\frac{1}{N} \sum_{\mathbf{k}} \frac{A(\mathbf{k}) - B(\mathbf{k}) \cos^2 \Theta_{\mathrm{c}}}{E(h,\mathbf{k})} - 1 \right.\right.\right. \\
&\qquad \left.\left.\left. + \frac{1}{N} \sum_{\mathbf{k}} \frac{B(\mathbf{k}) \left(A(\mathbf{k}) - B(\mathbf{k}) \right)}{A(0) E(h,\mathbf{k})} \right) \right]^2 \right\}^{1/2} \\
&= m_{\mathrm{tot}} \left[\sqrt{1 - \cos^2 \Theta_{\mathrm{c}}} - \frac{\cos^2 \Theta_{\mathrm{c}}}{\sqrt{1 - \cos^2 \Theta_{\mathrm{c}}}} \frac{1}{2S} \left(\frac{1}{N} \sum_{\mathbf{k}} \frac{A(\mathbf{k}) - B(\mathbf{k}) \cos^2 \Theta_{\mathrm{c}}}{E(h,\mathbf{k})} - 1 \right.\right. \\
&\qquad \left.\left. + \frac{1}{N} \sum_{\mathbf{k}} \frac{B(\mathbf{k}) \left(A(\mathbf{k}) - B(\mathbf{k}) \right)}{A(0) E(h,\mathbf{k})} \right) \right]
\end{aligned}$$

$$
\begin{aligned}
&= S\left[1-\frac{1}{2S}\left(\frac{1}{N}\sum_{\mathbf{k}}\frac{A(\mathbf{k})-B(\mathbf{k})\cos^2\Theta_{\mathrm{c}}}{E(h,\mathbf{k})}-1\right)\right]\sin\Theta_{\mathrm{c}} \\
&\quad \left[1-\frac{\cos^2\Theta_{\mathrm{c}}}{\sin^2\Theta_{\mathrm{c}}}\frac{1}{2S}\left(\frac{1}{N}\sum_{\mathbf{k}}\frac{A(\mathbf{k})-B(\mathbf{k})\cos^2\Theta_{\mathrm{c}}}{E(h,\mathbf{k})}-1+\frac{1}{N}\sum_{\mathbf{k}}\frac{B(\mathbf{k})\left(A(\mathbf{k})-B(\mathbf{k})\right)}{A(0)E(h,\mathbf{k})}\right)\right]
\end{aligned}
\tag{A.14}
$$

Taking into account only terms up to order $1/S$, the staggered moment in the presence of a magnetic field is thus given by

$$
\begin{aligned}
m_{\mathbf{Q}} &= S\sin\Theta_{\mathrm{c}}\left\{1-\frac{1}{2S}\underbrace{\left[\frac{1}{N}\sum_{\mathbf{k}}\frac{A(\mathbf{k})-B(\mathbf{k})\cos^2\Theta_{\mathrm{c}}}{E(h,\mathbf{k})}-1\right]}_{\text{corrections to } m_{\mathrm{tot}}}\right. \\
&\qquad \left.-\frac{\cos^2\Theta_{\mathrm{c}}}{\sin^2\Theta_{\mathrm{c}}}\frac{1}{2S}\underbrace{\left[\underbrace{\frac{1}{N}\sum_{\mathbf{k}}\frac{A(\mathbf{k})-B(\mathbf{k})\cos^2\Theta_{\mathrm{c}}}{E(h,\mathbf{k})}-1}_{\text{corrections to } m_{\mathrm{tot}}}+\underbrace{\frac{1}{N}\sum_{\mathbf{k}}\frac{B(\mathbf{k})\left(A(\mathbf{k})-B(\mathbf{k})\right)}{A(0)E(h,\mathbf{k})}}_{\text{corrections to } m_0}\right]}_{\text{corrections to } \Theta_{\mathrm{c}}}\right\}.
\end{aligned}
\tag{A.15}
$$

The staggered moment has corrections originating from the total moment m_{tot} as well as the canting angle Θ_{c}. Eq. A.15 may also be written in the compact form of Eq. 3.45.

Bibliography

[1] H. Diep, *Frustrated spin systems.* World Scientific, 2004.

[2] G. H. Wannier, "Antiferromagnetism. the triangular Ising net", *Phys. Rev.*, vol. 79, pp. 357–364, Jul 1950.

[3] A. Yoshimori, "A new type of antiferromagnetic structure in the rutile type crystal", *Journal of the Physical Society of Japan*, vol. 14, no. 6, pp. 807–821, 1959.

[4] J. Villain, "La structure des substances magnetiques", *Journal of Physics and Chemistry of Solids*, vol. 11, no. 3–4, pp. 303 – 309, 1959.

[5] T. A. Kaplan, "Classical spin-configuration stability in the presence of competing exchange forces", *Phys. Rev.*, vol. 116, pp. 888–889, Nov 1959.

[6] T. A. Kaplan, "Some effects of anisotropy on spiral spin-configurations with application to rare-earth metals", *Phys. Rev.*, vol. 124, pp. 329–339, Oct 1961.

[7] R. J. Elliott, "Phenomenological discussion of magnetic ordering in the heavy rare-earth metals", *Phys. Rev.*, vol. 124, pp. 346–353, Oct 1961.

[8] G. Toulouse *Commun. Phys.*, vol. 2, p. 115, 1977.

[9] J. Vannimenus and G. Toulouse, "Theory of the frustration effect. II. Ising spins on a square lattice", *Journal of Physics C: Solid State Physics*, vol. 10, no. 18, p. L537, 1977.

[10] G. Toulouse, "The frustration model", in *Modern Trends in the Theory of Condensed Matter* (A. Pekalski and J. Przystawa, eds.), vol. 115 of *Lecture Notes in Physics*, pp. 195–203, Springer Berlin / Heidelberg, 1980. 10.1007/BFb0120136.

[11] J. Villain, "Spin glass with non-random interactions", *Journal of Physics C: Solid State Physics*, vol. 10, no. 10, p. 1717, 1977.

[12] J. Villain, R. Bidaux, J.-P. Carton, and R. Conte, "Order as an effect of disorder", *J. Phys. France*, vol. 41, no. 11, pp. 1263–1272, 1980.

[13] D. Bergman, J. Alicea, E. Gull, S. Trebst, and L. Balents, "Order-by-disorder and spiral spin-liquid in frustrated diamond-lattice antiferromagnets", *Nat Phys*, vol. 3, pp. 487–491, 07 2007.

[14] E. Rastelli and A. Tassi, "Order produced by quantum disorder in the Heisenberg rhombohedral antiferromagnet", *Journal of Physics C: Solid State Physics*, vol. 20, no. 15, p. L303, 1987.

[15] C. L. Henley, "Ordering due to disorder in a frustrated vector antiferromagnet", *Phys. Rev. Lett.*, vol. 62, pp. 2056–2059, Apr 1989.

[16] A. Chubukov, "Order from disorder in a Kagomé antiferromagnet", *Phys. Rev. Lett.*, vol. 69, pp. 832–835, Aug 1992.

[17] P. Fazekas, *Lecture notes on electron correlation and magnetism.* Series in modern condensed matter physics, World Scientific, 1999.

[18] H. Kramers, "L'interaction entre les atomes magnétogènes dans un cristal paramagnétique", *Physica*, vol. 1, no. 1–6, pp. 182 – 192, 1934.

[19] L. Passell, O. W. Dietrich, and J. Als-Nielsen, "Neutron scattering from the Heisenberg ferromagnets EuO and EuS. I. The exchange interactions", *Phys. Rev. B*, vol. 14, pp. 4897–4907, Dec 1976.

[20] I. Yamada, "Magnetic properties of K_2CuF_4 —a transparent two-dimensional ferromagnet", *Journal of the Physical Society of Japan*, vol. 33, no. 4, pp. 979–988, 1972.

[21] E. Manousakis, "The spin-$\frac{1}{2}$ heisenberg antiferromagnet on a square lattice and its application to the cuprous oxides," *Rev. Mod. Phys.*, vol. 63, pp. 1–62, Jan 1991.

[22] J. Sadoc, R. Mosseri, and R. Mosseri, *Geometrical Frustration.* Collection Alea-Saclay: Monographs and Texts in Statistical Physics, Cambridge University Press, 2006.

[23] L. Hulthén, "Über das austauschproblem eines kristalles", *Arkiv för Matematik, Astronomi och Fysik*, vol. 26A, no. 11, p. 1, 1938.

[24] P. Anderson, "Resonating valence bonds: A new kind of insulator?", *Materials Research Bulletin*, vol. 8, no. 2, pp. 153 – 160, 1973.

[25] P. Fazekas and P. W. Anderson, "On the ground state properties of the anisotropic triangular antiferromagnet", *Philosophical Magazine*, vol. 30, no. 2, pp. 423–440, 1974.

[26] L. Balents, "Spin liquids in frustrated magnets", *Nature*, vol. 464, pp. 199–208, 03 2010.

[27] P. Chandra and B. Doucot, "Possible spin-liquid state at large S for the frustrated square Heisenberg lattice", *Phys. Rev. B*, vol. 38, pp. 9335–9338, Nov 1988.

[28] E. Dagotto and A. Moreo, "Phase diagram of the frustrated spin-$\frac{1}{2}$ Heisenberg antiferromagnet in 2 dimensions", *Phys. Rev. Lett.*, vol. 63, pp. 2148–2151, Nov 1989.

[29] D. Poilblanc, E. Gagliano, S. Bacci, and E. Dagotto, "Static and dynamical correlations in a spin-$\frac{1}{2}$ frustrated antiferromagnet", *Phys. Rev. B*, vol. 43, pp. 10970–10983, May 1991.

[30] L. Capriotti, F. Becca, A. Parola, and S. Sorella, "Suppression of dimer correlations in the two-dimensional $J_1 - J_2$ Heisenberg model: An exact diagonalization study", *Phys. Rev. B*, vol. 67, p. 212402, Jun 2003.

[31] Y. Okamoto, M. Nohara, H. Aruga-Katori, and H. Takagi, "Spin-liquid state in the $S = \frac{1}{2}$ hyperkagome antiferromagnet $\mathrm{Na_4Ir_3O_8}$", *Phys. Rev. Lett.*, vol. 99, p. 137207, Sep 2007.

[32] S. Yan, D. A. Huse, and S. R. White, "Spin-liquid ground state of the $S = \frac{1}{2}$ Kagome Heisenberg antiferromagnet", *Science*, vol. 332, no. 6034, pp. 1173–1176, 2011.

[33] Y.-M. Lu, Y. Ran, and P. A. Lee, "$\mathbb{Z}_2$ spin liquids in the $S = \frac{1}{2}$ Heisenberg model on the Kagome lattice: A projective symmetry-group study of schwinger fermion mean-field states", *Phys. Rev. B*, vol. 83, p. 224413, Jun 2011.

[34] P. W. Anderson, "The resonating valence bond state in $\mathrm{La_2CuO_4}$ and superconductivity", *Science*, vol. 235, no. 4793, pp. 1196–1198, 1987.

[35] J. Reuther and P. Wölfle, "$J_1 - J_2$ frustrated two-dimensional Heisenberg model: Random phase approximation and functional renormalization group", *Phys. Rev. B*, vol. 81, p. 144410, Apr 2010.

[36] T. Thio, T. R. Thurston, N. W. Preyer, P. J. Picone, M. A. Kastner, H. P. Jenssen, D. R. Gabbe, C. Y. Chen, R. J. Birgeneau, and A. Aharony, "Antisymmetric exchange and its influence on the magnetic structure and conductivity of La_2CuO_4," *Phys. Rev. B*, vol. 38, pp. 905–908, Jul 1988.

[37] G. Shirane, Y. Endoh, R. J. Birgeneau, M. A. Kastner, Y. Hidaka, M. Oda, M. Suzuki, and T. Murakami, "Two-dimensional antiferromagnetic quantum spin-fluid state in La_2CuO_4", *Phys. Rev. Lett.*, vol. 59, pp. 1613–1616, Oct 1987.

[38] S. Chakravarty, B. I. Halperin, and D. R. Nelson, "Low-temperature behavior of two-dimensional quantum antiferromagnets", *Phys. Rev. Lett.*, vol. 60, pp. 1057–1060, Mar 1988.

[39] R. Coldea, S. M. Hayden, G. Aeppli, T. G. Perring, C. D. Frost, T. E. Mason, S.-W. Cheong, and Z. Fisk, "Spin waves and electronic interactions in La_2CuO_4", *Phys. Rev. Lett.*, vol. 86, pp. 5377–5380, Jun 2001.

[40] P. Thalmeier, M. E. Zhitomirsky, B. Schmidt, and N. Shannon, "Quantum effects in magnetization of $J_1 - J_2$ square lattice antiferromagnet", *Phys. Rev. B*, vol. 77, p. 104441, Mar 2008.

[41] J. Richter and J. Schulenburg, "The spin-$\frac{1}{2}$ $J_1 - J_2$ Heisenberg antiferromagnet on the square lattice: Exact diagonalization for $N = 40$ spins", *The European Physical Journal B - Condensed Matter and Complex Systems*, vol. 73, pp. 117–124, 2010. 10.1140/epjb/e2009-00400-4.

[42] L. Pauling, "A theory of ferromagnetism," *Proceedings of the National Academy of Sciences*, vol. 39, no. 6, pp. 551–560, 1953.

[43] M. Mambrini, A. Läuchli, D. Poilblanc, and F. Mila, "Plaquette valence-bond crystal in the frustrated heisenberg quantum antiferromagnet on the square lattice," *Phys. Rev. B*, vol. 74, p. 144422, Oct 2006.

[44] N. Shannon, T. Momoi, and P. Sindzingre, "Nematic order in square lattice frustrated ferromagnets", *Phys. Rev. Lett.*, vol. 96, p. 027213, 2006.

[45] S. Sachdev, “Quantum phase transitions of antiferromagnets and the cuprate superconductors,” in *Modern Theories of Many-Particle Systems in Condensed Matter Physics* (D. C. Cabra, A. Honecker, and P. Pujol, eds.), vol. 843 of *Lecture Notes in Physics*, pp. 1–51, Springer Berlin / Heidelberg, 2012. 10.1007/978-3-642-10449-7-1.

[46] R. Shindou, S. Yunoki, and T. Momoi, “Projective studies of spin nematics in a quantum frustrated ferromagnet,” *Phys. Rev. B*, vol. 84, p. 134414, Oct 2011.

[47] B. Schmidt, M. Siahatgar, and P. Thalmeier, “Frustrated local-moment models for iron pnictide magnetism”, *Phys. Rev. B*, vol. 81, no. 16, 2010.

[48] J. Zhao, D. T. Adroja, D.-X. Yao, R. Bewley, S. Li, X. F. Wang, G. Wu, X. H. Chen, J. Hu, and P. Dai, “Spin waves and magnetic exchange interactions in $\mathrm{CaFe_2As_2}$”, *Nat Phys*, vol. 5, pp. 555–560, 08 2009.

[49] K. Kubo and P. Thalmeier, “Multiorbital effects on antiferromagnetism in Fe-pnictides”, *Journal of the Physical Society of Japan*, vol. 78, no. 8, p. 083704, 2009.

[50] A. N. Yaresko, G.-Q. Liu, V. N. Antonov, and O. K. Andersen, “Interplay between magnetic properties and fermi surface nesting in iron pnictides,” *Phys. Rev. B*, vol. 79, p. 144421, Apr 2009.

[51] M. J. Han, Q. Yin, W. E. Pickett, and S. Y. Savrasov, “Anisotropy, itineracy, and magnetic frustration in high-T_C iron pnictides”, *Phys. Rev. Lett.*, vol. 102, p. 107003, Mar 2009.

[52] R. Nath, A. A. Tsirlin, H. Rosner, and C. Geibel, “Magnetic properties of $\mathrm{BaCdVO(PO_4)_2}$: A strongly frustrated spin-$\frac{1}{2}$ square lattice close to the quantum critical regime”, *Phys. Rev. B*, vol. 78, p. 064422, Aug 2008.

[53] N. S. Kini, E. E. Kaul, and C. Geibel, “$\mathrm{Zn_2VO(PO_4)_2}$: an $S = \frac{1}{2}$ Heisenberg antiferromagnetic square lattice system”, *Journal of Physics: Condensed Matter*, vol. 18, no. 4, p. 1303, 2006.

[54] E. E. Kaul, H. Rosner, N. Shannon, R. V. Shpanchenko, and C. Geibel, “Evidence for a frustrated square lattice with ferromagnetic nearest-neighbor interaction in the new compound $\mathrm{Pb_2VO(PO_4)_2}$”, *Journal of Magnetism and*

Magnetic Materials, vol. 272-276, no. Part 2, pp. 922 – 923, 2004. Proceedings of the International Conference on Magnetism (ICM 2003).

[55] E. E. Kaul, *Experimental Investigation of New Low-Dimensional Spin Systems in Vanadium Oxides.* PhD thesis, Technische Universität Dresden, 2005.

[56] M. Skoulatos, J. Goff, N. Shannon, E. Kaul, C. Geibel, A. Murani, M. Enderle, and A. Wildes, "Spin correlations in the frustrated square lattice $Pb_2VO(PO_4)_2$", *Journal of Magnetism and Magnetic Materials*, vol. 310, no. 2, Part 2, pp. 1257 – 1259, 2007. Proceedings of the 17th International Conference on Magnetism, The International Conference on Magnetism.

[57] R. Melzi, S. Aldrovandi, F. Tedoldi, P. Carretta, P. Millet, and F. Mila, "Magnetic and thermodynamic properties of Li_2VOSiO_4: a two-dimensional $S = \frac{1}{2}$ frustrated antiferromagnet on a square lattice", *Phys. Rev. B*, vol. 64, p. 024409, Jun 2001.

[58] R. A. Ewings, T. G. Perring, R. I. Bewley, T. Guidi, M. J. Pitcher, D. R. Parker, S. J. Clarke, and A. T. Boothroyd, "High-energy spin excitations in $BaFe_2As_2$ observed by inelastic neutron scattering", *Phys. Rev. B*, vol. 78, p. 220501, Dec 2008.

[59] R. J. McQueeney, S. O. Diallo, V. P. Antropov, G. D. Samolyuk, C. Broholm, N. Ni, S. Nandi, M. Yethiraj, J. L. Zarestky, J. J. Pulikkotil, A. Kreyssig, M. D. Lumsden, B. N. Harmon, P. C. Canfield, and A. I. Goldman, "Anisotropic three-dimensional magnetism in $CaFe_2As_2$", *Phys. Rev. Lett.*, vol. 101, p. 227205, Nov 2008.

[60] S. O. Diallo, V. P. Antropov, T. G. Perring, C. Broholm, J. J. Pulikkotil, N. Ni, S. L. Bud'ko, P. C. Canfield, A. Kreyssig, A. I. Goldman, and R. J. McQueeney, "Itinerant magnetic excitations in antiferromagnetic $CaFe_2As_2$", *Phys. Rev. Lett.*, vol. 102, p. 187206, May 2009.

[61] N. Tsyrulin, F. Xiao, A. Schneidewind, P. Link, H. M. Rønnow, J. Gavilano, C. P. Landee, M. M. Turnbull, and M. Kenzelmann, "Two-dimensional square-lattice $S = \frac{1}{2}$ antiferromagnet $Cu(pz)_2(ClO_4)_2$", *Phys. Rev. B*, vol. 81, p. 134409, Apr 2010.

[62] N. Tsyrulin, T. Pardini, R. R. P. Singh, F. Xiao, P. Link, A. Schneidewind, A. Hiess, C. P. Landee, M. M. Turnbull, and M. Kenzelmann, "Quantum ef-

fects in a weakly frustrated $S = \frac{1}{2}$ two-dimensional Heisenberg antiferromagnet in an applied magnetic field", *Phys. Rev. Lett.*, vol. 102, p. 197201, May 2009.

[63] T. Lancaster, S. J. Blundell, M. L. Brooks, P. J. Baker, F. L. Pratt, J. L. Manson, M. M. Conner, F. Xiao, C. P. Landee, F. A. Chaves, S. Soriano, M. A. Novak, T. P. Papageorgiou, A. D. Bianchi, T. Herrmannsdörfer, J. Wosnitza, and J. A. Schlueter, "Magnetic order in the $S = \frac{1}{2}$ two-dimensional molecular antiferromagnet copper pyrazine perchlorate $\mathrm{Cu(pz)_2(ClO_4)_2}$", *Phys. Rev. B*, vol. 75, p. 094421, Mar 2007.

[64] F. Xiao, "Two-dimensional xy behavior observed in quasi-two-dimensional quantum Heisenberg antiferromagnets"", *Phys. Rev. B*, vol. 79, no. 13, 2009.

[65] M. Siahatgar, B. Schmidt, and P. Thalmeier, "Staggered-moment dependence on field-tuned quantum fluctuations in two-dimensional frustrated antiferromagnets", *Phys. Rev. B*, vol. 84, p. 064431, Aug 2011.

[66] T. Ohyama and H. Shiba, "Nonlinear excitations in quasi-one-dimensional triangular antiferromagnets", *Journal of the Physical Society of Japan*, vol. 62, no. 9, pp. 3277–3293, 1993.

[67] T. Ohyama and H. Shiba, "Spin dynamics and quantum fluctuations in quasi-one-dimensional triangular antiferromagnets: Magnetic field effects", *Journal of the Physical Society of Japan*, vol. 63, no. 9, pp. 3454–3473, 1994.

[68] M. Y. Veillette, J. T. Chalker, and R. Coldea, "Ground states of a frustrated spin-$\frac{1}{2}$ antiferromagnet: $\mathrm{Cs_2CuCl_4}$ in a magnetic field", *Physical Review B (Condensed Matter and Materials Physics)*, vol. 71, no. 21, p. 214426, 2005.

[69] B. Schmidt, P. Thalmeier, and N. Shannon, "Magnetocaloric effect in the frustrated square lattice $J_1 - J_2$ model", *Phys. Rev. B*, vol. 76, p. 125113, Sep 2007.

[70] T. Holstein and H. Primakoff, "Field dependence of the intrinsic domain magnetization of a ferromagnet", *Phys. Rev.*, vol. 58, pp. 1098–1113, Dec 1940.

[71] C. J. Hamer, Z. Weihong, and P. Arndt, "Third-order spin-wave theory for the Heisenberg antiferromagnet", *Phys. Rev. B*, vol. 46, pp. 6276–6292, Sep 1992.

[72] Y. Saad, *Numerical Methods for Large Eigenvalue Problems.* Classics in Applied Mathematics, Society for Industrial and Applied Mathematics, 2011.

[73] G. Golub and C. Loan, *Matrix Computations.* Johns Hopkins studies in the mathematical sciences, Johns Hopkins University Press, 1996.

[74] J. G. F. Francis, "The QR transformation a unitary analogue to the LR transformation Part 1", *The Computer Journal*, vol. 4, no. 3, pp. 265–271, 1961.

[75] A. S. Householder, "Unitary triangularization of a non-symmetric matrix", *J. ACM*, vol. 5, pp. 339–342, October 1958.

[76] J. W. Demmel, *Applied numerical linear algebra.* Society for Industrial and Applied Mathematics, 1997.

[77] Y. Saad, *Iterative methods for sparse linear systems.* Society for Industrial and Applied Mathematics, 2003.

[78] W. E. Arnoldi, "The principle of minimized iterations in the solution of the matrix eigenvalue problem", *Quarterly of Applied Mathematics*, vol. 9, pp. 17–29, 1951.

[79] C. Lanczos, "An iteration method for the solution of the eigenvalue problem of linear differential and integral operators", *Journal of Research of the National Bureau of Standards*, vol. 45, pp. 255–282, 1950.

[80] R. von Mises and H. Pollaczek-Geiringer, "Praktische verfahren der gleichungsauflösung", *Zeitschrift für Angewandte Mathematik und Mechanik*, vol. 9, pp. 152–164, 1929.

[81] C. Paige, *The Computation of Eigenvalues and Eigenvectors of Very Large Sparse Matrices.* PhD thesis, University of London, England, 1971.

[82] C. Paige, "Error analysis of the Lanczos algorithm for tridiagonalizing a symmetric matrix", *J. Inst. Math. Appl.*, vol. 18, pp. 341–349, 1976.

[83] J. Cullum and R. Willoughby, *Lanczos Algorithms for Large Symmetric Eigenvalue Computations: Theory.* Classics in applied mathematics, Society for Industrial and Applied Mathematics, 2002.

[84] G. L. G. Sleijpen and H. A. V. der Vorst, "A Jacobi–Davidson iteration method for linear eigenvalue problems", *SIAM Journal on Matrix Analysis and Applications*, vol. 17, no. 2, pp. 401–425, 1996.

[85] A. Weiße and H. Fehske, "Exact diagonalization techniques", in *Computational Many-Particle Physics* (H. Fehske, R. Schneider, and A. Weiße, eds.), vol. 739 of *Lecture Notes in Physics*, pp. 529–544, Springer Berlin / Heidelberg, 2008.

[86] G. Grosso, L. Martinelli, and G. Pastori Parravicini, "Lanczos-type algorithm for excited states of very-large-scale quantum systems", *Phys. Rev. B*, vol. 51, pp. 13033–13038, May 1995.

[87] H. J. Schulz, T. A. L. Ziman, and D. Poilblanc, "Magnetic order and disorder in the frustrated quantum Heisenberg antiferromagnet in two dimensions", *J. Phys. I France*, vol. 6, no. 5, pp. 675–703, 1996.

[88] B. Bernu, P. Lecheminant, C. Lhuillier, and L. Pierre, "Exact spectra, spin susceptibilities, and order parameter of the quantum Heisenberg antiferromagnet on the triangular lattice", *Phys. Rev. B*, vol. 50, no. 14, pp. 10048–10062, 1994.

[89] A. W. Sandvik, "Finite-size scaling of the ground-state parameters of the two-dimensional Heisenberg model", *Phys. Rev. B*, vol. 56, pp. 11678–11690, Nov 1997.

[90] J. Jaklič and P. Prelovšek, "Lanczos method for the calculation of finite-temperature quantities in correlated systems", *Phys. Rev. B*, vol. 49, pp. 5065–5068, Feb 1994.

[91] J. Jaklič and P. Prelovšek, "Finite-temperature properties of doped antiferromagnets", *Advances in Physics*, vol. 49, no. 1, pp. 1–92, 2000.

[92] M. Aichhorn, M. Daghofer, H. G. Evertz, and W. von der Linden, "Low-temperature Lanczos method for strongly correlated systems", *Phys. Rev. B*, vol. 67, p. 161103, Apr 2003.

[93] N. Ashcroft and N. Mermin, *Solid state physics.* Holt-Saunders International Editions: Science : Physics, Holt, Rinehart and Winston, 1976.

[94] B. Schmidt and P. Thalmeier, "Third-order magnetic susceptibility of the frustrated square-lattice antiferromagnet", *Physica B: Condensed Matter*,

vol. 359–361, no. 0, pp. 1387 – 1390, 2005. Proceedings of the International Conference on Strongly Correlated Electron Systems.

[95] A. Schrijver, *Theory of linear and integer programming.* Wiley-Interscience series in discrete mathematics and optimization, Wiley, 1998.

[96] P. D. Domich, R. Kannan, and J. Trotter, L. E., "Hermite normal form computation using modulo determinant arithmetic", *Mathematics of Operations Research*, vol. 12, no. 1, pp. pp. 50–59, 1987.

[97] J. N. Lyness, T. Sørevik, and P. Keast, "Notes on integration and integer sublattices", *Math. Comp.*, vol. 56, no. 193, pp. 243–255, 1991.

[98] G. E. Stewart, D. D. Betts, and J. S. Flynn, "Extension of the method of exact diagonalization of quantum spin models to finite face centered cubic lattices and estimation of the $T = 0$ properties of the $S = \frac{1}{2}$ XY ferromagnet on the infinite fcc lattice", *J. Phys. Soc. Jpn.*, vol. 66, no. 10, pp. 3231–3236, 1997.

[99] A. K. Lenstra, H. W. Lenstra, and L. Lovász, "Factoring polynomials with rational coefficients", *Mathematische Annalen*, vol. 261, pp. 515–534, 1982. 10.1007/BF01457454.

[100] O. Haan, J. U. Klaetke, and K. H. Mütter, "Ground-state staggered magnetization of the antiferromagnetic Heisenberg model", *Phys. Rev. B*, vol. 46, no. 9, pp. 5723–5726, 1992.

[101] D. Betts, H. Lin, and J. Flynn, "Improved finite-lattice estimates of the properties of two quantum spin models on the infinite square lattice", *Can. J. Phys.*, vol. 77, no. 5, pp. 353–369, 1999.

[102] P. Hasenfratz and F. Niedermayer, "Finite size and temperature effects in the af Heisenberg model", *Zeitschrift für Physik B Condensed Matter*, vol. 92, pp. 91–112, 1993. 10.1007/BF01309171.

[103] H. Neuberger and T. Ziman, "Finite-size effects in Heisenberg antiferromagnets", *Phys. Rev. B*, vol. 39, pp. 2608–2618, Feb 1989.

[104] D. S. Fisher, "Universality, low-temperature properties, and finite-size scaling in quantum antiferromagnets", *Phys. Rev. B*, vol. 39, pp. 11783–11792, Jun 1989.

[105] J. Darriet, M. S. Haddad, E. N. Duesler, and D. N. Hendrickson, "Crystal structure and magnetic properties of bis(pyrazine)copper(ii) perchlorate, $Cu(pyz)_2(ClO_4)_2$, a two-dimensional Heisenberg antiferromagnet", *Inorganic Chemistry*, vol. 18, no. 10, pp. 2679–2682, 1979.

[106] F. M. Woodward, P. J. Gibson, G. B. Jameson, C. P. Landee, M. M. Turnbull, and R. D. Willett, "Two-dimensional Heisenberg antiferromagnets: Syntheses, x-ray structures, and magnetic behavior of $Cu(pz)_2(ClO_4)_2$, $Cu(pz)_2(BF_4)_2$, and $Cu(pz)_2(NO_3)(PF_6)$", *Inorganic Chemistry*, vol. 46, pp. 4256–4266, 04 2007.

[107] N. Shannon, B. Schmidt, K. Penc, and P. Thalmeier, "Finite temperature properties and frustrated ferromagnetism in a square lattice Heisenberg model", *The European Physical Journal B - Condensed Matter and Complex Systems*, vol. 38, pp. 599–616, 2004. 10.1140/epjb/e2004-00156-3.

[108] M. M. Korshunov, I. Eremin, D. V. Efremov, D. L. Maslov, and A. V. Chubukov, "Nonanalytic spin susceptibility of a fermi liquid: The case of fe-based pnictides", *Phys. Rev. Lett.*, vol. 102, p. 236403, Jun 2009.

[109] S.-P. Kou, T. Li, and Z.-Y. Weng, "Coexistence of itinerant electrons and local moments in iron-based superconductors", *EPL (Europhysics Letters)*, vol. 88, no. 1, p. 17010, 2009.

[110] A. A. Tsirlin, B. Schmidt, Y. Skourski, R. Nath, C. Geibel, and H. Rosner, "Exploring the spin-$\frac{1}{2}$ frustrated square lattice model with high-field magnetization studies", *Phys. Rev. B*, vol. 80, p. 132407, Oct 2009.

[111] A. Honecker, J. Schulenburg, and J. Richter, "Magnetization plateaus in frustrated antiferromagnetic quantum spin models", *Journal of Physics: Condensed Matter*, vol. 16, no. 11, p. S749, 2004.

[112] M. E. Zhitomirsky, A. Honecker, and O. A. Petrenko, "Field induced ordering in highly frustrated antiferromagnets", *Phys. Rev. Lett.*, vol. 85, pp. 3269–3272, Oct 2000.

[113] J. C. Bonner and M. E. Fisher, "Linear magnetic chains with anisotropic coupling", *Phys. Rev.*, vol. 135, pp. A640–A658, Aug 1964.

[114] A. A. Tsirlin and H. Rosner, “Extension of the spin-$\frac{1}{2}$ frustrated square lattice model: The case of layered vanadium phosphates”, *Phys. Rev. B*, vol. 79, p. 214417, Jun 2009.

[115] H. Rosner, R. R. P. Singh, W. H. Zheng, J. Oitmaa, and W. E. Pickett, “High-temperature expansions for the $J_1 - J_2$ Heisenberg models: Applications to ab initio calculated models for Li_2VOSiO_4 and Li_2VOGeO_4”, *Phys. Rev. B*, vol. 67, p. 014416, Jan 2003.

[116] G. Misguich, B. Bernu, and L. Pierre, “Determination of the exchange energies in li_2vosio_4 from a high-temperature series analysis of the square-lattice $J_1 -$ $- J_2$ Heisenberg model”, *Phys. Rev. B*, vol. 68, p. 113409, Sep 2003.

[117] S. Zhou and Z. Wang, “Electron correlation and spin density wave order in iron pnictides”, *Phys. Rev. Lett.*, vol. 105, p. 096401, Aug 2010.

[118] F. Cricchio, O. Grånäs, and L. Nordström, “Low spin moment due to hidden multipole order from spin-orbital ordering in LaFeAsO”, *Phys. Rev. B*, vol. 81, p. 140403, Apr 2010.

[119] C.-C. Lee, W.-G. Yin, and W. Ku, “Ferro-orbital order and strong magnetic anisotropy in the parent compounds of iron-pnictide superconductors”, *Phys. Rev. Lett.*, vol. 103, p. 267001, Dec 2009.

[120] Y.-Z. Zhang, I. Opahle, H. O. Jeschke, and R. Valentí, “Itinerant nature of magnetism in iron pnictides: A first-principles study”, *Phys. Rev. B*, vol. 81, p. 094505, Mar 2010.

[121] W. Lv, F. Krüger, and P. Phillips, “Orbital ordering and unfrustrated $(\pi, 0)$ magnetism from degenerate double exchange in the iron pnictides”, *Phys. Rev. B*, vol. 82, p. 045125, Jul 2010.

[122] A. Chubukov, “Pairing mechanism in fe-based superconductors”, *Annual Review of Condensed Matter Physics*, vol. 3, no. 1, pp. 57–92, 2012.

[123] A. Hewson, *The Kondo problem to heavy fermions.* Cambridge University Press, 1993.

[124] D. M. Newns and N. Read, “Mean-field theory of intermediate valence/heavy fermion systems”, *Advances in Physics*, vol. 36, no. 6, p. 799, 1987.

[125] N. E. Bickers, “Review of techniques in the large-N expansion for dilute magnetic alloys”, *Rev. Mod. Phys.*, vol. 59, p. 845, 1987.

[126] G. Zwicknagl, “Heavy fermion compounds”, *Advances in Physics*, vol. 41, p. 203, 1992.

[127] G. Khaliullin and P. Fulde, “Magnetic impurity in a system of correlated electrons”, *Phys. Rev. B*, vol. 52, no. 13, p. 9514, 1995.

[128] M. Neef, S. Tornow, V. Zevin, and G. Zwicknagl, “Kondo effect in a metal with correlated conduction electrons: diagrammatic approach”, *Phys. Rev. B*, vol. 68, p. 035114, 2003.

[129] T. Schork and P. Fulde, “Interaction of a magnetic impurity with strongly correlated conduction electrons”, *Phys. Rev. B*, vol. 50, no. 3, p. 1345, 1994.

[130] Y. M. Li, “Effect of conduction-electron interactions on anderson impurities”, *Phys. Rev. B*, vol. 52, no. 10, p. R6979, 1995.

[131] R. Takayama and O. Sakai, “Single impurity anderson model with coulomb repulsion between conduction electrons on the nearest neighbor ligand orbitals”, *J. Phys. Soc. Jpn.*, vol. 67, no. 6, p. 1844, 1998.

[132] K. Itai and P. Fazekas, “Interaction effect in the Kondo energy of the periodic anderson-hubbard model”, *Phys. Rev. B*, vol. 54, p. R752, 1996.

[133] N. Shibata, T. Nishino, K. Ueda, and C. Ishii, “Spin and charge gaps in the one-dimensional Kondo-lattice model with coulomb interaction between conduction electrons”, *Phys. Rev. B*, vol. 53, no. 14, p. R8828, 1996.

[134] M. Feldbacher, C. Jurecka, F. F. Assaad, and W. Brenig, “Single-hole dynamics in the half-filled two-dimensional Kondo-hubbard model”, *Phys. Rev. B*, vol. 66, p. 045103, 2002.

[135] C. Jurecka and W. Brenig, “Bond-operator mean-field theory of the half-filled Kondo lattice model”, *Phys. Rev. B*, vol. 64, p. 092406, 2001.

[136] I. Zerec, B. Schmidt, and P. Thalmeier, “Finite temperature properties of Kondo lattice-type model with exact diagonalization”, *Physica B*, vol. 378-380, p. 702, 2006.

[137] I. Zerec, B. Schmidt, and P. Thalmeier, "Kondo lattice model studied with the finite temperature Lanczos method", *Phys. Rev. B*, vol. 73, p. 245108, Jun 2006.

[138] J. Igarashi, T. Tonegawa, M. Kaburagi, and P. Fulde, "Magnetic impurities coupled to quantum antiferromagnets in one dimension", *Phys. Rev. B*, vol. 51, no. 9, p. 5814, 1995.

[139] G.-M. Zhang, Q. Gu, and L. Yu, "Kondo spin liquid and magnetically long-range ordered states in the Kondo necklace model", *Phys. Rev. B*, vol. 62, no. 1, p. 69, 2000.

[140] A. Langari and P. Thalmeier, "Antiferromagnetic and spin-gap phases of the anisotropic Kondo necklace model", *Phys. Rev. B*, vol. 74, p. 024431, 2006.

[141] P. Thalmeier and A. Langari, "Field-induced quantum phase transition in the anisotropic Kondo necklace model", *Phys. Rev. B*, vol. 75, p. 174426, 2007.

[142] N. Néel, J. Kröger, R. Berndt, T. O. Wehling, A. I. Lichtenstein, and M. I. Katsnelson, "Controlling the Kondo effect in CoCu_n clusters atom by atom", *Phys. Rev. Lett.*, vol. 101, p. 266803, 2008.

[143] N. Néel, R. Berndt, J. Kröger, T. O. Wehling, A. I. Lichtenstein, and M. I. Katsnelson, "Two-site Kondo effect in atomic chains", *Phys. Rev. Lett.*, vol. 107, p. 106804, Sep 2011.

[144] B. Schmidt, M. Siahatgar, and P. Thalmeier, "Ordered moment in the anisotropic and frustrated square lattice Heisenberg model", *Phys. Rev. B*, vol. 83, no. 7, 2011.

[145] H. Tsunetsugu, Y. Hatsugai, K. Ueda, and M. Sigrist, "Spin-liquid ground state of the half-filled Kondo lattice model in one dimension", *Phys. Rev. B*, vol. 46, no. 5, p. 3175, 1992.

[146] I. Affleck, "The Kondo screening cloud: what it is and how to observe it", in *Perspectives of Mesoscopic Physics - Dedicated to Prof Yoseph Imry's 70th Birthday*, 2009.

[147] A. P. Ramirez, P. Coleman, P. Chandra, E. Brück, A. A. Menovsky, Z. Fisk, and E. Bucher, "Nonlinear susceptibility as a probe of tensor spin order in uru2si2", *Phys. Rev. Lett.*, vol. 68, no. 17, p. 2680, 1992.

[148] C. Brünger and F. F. Assaad, "Single-hole dynamics in the Kondo necklace and bilayer Heisenberg model on a square", *Phys. Rev. B*, p. 205107, 2006.

[149] S. Doniach, "The Kondo lattice and weak antiferromagnetism", *Physica B+C*, vol. 91, pp. 231 – 234, 1977.

[150] V. N. Kotov, O. Sushkov, Z. Weihong, and J. Oitmaa, "Novel approach to description of spin-liquid phases in low-dimensional quantum antiferromagnets", *Phys. Rev. Lett.*, vol. 80, no. 26, p. 5790, 1998.

[151] F. F. Assaad, "Quantum Monte Carlo simulations of the half-filled two-dimensional Kondo lattice model", *Phys. Rev. Lett.*, vol. 83, p. 796, 1999.

[152] W. Brenig, "Finite-temperature properties of the two-dimensional SU(2) Kondo necklace", *Phys. Rev. B*, vol. 73, p. 104450, 2006.

[153] H. Rezania, A. Langari, and P. Thalmeier, "Green's function approach to quantum criticality in the anisotropic Kondo necklace model", *Phys. Rev. B*, vol. 77, p. 094438, 2008.

[154] S. Sachdev and R. N. Bhatt, "Bond-operator representation of quantum spins: Mean-field theory of frustrated quantum Heisenberg antiferromagnets", *Physical Review B (Condensed Matter)*, vol. 41, no. 13, pp. 9323–9329, 1990.

Acknowledgements

I gratefully acknowledge the support from many people. Without their kindness it would not have been possible to finish this work. First of all, I like to thank Prof. Dr. Gertrud Zwicknagl for mentoring this thesis and giving me the opportunity to collaborate with her. Her acceptance and encouragements made the completion of this work possible. Above all, I am extremely fortunate and honored to work with Dr. Peter Thalmeier of the Max-Planck-Institut für Chemische Physik fester Stoffe, whom I indebtedly learned a lot not just from countless scientific discussions and insightful ideas, but also from his excellence and vast expertise. I am most obliged to his patience, guidance, and daily support throughout the whole time period of my doctoral studies.

I am in great debt to Dr. Burkhard Schmidt, for providing invaluable suggestions and productive feedbacks regarding physics and computer programming techniques and technologies. Working with him is an indispensable experience for me that lead to a most valuable collaboration. Out of many ideas that I learned from him, simplicity was the most essential lesson for me. I would like to thank also my friends and colleagues from the Max-Planck-Institut für Chemische Physik fester Stoffe, who supported me during my time in there. In particular I am grateful to Dr. Alireza Akbari, Dr. Deepa Kasinathan, and Ms. Claudia Strohbach. I acknowledge the kind financial support of Max-Planck-Institut für Chemische Physik fester Stoffe, and the International Max Planck Research School for “Dynamical Processes in Atoms, Molecules and Solids”.

Last, but by no means least, I thank my friends from Dresden, Tehran, and all over the world, for their support and encouragements, and my family, for all the love and understanding.

For errors or inadequacies that may exist in this work, the responsibility is entirely my own.

With love, this work is dedicated to Farideh, Nader, Forough, Nahid, Fatemeh, Maryam, Sarah, and the memory of Fereydoon.

Lebenslauf

11.1.1983	geboren in Teheran, Iran
1989 – 1994	Schulzeit in der Grundschule, Teheran
1994 – 2001	Mittelschule und Sekundarschule im Programm der Begabtenförderung
2001	Beginn des Studiums der Physik in Shahid-Beheshti Universität in Teheran
2001 – 2004	Teilzeitarbeit als Softwareentwickler in der Firma Negasht
2002 – 2008	Lehrtätigkeit in Programmierung in der Allameh-Helli Mittelschule
2005	B.Sc in Physik
	Beginn des Studiums der Physik in Sharif Universität in Teheran
2006	Lehrtätigkeit Physik in der Allameh-Helli Sekundarschule
2008	M.Sc in Physik mit dem Thema „Finite-Temperature Properties of the Anisotropic One-Dimensional Heisenberg Model in a Transverse Magnetic Field“
2009	Beginn mit dem Promotionsstudium am Max-Planck-Institut für Chemische Physik fester Stoffe (MPI-CPfS), und den Technischen Universitäten Dresden und Braunschweig. Anfertigung der vorliegenden Dissertation „Frustrated Quantum Magnets and Correlated Kondo Systems“, betreut von Prof. Dr. G. Zwicknagl und Priv. Doz. Dr. P. Thalmeier